FROM SAMPLE TO SIGNAL IN LASER-INDUCED BREAKDOWN SPECTROSCOPY: AN EXPERIMENTAL ASSESSMENT OF EXISTING ALGORITHMS AND THEORETICAL MODELING APPROACHES

By

KATHLEEN KATE HERRERA

A DISSERTATION PRESENTED TO THE GRADUATE SCHOOL
OF THE UNIVERSITY OF FLORIDA IN PARTIAL FULFILLMENT
OF THE REQUIREMENTS FOR THE DEGREE OF
DOCTOR OF PHILOSOPHY

UNIVERSITY OF FLORIDA

2008

© 2008 Kathleen Kate Herrera

"I may not be there yet, but I'm closer to my goal than I was yesterday."−Anonymous

ACKNOWLEDGMENTS

I would like to express my deepest gratitude, first and foremost, to my research adviser, Dr. James D. Winefordner for all the support, guidance and advice he has given me all these years. I would not have made it this far if he had not encouraged me at a time when I felt that I could not go on much longer. I consider myself very fortunate and I am incredibly proud to have been a part of the Winefordner group. I would also like to acknowledge to Dr. Nicoló F. Omenetto for patiently and enthusiastically following my research from beginning to end. I learned how to be a good and effective researcher from our regular meetings in his office. His passion for science is truly amazing and contagious. This research would not have been what it is now if not for all his wonderful scientific ideas. I am also grateful to Dr. Benjamin W. Smith for all the invaluable help he has provided in the lab and for all the insightful comments during group meetings.

I have much appreciation for Dr. Igor B. Gornushkin for teaching me the Monte Carlo LIBS approach and LIBS in general. I am completely in awe of his knowledge about spectroscopy, mathematics, physics, and programming. I am greatly indebted to him for the time he has taken to modify the MATLAB program for me countless of times. I would also like to thank Dr. Elisabetta Tognoni from the Institute for Chemical-Physical Processes of CNR in Pisa, Italy for sharing with me her knowledge on CF-LIBS and for patiently corresponding with me through e-mail to answer all my questions on CF-LIBS.

I thank all the previous and current members of the Winefordner-Omeneto-Smith research group, especially Dr. Galan Moore, Heh-Young Moon and Benóit Lauly for all the insightful discussions on LIBS. Lastly, I would like to extend my sincerest gratitude to my family and friends for their unwavering support and encouragement.

TABLE OF CONTENTS

page

ACKNOWLEDGMENTS 4

LIST OF TABLES 9

LIST OF FIGURES 14

LIST OF ABBREVIATIONS, CONSTANTS AND SYMBOLS 19

Abbreviations 19
Constants 20
Symbols 20
Roman Symbols 20
Greek Symbols 23

ABSTRACT 26

CHAPTER

1 BACKGROUND AND SIGNFICANCE 28

2 BRIEF OVERVIEW OF LASER-INDUCED BREAKDOWN SPECTROSCOPY 35

Introduction 35
Historical Background 35
General LIBS Process 37
Laser-Material Coupling 38
Ablation, Vaporization and Breakdown 39
Expansion 40
Emission 42
Cooling and Crater Formation 43

3 SPECTRAL LINE PROFILE, BROADENING MECHANISMS AND INSTRUMENTAL FUNCTION 49

Introduction 49
Line Broadening Mechanisms 50
Doppler Broadening 50
Pressure Broadening 51
Van der Waals broadening. 51
Resonance broadening. 52
Stark broadening. 53
Self-Absorption Broadening 53
Self-absorption check. 54
Duplication factor. 56

Instrumental Function 56
Influence of Slits 57
Influence of Aberrations 57
Spherical aberration 58
Coma. 58
Astigmatism. 58
Influence of Diffraction 59
Overall Line Profiles 59

4 EXPERIMENTAL CHARACTERIZATION OF INSTRUMENTAL SYSTEM AND OPTIMIZATION OF OPERATING CONDITIONS 67

Introduction 67
Experimental Set-up 67
Calibration of the Micrometer Slit Dial 69
Optimization of the Slit Width 71
Development of a Method for Spectral Data Acquisition 72
Determination of the Instrumental Function 75
Determination of the Detector Spectral Efficiency 77
Determination of the Effect of CCD Pixel Binning 77
Optimization of the Number of Accumulated Laser Shots and Sampling Procedure 78

5 QUANTITATIVE STANDARD-FREE ALGORITHMS IN LASER-INDUCED BREAKDOWN SPECTROSCOPY 94

Introduction 94
Calibration-Free Laser-Induced Breakdown Spectroscopy (CF-LIBS) 94
Working Hypotheses 94
Stoichiometric ablation. 95
Local thermodynamic equilibrium. 98
Optically thin plasma. 102
Measurement of Integrated Line Intensity 103
Determination of Electron Number Density 105
Saha-Boltzmann method. 105
Stark broadening method. 105
Determination of Laser-Induced Plasma Temperature 109
Boltzmann plot method. 109
Saha-Boltzmann plot method. 110
Determination of Relative Concentration and Experimental Factor 111
Monte Carlo Simulated Annealing Optimization Method for Laser-Induced Breakdown Spectroscopy (MC-LIBS) 112
Working Hypotheses and General Theoretical Considerations 112
Calculation of Total Number Density, Temperature and Their Initial Distributions 113
Calculation of Number Density of Atoms, Ions and Electrons 116
Calculation of Emission Spectral Radiance and Line Profile 117

Rough approximation. 117
Detailed approximation. 119
Spectral line profile. 120
Solution to the Inverse Problem 121

6 COMPARATIVE STUDY OF TWO STANDARD-FREE APPROACHES IN LASER-INDUCED BREAKDOWN SPECTROSCOPY 129

Introduction 129
Experimental 131
Results and Discussion 132
Standard-Free Analysis of Aluminum Alloys 132
General assessment of procedure. 132
Determination of electron number density and temperature. 135
Determination of relative composition. 138
Spatially-Resolved Standard-Free Analysis of Aluminum Alloy 141
Spatially-resolved emission spectra. 141
Determination of electron number density and temperature. 144
Determination of relative composition. 147
Conclusion 149

7 SEMI-QUANTITATIVE ANALYSIS OF DIFFERENT SAMPLES BY CALIBRATION-FREE LASER-INDUCED BREAKDOWN SPECTROSCOPY 200

Introduction 200
Experimental 203
Results and Discussion 204
Temporally-Resolved Analysis of Aluminum Alloys 204
Quantitative Analysis of Brass 208
Calibration-free LIBS. 208
CF-LIBS versus conventional LIBS. 210
Quantitative Analysis of Aluminum Alloys 211
Calibration-free LIBS. 211
CF-LIBS versus conventional LIBS. 214
Quantitative Analysis of Soils 215
Quantitative Analysis of Different Types of Alloys 217
Conclusion 219

8 CONCLUSION AND FUTURE WORK 258

Summary and Concluding Remarks 258
Future Research Directions 261

APPENDIX

A CALCULATION OF RADIAL EXPANSION VELOCITY PROPORTIONALITY CONSTANT IN MC-LIBS 264

B CALCULATION OF THE TOTAL ELEMENT NUMBER DENSITY IN MC-LIBS.....267

C CALCULATION OF PLASMA TEMPERATURE IN MC-LIBS.....270

D CALCULATION OF ATOM, ION AND ELECTRON NUMBER DENSITIES IN MC-LIBS.....274

E CERTIFIED CONCENTRATION VALUES OF REFERENCE STANDARDS.....277

LIST OF REFERENCES.....279

BIOGRAPHICAL SKETCH.....291

LIST OF TABLES

Table		page
4-1	Results of the calibration of the micrometer slit dial	92
4-2	Calculated central wavelengths for spectral data acquisition	93
5-1	Calculated FWHM of reduced Stark profiles in nm per cgs field strength unit	128
6-1	List of spectral lines used in the CF-LIBS analysis of Al alloy B8	182
6-2	List of spectral lines used in the CF-LIBS analysis of Al alloy D33	183
6-3	List of spectral lines used in the CF-LIBS analysis of Al alloy S4	184
6-4	List of spectral lines used in the CF-LIBS analysis of Al alloy SM10	185
6-5	List of spectral lines used in the CF-LIBS analysis of Al alloy V14	186
6-6	List of spectral lines used in the CF-LIBS analysis of Al alloy Z8	187
6-7	List of spectral lines used in the Monte Carlo LIBS simulations	189
6-8	Electron number density (in cm^{-3}) and temperature (in K) values calculated using MC-LIBS and CF-LIBS for 6 Al alloy standards	190
6-9	Relative concentration values and relative errors (in %) calculated from CF-LIBS analysis of aluminum alloys B8 and D33	190
6-10	Relative concentration values and relative errors (in %) calculated from CF-LIBS analysis of aluminum alloys S4 and SM10	190
6-11	Relative concentration values and relative errors (in %) calculated from CF-LIBS analysis of aluminum alloys V14 and Z8	191
6-12	Number densities (in cm^{-3}) calculated from MC-LIBS analysis of six different aluminum alloys	191
6-13	Relative concentration values and relative errors (in %) calculated from MC-LIBS and CF-LIBS analysis of Al alloy B8	191
6-14	Relative concentration values and relative errors (in %) calculated from MC-LIBS and CF-LIBS analysis of Al alloy D33	192
6-15	Relative concentration values and relative errors (in %) calculated from MC-LIBS and CF-LIBS analysis of Al alloy S4	192

6-16 Relative concentration values and relative errors (in %) calculated from MC-LIBS and CF-LIBS analysis of Al alloy SM10 192

6-17 Relative concentration values and relative errors (in %) calculated from MC-LIBS and CF-LIBS analysis of Al alloy V14 192

6-18 Relative concentration values and relative errors (in %) calculated from MC-LIBS and CF-LIBS analysis of Al alloy Z8 193

6-19 Atomic masses (in g) of different elements in the aluminum alloy sample 193

6-20 Electron number density (in cm^{-3}) and temperature (in K) values calculated using MC-LIBS and CF-LIBS for Al alloy standard D33 at different spatial positions 193

6-21 Sigmoidal fitting parameters for the spatial evolution of temperature 194

6-22 Sigmoidal fitting parameters for the spatial evolution of electron number density 194

6-23 Relative concentration values (in %) calculated from CF-LIBS analysis of aluminum alloys D33 at different spatial positions 195

6-24 Relative errors (in %) of calculated CF-LIBS concentration values at different spatial positions 195

6-25 Relative concentration values, relative errors (in %) and number densities (in cm^{-3}) calculated from MC-LIBS and CF-LIBS analysis of Al alloy D33 at spatial position A 196

6-26 Relative concentration values, relative errors (in %) and number densities (in cm^{-3}) calculated from MC-LIBS and CF-LIBS analysis of Al alloy D33 at spatial position B 196

6-27 Relative concentration values, relative errors (in %) and number densities (in cm^{-3}) calculated from MC-LIBS and CF-LIBS analysis of Al alloy D33 at spatial position C 196

6-29 Relative concentration values, relative errors (in %) and number densities (in cm^{-3}) calculated from MC-LIBS and CF-LIBS analysis of Al alloy D33 at spatial position E 197

6-30 Relative concentration values, relative errors (in %) and number densities (in cm^{-3}) calculated from MC-LIBS and CF-LIBS analysis of Al alloy D33 at spatial position F 197

6-31 Relative concentration values, relative errors (in %) and number densities (in cm^{-3}) calculated from MC-LIBS and CF-LIBS analysis of Al alloy D33 at spatial position G 198

6-32 Relative concentration values, relative errors (in %) and number densities (in cm^{-3}) calculated from MC-LIBS and CF-LIBS analysis of Al alloy D33 at spatial position H.....198

6-33 Relative concentration values, relative errors (in %) and number densities (in cm^{-3}) calculated from MC-LIBS and CF-LIBS analysis of Al alloy D33 at spatial position I. 198

6-34 Relative concentration values, relative errors (in %) and number densities (in cm^{-3}) calculated from MC-LIBS and CF-LIBS analysis of Al alloy D33 at spatial position J. 198

6-35 Relative concentration values, relative errors (in %) and number densities (in cm^{-3}) calculated from MC-LIBS analysis of Al alloy D33 at spatial position K 199

7-1 Electron number density, temperature and relative standard deviation calculated for aluminum alloy B8 at 5 different delay times.....248

7-2 Electron number density, temperature and relative standard deviation calculated for aluminum alloy SM10 at 6 different delay times.....248

7-3 Relative concentration values (in %) calculated from CF-LIBS analysis of aluminum alloy B8 at 5 different delay times 248

7-4 Relative concentration values (in %) calculated from CF-LIBS analysis of aluminum alloy SM10 at 6 different delay times.....249

7-5 Relative errors (in %) calculated from CF-LIBS analysis of aluminum alloy B8 at 5 different delay times 249

7-6 Relative errors (in %) calculated from CF-LIBS analysis of aluminum alloy SM10 at 6 different delay times 249

7-7 Relative concentration values and relative errors (in %) calculated from CF-LIBS analysis of 10 NIST brass standards 250

7-8 Temperature, electron number density and minimum electron number density for LTE calculated from CF-LIBS analysis 10 NIST brass standards 250

7-9 Spectroscopic parameters of Zn spectral lines used in the calibration curves for brass analysis.....251

7-10 Zn calibration curve parameters and limits of detection.....251

7-11 Relative concentration of Zn (in %) calculated using CF-LIBS and conventional LIBS approaches.....251

7-12 Relative errors (in %) in calculated Zn concentration 251

7-13 Electron number density and minimum electron number density for LTE calculated for 6 Al alloy standards at different ambient pressures 252

7-14 Laser-induced plasma temperatures calculated for 6 Al alloy standards at different ambient pressures....252

7-15 Relative concentration values and relative errors (in %) calculated from CF-LIBS analysis of aluminum alloy B8 at 3 different pressures....253

7-16 Relative concentration values and relative errors (in %) calculated from CF-LIBS analysis of aluminum alloy SM10 at 3 different pressures....253

7-17 Relative concentration values and relative errors (in %) calculated from CF-LIBS analysis of aluminum alloy D33 at 2 different pressures....253

7-18 Relative concentration values and relative errors (in %) calculated from CF-LIBS analysis of aluminum alloy S4 at 2 different pressures 254

7-19 Relative concentration values and relative errors (in %) calculated from CF-LIBS analysis of aluminum alloy V14 at 2 different pressures....254

7-20 Relative concentration values and relative errors (in %) calculated from CF-LIBS analysis of aluminum alloy Z8 at 2 different pressures 254

7-21 Spectroscopic parameters of spectral lines used in the calibration curves for Al alloy analysis....255

7-22 Cu and Si calibration curve parameters and limits of detection 255

7-23 Relative concentration of Cu (in %) calculated using CF-LIBS and conventional LIBS approaches....255

7-24 Relative errors (in %) in calculated Cu concentration....255

7-25 Relative concentration of Si and relative errors (in %) calculated using CF-LIBS and conventional LIBS approaches 255

7-26 Relative concentration values and relative errors (in %) calculated from CF-LIBS analysis of Montana soil NIST SRM 2711 and Estuarine sediment NIST SRM 1646 ...256

7-27 Relative concentration values and relative errors (in %) calculated from CF-LIBS analysis of Buffalo River sediment NIST SRM 2704 and Montana soil NIST SRM 2710....256

7-28 Relative concentration values and relative errors (in %) calculated from CF-LIBS analysis of Canadian soils SO-2 and SO-3 256

7-29 Temperature, electron number density and minimum electron number density for LTE calculated from CF-LIBS analysis of 6 soil standards 256

7-30 Relative concentration values and relative errors (in %) calculated from CF-LIBS analysis of Ti alloy pellet Alfa Aesar 88395 and Ti alloy metal NIST SRM 654b 257

7-31 Relative concentration values and relative errors (in %) calculated from CF-LIBS analysis of Zn alloys NIST SRM 627 and 629 257

7-32 Relative concentration values and relative errors (in %) calculated from CF-LIBS analysis of Ni alloy pellet NIST SRM 882 and Cu-Ni alloy metal NIST SRM 1276a ...257

7-33 Temperature and electron number density calculated from CF-LIBS analysis of 6 alloy standards 257

E-1 Elemental percentage composition of South African aluminum alloy standards 277

E-2 Elemental percentage composition of NIST brass standards.....277

E-3 Elemental percentage composition of NIST and Canadian soil standards 278

E-4 Elemental percentage composition of different alloy standards 278

LIST OF FIGURES

Figure		page
2-1	Diagram of a typical laboratory LIBS apparatus	44
2-2	Schematic representation of the main processes in LIBS	45
2-3	Schematic illustration of the laser-induced plasma and various interaction zones	46
2-4	Timing of the different physical phenomena observed during the plasma expansion	47
2-5	Temporal history of the laser-induced plasma showing the different predominant emitting species	47
2-6	Simplified energy level diagram showing the different transitions which produce the continuum and line emissions	48
3-1	Line profile, half-width, kernel and wings of a spectral line	61
3-2	Spectral line profiles as a function of increasing atomic concentration	62
3-3	An example of a self-reversed spectral line profile	62
3-4	Self-absorption check	63
3-5	Convolution of the entrance and exit slit widths	64
3-6	Effect of spherical aberration on a lens	64
3-7	Effect of coma	64
3-8	Effect of astigmatism on a concave mirror used off-axis	65
3-9	Effect of diffraction	65
3-10	Overall spectral line profile	66
4-1	Experimental LIBS set-up for experiments under atmospheric conditions	81
4-2	Schematic diagram of cable connections and the corresponding timing sequence used in the experimental system	82
4-3	Experimental LIBS set-up for experiments under vacuum conditions	83
4-4	Ray diagram for Fraunhofer diffraction by a single slit and the corresponding intensity distribution and image of the diffraction pattern	84
4-5	Experimental set-up used in the calibration of the micrometer slit dial	85

4-6 Experimental set-up used in the optimization of the slit width and measurement of the instrumental function 85

4-7 Effect of slit width on the normalized intensity distribution and full width at half maximum 86

4-8 Example of a merged spectrum 87

4-9 A schematic diagram of the components of a Czerny-Turner-based spectrometer and the respective rays and angles formed when light enters the slit 87

4-10 Determination of the instrumental function 88

4-11 Determination of the detector spectral efficiency 89

4-12 Effect of binning 90

4-13 Effect of laser shot accumulation 91

5-1 Temporal evolution of the Hα line at 656.272 nm 123

5-2 Boltzmann plot obtained using Fe I lines in an aluminum alloy sample 123

5-3 Energy levels of atomic (I) and ionic (II) species 124

5-4 Saha-Boltzmann plots of different elements 125

5-5 Illustration of the coordinate system used in the semi-empirical vacuum plasma expansion model 126

5-6 Correlation between the experimental and simulated spectrum 126

5-7 Extrema of a function in an interval 127

6-1 Section of laser-induced breakdown spectra of different aluminum alloys. 153

6-2 Images of laser-induced plasmas obtained from different aluminum alloy samples 153

6-3 Effect of the number of iterations per parameter on the correlation coefficient *R* and computer run time of a 3.1 GHz PC 154

6-4 The Stark broadened hydrogen alpha line at 656.272 nm in the aluminum alloy spectra used for electron number density determination in CF-LIBS 155

6-5 Saha-Boltzmann plots of selected elements in aluminum alloy sample 156

6-6 Spatial and temporal evolution of temperature and electron number density obtained using the MC-LIBS approach for aluminum alloy samples. 157

6-7 Spatial evolution of temporally-integrated temperature and electron number density obtained using the MC-LIBS approach for aluminum alloy sample 159

6-8 Comparison of electron number densities and plasma temperatures calculated using MC-LIBS and CF-LIBS approaches.....160

6-9 Relative elemental compositions of aluminum alloy samples obtained with CF-LIBS compared with certified values 161

6-10 Relative percentage errors of the elemental composition calculated using CF-LIBS 162

6-11 Comparison of experimental spectra of aluminum alloys and the best-fit simulated spectra calculated with MC-LIBS.....163

6-12 Relative concentration values obtained using MC-LIBS and CF-LIBS compared with certified values (black bars) 164

6-13 Relative errors of calculated concentration values obtained using MC-LIBS and CF-LIBS 165

6-14 Image of the laser-induced plasma obtained from an Al alloy D33 using a delay time of 50 ns and gate width of 100 ns under 0.1 mbar pressure.....166

6-15 Spatially-resolved spectra of different neutral and singly-ionized lines.....167

6-16 Spectrally-integrated intensities of different neutral and singly-ionized lines at various spatial positions.....168

6-17 Spatial frequency distribution profile of different species in the aluminum alloy plasma 169

6-18 Electron number density and temperature values calculated at different spatial positions using CF-LIBS and MC-LIBS 170

6-19 Saha-Boltzmann plots of selected elements in aluminum alloy sample D33 at different spatial positions.....171

6-20 Spatial and temporal evolution of temperature and electron number density obtained using the MC-LIBS approach for aluminum alloy sample D33 172

6-21 Spatial evolution of temporally-integrated temperature and electron number density obtained using the MC-LIBS approach for aluminum alloy sample D33 176

6-22 Relative concentration values at different spatial positions calculated with CF-LIBS ...177

6-23 Comparison of experimental spectra of aluminum alloy D33 and the best-fit simulated spectra calculated with MC-LIBS at different spatial positions.....178

6-24 Number densities (cm^{-3}) of different elements in the alloy sample calculated at different spatial positions using MC-LIBS 179

6-25 Relative concentration values calculated at different spatial positions using MC-LIBS and CF-LIBS compared with certified values 180

6-26 Relative errors of calculated concentration values at different spatial positions calculated using MC-LIBS and CF-LIBS 181

7-1 Section of the wide spectral range data of aluminum alloy samples at different delay times. 221

7-2 Temporal evolution of the number of identified neutral lines and singly-ionized lines for the different elements present in the aluminum alloy samples 222

7-3 Temporal evolution of laser-induced plasmas obtained from the aluminum alloy samples 224

7-4 Temporal evolution of the electron number density calculated using the Hα line at 656.272 nm for the aluminum alloy samples 225

7-5 Saha-Boltzmann plots of selected lines at different delay times 226

7-6 Temporal evolution of temperature calculated for selected elements in the aluminum alloy samples 228

7-7 Temporal evolution of averaged plasma temperatures 229

7-8 Elemental concentrations of the aluminum alloy samples calculated from CF-LIBS at different delay times 230

7-9 Relative errors calculated from CF-LIBS results of the aluminum alloy samples 232

7-10 LIBS measurements of 10 NIST brass standards 233

7-11 Results of the CF-LIBS analysis of 10 NIST brass standards 234

7-12 Calibration curves constructed for the quantitative analysis of Zn in brass samples 235

7-13 Images of the laser-induced plasma obtained from different aluminum alloys at different ambient pressures. 236

7-14 Section of laser-induced breakdown spectra of the aluminum alloy samples at different ambient pressures 237

7-15 Calculated electron number density and temperature values for different aluminum alloys under different ambient pressures. 238

7-16 Relative elemental concentrations of the aluminum alloy samples at different ambient pressures 239

7-17 Relative errors of calculated elemental concentrations of the aluminum alloy samples at different ambient pressures 240

7-18 Calibration curves constructed for the quantitative analysis of Cu and Si in the aluminum alloy samples 241

7-19 LIBS measurements of 6 soil standards 242

7-20 Relative elemental concentrations of soil standards calculated from CF-LIBS 243

7-21 The relative errors of calculated elemental concentrations of soil standards and the calculated electron number density and temperature values of the laser-induced plasmas 244

7-22 LIBS measurements of 6 different alloy standards 245

7-23 Relative elemental concentrations of alloy standards calculated from CF-LIBS. 246

7-24 The relative errors of calculated elemental concentrations of alloy standards and the calculated electron number density and temperature values of the laser-induced plasmas 247

8-1 A general schematic diagram of CF-LIBS and MC-LIBS analysis from sample to signal 263

LIST OF ABBREVIATIONS, CONSTANTS AND SYMBOLS

Abbreviations

AES	Atomic emission spectroscopy
CF-LIBS	Calibration-free laser-induced breakdown spectroscopy
CNR	Consiglio Nazionale delle Richerche
GF-AAS	Graphite furnace atomic absorption spectroscopy
IB	Inverse bremsstrahlung
ICCD	Intensified charge-coupled device
ICP-AES	Inductively-coupled plasma atomic emission spectroscopy
ICP-MS	Inductively-coupled plasma mass spectrometry
IPCF	Istituto per i Processi Chimico-Fisici
LA	Laser ablation
LA-OES	Laser ablation optical emission spectroscopy
LIBS	Laser-induced breakdown spectroscopy
LIPS	Laser-induced plasma spectroscopy
LSS	Laser spark spectroscopy
LTE	Local thermodynamic equilibrium
LTSD	Lens-to-sample distance
MC-LIBS	Monte Carlo simulated annealing optimization method for laser-induced breakdown spectroscopy
MPI	Multiphoton ionization
RSD	Relative standard deviation
SAC	Self-absorption correction
S/N	Signal-to-noise ratio

Constants

c	Speed of light in vacuum	2.9979×10^{8} m s^{-1}
e	Elementary charge	1.6022×10^{-19} C
ε_0	Permittivity of free space	8.8542×10^{-12} C^2 N^{-1} m^{-2}
h	Planck's constant	6.6261×10^{-34} J s
k_B	Boltzmann constant	1.3807×10^{-23} J K^{-1}
m_e	Electron mass	9.1094×10^{-31} kg
N_A	Avogadro's number	6.0221×10^{23} mol^{-1}
σ	Stefan-Boltzmann's constant	5.6705×10^{-8} W m^{-2} K^{-4}

Symbols

Roman Symbols

A_{ki}	Transition probability for spontaneous emission between states k and i, s^{-1}
a	Width of the beam emerging from the dispersion element, mm
$a(r,t)$	Line damping parameter, dimensionless
B_{λ}^{bb}	Blackbody spectral radiance, (J s^{-1} cm^{-2} sr^{-1} nm^{-1})
B_{lu}^{j}	Einstein coefficient for absorption transition, cm^3 erg^{-1} s^{-1} Hz
C^s	Relative number density of species s
D	Duplication factor, dimensionless
d	Laser spot diameter, cm
d	Groove spacing, nm $groove^{-1}$
ΔE	Energy difference, eV
E_i	Energy of lower level i
E_k	Energy of upper level k
F	CF-LIBS experimental factor, cm^{-3}

F_{abs}	Absolute spectral efficiency
F_{det}	Optical efficiency of detection system
$F_{rel}(\lambda)$	Optical efficiency of detection system
f	Focal length of the spectrometer, mm
f_{ik}	transition oscillator strength, dimensionless
G	Free-free Gaunt factor, dimensionless
G	Number of grooves per millimeter, grooves mm^{-1}
g_i	Statistical weight of lower level i, dimensionless
g_k	Statistical weight of upper level k, dimensionless
j	Plasma constituent
k_{ion}	Ionization rate coefficient, $cm^3\ s^{-1}$
l	Optical path length, cm
$\bar{I}(\lambda)$	Wavelength-integrated intensity of emitted light, W cm^{-3}
I_{ki}	Integrated line intensity, photons $cm^{-3}\ s^{-1}$
$\overline{I_{ki}}$	Corrected experimental integrated line intensity
$I_{ki,meas}$	Measured integrated line intensity, counts
$I_1(\lambda)$	Measured line profile without the spherical mirror
$I_2(\lambda)$	Measured line profile with the spherical mirror
I_ν	Radiation spectral radiance, erg $s^{-1}\ cm^{-2}\ Hz^{-1}\ sr^{-1}$
M	Atomic or molecular weight, g mol^{-1} or amu
m	Mass, kg
m	Diffraction order, dimensionless
N_{pixel}	Number of column pixels
n_D	Number of particles in the Debye sphere, cm^{-3}

n_e	Electron number density, cm^{-3}
$n^I,\ n_a^j$	Neutral atom number density, cm^{-3}
$n^{II},\ n_i^j$	Singly-ionized number density, cm^{-3}
$n^j(r,t)$	Total number density of constituent *j* as a function of radial coordinate *r* and time *t*, cm^{-3}
n_{tot}	Total particle number density, cm^{-3}
n_k^s	Number density of species *s* at level *k*, cm^{-3}
n_{tot}^s	Total number density of species *s*, cm^{-3}
P_{lu}^j, P_ν	Normalized line profile, dimensionless
p	Pressure, dyne cm^{-2}
q	Energy loss due to radiation per unit volume per unit time, erg cm^{-3} s^{-1}
R	Correlation coefficient, dimensionless
R	Interparticle distance, cm
R	Outer boundary of plasma
R_λ	Ratio of spectral line intensities with two plasma lengths, dimensionless
R^c	Ratio of intensities of continuum radiation with two plasma lengths, dimensionless
R_d	Reciprocal linear dispersion, nm mm^{-1}
r	Radial coordinate of particle in the plasma, cm
s	Atomic species
T_e	Electron temperature, K
T_{exc}	Excitation temperature, K
T_{eV}	Temperature, eV
T_{ion}	Ionization temperature, K
T_K	Temperature, K

t_{delay}	Delay time, s
t_{exp}	Plasma expansion time, s
t_{gate}	Gate width, s
t_{ion}	Ionization time , s
$U(T)$	Partition function, dimensionless
$u(r,t)$	Radial expansion velocity, cm s^{-1}
V	Perturbation of energy level, J
$V(t)$	Velocity of plasma boundary, cm s^{-1}
w	Electron-impact half-width, nm
w	Slit width, μm
w_{pixel}	Pixel size, μm
z	Charge number, dimensionless

Greek Symbols

α	Incidence angle
α	Ion-broadening parameter, dimensionless
α	Polarizability, m^3
α	Target absorptivity, cm^{-1}
$\alpha_{1/2}$	Reduced Stark profile, nm
α^j	Ratio of specific heat capacities of species *j*, dimensionless
β	Diffraction angle
ε	Internal energy per unit mass, erg g^{-1}
$\varepsilon_{c,\lambda}$	Non-integrated continuum radiation intensity, W cm^{-3} nm^{-1}
$\zeta(t)$	Proportionality coefficient between collective velocity of particles and radius, s^{-1}
θ	Grating rotation angle

θ	Polar angle
$\kappa(\lambda)$,	Absorption coefficient, cm^{-1}
κ_ν'	Total absorption coefficient, cm^{-1}
κ^{Σ}_{mean}	Planck mean absorption coefficient, cm^{-1}
κ^{Σ}_{ff}	Free-free absorption coefficient, cm^{-1}
κ^{Σ}_{fb}	Free-bound absorption coefficient, cm^{-1}
κ^{Σ}_{bb}	Bound-bound absorption coefficient, cm^{-1}
$\Lambda(\nu,t)$	Line shift normalized by Doppler width, dimensionless
λ	Wavelength, nm
$\Delta\lambda$	Spectral line width, nm
$\Delta\lambda_D$	Doppler line width, nm
$\Delta\lambda_d$	Diffraction-limited spectral bandpass, nm
$\Delta\lambda_G$	Gaussian line width, nm
$\Delta\lambda_I$	Instrumental line width, nm
$\Delta\lambda_L$	Lorentzian line width, nm
$\Delta\lambda_{range}$	Spectral range, nm
$\Delta\lambda_{res}$	Resonance line width, nm
$\Delta\lambda_s$	Geometric spectral bandpass, nm
$\Delta\lambda_{Stark}$	Stark line width, nm
$\Delta\lambda_{Stark\ shift}$	Stark line shift, nm
$\Delta\lambda_V$	Voigt line width, nm
$\Delta\lambda_{VDW}$	Van der Waals line width, nm
$\Delta\lambda_{VDW\ shift}$	Van der Waals line shift, nm
μ^j	Atomic mass of species j, g

ν	Frequency, Hz
ξ	Free-bound continuum correction factor, dimensionless
ξ_z	Factor for electron atom structure, dimensionless
ρ	Generalized number density of species, cm^{-3}
$\tau(\lambda)$	Optical depth, dimensionless
Φ	Exit or take-off angle
υ	Plasma expansion velocity, $10^5 - 10^6$ cm s^{-1}
χ	Ionization potential, eV
$\Delta\chi$	Lowering of the ionization potential, eV
Ω	Solid angle, sr

Abstract of Dissertation Presented to the Graduate School
of the University of Florida in Partial Fulfillment of the
Requirements for the Degree of Doctor of Philosophy

FROM SAMPLE TO SIGNAL IN LASER-INDUCED BREAKDOWN SPECTROSCOPY: AN EXPERIMENTAL ASSESSMENT OF EXISTING ALGORITHMS AND THEORETICAL MODELING APPROACHES

By

Kathleen Kate Herrera

August 2008

Chair: James D. Winefordner
Major: Chemistry

In recent years, laser-induced breakdown spectroscopy (LIBS) has become an increasingly popular technique for many diverse applications. This is mainly due to its numerous attractive features including minimal to no sample preparation, minimal sample invasiveness, sample versatility, remote detection capability and simultaneous multi-elemental capability. However, most of LIBS applications are limited to semi-quantitative or relative analysis due to the difficulty in finding matrix-matched standards or a constant reference component in the system for calibration purposes. Therefore, methods which do not require the use of reference standards, hence, standard-free, are highly desired.

In this research, a general LIBS system was constructed, calibrated and optimized. The corresponding instrumental function and relative spectral efficiency of the detection system were also investigated. In addition, development of a spectral acquisition method was necessary so that data in the wide spectral range from 220 to 700 nm may be obtained using a non-echelle detection system. This requires multiple acquisitions of successive spectral windows and splicing the windows together with optimum overlap using an in-house program written in Q-basic.

Two existing standard-free approaches, the calibration-free LIBS (CF-LIBS) technique and the Monte Carlo simulated annealing optimization modeling algorithm for LIBS (MC-LIBS), were experimentally evaluated in this research. The CF-LIBS approach, which is based on the Boltzmann plot method, is used to directly evaluate the plasma temperature, electron number density and relative concentrations of species present in a given sample without the need for reference standards. In the second approach, the initial value problem is solved based on the model of a radiative plasma expanding into vacuum. Here, the prediction of the initial plasma conditions (i.e., temperature and elemental number densities) is achieved by a step-wise Monte Carlo optimization of calculated synthetic spectra in order to obtain a close correlation with experimentally measured ones.

The two approaches were applied to the laser-induced breakdown spectra of different types of samples: aluminum alloys, brass, soil, and powder alloys. Experiments were performed under atmospheric and vacuum conditions. Spatially- and temporally-resolved studies were also carried out. From the results obtained with CF-LIBS, the technique can be considered semi-quantitative to quantitative depending on the experimental parameters used and the type of samples analyzed. Comparison of CF-LIBS with conventional calibration curves was also carried out and the results obtained from CF-LIBS agree well with certified values. From the simulations performed using the Monte Carlo approach, relatively high correlation coefficients between synthetic and calculated spectra were obtained ($R > 0.9$).

CHAPTER 1
BACKGROUND AND SIGNFICANCE

Laser-induced breakdown spectroscopy (LIBS) is a fast and useful qualitative [1, 2] and semi-quantitative [3, 4] technique for the determination of elemental composition of a wide range of materials, such as metal alloys [5-7], glasses [8-10], liquids [11-13], aerosols [14-16], painted artworks [17-19], archaeological artifacts [20-22], etc., under various analytical conditions. LIBS is based on the spectral and time-resolved analysis of atomic and ionic emission from a laser-induced plasma (LIP), obtained by focusing an intense laser pulse onto the sample surface [23]. The material present in the focal volume undergoes instantaneous ablation and vaporization accompanied by rapid dissociation into atoms and ions in excited states, as well as free electrons [24]. During the expansion and the cooling of the plasma in the ambient atmosphere or in vacuum, several simultaneous processes occur which produce the continuum and line emission: bremsstrahlung (free-free transitions), radiative recombination (free-bound transitions), and radiative relaxation of excited atoms, ions or molecules (bound-bound transitions) [25]. Temporal resolution is required for discrimination between early plasma continuum and delayed atomic and ionic line emissions. The latter allow for a qualitative identification of species in the plasma while their relative line intensities give a quantitative measure of the concentration of the corresponding elements [26].

The increasing popularity of LIBS over more conventional methods of atomic spectroscopy, such as GF-AAS and ICP-AES, is due to its several attractive features [27]. It is a simple and relatively non-invasive technique, because both the ablation and excitation processes are performed in a single step, in situ and in real time, and only a very small amount of the sample is vaporized. Sample preparation is often unnecessary; therefore, the risk of sample contamination is reduced and measurement time is shortened. The sample versatility and

simultaneous multi-elemental capability of LIBS make this method suitable for a number of diverse applications, such as space exploration [28-30], environmental monitoring [31-33], forensic analysis [34-36], military and homeland security [37-39], cultural heritage [20-22], and production control and quality assurance [40-42].

In spite of the numerous advantages of LIBS, there are a few drawbacks which limit the applicability of the method, particularly for quantitative analysis. The most relevant are its poor figures of merit (accuracy, precision, detection limits) in comparison to conventional techniques. According to Castle et al. [43], the unsatisfactory analytical performance of LIBS is due to several factors, including sample inhomogeneity, shot-to-shot variability of the laser pulse, and matrix effects. The latter is one of, if not the most challenging aspect in LIBS quantitative analysis and is characterized by the strong dependence of atomic emission spectra on relatively small variations in sample composition [44]. Matrix effects can be minimized by calibration with proper reference samples having the same matrix composition or by normalization of the analyte signal by a reference signal [23]. However, in the case of highly variable or fully unknown matrices, these approaches would limit the method to semi-quantitative analysis [26]. It should also be emphasized that in many applications it is difficult to find matrix-matched standards or a constant reference component in the system. Hence, methods which do not require the use of reference standards (standard-free) are highly desired.

Detailed investigations of the various types of matrix effects have been carried out in order to maximize the potential of LIBS for quantitative measurements. Wisbrun et al. [45] studied the effect of persistent aerosols produced above soil and sand samples. Their results show that aerosol production is dependent on laser repetition rate. They also demonstrated that a linear dependence exists between particle size and analytical signal as predicted by their zero order

model. Eppler et al. [46] investigated the effects of chemical speciation and matrix composition on lead and barium measurements using soil and sand matrices. Their results suggest that analyte emission is dependent on both factors. Suggestions to explain this dependency were given but no definite conclusions were made. Bulatov et al. [47] employed LIBS to investigate the matrix effects of sand/soil mixtures through a combination of spatial and temporal resolutions. They noted that there is an optimum distance from the surface for obtaining the highest trace element sensitivity in a given matrix. The same group performed further matrix effect studies by shockwave propagation and concluded that matrix effects can be characterized by the amount of energy coupled into the plasma [48]. Gondal et al. [49] investigated the role of different binding materials for trace Mg analysis using LIBS and determined that KBr gives the highest LIBS sensitivity, largest ablated mass and deepest crater compared to starch, poly(vinyl alcohol), silver and aluminum. They attributed these to the differences in latent heat of vaporization for various elements in the binder and the grain size of matrix.

Several solutions to the matrix effects problem have been proposed in recent years. Chaleard et al. [50] developed an analytical procedure which enables matrix effects correction for quantitative multi-matrix analysis. Their approach is based on the assumption that intensities of emission lines are a function of the ablated mass and the plasma excitation temperature, which were evaluated by acoustic wave measurements and two-line intensity ratio, respectively. In their results, normalization of the net intensities with respect to these two parameters yielded a single slope calibration curve for a series of samples with varying matrices. Xu et al. [51] established a method which compensates for the pulse-to-pulse fluctuations in LIBS based on the assumption that a similar variation pattern is observed for both the signal intensity and baseline. They applied their model to the analysis of 50 single-shot spectra of Zn-contaminated aerosols

and obtained a linear relationship between the corrected intensities and Zn concentration. They noted that their method provides absolute concentrations and does not require an internal reference standard, although standard samples are still necessary to construct the calibration curves. However, according to Gornushkin et al. [52], the method proposed by Xu et al. lacks generality in its applicability based on their own experimental results and the underlying analytical and physical interpretation of the single-shot model. They argued that although the method has been shown to work for the analysis of Zn in particulate matter, the success of the application might be restricted to very few matrices or might have been fortuitous. Gornushkin et al. [53] then proposed a surface density-based calibration method for the determination of magnesium in powdered samples in which a "mechanical" effect was assumed to strongly influence the emission intensities. The authors recommended the technique for the analysis of various types of finely ground samples where ~10% precision and ~10-20% relative error are acceptable.

The aforementioned studies are just few of the numerous investigations that various groups have done on matrix effects; each can be regarded as a research tool for the progress of LIBS in quantitative applications and possibly towards the realization of the ultimate goal in analytical spectroscopy, i.e., absolute analysis. Nevertheless, there is still a need for a procedure that will completely take into account the adverse influence of matrix effects on LIBS quantitative analysis or, at least, alleviate the difficulties related to the requirement of matrix-matched reference standards, particularly for very complex cases, such as multi-elemental determinations in *a priori* unknown conditions. Accordingly, Ciucci et al. [54-57] developed and patented an innovative LIBS algorithm that eliminates the use of reference standards and calibration curves. This calibration-free method (CF-LIBS) allows quantitative information to be obtained by

interpretation of the experimental results using the basic physics of the laser-induced plasma, assuming that some fundamental conditions, such as local thermodynamic equilibrium (LTE), stoichiometric ablation, and optically thin plasma, are verified.

In close relation to the goal of absolute analysis, several publications on theoretical modeling of laser-induced plasma expansion have an inherent yet untapped analytical significance. Some models are capable of predicting the detailed spectral distribution of plasma radiation. Mazhukin et al. [58] mathematically analyzed the influence of radiative transfer on the dynamics of laser-induced plasma of aluminum vapor using two-dimensional radiation gas dynamics with multi-group diffusion approximation to describe the plasma radiation transfer. The model was able to predict the plasma spectrum not only in a wide spectral region but also in a narrow energy window. The latter has great significance in real plasma spectroscopy because observations are usually done in narrow spectral regions where the details of line profiles are more evident. De Giacomo et al. [59] performed a temporal evolution study of electron, atom and ion population densities in the plasma produced by KrF excimer laser on TiO and TiO_2 targets. The authors proposed a state-to-state collisional radiative model to describe kinetic processes and obtained good quantitative agreement with the experimentally determined particle number densities and temperature. Furthermore, Casavola et al. [60] developed a fluid dynamic model with chemical kinetics and determined the effect of different initial parameters, such as temperature, pressure, plume size and expansion velocity on the plasma expansion. Using the model, the authors were able to predict temporal evolution of titanium concentration at a specific distance from the target. In a rather similar aspect to that of CF-LIBS, a radiative, semi-empirical model of laser-induced plasma vacuum expansion proposed by Gornushkin et al. [61-64] also has the capability of providing quantitative analytical information. This is based on the

unique aspect of the model which allows for the prediction of initial conditions of the plasma expansion by a direct correlation of calculated synthetic spectra with experimentally measured ones using the Monte Carlo simulated annealing optimization approach (MC-LIBS).

As previously mentioned, there is an apparent need for a procedure or procedures that can be applied to samples of varying degrees of complexities without prior knowledge of its environment. The possibility of having reliable standard-free routines for quantitative LIBS analysis that could lead to absolute measurements opens up several avenues for the general applicability of LIBS to any type of samples under different analytical situations. In the present study, two out of several existing standard-free approaches in the literature were experimentally evaluated, the CF-LIBS and MC-LIBS approaches. Neither technique requires reference standards nor calibration curves. Each method was evaluated for its applicability in the quantitative analysis of different certified samples, such as aluminum alloy, brass, soil, powdered alloys, etc., in both atmospheric and vacuum conditions. CF-LIBS and MC-LIBS approaches were also applied to the analysis of spatially-resolved measurements performed under vacuum conditions. Development of a method for an efficient spectral data acquisition was also carried out in order to obtain an experimental spectrum with wide wavelength coverage using a gated, non-echelle LIBS system. The latter addressed the problem of the narrow wavelength range capability of the detection system used in this research. The assessment of the two approaches involved the optimization and calibration of several experimental parameters and the determination of the spectral efficiency and instrumental function of the detection system. In addition, each method was generally classified as quantitative, semi-quantitative or qualitative with quantitative estimates [65] depending on the relative percentage errors obtained from the

analysis of the standard samples. Limitations in the applicability of each method were also assessed based on the results of the experimental evaluation.

CHAPTER 2
BRIEF OVERVIEW OF LASER-INDUCED BREAKDOWN SPECTROSCOPY

Introduction

The laser-induced breakdown spectroscopy (LIBS) technique, also referred to as laser-induced plasma spectroscopy (LIPS), laser spark spectroscopy (LSS) or laser ablation optical emission spectroscopy (LA-OES), falls under the category of atomic emission spectroscopy (AES). In LIBS, the plasma is formed when a high-powered pulsed laser is focused onto or into a small volume of the sample, producing an irradiance inside the volume exceeding several megawatts per centimeter squared (10^6-10^9 W cm^{-2}). LIBS has been considered as one of the simplest and most convenient analytical methods for trace elemental analysis of solid, liquid and gaseous samples because the laser-induced plasma is used as vaporization, atomization, excitation and ionization source.

In this chapter, a succinct summary of the historical development of LIBS is described, as well as a general overview of the basic principles and characteristics of LIBS. The scope of the discussion of pertinent LIBS processes and mechanisms is limited to analysis of solid materials at high irradiances (>10^9 W cm^{-2}). In addition, a brief review of recent applications of LIBS to solid analysis is presented herein.

Historical Background

The development of LIBS has been summarized and discussed in great detail in Ref. [66] and several excellent review articles [67-76] which deals with different aspects of the technique have appeared in the past decade, hence, only the most significant events are included here. In 1960, Maiman [77] constructed the first optically-pumped ruby laser and shortly thereafter, Brech and Cross [78] observed and reported the first ruby laser-produced spectra. However, in their work and in most of the research which ensued, the laser was used mainly for ablation and

vaporization and an auxiliary electrical spark was required for cross-excitation to further enhance the signal intensity. In 1963, the first analytical application of laser-induced plasma for spectrochemical analysis of surfaces was demonstrated by Debras-Gudéon and Liodec [79], who used a "giant pulse" or Q-switched laser which produced craters with diameters of 100 μm. In 1964, Runge et al. [80] and Ferguson et al. [81] carried out similar experiments on metals and powdered solids, respectively. In the same year, temporal resolution was introduced through the introduction of streak cameras and rotating mirrors in the detection system in order to discriminate the early plasma continuum emission from late atomic and ionic line emissions. Also during this time period, commercial instruments were being manufactured by Carl Zeiss Jena Co. (Germany), Jarrell-Ash Corp. (USA) and JEOL Ltd. (Japan) but were discontinued by the late 1970s since they could not compete in accuracy and precision with conventional spark spectroscopy [66].

Following the initial investigations on laser-induced plasmas, more fundamental studies and applications of LIBS had been carried out, although most of the research works were published in the Russian literature [82-85]. Subsequently, the very first studies on matrix effects began in the late 1970s [86-88]. The initial findings showed that physical conditions and chemical composition play significant roles in LIBS signal intensities and repeatability.

Since the mid-1980s, there has been a continuous increase in research activity in LIBS which can be attributed mainly to the availability of more robust, smaller, faster and less costly laser sources, the development of sensitive gated imaging detectors, such as the intensified charge coupled devices (ICCD) and the advent of high-resolution dispersion optics, such as echelle-based spectrographs [74]. As LIBS advanced further into the last decade of the 20th century, more research groups emerged in the US, Australia, Canada, Spain and Italy. It was

also during this period that remote elemental analysis and portable instruments were demonstrated [89, 90]. In 1999, the Palleschi research group developed and patented the calibration-free LIBS (CF-LIBS) procedure for quantitative analysis without the requirement of reference standards or calibration curves [56, 57].

The development of LIBS from the invention of the first ruby laser to its recent adoption for planetary geological application on a mission to Mars in 2009 demonstrates the high-level of maturity that LIBS has achieved over the past several years. There is also an increasing interest in LIBS as an analytical method due to its high versatility. This is evident in the number of publications related to fundamentals and applications of LIBS that reached about 1,200 in the last five years. An exponential trend in the progression of LIBS publications is predicted to happen in the years to come [66].

General LIBS Process

In LIBS, the plasma is generated when a laser pulse of sufficient energy is focused on the sample surface. A typical laboratory LIBS system is shown in Fig. 2-1. The plasma emission is collected using a lens, as shown in Fig. 2-1, or by a fiber optic cable. The collected plasma emission is spectrally resolved by a dispersive wavelength selection system and then analyzed by a detector.

A single laser shot corresponds to one LIBS measurement. Generally, LIBS signal intensities from multiple laser shots are either accumulated or averaged. Previous studies have shown that this improves the analytical figures of merit of the measurement and averages out any slight inhomogeneity in the sample composition [91].

The laser-induced plasma is weakly ionized and consists of excited atoms and ions and free electrons. It is electrically neutral and the charged species often act in a collective manner [66]. The mechanisms of plasma formation and evolution consist of several complex phenomena

which are dependent on critical parameters such as laser irradiance, wavelength and pulse width, thermo-optical properties of the material and the pressure and composition of surrounding atmosphere [75, 92]. A simplified schematic representation of the main processes involved is shown in Fig. 2-2 [75] and a detailed discussion of each step and several related processes is presented herein.

Laser-Material Coupling

The initial step is characterized by the coupling of the optical energy into a small area of the solid (Fig. 2-2a). The amount of laser energy absorbed within the material is determined by the absorption and reflectance coefficients of the target, particularly in metals [93, 94]. The target absorptivity α, in cm^{-1}, which is critical in the determination of the breakdown threshold of metals, is expressed as:

$$\alpha = \frac{4\pi n}{\lambda} \tag{2-1}$$

where λ is the laser wavelength (cm), n is the imaginary part of the bulk refractive index and $1/\alpha$ is the absorption length (cm) which determines the real interaction thickness between laser irradiance and the target. The reflectance, on the other hand, has been reported to decrease under laser irradiation due to the apparent shortening of collision time between electrons and lattice. However, surface contamination, e.g. presence of absorbates or oxide layers, or macroscopic defects, e.g. flakes, pits or craters, lowers the reflectance of the surface compared to the bulk material. The presence of these impurities and defects actually affects the laser-material coupling to a great extent as they decrease the laser irradiance threshold to initiate vaporization of the surface [94].

Ablation, Vaporization and Breakdown

According to Russo [92], at irradiances higher than 10^9 W cm^{-2}, using lasers operating in the nanosecond regime or shorter, the absorption of energy results in an explosion or ablation of the material in the focal volume (Fig. 2-2b). The material removal is due to the instantaneous heating of the surface past its vaporization temperature. Energy dissipation through vaporization from the surface is relatively slow compared to the laser pulse duration and the pressure above the surface prevents further vaporization until the underlying material reaches a critical temperature. Once the temperature of the substrate is raised beyond its critical value through heat conduction, the surface then explodes and leads to the formation of a rapidly expanding vapor plume in front of the sample. Wen et al. [95] also pointed out that the rate of vaporization of the material at this point in the process is dependent only on the background gas pressure and not on the type of background gas. Chan and Russo [96] also considered the ablation process to be stoichiometric in this regime because of the more uniform non-thermal heating and the more explosive release of the ejected material. This implies that the composition of the latter is representative of the composition of the sample.

Consequently, the plasma formation is initiated when the breakdown threshold is reached and is generally a two-step process. The initial step is mainly influenced by the pressure above the surface and the laser wavelength. At low pressures, or at short wavelengths, where collision effects are considered negligible, the predominant mechanism is multiphoton ionization (MPI) which can be expressed as:

$$\mathrm{M} + mh\nu \rightarrow \mathrm{M}^+ + \mathrm{e}^- \qquad (2\text{-}2)$$

where m is the number of photons. This results when the number of photons simultaneously absorbed is greater than the ionization potential of an atom [97, 98]. Alternately, at high

pressures, or at long wavelengths, the plasma is initiated by inverse bremsstrahlung (IB) where electrons gain sufficient energy by absorption of laser radiation during collisions with neutrals. For this process to occur, an initial or seed electron in the focal volume must be present. As stated by Weyl [98], the presence of aerosols in the focal volume initiates breakdown since these particles heat up under laser irradiation and could create seed electrons by thermionic emission. Electrons can also be created when laser irradiances are high since the electric field may be strong enough to pull an electron in an outer shell out of its orbital through the tunnel effect. Also, electrons can be produced from a small amount of ionization which can be attributed to cosmic rays and natural radioactivity of the earth [98].

The second step in the plasma initiation is avalanche ionization, also referred to as cascade ionization or electron cascade growth, where the electrons formed by MPI or the energetic electrons produced by IB can impact ionize an atom or molecule through the reaction:

$$e^- + M \rightarrow M^+ + 2e^- \qquad (2\text{-}3)$$

This will lead to a cascade breakdown causing an exponential increase in the number of free electrons [98]. Once the plasma formation is initiated, the incoming energy from the laser pulse can sustain a high-temperature plasma in which the species in the vaporized material undergoes excitation.

Expansion

Descriptively, the plasma that is initially formed appears as a bright flash of intense light followed by a loud snapping sound due to the shockwave produced as it undergoes expansion outward in all directions from the focal volume as depicted in Fig. 2-2c. As the plasma propagates and interacts with its surroundings, it evolves through several different transient phases which are very well described in the literature [95, 99, 100]. A schematic drawing of the

laser-induced plasma and various interaction zones is presented in Fig. 2-3 [101, 102]. The corresponding timing of the different physical phenomena observed during the plasma expansion is illustrated in Fig. 2-4 [95]. The initial rate of plasma expansion is on the order of 10^5 m s^{-1} and is greatest towards the focusing lens of the laser beam since this is the source direction of optical energy into the plasma. This creates an ellipsoidal-shaped plasma due to non-isotropic expansion [76].

The propagation of the high-temperature and high-pressure plasma causes compression of the background gas producing an external shockwave which strengthens when the vapor plume reaches a critical electron number density (Fig. 2-4) [95, 100]. The heated gas layer then begins to strongly absorb a significant fraction of the laser energy and rapidly heats to plasma conditions. This begins a self-sustaining absorption process that results in plasma propagation into the ambient gas [99]. According to Root [99], the energy transfer from the plasma to the atmosphere during the expansion is a combination of thermal conduction, radiative transfer and shockwave heating, all of which are dependent on one or more of the following experimental parameters: laser energy, target vapor composition, ambient gas composition and pressure and laser wavelength [95, 103-105].

In viewpoint of Fig. 2-3, several regions and discontinuities are present during the expansion due to the interaction between the plasma and the ambient atmosphere and brief descriptions of each are given herein. The plasma core, which is the densest part of the plasma, only exists for the first several ns. In the simulated model developed by Wen et al. [100], the vapor plume region is considered the unshocked part of the laser-induced plasma since it is not in direct contact with the external shockwave. The internal shockwave, which occurs from the end of the laser pulse until about 100 ns (Fig. 2-4), is formed in the outer region of the vapor plume

due to the high backpressure created by the external shockwave. Wen et al. [95, 100] pointed out that for a supersonic vapor plume expansion, the internal shockwave is necessary for satisfying the pressure and velocity continuity conditions at the contact surface. In their simulation, the internal shockwave was shown to propagate back and forth between the contact surface and sample surface. The contact front simply describes the transition from material gas to ambient gas. It also illustrated in Fig. 2-3 that the inner region of the external shockwave is highly ionized compared to the outermost region. This is clearly due to heating of the atmosphere caused by the highly energetic plasma.

Emission

The resulting spectrum evolves rapidly in time due primarily to the pulsed nature of the laser-induced plasma (Fig. 2-2d). A schematic representation of the temporal history of the laser-induced plasma concerning the different predominant emitting species is illustrated in Fig. 2-5 [66]. The timescales shown in Fig. 2-4 and Fig. 2-5 are valid for a plasma initiated at 1 atm using a 1064 nm Nd:YAG laser with a pulse width between 4 and 10 ns. During the onset of the plasma formation when ionization is high, an intense broadband continuum of light dominates the plasma emission until about 300 ns after the laser pulse has been fired. This continuum emission is a result of bremsstrahlung or free-free (ff) transitions and radiative recombination or free-bound (fb) transitions. Line emissions, on the other hand, are due to radiative relaxation of atoms and ions in excited states. These transitions are called bound-bound transitions (bb). The simplified energy level diagram for all these transitions is shown in Fig. 2-6 [25]. In the bremsstrahlung process, photons are emitted when high energy electrons decelerate through collisions. Radiative recombination, on the other hand, occurs when a free electron is captured into an atomic or ionic energy level and liberates its excess kinetic energy in the form of a

photon [25]. Also, more neutral atoms begin to form as electron-ion recombination proceeds throughout the plasma lifetime. Some neutrals may also recombine to form molecules [66].

Temporal resolution is usually carried out in LIBS measurements in order to discriminate the early plasma continuum from late atomic and ionic line emissions. The important experimental parameters for time-resolved detection are delay time, t_{delay} and gate width, t_{gate}, where delay time is the time between the initiation of the laser pulse and the beginning of the gate width and the latter is the integration window during which the plasma emission is recorded (Fig. 2-5) [91].

Cooling and Crater Formation

The plasma starts to cool as its components liberate more energy through radiation or conduction. The cooling process also helps in the formation of polyatomic aggregates and clusters which are deposited together with molten material around the crater after a given time (Fig. 2-2e) [75]. The crater (Fig. 2-2f) that forms after the plasma has ceased has shape and dimensions which are dependent on the properties of the target material and the characteristics of the laser used (energy, pulse width and wavelength).

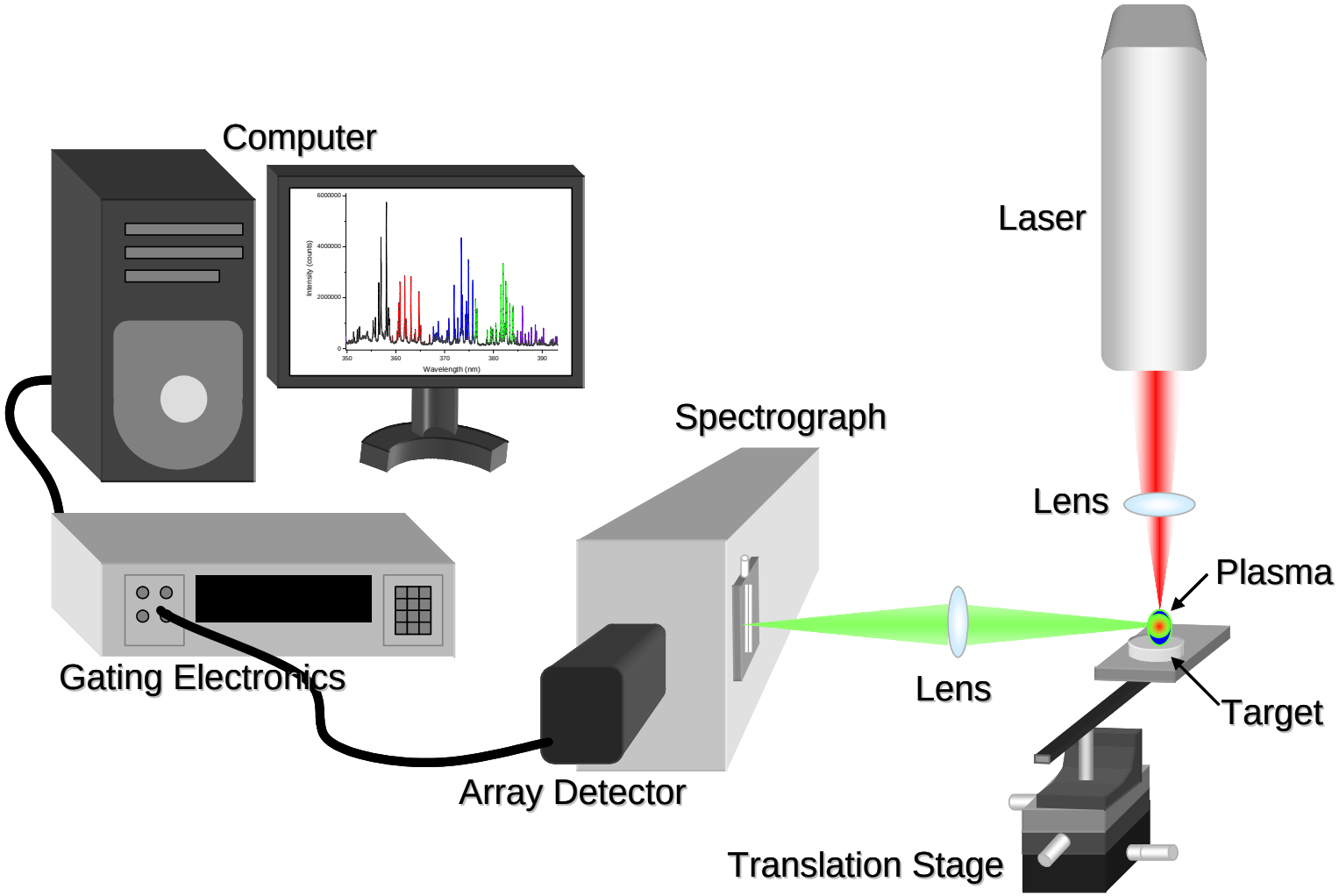

Figure 2-1. Diagram of a typical laboratory LIBS apparatus.

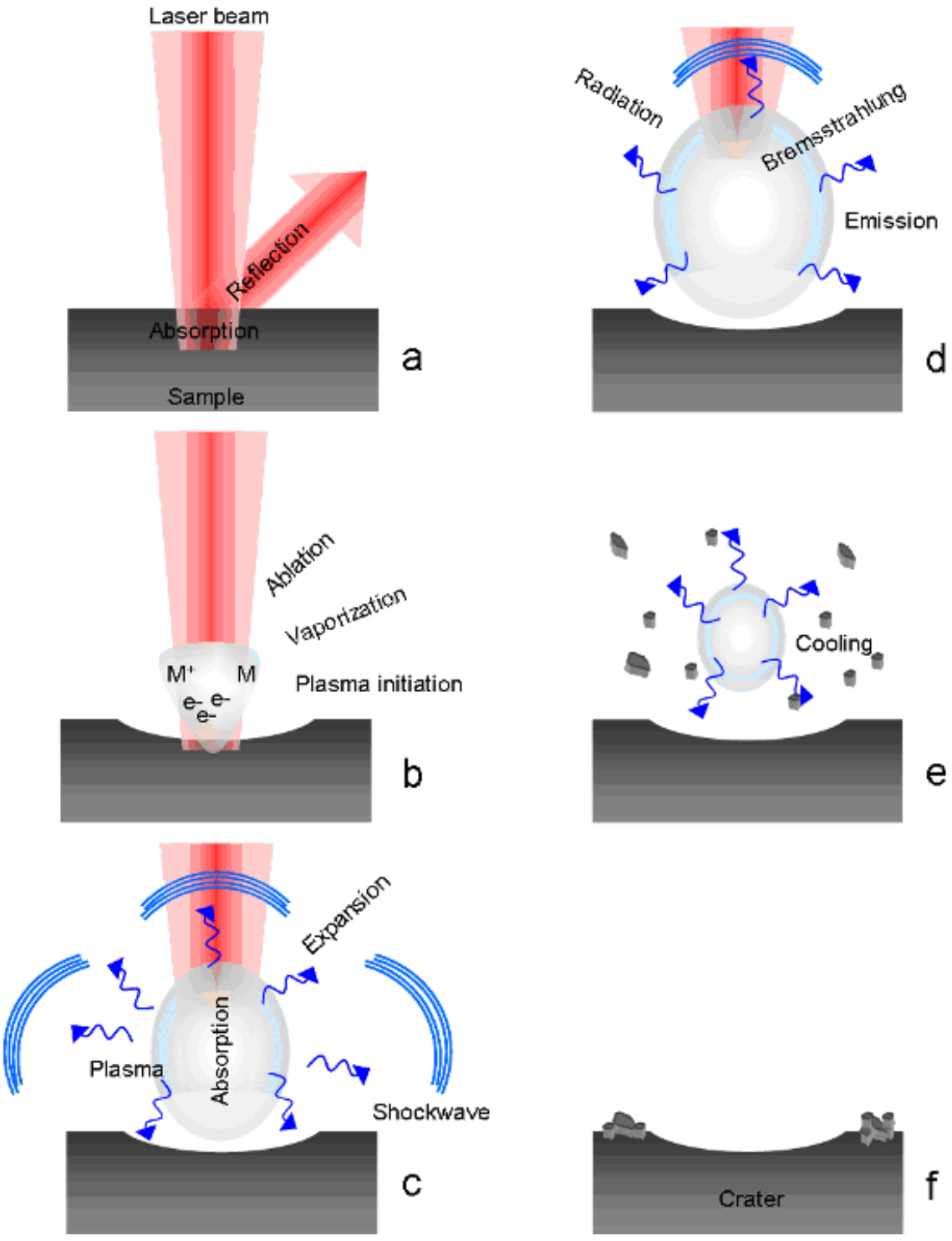

Figure 2-2. Schematic representation of the main processes in LIBS: (a) laser-material coupling, (b) ablation, vaporization and breakdown, (c) expansion and shockwave formation, (d) emission, (e) cooling and (f) crater formation (Adapted from Ref. [75]).

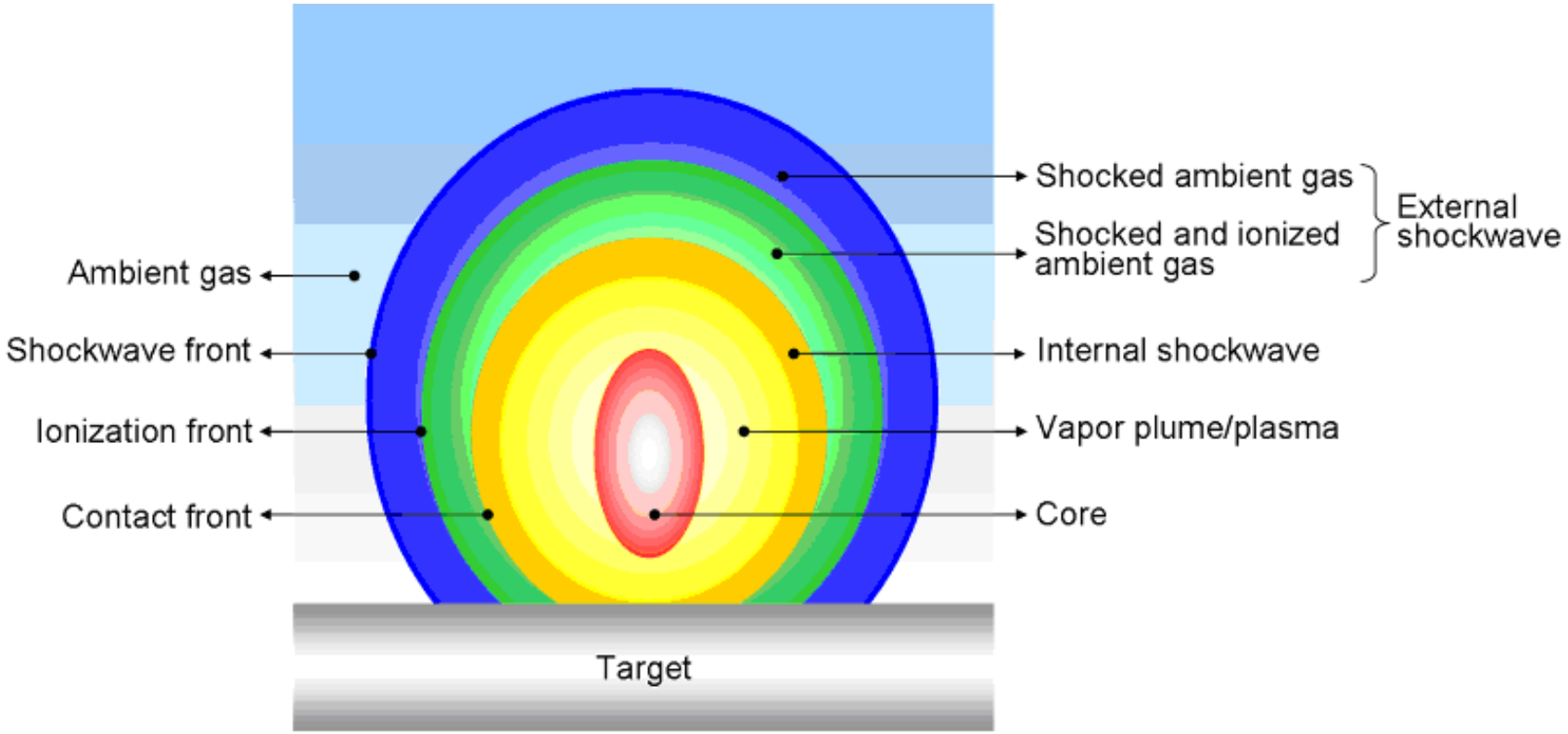

Figure 2-3. Schematic illustration of the laser-induced plasma and various interaction zones (Adapted from Ref. [101]).

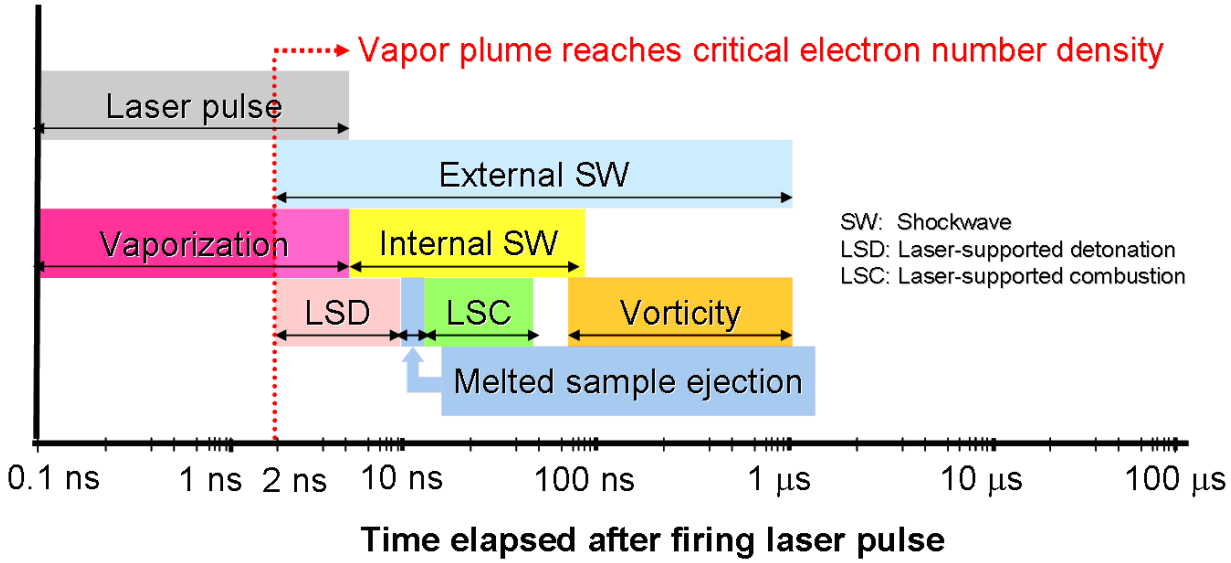

Figure 2-4. Timing of the different physical phenomena observed during the plasma expansion (Adapted from Ref. [95].

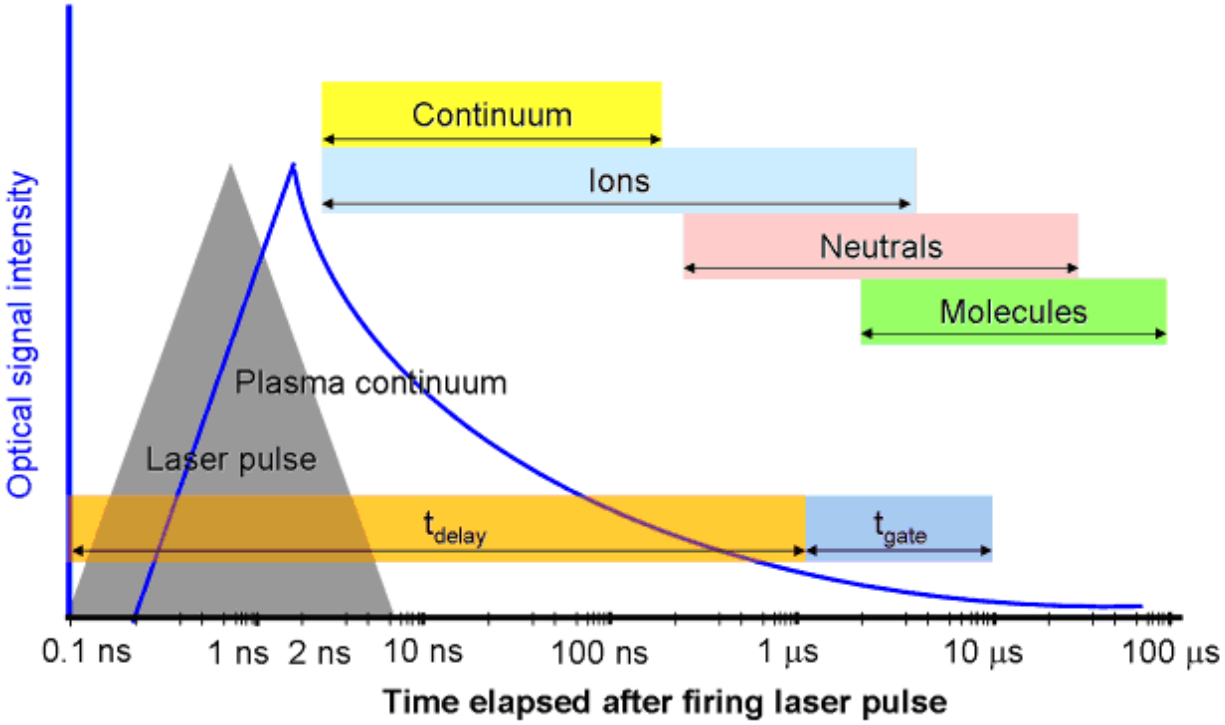

Figure 2-5. Temporal history of the laser-induced plasma showing the different predominant emitting species (Adapted from Ref. [66]).

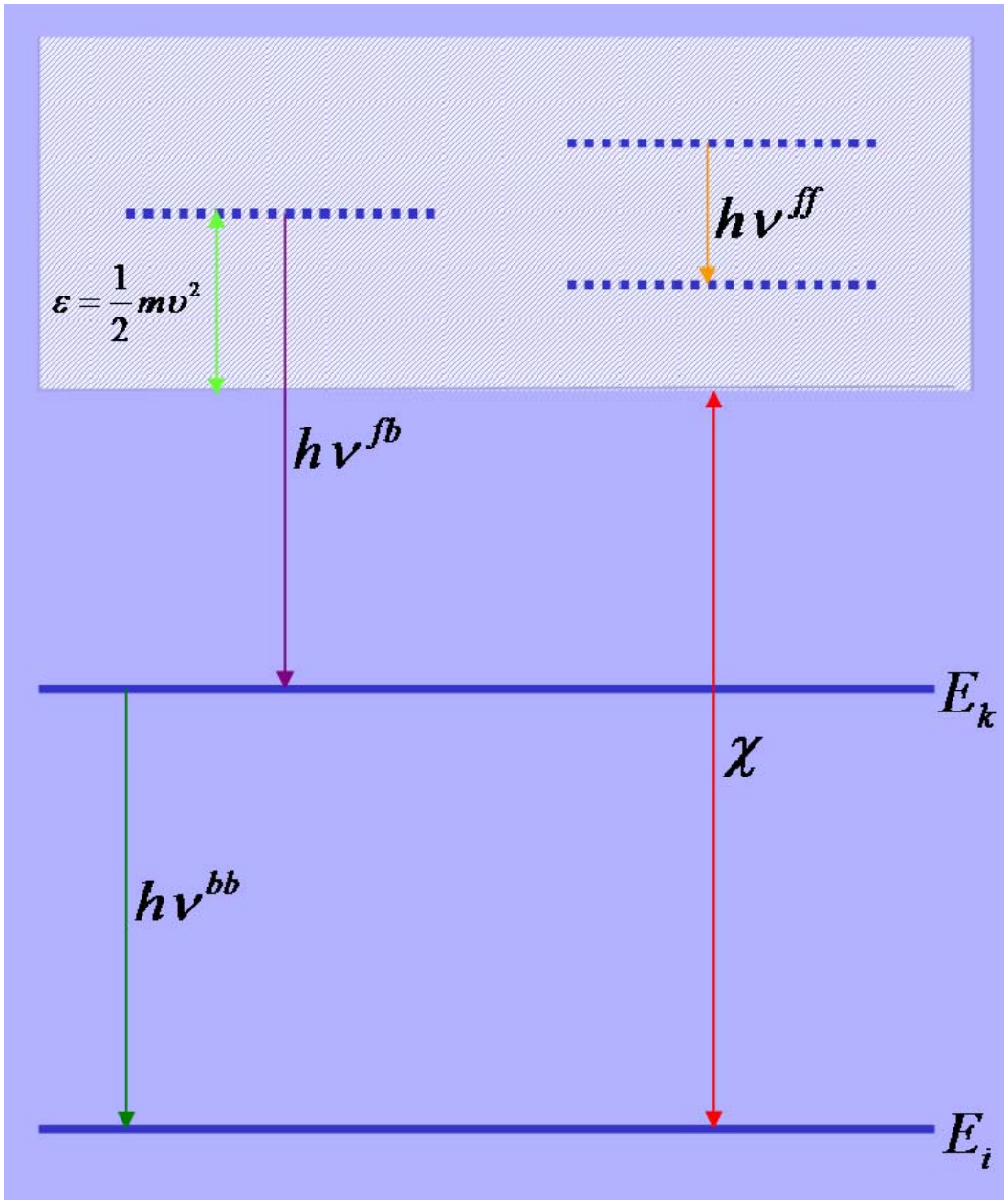

Figure 2-6. Simplified energy level diagram showing the different transitions which produce the continuum and line emissions. Free-free (ff) transitions or bremsstrahlung correspond to loss or gain of energy by an electron in the field of an ion. Free-bound (fb) transitions, also called radiative recombination, occur when an ion captures an electron and makes a radiative transition to a bound state. Bound-bound transitions (bb) correspond to the radiative relaxation of excited atoms, ions or molecules. ε and χ are the kinetic and ionization energies, respectively. (Adapted from Ref. [25])

CHAPTER 3
SPECTRAL LINE PROFILE, BROADENING MECHANISMS AND INSTRUMENTAL FUNCTION

Introduction

During the lifetime of a laser-induced plasma, atoms and ions in the excited states undergo relaxation and radiation at characteristic wavelengths (or frequencies) is released. When emission is recorded, spectral lines with finite widths are obtained. Different broadening mechanisms may contribute to the finite width of a spectral line. These processes result in a spectral distribution of photons in the vicinity of the central wavelength, λ_0 [25, 106]. A hypothetical line profile, $I(\lambda)$, and the different spectral features are illustrated in Fig. 3-1 [107].

In brief, the line kernel is the spectral region within the half-width and the line wings are the spectral regions outside the kernel where $\lambda < \lambda_1$ and $\lambda > \lambda_2$. The wavelength interval, $\Delta\lambda$, between the two wavelengths λ_1 and λ_2 at which the intensity is equivalent to half the maximum intensity, I_0, is known as the full width at half maximum (FWHM) of the line. It is also sometimes referred to as half-width or line width.

The complete shape of the line profile depends on particular broadening process or processes and the importance of any line broadening mechanism is usually measured by the full width at half maximum. However, it should be noted that the FWHM does not necessarily impart information about the wings of the line [25]. In spectrochemical analysis, the spectral line profile is fundamental in the selection of line for analysis, especially if spectroscopic and quantitative information are desired. It also plays an important part in the comprehension of spectral interferences and in the general performance of the analytical calibration function. In addition, the analysis of line profiles is an essential diagnostic tool in the study of physical conditions of the plasma such as temperature and number densities of electrons, atoms and ions.

Only the major broadening effects that are commonly encountered in laser-induced plasmas, e.g., Doppler broadening, pressure broadening and self-absorption, are described herein. In addition, a comprehensive section is devoted to the instrumental function since spectral line profiles are highly convoluted and knowledge of the instrumental broadening is crucial in the determination of spectral line widths due to the atomic system under investigation.

Line Broadening Mechanisms

Doppler Broadening

Doppler broadening is the dominant broadening mechanism several microseconds after the initiation of the laser-induced plasma at low pressures assuming the medium is not optically thick [25, 107]. Doppler broadening is the result of the so-called Doppler effect which is the apparent shift in wavelength of the signal from a source moving towards or away from the observer. In general, a source moving towards an observer causes the wavelength to decrease (blue shift) and a source moving away from an observer causes it to increase (red shift). Hence, a large number of emitting and absorbing atoms along the optical path length which have different velocities will emit a spread of wavelengths [25]. For a Doppler-broadened spectral line the intensity distribution has a Gaussian profile and the statistical distribution of velocities is described by Maxwell's law if the motion is in thermal equilibrium. The full width at half maximum for Doppler broadening can be expressed as [106]:

$$\Delta\lambda_D = \lambda_0 \sqrt{\frac{8k_B T \ln 2}{mc^2}} \tag{3-1}$$

where T is the absolute temperature (K), m is the mass of radiating atom (kg), k_B is Boltzmann's constant (J K^{-1}) and c is the speed of light (m s^{-1}). Evaluation of the constants in Eq. 3-1 and expressing m by the atomic or molecular weight $M = mN_A$ where N_A is the Avogadro's number (mol^{-1}), the Doppler width simplifies to [106]:

$$\Delta\lambda_D = 7.16\times10^{-7}\,\lambda_0\sqrt{\frac{T}{M}} \tag{3-2}$$

Pressure Broadening

This broad type of broadening, also called collisional broadening, is due to the interaction of the emitters with different types of perturbers. The type of interaction can be expressed in terms of perturbation of energy levels, V, which varies with the interparticle distance R as given by [108]:

$$V(R) = \frac{C_x}{R^x} \tag{3-3}$$

where the value of x and the interaction constant C_x depend on the type of interaction considered.

When collisions are between neutral particles, the broadening is called van der Waals broadening and $x = 6$. When the interactions are between similar atoms, the broadening is called resonance or Holtzmark broadening and $x = 3$. When the broadening is due to charged perturbers, the broadening is called Stark broadening and $x = 2$ or 4 for linear or quadratic Stark effect, respectively [25, 106, 108]. Van der Waals and resonance broadening mechanisms are important in weakly ionized plasmas while Stark broadening is most important in highly-ionized and high density plasmas where the strong electric field from the charged species produces a broadening of the transitions between the split atomic levels.

Van der Waals broadening. This broadening is attributed to the interaction between neutral species. Specifically, a fluctuating dipole in the radiating atom induces a dipole to the neutral ground state atom and the corresponding interaction causes line broadening. This dipole-induced dipole interaction can be expressed as [108]:

$$V(R) = -\frac{\alpha p^2}{4\pi\varepsilon_0}\frac{1}{R^6} = \frac{C_6}{R^6} \tag{3-4}$$

where α is the polarizability of the perturber in m^3, p^2 is the mean square dipole moment, and ε_0 is the permittivity of free space. The negative sign indicates that the force is attractive. In addition, the mean square dipole moment is largest for most highly excited levels which implies that the perturbation undergoes a red shift. However, for small values of α, the force becomes repulsive and the perturbation is a blue shift. The value of x in this case is 12 which is described by the Lennard-Jones potential [108].

The corresponding broadening and shift (in m) due to van der Waals interaction, according to the impact approximation, are given by [109]:

$$\Delta\lambda_{VDW} = 2.71 C_6^{2/5} \upsilon^{3/5} n \frac{\lambda^2}{c} \tag{3-5}$$

$$\Delta\lambda_{VDW,shift} = 0.98 C_6^{2/5} \upsilon^{3/5} n \frac{\lambda^2}{c} \tag{3-6}$$

where λ is the transition wavelength in m, υ is the relative velocity in m s^{-1}, n is the number density of perturbing particles (m^{-3}) and C_6 is the interaction constant in m^6 s^{-1}, as given in Eq. 3-4.

Resonance broadening. This broadening mechanism is also known as Holtzmark broadening and occurs only between identical species. Also, resonance broadening is restricted to lines with the upper or lower level with an electric dipole transition to the ground state (resonance lines). This takes the form of a dipole-dipole interaction which results to symmetrically broadened and unshifted lines [25]. The FWHM in m can be expressed as [109]:

$$\Delta\lambda_{res} = \frac{3}{16}\left(\frac{g_i}{g_k}\right)^{1/2}\left(\frac{\lambda_0^3 e^2 f_{ik}}{\pi^2 \varepsilon_0 m_e c^2}\right) n \tag{3-7}$$

where g_i and g_k are the statistical weights of the lower and upper states, respectively, e and m_e are elementary charge (C) and mass (kg) of the electron, f_{ik} is the transition oscillator strength

(dimensionless) and the rest of the variables have already been defined and can also be found in pp. 19-23.

Stark broadening. The perturbation of the energy levels of a radiating atom by microscopic electric field of ions or electrons is called the Stark effect and it contributes significantly to line width broadening under typical LIBS conditions. For hydrogenic ions, where x =2, the Stark effect is linear which causes the symmetrical splitting of energy levels. The result is a symmetrically broadened, unshifted spectral line [25].

For non-hydrogenic elements, on the other hand, the interaction is described by a quadratic Stark effect where the perturbation is proportional to $1/R^4$. The quadratic Stark effect splits the energy levels asymmetrically and also shifts their center of gravity downwards [25]. The shift is usually towards the red and is the same for ions or electrons. The FWHM of a Stark-broadened line and the corresponding shift (in m) are given by [109]:

$$\Delta\lambda_{Stark} = 2\times10^{-22} w n_e \left[1 + 5.53\times10^{-6} N_e^{1/4} \alpha \times \left(1 - 0.0068 n_e^{1/6} T^{-1/2}\right)\right] \quad (3\text{-}8)$$

$$\Delta\lambda_{Stark,shift} = 1\times10^{-22} w n_e \left[\frac{d}{w} + 6.32\times10^{-6} n_e^{1/4} \alpha \times (1 - 0.0068 n_e^{1/6} T^{-1/2})\right] \quad (3\text{-}9)$$

where n_e is the electron number density in m^{-3}, w is the electron impact half-width in m, d/w is the ratio of shift to width (dimensionless) and α is the ion-broadening parameter (dimensionless).

Self-Absorption Broadening

When a significant fraction of photons emitted by excited atoms is absorbed by atoms in the lower level along the optical path between emission volume and detector, self-absorption occurs. This is common for transitions involving ground or near ground states, i.e., resonance or near-resonance transitions, respectively. Self-absorption distorts and broadens the line profile as shown in Fig. 3-2 [106]. At low atomic concentrations, the entire line profile grows with

concentration. However, as self-absorption occurs, the line profile begins to saturate and attains a flat-top shape (Fig. 3-2).

A related phenomenon to self-absorption is self-reversal which is characterized by a dip at the center of the line profile (Fig. 3-3). This usually occurs if the media does not have homogeneous temperature distribution, i.e., a hot inner core is enveloped by a cooler outer layer of much lower electron number density where the line center can be strongly absorbed [106]. Although, it is very easy to recognize a self-reversed line because of the dip in the line center, it is oftentimes difficult to determine if a line suffers from self-absorption due to the good adherence of Stark-broadened line profiles to dispersion shapes [110].

Self-absorption check. A straightforward experimental check for self-absorption is described by Konjevic [110] where a concave or spherical mirror is placed at the radius of curvature, $r_{c,}$ which is twice the focal length of the mirror. This particular configuration, as shown in Fig. 3-4a, doubles the path length which implies that if a line is not self-absorbed, the signal intensity should double as well. In practical terms, line profiles are recorded with and without the spherical mirror and then one observes whether the profiles are proportional everywhere to the same factor [110]. If the proportionality factor is not preserved for the high intensity region at or near the line center but instead becomes smaller, then self-absorption is present. If the product of the absorption coefficient $\kappa(\lambda)$ and path length l is not large ($\kappa(\lambda)\, l <$ 1), the measured intensity may be corrected to the limit of an optically thin layer ($\kappa(\lambda)\, l \quad 1$) [110]. However, if absorption is extremely large, i.e., $\kappa(\lambda)\, l \quad 1$, the intensity of the plasma radiation approaches that of a blackbody and the line profile cannot be recovered. Konjevic [110] described in detail the steps involved in the evaluation of correction for self-absorbed line

profiles using the configuration described in Fig. 3-4 and only the pertinent steps are briefly discussed herein.

Assuming that the plasma is in local thermodynamic equilibrium (LTE), the intensity of radiation $I_\lambda(\lambda)$ can be expressed as:

$$I_\lambda(\lambda) = B_\lambda^{bb}\left(1 - \exp\left[-\kappa(\lambda)l\right]\right) \tag{3-10}$$

where B_λ^{bb} is the blackbody spectral radiance as given by Planck's law (Eq. 3-11).

$$B_\lambda^{bb} = \frac{2hc^2}{\lambda^5}\frac{1}{\exp\left(hc/\lambda k_B T\right) - 1} \tag{3-11}$$

At the optically thin case where $\kappa(\lambda)\, l \quad 1$, the term $\exp(-\kappa(\lambda)\, l)$ can be simplified to $1- \kappa(\lambda)\, l$, hence, Eq. 3-10 becomes:

$$I_\lambda(\lambda) = B_\lambda^{bb}\kappa(\lambda)l \tag{3-12}$$

The correction factor K is then given by taking the ratio of Eq. 3-12 and Eq. 3-10:

$$K = \frac{\kappa(\lambda)l}{1 - \exp\left[-\kappa(\lambda)l\right]} \tag{3-13}$$

The corrected line profile is then obtained by multiplying the self-absorbed profile with the correction factor K. Experimentally, K can be determined by recording $I_2(\lambda)$ and $I_1(\lambda)$ which are the spectral line profiles recorded with and without the spherical mirror, respectively (Fig. 3-4b). From the spectra recorded, the ratio R_λ can be determined by:

$$R_\lambda = \frac{I_2(\lambda)}{I_1(\lambda)} = 1 + G\exp\left[-\kappa(\lambda)l\right] \tag{3-14}$$

where G is a factor which takes into account the mirror reflectivity and geometrical effects. For the continuum radiation, $\kappa(\lambda) = 0$ and

$$R^c = \frac{I_2^c}{I_1^c} = 1 + G \tag{3-15}$$

$\kappa(\lambda)l$ can be solved by combining Eqs. 3-14 and 3-15:

$$\kappa(\lambda)l = \ln\left(\frac{R^c - 1}{R_\lambda - 1}\right) \tag{3-16}$$

Hence, the correction factor K may be expressed as:

$$K = \frac{\ln\left(\frac{R^c - 1}{R_\lambda - 1}\right)}{1 - \left(\frac{R_\lambda - 1}{R^c - 1}\right)} \tag{3-17}$$

Duplication factor. A parameter also related to self-absorption is the duplication factor, D, which has previously been defined by Alkemade [111] as the relative increase in line intensity (or integral absorption) caused by doubling the product $n_a f_{ik} l$ where n_a is the atomic number density.

$$D = \frac{I(2n_a f_{ik} l) - I(n_a f_{ik} l)}{I(n_a f_{ik} l)} \tag{3-18}$$

This means that when the optical path length is doubled, as in the case described previously when a spherical mirror is used and the medium is optically thin, the duplication factor is unity. However, at the optically thick limits, D approaches a value equal to 0.415 [111].

Instrumental Function

If a source emits radiation which consists of a single monochromatic wavelength λ_0 and is detected by a perfect spectrometer, the output should be identical to the spectrum of the emission which is a perfect line at exactly λ_0. But in reality, spectrometers are not ideal and they produce an apparent spectral broadening of the purely monochromatic wavelength. The line profile now has a finite width and is known as the instrumental line profile or instrumental function.

It is crucial to have knowledge of the instrumental function since emission wavelengths are usually in the same order of magnitude or even narrower than the instrumental profile that the

latter determines its shape. In general, it is always best to virtually eliminate the contribution of instrumental broadening by using high-resolution spectrometer whose instrumental width is of the order of one-tenth or less than the observed experimental profile [110]. Unfortunately, that is not possible in several cases, hence, the next alternative is to deconvolute the line profile and that requires experimental determination of the instrumental function.

The shape of the instrumental profile is a function of various parameters such as:

- width of the entrance slit
- width of the exit slit or the size of pixel in the case of a multi-channel array detector
- diffraction effects
- aberration effects
- quality of the components and alignment of the system

Influence of Slits

If the slits are of finite widths and there are no other contributing effects to broaden the line then the contribution of the slit to the overall instrumental line profile is the convolution of the entrance and exit slit images. Examples of the convolution of the entrance and exit slits depending on their respective widths are illustrated in Fig. 3-5. The FWHM in this case is equal to the geometric spectral bandpass $\Delta\lambda_s$ except at very narrow slit widths where aberration and diffraction effects must be considered. The geometric spectral bandpass is given by [106]:

$$\Delta\lambda_s = R_d \times w_{slit} \tag{3-19}$$

where R_d is the reciprocal linear dispersion (nm mm^{-1}) which is a property of the detection system and represents the number of wavelength intervals contained in each interval of distance along the focal plane and w_{slit} is the slit width.

Influence of Aberrations

Several different forms of aberrations affect the instrumental profile. These aberrations are deviations of the optical elements from ideal or first-order behavior. In actual practice,

aberrations occur in combinations rather than alone. The three most common aberrations for optical systems are spherical aberration, coma and astigmatism.

Spherical aberration. Spherical aberration is the result of rays emanating away from the surface of an optical surface. For converging elements, off-axis or marginal rays are focused closer to the element than paraxial rays. Parallel rays produce a circle in the focal plane [106]. This phenomenon is illustrated in Fig. 3-6. In addition, spherical aberration is dependent on lens shape, orientation and conjugate ratio, as well as on the index of refraction of the materials present [112]. Generally, this form of aberration can be reduced by placing an aperture stop in front or behind the lens to block off-axis rays but this also causes reduction in the irradiance of image.

Coma. Coma arises from differences in the optical path lengths of various rays to the focal plane in an off-axis system. Parallel rays which are striking the lens at a slight angle θ causes the image to develop a comet-like tail, as shown in Fig. 3-7a. This skewing of rays in the focal plane results in the broadening of the base on one side of a spectral line, as depicted in Fig. 3-7b [106]. As with spherical aberration, correction can be achieved by using multiple surfaces. Also, a clearer and sharper image may be obtained by placing an aperture in the optical system to eliminate more off-axis rays [112].

Astigmatism. Another type of aberration usually encountered in optical systems is astigmatism. It arises when the point object is considerably off-axis and results in two distinct focal lengths for rays in two different planes (tangential and sagittal), as shown Fig. 3-8. The figure illustrates that tangential rays from an object come to a focus nearer to the lens than do rays in the sagittal plane [112]. In other words, when an image is evaluated at the tangential

focus, a line in the sagittal direction is observed and vice versa. Astigmatism causes blurring of the image which can result in a loss of wavelength resolution (broadening) [113].

Influence of Diffraction

Diffraction, which is defined as the deviation of light from rectilinear propagation when it encounters an obstacle, is another optical phenomenon which affects the instrumental function [106]. If the slit widths are infinitesimally narrow and aberrations are negligible, the resulting instrumental line profile is that of a classic diffraction pattern. Diffraction affects the shape of the intensity distribution profile by broadening the image by $\Delta\lambda_d$ and rounding off the corners as illustrated in Fig. 3-9. $\Delta\lambda_d$ is the diffraction-limited spectral bandpass which can be expressed as [107]:

$$\Delta\lambda_d = R_d \times w_d = R_d \times \frac{2\lambda f}{a} \tag{3-20}$$

where w_d is the diffraction-limited slit width, f is the focal length of the spectrometer and a is the width of the beam emerging from the dispersion element [106]. Although spectral resolution is limited by aperture diffraction (e.g., grating or prism) not by slit diffraction, it is the latter which imposes a limitation on the transmitted intensity at small slit widths, hence, a lower limit to the useful width of the entrance slit given by w_d in Eq. 3-20 [107].

Overall Line Profiles

Doppler and instrumental line profiles usually have a Gaussian distribution and collisional processes follow a Lorentzian function. When both pressure and Doppler broadening are present along with a substantial contribution from instrumental broadening, the resulting line profile is a combination of Lorentzian and Gaussian line shapes. Assuming that the three broadening types are independent processes, the overall line profile is obtained by convoluting the three profiles. The result is a Voigt profile with a FWHM given by:

$$\Delta\lambda_V = \frac{\Delta\lambda_L}{2} + \sqrt{\left(\frac{\Delta\lambda_L}{2}\right)^2 + \Delta\lambda_G^2} \tag{3-21}$$

where $\Delta\lambda_L$ and $\Delta\lambda_G$ are the line widths of the Lorentzian and Gaussian profiles, respectively. Furthermore, the wings of a Voigt profile are almost entirely determined by the Lorentzian component and the central part of the Voigt and its FWHM are essentially determined by the Gaussian component, as illustrated in Fig. 3-10.

It is also very important to note that a Gaussian profile may be itself a convolution of two or more Gaussian profiles, e.g. Doppler and instrumental line profiles, the FWHM in this case is given by:

$$\Delta\lambda_G = \sqrt{\Delta\lambda_D^2 + \Delta\lambda_I^2} \tag{3-22}$$

where $\Delta\lambda_I$ is the line width of the instrumental profile. Similarly, a Lorentzian profile may also be a convolution of two or more Lorentzian profiles and the resultant FWHM can be expressed as:

$$\Delta\lambda_L = \Delta\lambda_{L,1} + \Delta\lambda_{L,2} \tag{3-23}$$

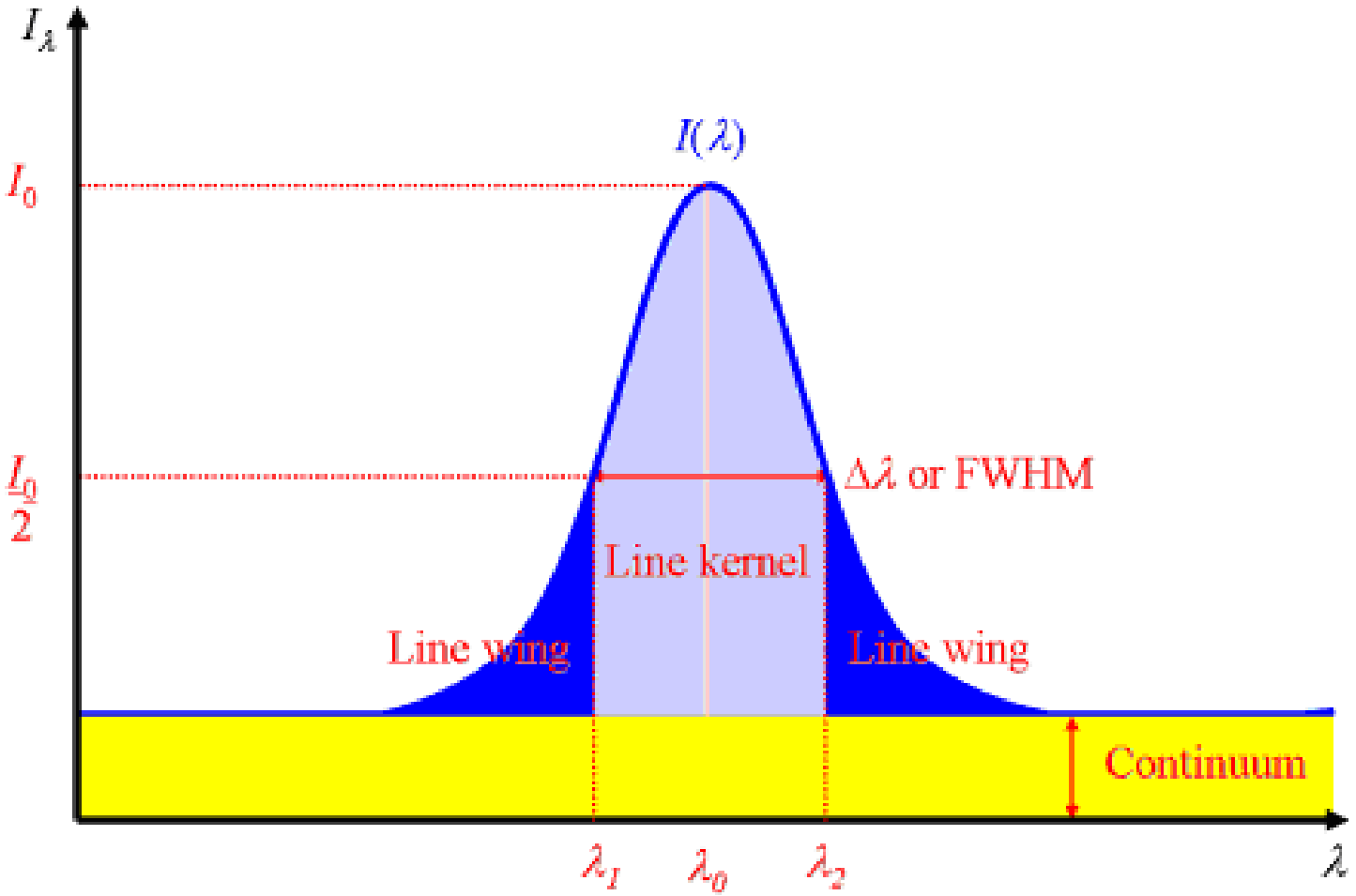

Figure 3-1. Line profile, half-width, kernel and wings of a spectral line. The function $I(\lambda)$ in the vicinity of λ_0 is the line profile. The wavelength interval $\Delta\lambda = |\lambda_2 - \lambda_1|$ between the two wavelengths λ_1 and λ_2 is the full width at half maximum (FWHM) of the line. The line kernel is the spectral region within the half-width and the line wings are the spectral regions outside the kernel where $\lambda < \lambda_1$ and $\lambda > \lambda_2$. (Adapted from Ref. [107])

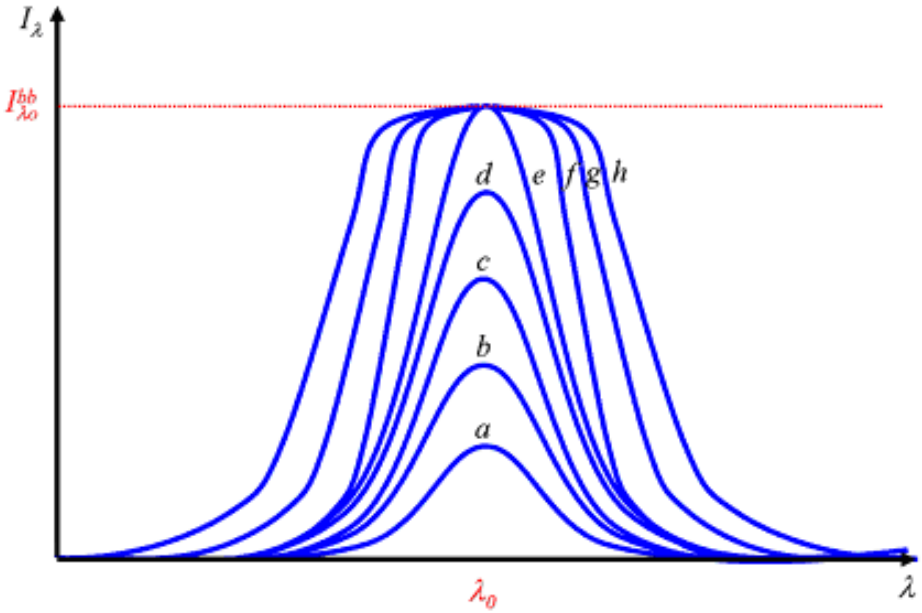

Figure 3-2. Spectral line profiles as a function of increasing atomic concentration (a through h). The line center reaches the blackbody intensity limit at high atom densities. (Adapted from Ref. [106])

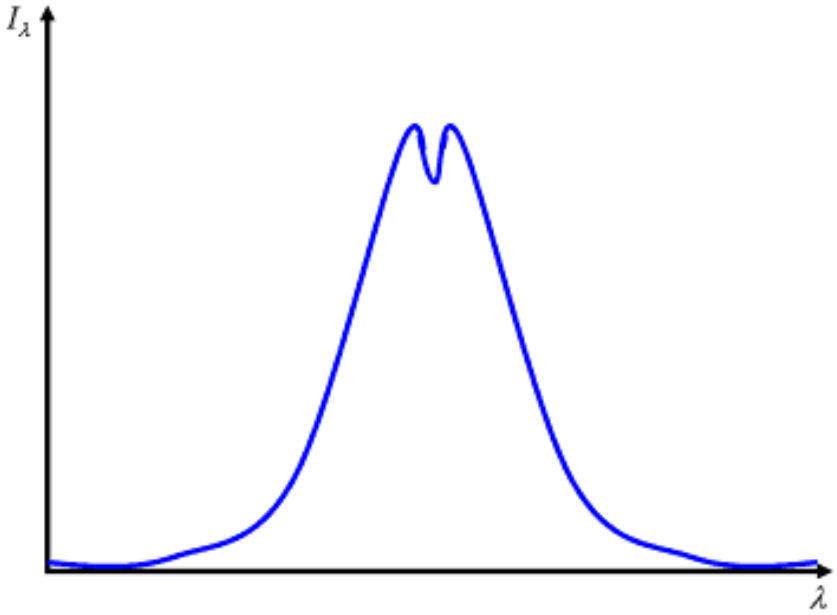

Figure 3-3. An example of a self-reversed spectral line profile.

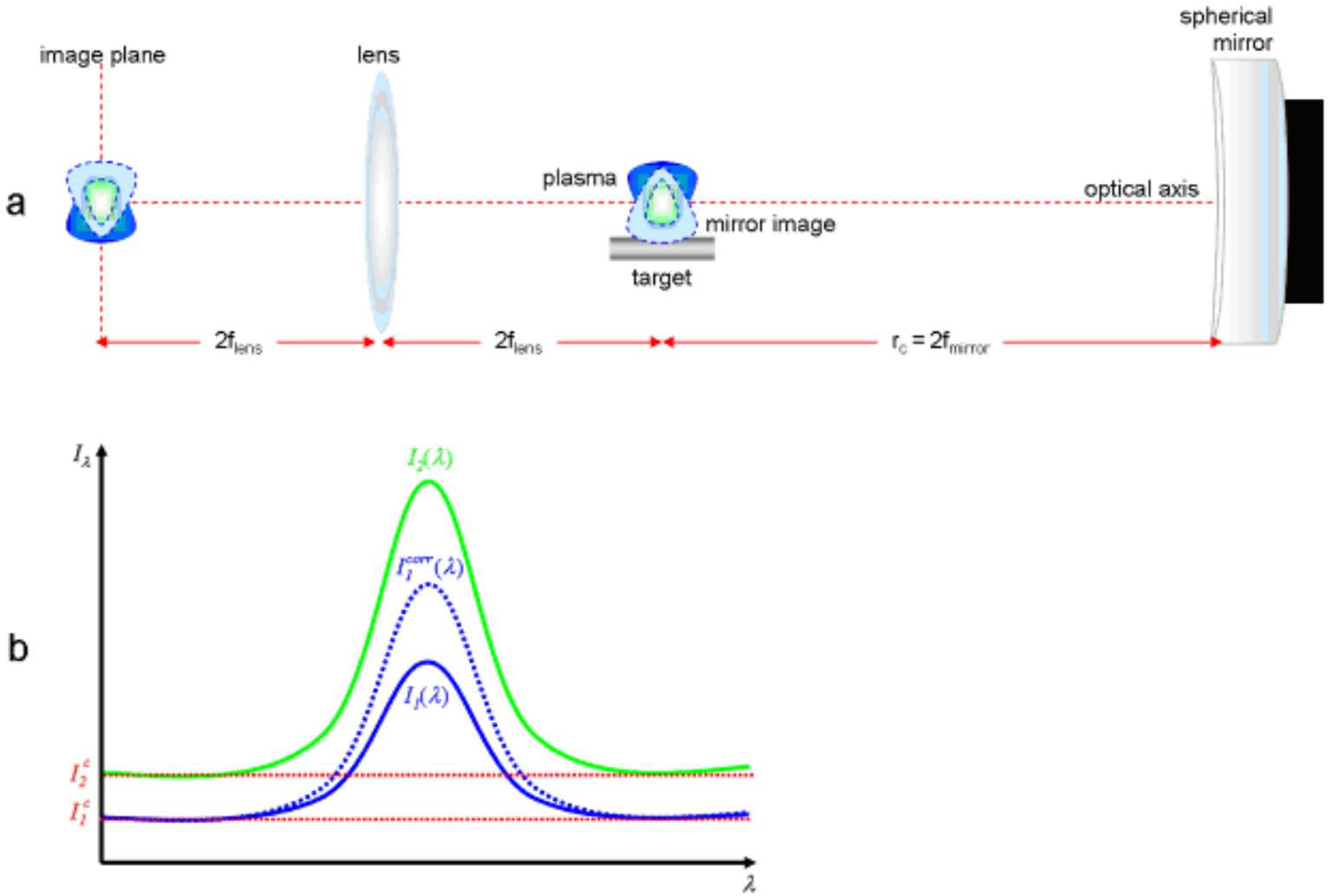

Figure 3-4. Self-absorption check. (a) A spherical mirror is placed at the radius of curvature and the corresponding (b) spectral line profiles $I_1(\lambda)$ and $I_2(\lambda)$ with single and double plasma length, respectively, are recorded. (Adapted from Ref. [110])

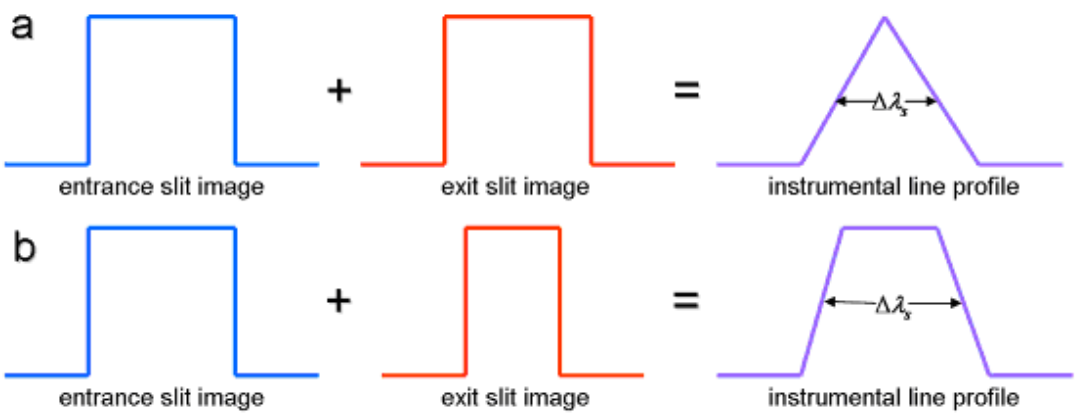

Figure 3-5. Convolution of the entrance and exit slit widths. (a) Equal entrance and exit slit widths results in a triangular-shaped instrumental profile and (b) Unequal entrance and exit slit widths results in a trapezoidal-shaped profile.

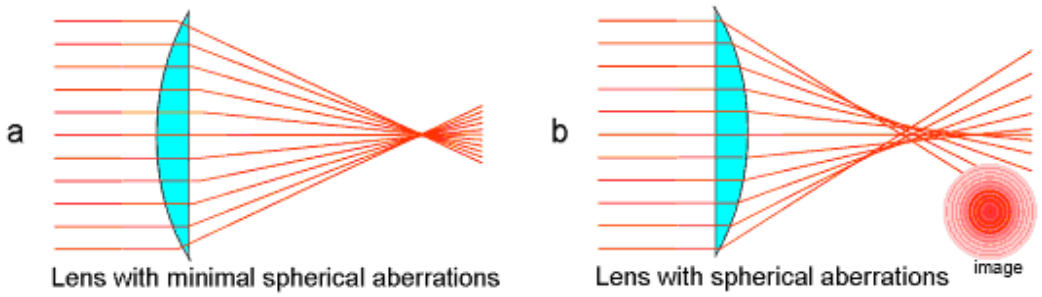

Figure 3-6. Effect of spherical aberration on a lens. The corresponding image formed on the focal plane is a circle with blurred edges. (Adapted from Ref. [106])

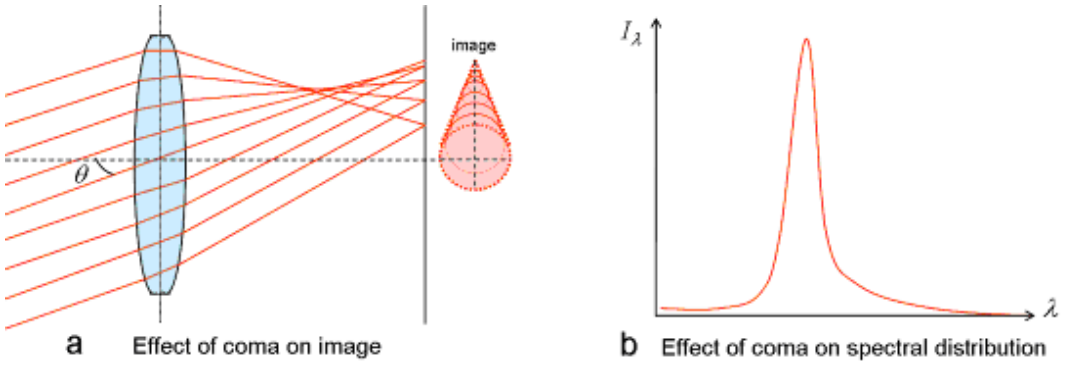

Figure 3-7. Effect of coma: (a) on an image and (b) on the spectral distribution (Adapted from Ref. [114]).

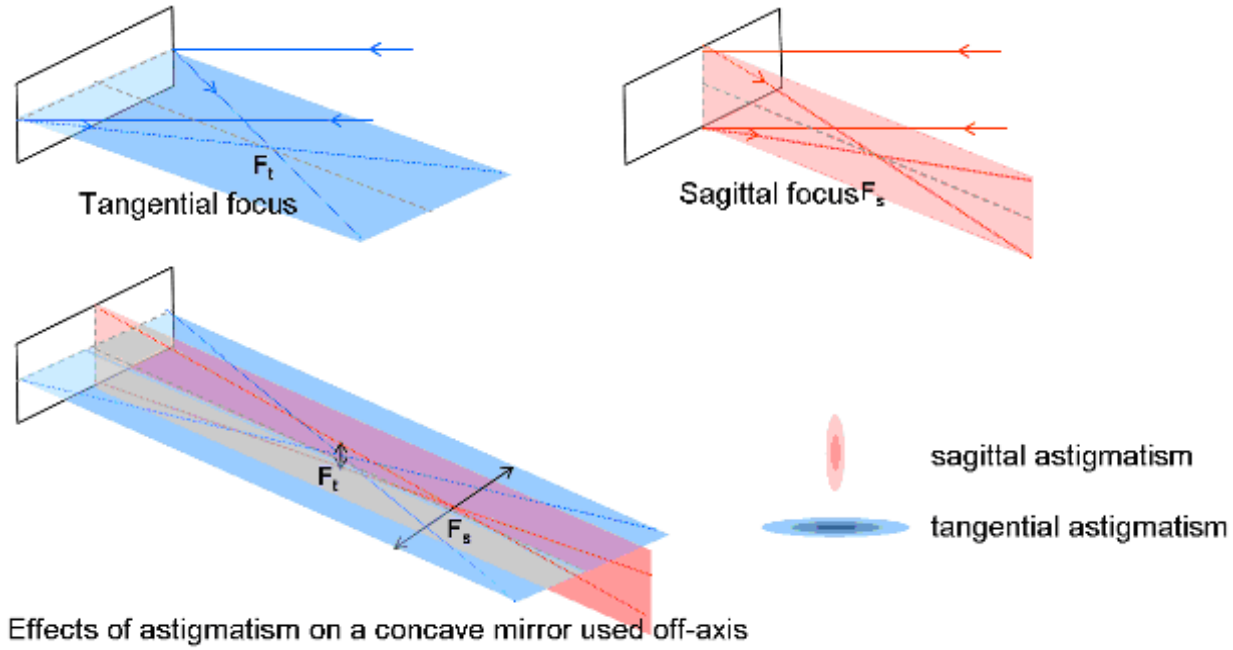

Figure 3-8. Effect of astigmatism on a concave mirror used off-axis. If the image plane is at the tangential focus, F_t, sagittal astigmatism occurs and if the image plane is at the sagittal focus, F_s, tangential astigmatism occurs. (Adapted from Ref. [114])

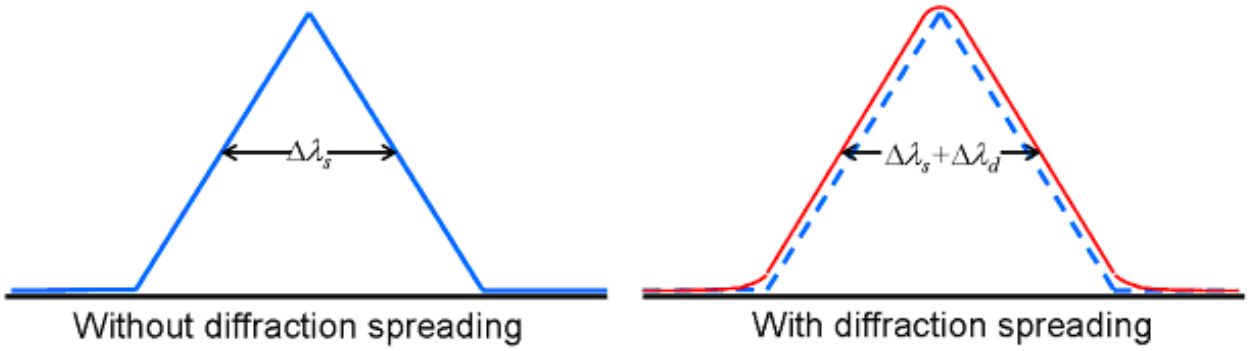

Figure 3-9. Effect of diffraction. The instrumental line profile is broadened by $\Delta\lambda_d$ due to diffraction spreading.

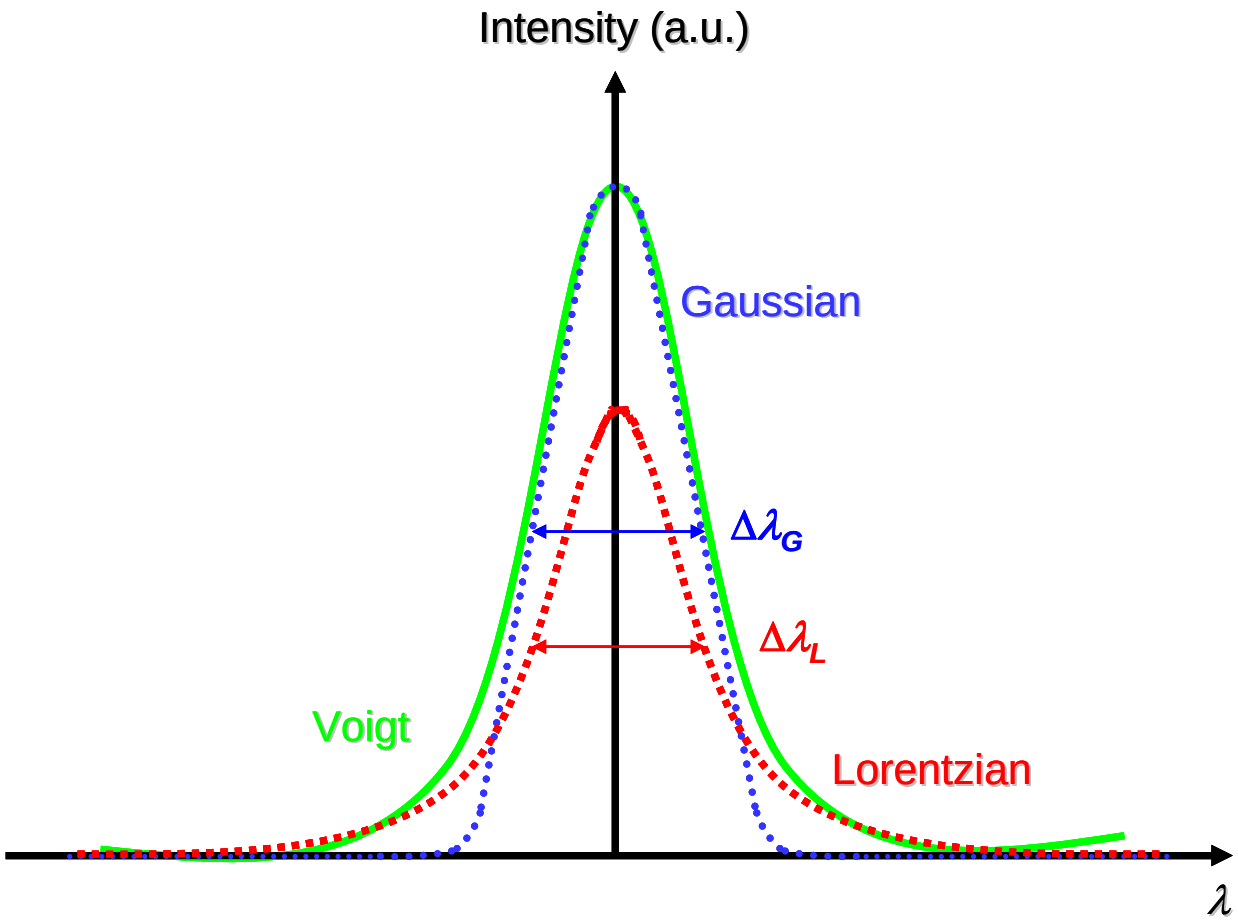

Figure 3-10. Overall spectral line profile. The convolution of Gaussian (blue) and Lorentzian profiles (red) results in a Voigt (green) profile. (Adapted from Ref. [107])

CHAPTER 4
EXPERIMENTAL CHARACTERIZATION OF INSTRUMENTAL SYSTEM AND OPTIMIZATION OF OPERATING CONDITIONS

Introduction

Complete characterization of the experimental set-up and data acquisition is important in any system to enhance accuracy and precision, particularly if quantitative information is desired. Several parameters were optimized and calibrated in this research which included the slit width, instrumental function, detector spectral efficiency, grating rotation angle, number of vertical CCD pixels for binning, and the number of laser shots accumulated.

Experimental Set-up

The schematic diagram of the experimental system used for LIBS experiments performed under atmospheric conditions is depicted in Fig. 4-1. It consisted of a laser, a spectrometer, an intensified charge-coupled device (ICCD), detector gating and control electronics, and a computer for control and data acquisition. A Q-switched Nd:YAG laser (Brilliant T27; Quantel USA) delivered a maximum pulse energy of 360 mJ at the fundamental wavelength of 1064 nm and produced a 5.3 ns duration pulse at a maximum repetition frequency of 10 Hz. The pulsed laser beam was focused to a 0.070 cm diameter spot on the target by using a 3.5 cm diameter, 10 cm focal length lens. For the present research, a pulse energy of 90 mJ was used which provided an incident laser irradiance of 5 GW cm^{-2}.

A simple positioning system consisting of a helium-neon laser, a photodiode detector and a multi-meter was used to monitor the position of the target surface with respect to the laser focusing lens. The positioning system was optimized so that half the value of the voltage read when there was no sample indicated the correct lens-to-sample distance (LTSD). This allowed samples of varying thicknesses to be analyzed without compromising reproducibility. Movement of the sample was accomplished by using an x, y, z translation stage. For all

measurements, the sample was translated every 10 laser shots. A controlled stream of air was also blown across the surface of the sample to carry away the dust plume formed by the laser radiation shockwave.

Plasma emission was collected by a 5 cm diameter lens with a focal length of 7.5 cm. An adjustable iris was attached to the lens in order to correctly match the F-number of the spectrometer which is an F/6.5 system. The diameter of the aperture used was 2.3 cm. The 1:1 image of the plasma was focused onto a 35-μm wide entrance slit of a 0.5 m focal length Czerny-Turner-based spectrometer (SpectraPro-500i; Acton Research Corp.) equipped with three gratings: 1200, 2400 and 3600 grooves mm^{-1} grating. However, only the 2400 grooves mm^{-1} grating was used in this research since it provided a good compromise between spectral resolution and spectral window size. The system was coupled to a two-dimensional intensified charge-coupled device (ICCD-576S/RB-E; Princeton Instruments) and its controller (ST-138; Princeton Instruments) and a programmable pulse delay generator (PG-200; Princeton Instruments) was used to gate the detection. The firing of the laser flash lamp was triggered by a boxcar (SR250; Stanford Research Systems) and the corresponding Q-switch output served as the trigger for the pulse generator. The repetition frequency was kept at 1 Hz for all measurements. The data acquisition was controlled using Winspec32 software (Version 2.5.18.2; Princeton Instruments) installed on an Intel Pentium 4 1.80 GHz computer.

A schematic of the cable connections and the corresponding timing sequence are shown in Figs. 4-2a and 4-2b, respectively. In this particular timing mode, the laser acted as the master and sends out a trigger to the pulse generator to open the shutter and to begin the gated detection. An oscilloscope (TD 520A, Tektronix, Inc.) was used to measure the sequence of acquisition which began from the output trigger sent out by the boxcar to the laser flash lamp.

For experiments carried out in vacuum, the configuration was similar to that of Fig. 4-1 only with an aluminum vacuum cell instead of a sample stage. The schematic diagram is illustrated in Fig. 4-3. One end of the vacuum chamber was connected to a roughing pump and a Pirani pressure gauge and digital controller (Edwards) through a three-way valve while the other end was connected to a needle valve for air flow control. This configuration allowed samples to be changed without turning off the vacuum pump in between measurements.

All measurements were temporally resolved with a suitable delay interval and proper gate width to discriminate the early plasma continuum from late line emissions and to maximize the signal-to-noise ratio as well.

Calibration of the Micrometer Slit Dial

Knowledge of the exact value of the slit width used in any type of spectrochemical analysis is critical in the determination of the contribution of the instrumental broadening since the product of the slit width and reciprocal linear dispersion gives the geometric spectral bandpass. The importance of understanding the effects of instrumental broadening and other types of broadening mechanisms on spectral line profiles have already been discussed in Chapter 3. Therefore, prior to any LIBS measurements, the slit dial of the spectrometer was calibrated to guarantee correct reading of the slit width.

The calibration of the micrometer slit dial is based on the Fraunhofer diffraction pattern formed when parallel rays strike a slit aperture, as shown in Fig. 4-4. The rays from the slit that reach P_0 have the same path lengths and the sinusoidal waves are in phase and add to produce a larger-amplitude resultant due to constructive interference [106]. However, in the case of the rays which reach P_1, a minimum in irradiance results in destructive interference. The general formula for diffraction minima is given by:

$$w \sin \theta' = m\lambda \tag{4-1}$$

where w is the slit width and m is the diffraction order. Based on the geometry in the schematic given in Fig. 4-4, the following relationship can be obtained:

$$\tan\theta = \frac{x}{f} \tag{4-2}$$

where x is the distance from the central diffraction maximum to a diffraction minima and f is the focal length. In general, for very small angles, the small angle approximation can be applied, i.e., $\tan\theta \approx \theta$ and $\sin\theta' \approx \theta'$ and for focal lengths much larger than the slit widths, $\theta = \theta'$, hence:

$$w = \frac{m\lambda f}{x} \tag{4-3}$$

which is the condition for diffraction minima. By extension, the general formula for successive maxima can be expressed as:

$$w = \frac{\left(m + \frac{1}{2}\right)\lambda f}{x'} \tag{4-4}$$

where x' is the distance from the central diffraction maximum to another maximum.

The slit dial calibration experiment was carried out by focusing a helium-neon (He-Ne) laser onto the entrance slit of the spectrometer, as illustrated in Fig. 4-5. The exit slit was covered in case stray light reached the detector to avoid damaging the intensified charge-coupled device even though the system was not switched on. A small screen, e.g. a piece of paper, was placed at the first focal plane (right in front of the collimating mirror) for viewing and marking of the resulting diffraction pattern formed at different slit widths. The image formed at the focal plane is depicted in Fig. 4-5. Due to the ease of marking the diffraction maxima rather than the minima, Eq. 4-4 was used to calibrate the slit dial at varying nominal slit widths. The value of f used in the calculations is not the nominal focal length of the spectrometer but the actual distance

between the entrance slit and the viewing screen which is equal to 48.5151 cm. The small difference is due to protective boundary that is in front of the collimating mirror. The value of λ is equal to the wavelength of the He-Ne laser beam which is 0.6328 μm. The results of the calibration are summarized in Table 4-1. The offset was calculated by taking the absolute value of the difference between the calculated and nominal slit widths. From the results obtained, the zero of the micrometer slit dial corresponds to approximately 15.3 ± 0.8 μm.

Optimization of the Slit Width

The slit width was optimized in order to determine the minimum value that an entrance slit can be opened without compromising throughput or the maximum value that it can be opened without degrading the resolution. In other words, diffraction and/or aberration-limited slit width have to be determined. The optimization was carried out by illuminating the entrance slit with a Hg hollow cathode lamp (Fisher Scientific Co.). The schematic of the set-up is illustrated in Fig. 4-6. The measurements were taken with the ICCD switched to shutter mode and the acquisition set to spectroscopy and free run modes. Different exposure times were used depending on the wavelength under investigation to avoid saturation of the ICCD. The hollow cathode lamp was maintained at a current of 15 mA. Several Hg lines were recorded at 10 different slit widths starting from 15 μm to 105 μm at a 10 μm interval. Triplicate measurements were carried out.

One of the spectral lines used in the optimization was Hg I at 294.263 nm and the normalized spectra at different slits widths are shown in Fig. 4-7a. The lines were fitted with a Gaussian function using an in-house fitting program written in MATLAB. The corresponding half widths determined from the fit were plotted against the slit widths and the result is shown in Fig. 4-7b. It can be observed that the FWHM increases in proportion to the slit width at values greater than 35 μm. However, at slit widths less than 35 μm, the FWHM remains approximately

constant and is larger than the calculated geometric spectral bandpass since the image of a given λ at the focal plane is no longer the width of the slit but larger. This is because the spectral bandpass is controlled by aberrations and diffraction as well as dispersion. Other wavelengths of Hg I were also recorded and the plot of their half-widths against the slit width is shown Fig. 4-7c. It is evident from all wavelengths considered that the resolution can no longer be improved even if the slit width is further decreased to values lower than 35 μm. Hence, the slit width used in all succeeding measurements is 35 μm.

Using the expression given in Eq. 3-20 [107], the diffraction-limited spectral bandpass, $\Delta\lambda_d$, can be calculated for Hg I at λ equal to 294.263 nm using the following instrumental parameters:

- reciprocal linear dispersion, $R_d = 0.7252$ nm mm^{-1}
- focal length, $f = 500$ mm
- effective aperture width, $a = 59.18$ mm

The result is approximately equal to 0.0036 nm which is much narrower than the experimental FWHM determined which is about 0.048 nm. This is because aside from diffraction and aberration effects, the main parameter which determines the limiting slit width or limiting resolution in this particular case is the pixel size of the CCD. According to the Nyquist sampling theory, in order to assure perfect image reconstruction, the resolution must be calculated over 2.5 pixels. This implies that for a CCD with a pixel size of 22.5 μm, the limiting resolution at 294.263 nm is 0.041 nm which is closer to the experimentally determined FWHM.

Development of a Method for Spectral Data Acquisition

In order to obtain quantitative elemental information using approaches which do not require the use of calibration curves or reference standards, the plasma emission spectrum must contain lines, ideally, from different ionization stages for all elements present in the sample. In

other words, a spectrum with a relatively wide spectral range is required. This can readily be achieved using an echelle spectrometer coupled to a CCD or an ICCD since they are designed to provide simultaneous recording of a wide wavelength range spectrum in a single acquisition. However, in this research, a plane grating spectrometer coupled to an ICCD was used which has the shortfall of providing a very narrow spectral window. Hence, development of a spectral acquisition method was necessary so that data in the wide spectral range from 220 to 700 nm may be obtained using a non-echelle detection system. This required multiple acquisitions of successive spectral windows and merging the windows together with optimum overlap using an in-house merging program written in Q-Basic. An example of a merged spectrum is shown in Fig. 4-8 where different colors depict the spectral windows spliced together. A spectrum such as this one, with a spectral range from 220 to 700 nm, required 67 individual spectral acquisitions. This also necessitated 67 grating rotations in order to move from one spectral window to the next. The size of the spectral window is not constant since dispersion varies with the wavelength as well. The spectral window size in the UV region is about 10 nm and decreases to about 6 nm at higher wavelengths for a 2400 grooves mm^{-1} grating.

Knowledge of the angles and dispersion characteristics of a plane grating spectrometer and the physical characteristics of the ICCD are pertinent in the proper selection of the optimum central wavelength for successive spectral windows in order to achieve optimum overlap (minimal to no gaps) in between windows when merged together. Fig. 4-9 shows a schematic of the components of a Czerny-Turner-based grating spectrometer and the respective rays and angles formed when light enters the slit. In brief, the rays emitted by the plasma are reflected off by the first mirror onto the collimating mirror. Then, the collimated light strikes the grating and is dispersed onto the focusing mirror which focuses the dispersed wavelengths at the focal plane

for detection with an ICCD. The angle theta (θ) that is formed between the axis of rotation and the axis normal to the grating is the grating rotation angle. Alpha (α) is the angle of incidence or the angle formed between the incident ray and the normal axis and beta (β) is the angle of diffraction or the angle formed between the diffracted ray and the normal axis. Phi (Φ) is the exit or take-off angle which is a constant value depending on the grating, in this case, Φ is equal to 8.585°. The distance between the entrance slit to the collimating mirror is the focal length *f*, which is the same distance from the focusing mirror to the focal plane.

The first step in the method development is the determination of the grating rotation angle which can easily be solved using the grating equation:

$$m\lambda = d\left(\sin\alpha + \sin\beta\right) = 2d\sin\theta\cos\Phi = 2\times10^{6}\,\frac{\sin\theta\cos\Phi}{G} \tag{4-5}$$

where *m* is the diffraction order, *d* is the groove spacing in nm groove^{-1} and *G* is the number of illuminated grooves in the grating. By simple manipulation, the grating rotation angle can be expressed as:

$$\theta = \arcsin\left(\frac{m\cdot\lambda\cdot G}{2\times10^{6}\cdot\cos\Phi}\right) \tag{4-6}$$

Once the grating rotation angle is known, the reciprocal linear dispersion for a specific wavelength is calculated. Using simple geometric relations, the reciprocal linear dispersion is given by:

$$R_d = \frac{d\lambda}{dx} = d\,\frac{\cos\beta}{f\cdot m} = d\,\frac{\cos\left(\theta+\Phi\right)}{f\cdot m} = \left(\frac{\cos(\Phi+\theta)\cdot10^{6}}{G\cdot f\cdot m}\right) \tag{4-7}$$

The third step in the method development is the determination of the spectral range, $\Delta\lambda_{range}$, at a specific central wavelength. The spectral range of the system varies with the

reciprocal linear dispersion and is also dependent on the pixel size of the CCD, w_{pixel}, as well as the number of column pixels, N_{pixel}, and can be calculated using the simple equation:

$$\Delta\lambda_{range} = R_d \cdot w_{pixel} \cdot N_{pixel} \tag{4-8}$$

Furthermore, since the central wavelength of the first spectral window, $\lambda_{c,1}$, is already predetermined and is equal to 225 nm, the starting wavelength, $\lambda_{s,2}$, for the second spectral window can be calculated using the equation:

$$\lambda_{s,2} = \lambda_{c,1} + \left(\frac{\Delta\lambda_{range,1}}{2} \right) \tag{4-9}$$

For a 10-pixel overlap between windows, the starting wavelength can be adjusted accordingly using the following equation:

$$\lambda_{s',2} = \lambda_{s,2} - 10 \cdot R_d \cdot w_{pixel} \tag{4-10}$$

Finally, the central wavelength for the subsequent window can now be determined once the adjusted starting wavelength $\lambda_{s',2}$ is known:

$$\lambda_{c,2} = \lambda_{s',2} + \left(\frac{\Delta\lambda_{range,2}}{2} \right) \tag{4-11}$$

The whole process can be repeated several times depending on the size of the spectral range desired. In this research, 67 central wavelengths were calculated for an optimum merging of spectral windows within the range of 220 to 700 nm. Table 4-2 lists the 67 calculated central wavelengths used in all measurements.

Determination of the Instrumental Function

As previously discussed in Chapter 3, the determination of the instrumental or slit function is fundamental especially in cases where the line width of a spectral line profile is of comparable magnitude to the spectral bandwidth of the instrument. The resulting complex convolution

integral can be analytically or numerically solved if the instrumental function has been completely characterized. In addition, the instrumental function is required in plasma expansion modeling algorithms particularly if the calculated theoretical emission spectrum has to be compared to an experimentally acquired one.

The same experimental configuration as in the optimization of the slit width was used in order to determine the instrumental function (Fig. 4-6). The hollow cathode lamp which emits several spectral lines from both mercury and argon was used under a constant current of 5 mA. Triplicate measurements were carried out using an exposure time of 100 ms. All Hg and Ar lines detected between the spectral range of 220 and 700 nm were fitted with a pseudo Voigt function and the corresponding line widths were calculated from the fit. The spectra are shown in Fig. 4-10a and the plots of the FWHM versus wavelength are shown in Fig. 4-10b. The resulting instrumental function was fitted with a second-order polynomial fit using Origin 7.5. The average of the fits is shown in Fig. 4-10c, as well as the theoretical spectral bandpass calculated using a slit width of 35 μm. The same decreasing trend can be observed between the experimentally determined spectral bandwidth and the calculated theoretical spectral bandpass. Furthermore, the experimentally obtained values are significantly higher since it does not only take into account the width of the slit but all the other optical components of the detection system. The experimental reciprocal linear dispersion function can be easily evaluated from the instrumental function by dividing it by the slit width used in the experiment. The resulting second-order polynomial fit of the dispersion is shown in Fig. 4-10d and the corresponding polynomial equation for the dispersion function is given by:

$$R_d = 1.76486 - 0.001\lambda - 9.83987 \times 10^{-7} \lambda^2 \quad (4\text{-}12)$$

Determination of the Detector Spectral Efficiency

The efficiency of the grating and the spectral response of the detector must be known over the whole spectral range of interest since their response is usually not flat with wavelength. The spectral efficiency of the detection system was determined using deuterium and halogen calibrated light sources (DH-2000; Ocean Optics). The experiment was performed by placing the fiber optic approximately at the plasma position. For experiments which require the use of a vacuum cell, the fiber optic was placed behind the sample chamber in order to correct for the effect of the quartz window on plasma emission. The theoretical response curves of the deuterium and halogen lamps are shown in Fig. 4-11a and the experimental response curves of the detection system is shown in Fig. 4-11b. The relative response curve shown in Fig. 4-11c was obtained by dividing the experimental response by the theoretical response. Due to the difference in the optical power between the two sources, it can be observed that the outputs from the deuterium and the halogen sources do not overlap. However, a simple multiplication of a constant factor to the halogen response curve corrects for this difference. All experimental spectra are corrected for the detector spectral efficiency using the merged spectral efficiency data shown in Fig. 4-11d. For experiments that require the use of a vacuum sample chamber, the spectra were corrected using the spectral efficiency shown in Fig. 4-11e.

Determination of the Effect of CCD Pixel Binning

Another parameter that was evaluated in this research is the number of CCD vertical pixels to be included in the binning process. Binning is a clocking scheme that allows charges from adjacent pixels on a CCD array to be combined or summed. It is also a consequence of carrying out measurements in spectroscopy mode rather than imaging mode. This can offer advantages of faster readout speeds and improved signal to noise ratios at the expense of reduced spatial resolution. In spectroscopic CCD systems, a spectral line is typically an image of the slit formed

on the CCD. The image of the slit typically has a high aspect ratio, i.e., very long and thin, and is orientated perpendicular to the readout register of the CCD. The signal from a single spectral line can be binned to achieve the best signal to noise ratio (S/N) without any deterioration in spectral resolution [115].

Shown in Fig. 4-12a is the zero order image of a soil plasma taken at a delay time of 1 μs and 0.5 μs integration time, as well as the different number of pixels included in each binning process. The effect of binning was determined using a Mg I line at 285.3 nm shown in Fig. 4-12b. The integrated intensities at different binning sets is shown on the first panel of Fig. 4-12c and it can be observed that the intensity increases as more pixels are summed which is to be expected. The background signal was also calculated and it also increased, almost linearly with the number of pixels binned. The corresponding relative standard deviation or RSD was also determined and it improved as more pixels are binned. It can be concluded that binning more pixels is better in terms of signal, RSD and S/N but only up to a certain limit. In this case, the limit is set by the constant S/N and RSD observed for binning sets 5 and 6. From the results obtained, the limit to the number of pixels included in the binning for all succeeding measurements was the height of the plasma, since binning more than the height of the plasma increased the background more than the signal. Therefore, the emission measurements are spatially-integrated over the full height of the plasma and as a consequence, the succeeding values obtained for electron number density and temperature determinations are spatially-integrated as well.

Optimization of the Number of Accumulated Laser Shots and Sampling Procedure

Castle et al. [43] comprehensively investigated the effect of several "controllable" variables on the precision of LIBS measurements. In this research, a similar experiment was

undertaken in order optimize the experimental operating conditions in terms of the number of accumulated laser shots for a single spectral acquisition by comparing the relative standard deviation (RSD) obtained for inter-measurements. Inter-measurements, based on the definition given in Ref. [43], are measurements consisting of the summation of spectra from several laser shots. An investigation of the effect of sampling a fresh spot (set A) or the same spot (set B) on LIBS inter-measurement precision was carried out as well. Set A was carried out by recording the spectra of 80 individual laser shots while the sample was being translated every shot in order to sample a fresh surface. Set B, on the other hand, was taken by recording the spectra of 80 individual laser shots while the sample was translated every 20 shots. In this manner, 5, 10 and 20 shots can be accumulated which results to 8, 8, and 4 inter-measurements, respectively, for both sets considered. The LIBS measurements were performed on an aluminum alloy standard S-11 using a delay of 1.0 μs and a gate width of 1.0 μs. The components of the alloy are summarized in Table E-1 in Appendix E.

The analytical line investigated in this study is the singly-ionized Al line at 281.619 nm and the corresponding spectra for the two sets carried out in conjunction with the different number of laser shots accumulated are shown in Fig. 4-13a and 4-13b. The signal intensities shown are the average of inter-measurements and the error bars correspond to the standard deviation calculated. The resulting spectrally integrated line intensity is plotted against the number of shots accumulated in each set and is shown in Fig. 4-13c. The intensities increased with the number of laser shots and are generally much higher for set A when translational sampling is carried out similar to the results obtained by Castle et al. [43]. The corresponding RSD calculated by using the accumulated signal intensities from sequential measurements was plotted against the number of laser shots accumulated for sets A and B and the precision was

highest when 10 shots were accumulated as shown in Fig. 4-13. Also, comparing translational sampling from stationary sampling at 10 accumulated shots, the precision is highest when a new surface is sampled per shot, however, the difference between the RSD's are not very significant. Hence, in all measurements that followed, accumulation of 10 laser shots on the same spot was carried out. Such an accumulation allows averaging of the shot-to-shot fluctuations in the plasma and improves the signal-to-noise ratio. This also gives the simple advantage of conserving the amount of target surface sampled for each spectral window acquired since multiple narrow spectral windows from 220 to 700 nm were recorded for a LIBS quantitative analysis.

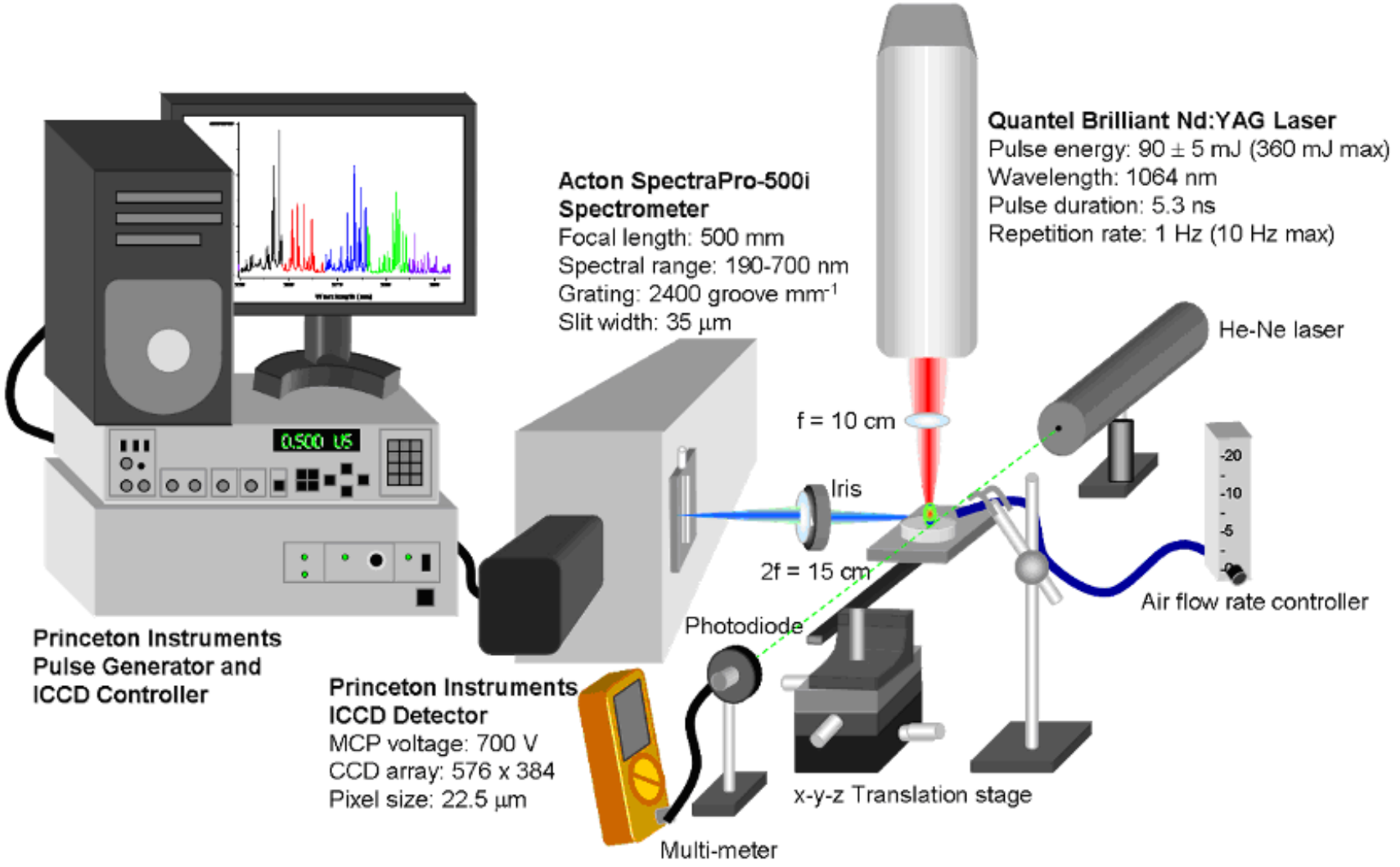

Figure 4-1. Experimental LIBS set-up for experiments under atmospheric conditions.

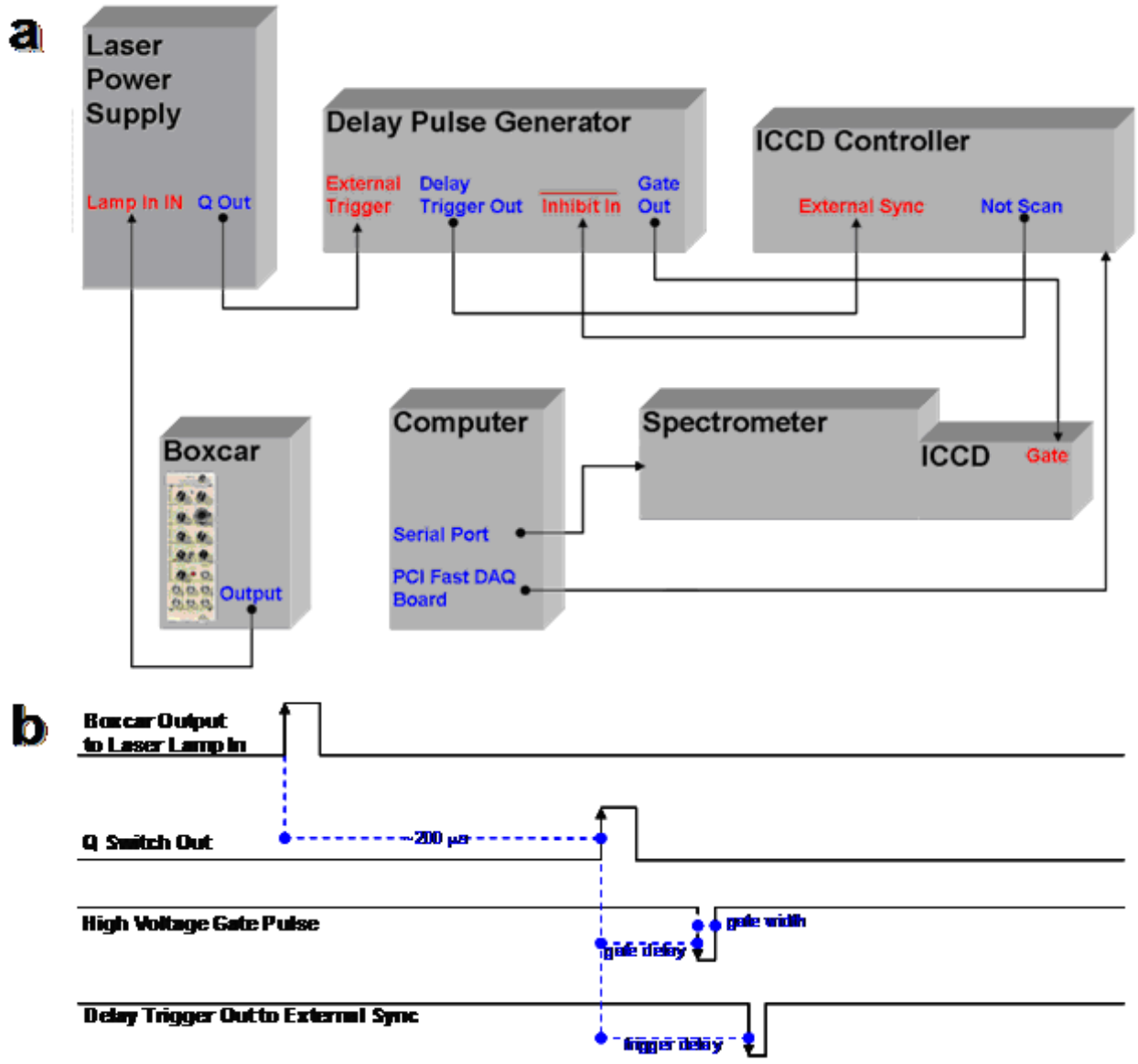

Figure 4-2. Schematic diagram of (a) cable connections and the corresponding (b) timing sequence used in the experimental system. The pulse widths depicted in (b) are not to scale.

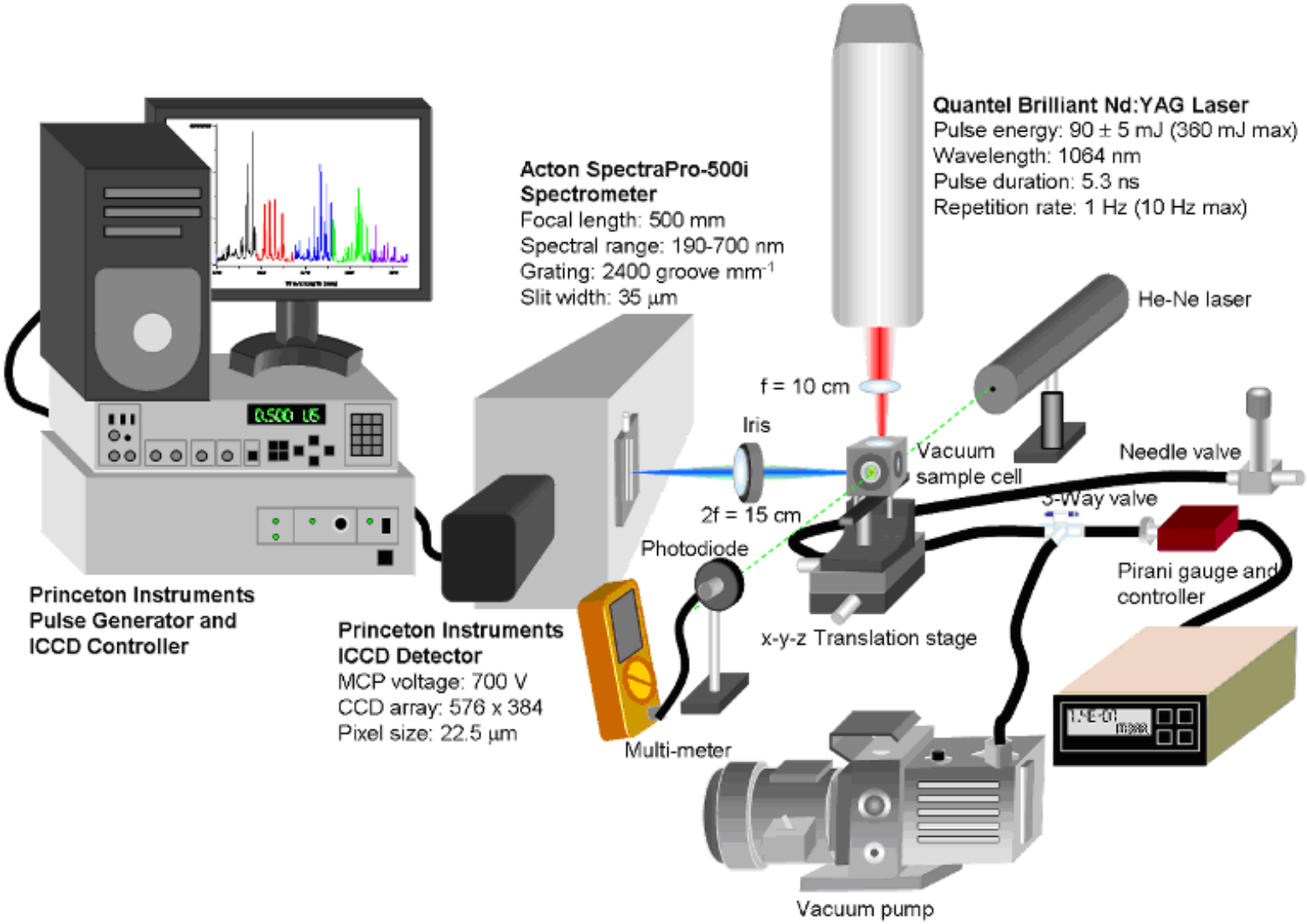

Figure 4-3. Experimental LIBS set-up for experiments under vacuum conditions.

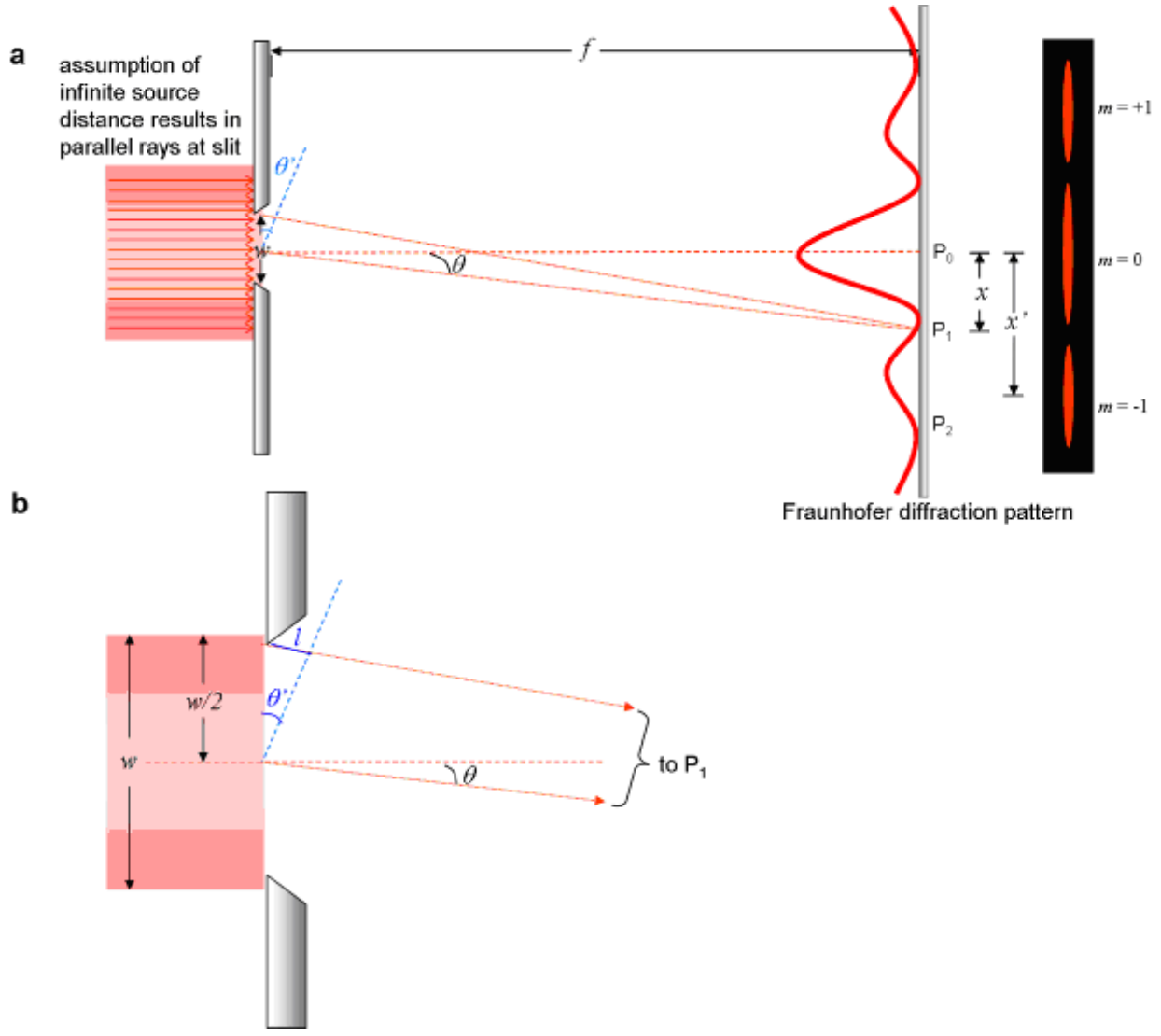

Figure 4-4. Ray diagram for Fraunhofer diffraction by a single slit and the corresponding intensity distribution and image of the diffraction pattern. In (a) parallel source rays illuminate the slit where diffraction occurs. The diffraction minimum at P_1 is seen to arise in (b) from the superposition of rays diffracted at angle θ that are at a distance $w/2$ apart. (Adapted from Ref. [106])

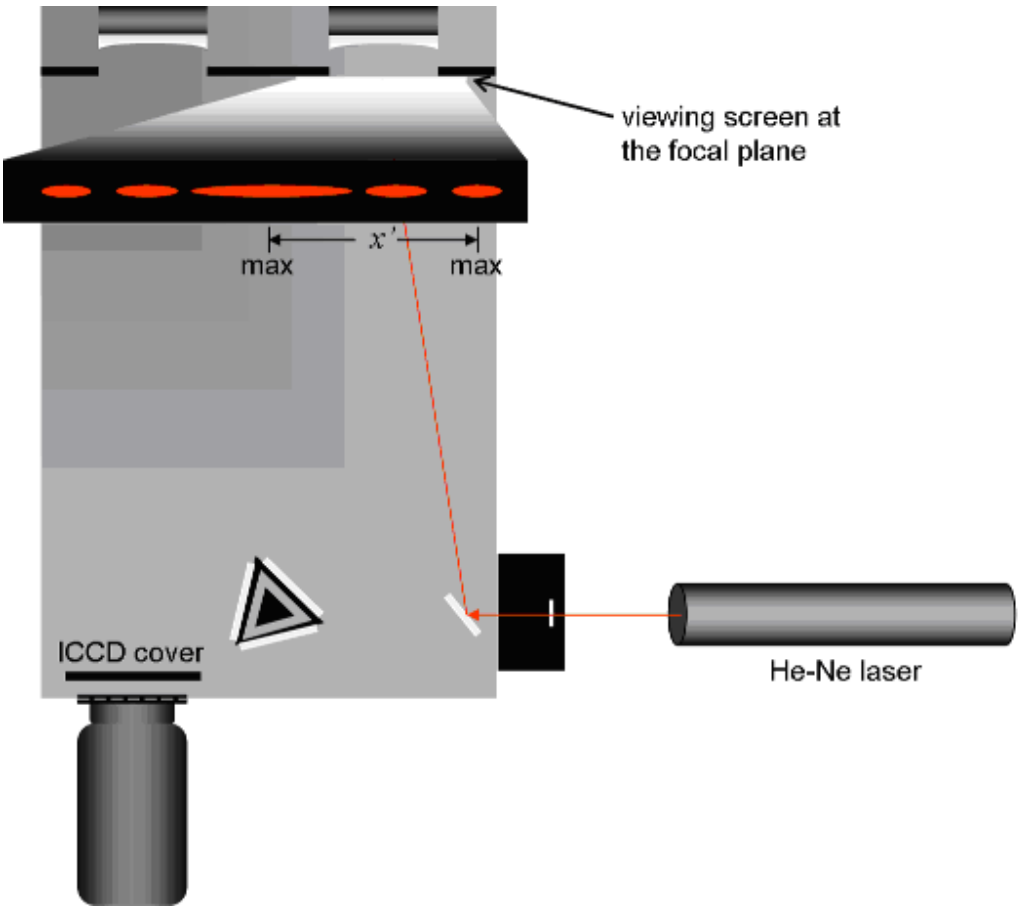

Figure 4-5. Experimental set-up used in the calibration of the micrometer slit dial.

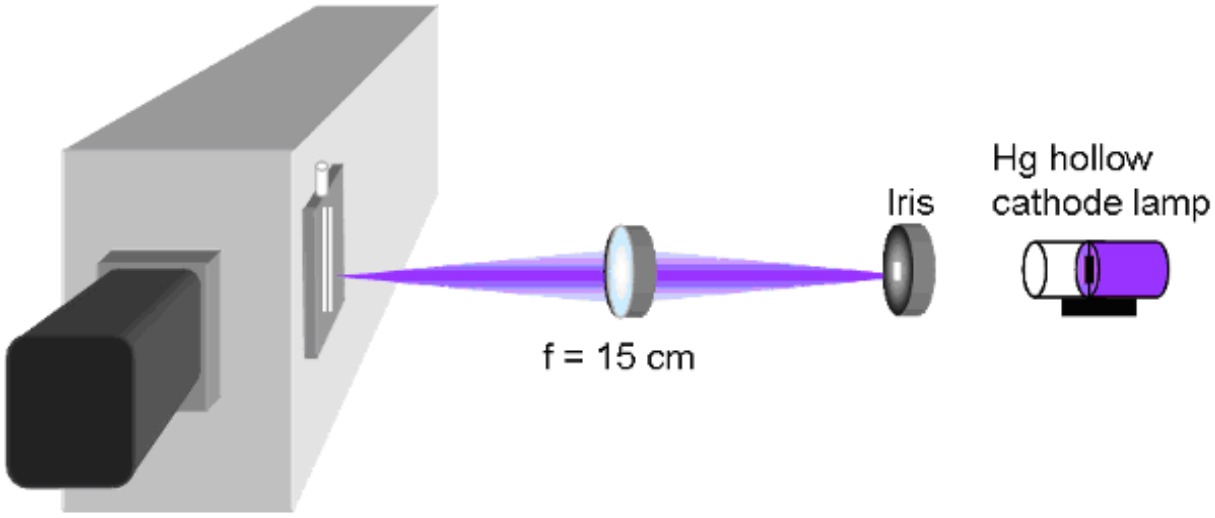

Figure 4-6. Experimental set-up used in the optimization of the slit width and measurement of the instrumental function.

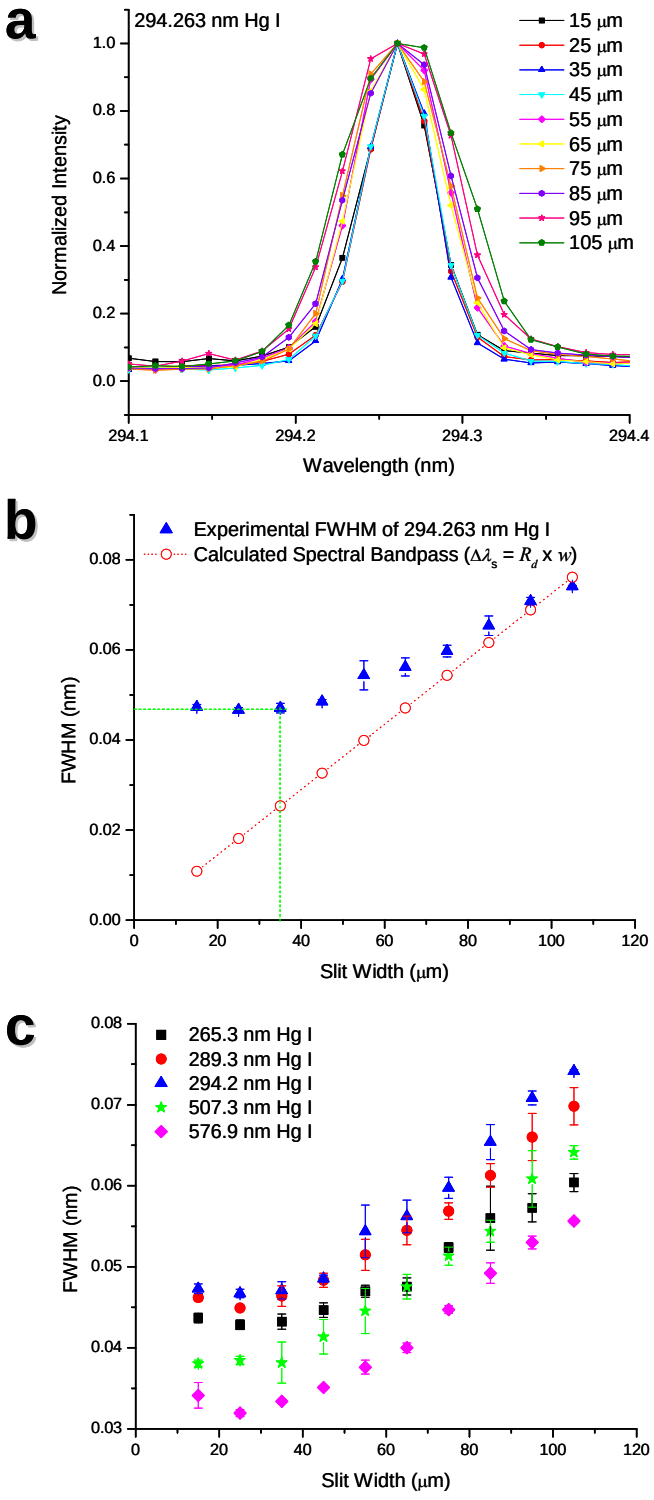

Figure 4-7. Effect of slit width on the (a) normalized intensity distribution and (b) full width at half maximum of 294.263 nm Hg I line, and (c) full width at half maxima of other Hg I lines.

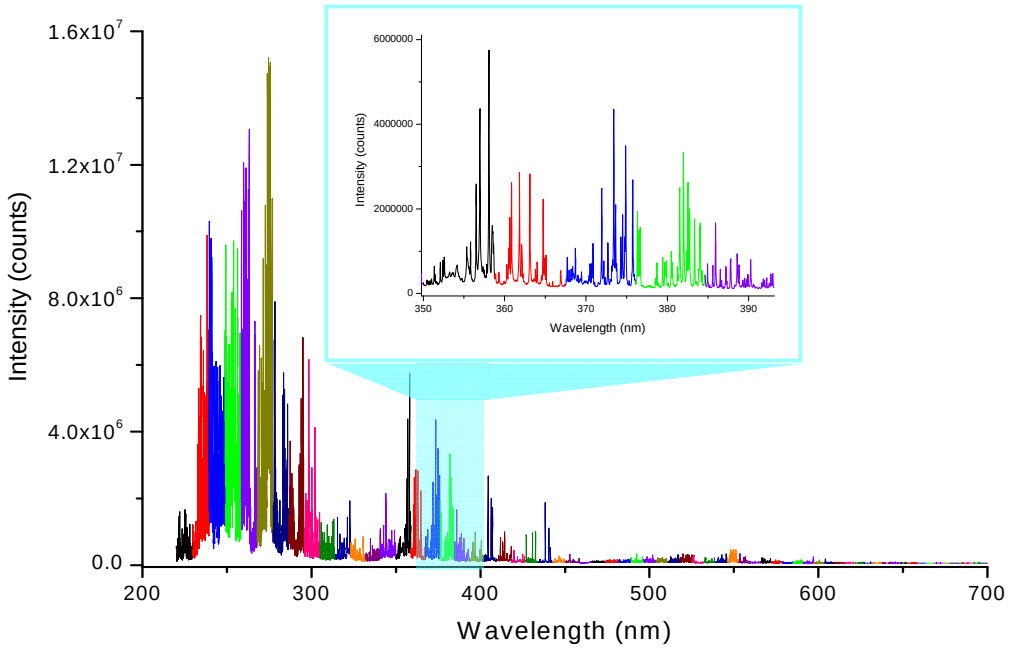

Figure 4-8. Example of a merged spectrum. The different colors depict the 67 individual spectral windows optimally spliced together using an in-house merging software written in Q-Basic.

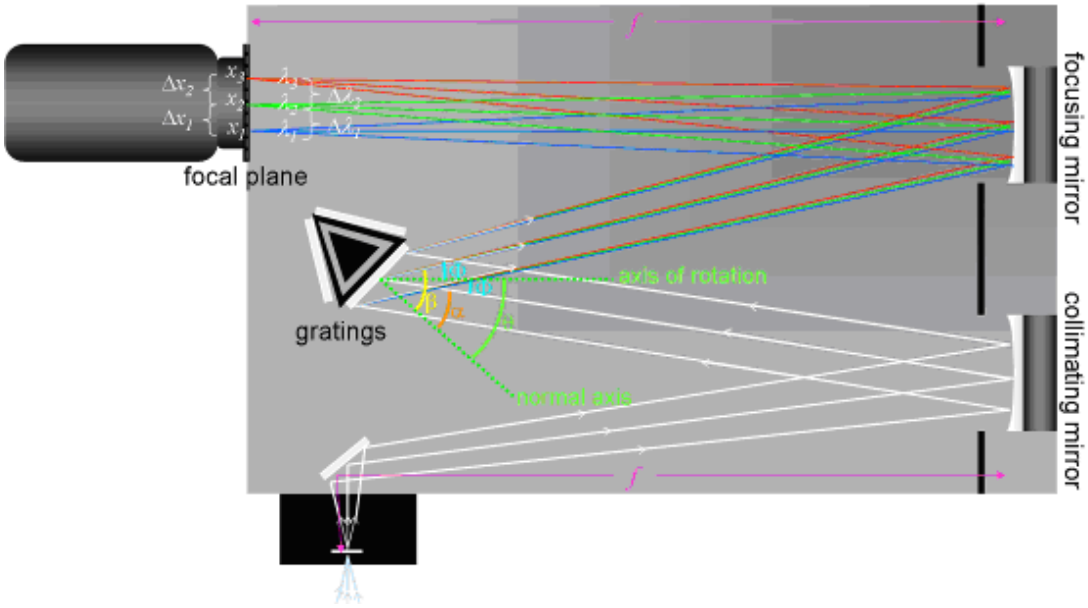

Figure 4-9. A schematic diagram of the components of a Czerny-Turner-based spectrometer and the respective rays and angles formed when light enters the slit.

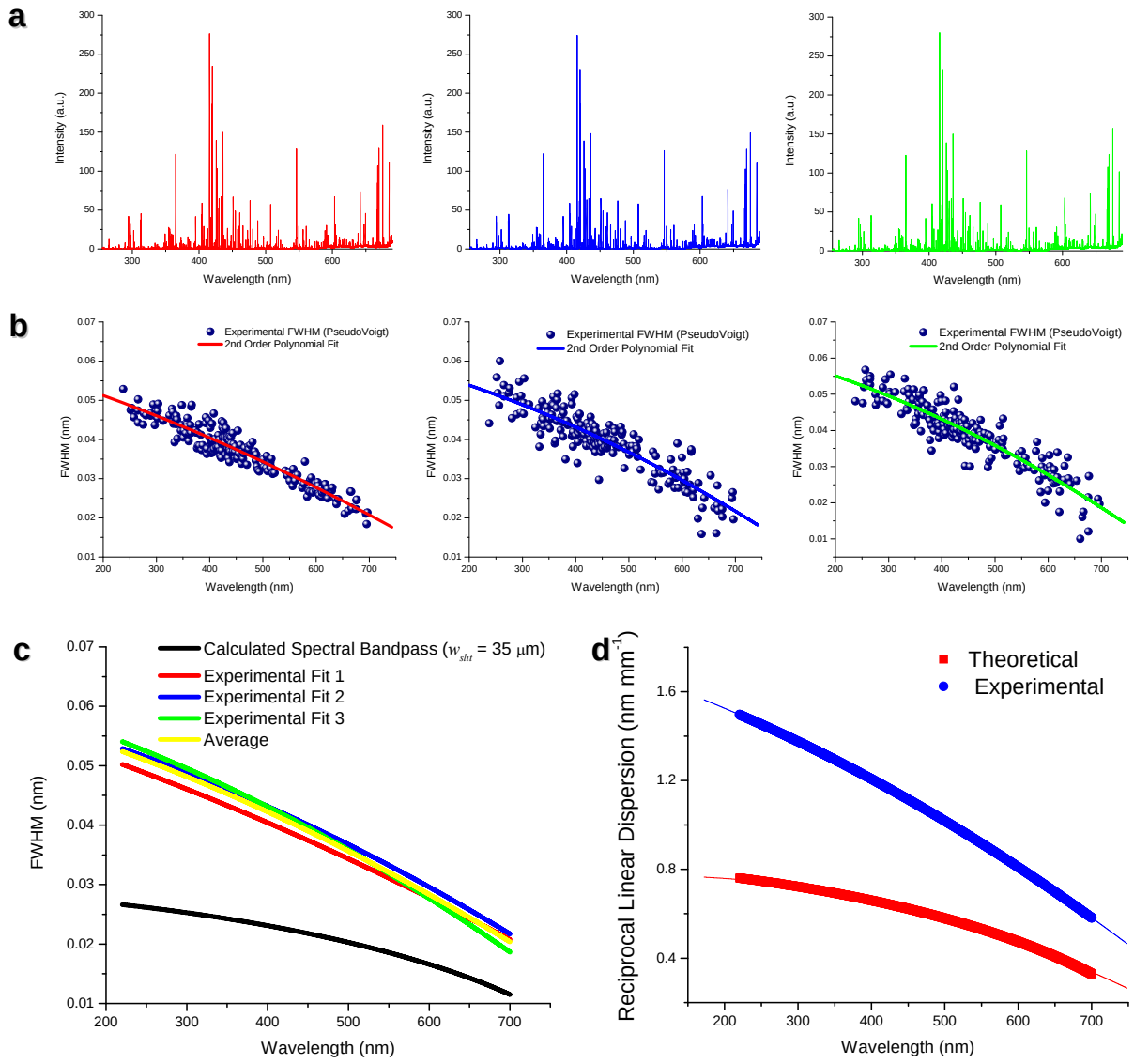

Figure 4-10. Determination of the instrumental function. (a) Spectra taken using a Hg hollow cathode lamp in Ar buffer gas. (b) The line widths calculated from the fitting of spectral lines are plotted as a function of wavelength. (c) The instrumental function was fitted with a second order polynomial and the average of the three trials is shown in yellow. The corresponding theoretical spectral bandpass is also shown on the same plot (black solid line). (d) Comparison between theoretical (red) and experimental reciprocal linear dispersion function (blue).

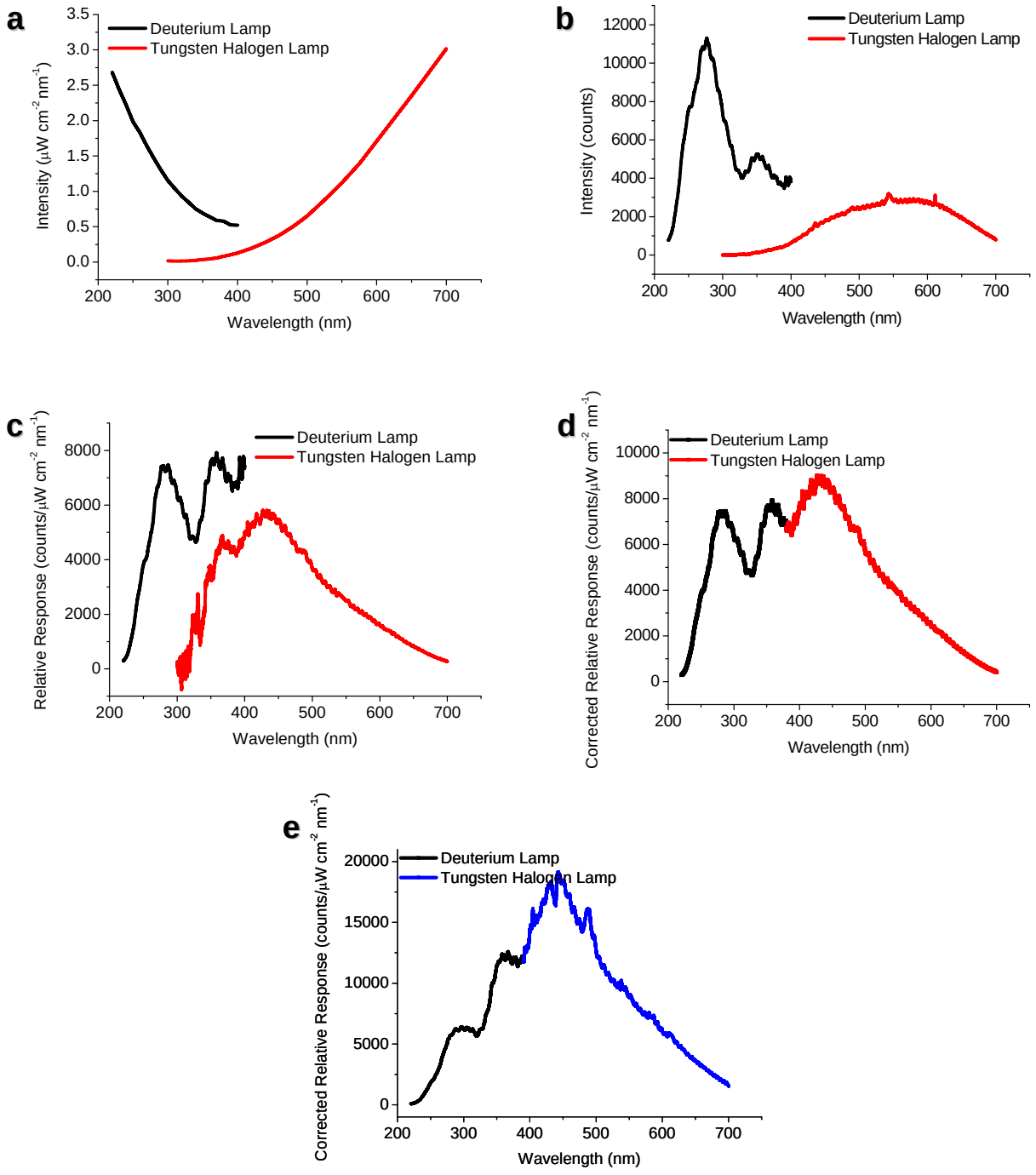

Figure 4-11. Determination of the detector spectral efficiency. (a) Theoretical response curves of deuterium (black) and halogen (red) lamps. (b) Experimental response curves of the detection system. (c) Relative spectral efficiency of the detection system. (d) Corrected relative detector spectral efficiency. (e) Corrected relative detector spectral efficiency for experiments using a vacuum chamber.

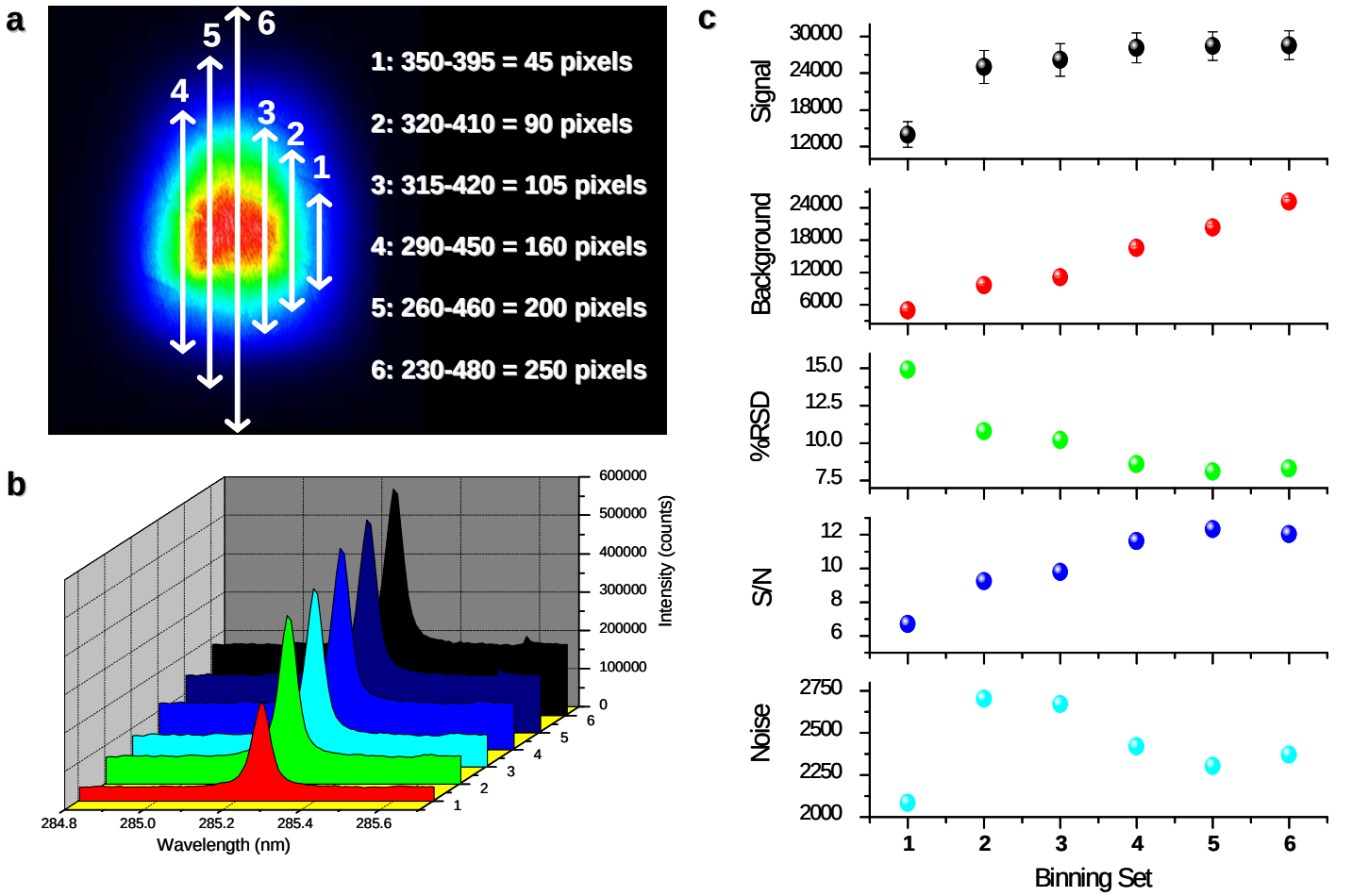

Figure 4-12. Effect of binning. (a) Image of the laser-induced plasma obtained from a soil sample and the corresponding binning set parameters. (b) The effect of binning was monitored using a Mg I line at 285.3 nm. (c) The signal, background, RSD, S/N and noise as a function of binning set.

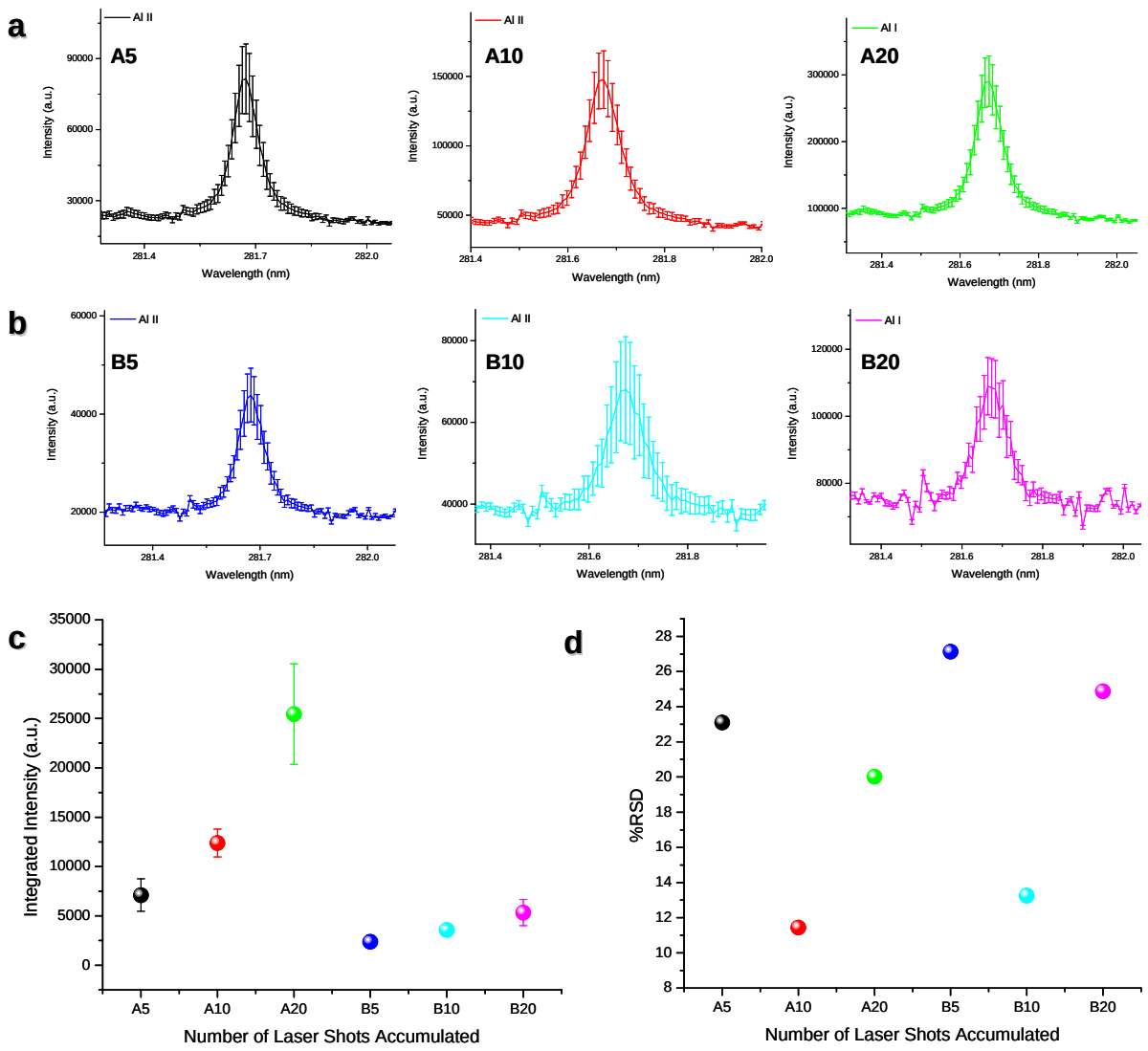

Figure 4-13. Effect of laser shot accumulation on the spectra of singly-ionized aluminum line at 281.619 nm taken with (a) translational sampling and (b) stationary sampling and its corresponding influence on (c) integrated line intensity and (d) precision.

Table 4-1. Results of the calibration of the micrometer slit dial.

Nominal slit width (μm)	Diffraction order, *m*	Distance, *x'*(μm)	Calculated slit width, *w* (μm)	Calculated offset (μm)
0	+1	29.50	15.61	15.61
	-1	29.50	15.61	15.61
10	+1	18.25	25.23	15.23
	-1	18.25	25.23	15.23
	-2	31.25	24.56	14.56
20	+1	13.00	35.42	15.42
	-1	13.00	35.42	15.42
	-2	23.00	33.37	13.37
30	+2	17.00	45.15	15.15
	-3	23.50	45.72	15.72
	-4	30.50	45.30	15.30
40	+2	13.50	56.85	16.85
	-3	19.50	55.10	15.10

Table 4-2. Calculated central wavelengths for spectral data acquisition.

Central wavelength (nm)	Central wavelength (nm)
225.0	514.7
234.6	521.8
244.2	528.8
253.7	535.8
263.2	542.7
272.6	549.5
281.9	556.2
291.2	562.8
300.4	569.3
309.6	575.7
318.7	582.0
327.7	588.2
336.7	594.4
345.6	600.5
354.4	606.5
363.1	612.4
371.8	618.2
380.4	623.9
388.9	629.5
397.4	635.1
405.8	640.5
414.1	645.8
422.3	651.0
430.5	656.1
438.6	661.1
446.6	666.0
454.5	670.8
462.3	675.6
470.0	680.3
477.7	684.9
485.3	689.4
492.8	693.8
500.2	698.1
507.5	

CHAPTER 5
QUANTITATIVE STANDARD-FREE ALGORITHMS IN LASER-INDUCED BREAKDOWN SPECTROSCOPY

Introduction

Quantitative analysis in laser-induced breakdown spectroscopy (LIBS) is commonly achieved by construction of calibration curves using proper reference standards [30, 116-121]. This is of course limited by the availability of standards which are matrix-matched and in the case of highly variable or fully unknown matrices, the calibration curve approach limits the analysis usually to semi-quantitative only. In order to alleviate the limitation presented by the requirement of reference standards, standard-free techniques such as the calibration-free LIBS (CF-LIBS) and the Monte Carlo simulated annealing optimization for LIBS (MC-LIBS) were developed independently by two different research groups. The principles of the techniques are described comprehensively in this chapter.

Calibration-Free Laser-Induced Breakdown Spectroscopy (CF-LIBS)

The CF-LIBS approach was developed and patented in 1999 by the Istituto per i Processi Chimico-Fisici (IPCF) of the Consiglio Nazionale delle Richerche (CNR) in Pisa, Italy [57, 122]. The main points which initiated its development were the problems posed by matrix effects and the difficulty in obtaining matrix-matched reference standards, particularly for quantitative multi-elemental LIBS analysis in highly complex or unknown matrices. Detailed description of the algorithm is presented herein and can be found in Refs. [55-57, 122-125].

Working Hypotheses

The CF-LIBS measurement protocol applied in this research is based on three supporting assumptions regarding the experimental method of operation and the theoretical representation of the conditions of the plasma.

Stoichiometric ablation. The assumption of stoichiometric ablation forms the very foundation of the LIBS method [56]. During ablation, the plasma composition is representative of the actual sample composition when the laser irradiance at the sample surface is in the range of 10^9 W cm^{-2} or greater, a value which is usually achieved in LIBS experiments [124, 126]. According to Russo et al. [127], it is expected that even at moderately high laser intensities (≥1 GW cm^{-2}) using picosecond or femtosecond lasers, the energy focused onto the sample surface exceeds the latent heat of vaporization of all the sample components and that the thermal properties of each constituent will not have a significant effect on the mass removal, which implies that all sample constituents can be vaporized and subsequently removed. Reduction of fractionation may be an outcome of this non-thermal ablation mechanism due to the increase in the amount of sample mass removed regardless of the thermal properties of the components of the sample [127].

In addition, at much higher laser intensities (≥20 GW cm^{-2}), the phase transition involved is from solid to liquid to vapor even before the thermodynamic critical temperature is achieved. The amount of energy required to convert the sample mass from solid to vapor includes a large fraction of absorbed laser energy to satisfy the latent heat of melting and vaporization. Furthermore, when the temperature of the sample surface approaches the thermodynamic critical point, which is several times higher than the vaporization temperature, a similar amount of laser energy absorbed by the material can significantly transport more mass into the vapor phase. As a consequence, fractionation is reduced even further at this regime due to the rapid transition from a superheated liquid to a mixture of vapor and liquid droplets which are explosively ejected from the sample surface in micrometer-size droplets or particles [127].

Stoichiometric ablation still remains a big challenge in quantitative LIBS measurements due mainly to matrix effects. Several studies on laser-material interaction have been performed over the years in order to further understand the different processes and mechanisms involved, which is a step towards overcoming the matrix effect problem, thus, achieving a representative ablation of the sample. Bleiner et al. [128] investigated the effects of melting and vaporization of different metal targets during ICP-MS and LIBS analysis by modeling the laser-material interactions which included processes such as heating, melting and vaporization of the metal target, vapor plume expansion, plasma formation, and laser–plasma interaction. The variables incorporated in their complex algorithm were the optical absorption coefficients, reflectivities, and thermal diffusivity of the target surface. They concluded that the optical and thermal properties of metal targets have a significant effect on the target temperature under identical irradiation conditions. For example, Al exhibited the lowest surface temperature and its ablation was dominated by the formation of a melt phase, which enhanced the development of a high crater aspect ratio (depth/diameter). In the case of other metal targets, e.g., Fe, they found out that the vapor phase played a more important role in the surface recession mechanism. They stated that the practicality of their simulations and experiments was based on an understanding of the melting and vaporization mechanisms of ablation, as these are considered to be potentially responsible for the non-stoichiometric sampling of aerosols used for elemental and trace analysis.

Mao et al. [129] have also investigated laser ablation mechanisms using picosecond and nanosecond lasers. In their study, it was evident that there were different distinct mechanisms which dominated the ablation process depending on the pulse duration, wavelength and energy of the laser used while maintaining all the other experimental parameters constant. In their

study, they used a 266 nm Nd:YAG laser with a pulse width of 30 ns and a 248 nm KrF excimer laser with a pulse width of 35 ps. They showed that in the ablation of a brass sample, the ns-laser ablation approached the stoichiometric ratio of Cu and Zn only at 0.3 GW cm^{-2} and deviated from the stoichiometric value at higher irradiances. However, with ps-laser ablation, representative sampling was achieved at increasing irradiances. The authors indicated that thermal vaporization predominated at lower irradiances for the ns-laser ablation and a non-thermal mechanism which involved an interaction between space charges and ionized species at the sample surface appeared to account for the behavior for ps-laser ablation. They also pointed out that from an analytical point of view, the ps-laser was more appropriate for chemical analysis since it could provide a higher emission intensity and a wider irradiance range over which accurate stoichiometric analysis could be accomplished.

An investigation regarding elemental fractionation of aerosols was also undertaken by Chen et al. [14] using double pulse LIBS in an orthogonal configuration. They studied the temporal and spatial distributions of the aerosols generated by ablating a brass target with a Zn/Cu molar ratio of 0.81. The results indicated that the particulate material close to the surface of the target was enriched with Cu compared to the bulk at most times, except at early delay times (≤200 μs). They attributed this effect to the lower vaporization temperature of Zn compared to Cu, hence, leaving behind a molten pool of Cu. However, at the very beginning (≤200 μs delay), the molar ratio was closer to that of the bulk since the vaporization process took time and its effect on the molar ratio was minimal. In other words, the ablation at this stage was stoichiometric. They also reported that for aerosols analyzed at a longer distance from the surface and at much later times, the Zn/Cu molar ratio was higher than that of the bulk material. The authors rationalized that this was because sputtered particles reached the cold regions at

longer distances from the surface where they act as nucleation centers for vapor condensation. In addition, the composition of the vapor at this distance was enriched in the more volatile component, which was Zn in this case, hence, the Zn/Cu molar ratio was higher than that in the bulk. Although it was not directly stated in the study, it was evident from the results the importance of choosing the correct experimental conditions, specifically the temporal and spatial parameters, to ascertain that sampling would be representative of the bulk solid. Therefore, under careful choice of experimental conditions the assumption of stoichiometric ablation necessary for CF-LIBS may hold.

Local thermodynamic equilibrium. Another important assumption of the CF-LIBS approach is the existence of local thermodynamic equilibrium (LTE) in the actual temporal and spatial observation gate [54-56]. In this state, a common temperature describes the Boltzmann distribution of species in energy levels, the Saha distribution of population of ionization stages and the Maxwell distribution of kinetic energy of electrons, atoms and ions [25]. Accordingly, the excitation temperature in the Boltzmann relationship (Eq. 5-1), which determines the population of atomic and ionic energy levels, must be equal to the ionization temperature in the Saha equation (Eq. 5-2), which controls the distribution of atoms of the same element in different ionization stages [124]. All the parameters in Eqs. 5-1 and 5-2 are defined in pp. 19-23.

$$n_k^s = n_{tot}^s \frac{g_k \, \mathrm{e}^{-E_k / k_B T_{exc}}}{U^s(T)} \tag{5-1}$$

$$n_e \frac{n^{II}}{n^I} = \frac{\left(2\pi m_e k_B T_{ion}\right)^{3/2}}{h^3} \frac{2U^{II}(T)}{U^I(T)} \exp\left(-\frac{\chi - \Delta\chi}{k_B T_{ion}}\right) \tag{5-2}$$

The criterion for LTE is that electron collision rates must dominate over radiative ones so that the radiation distribution can be allowed to deviate from the Planck function. This is why the observed plasma radiation, which is often completely transparent or optically thin over very

wide range of wavelengths, is not a blackbody source [130]. In other words, an excited state must have a higher probability of undergoing de-excitation by inelastic collision with an electron than by spontaneous radiative decay. This is analogous to setting a minimum value for the electron number density, n_e. In physical terms, the criterion in order to satisfy the LTE condition as given by Thorne [25] is:

$$n_{e,LTE} >> 1.6 \times 10^{12} \sqrt{T_K} \left(\Delta E\right)^3 \text{cm}^{-3} \tag{5-3}$$

where T_K is the temperature (K) and ΔE is the largest energy transition considered (eV). This is also oftentimes referred to as the McWhirter criterion. A complete treatment on local thermodynamic equilibrium is described in Refs. [25, 130, 131].

An investigation of the state of local thermodynamic equilibrium in laser-induced plasmas was recently undertaken by Barthélemy et al. [132]. In their study, they used an aluminum target and measured the excitation temperature at different delay times by the Boltzmann plot method using several neutral iron lines over the range of 3.21-6.56 eV. They obtained excellent linear Boltzmann plots at all delay times considered which implies that the Boltzmann equilibrium condition is met. However, the excitation temperatures calculated at delay times less than 1 μs were lower than the ionization temperatures calculated using the Saha relations. Error bars on the excitation and ionization temperatures calculated, which included uncertainties in transition probabilities and electron number density as well as statistical errors, only began to overlap after about 0.8 μs. To further explore the existence or non-existence of LTE, they compared the temporal evolution of experimental and calculated line intensities of Mg I at 285.21 nm, Mg II at 279.55 nm and Al II at 281.62 nm. They reported a remarkable agreement between the experimental and calculated time-dependent intensities for the Mg I line with a slight under-population of the neutral states with respect to LTE conditions at delay times lower than 1 μs,

but still falling within the experimental errors. From these results, together with the Boltzmann equilibrium observed for the neutral states, they concluded that the neutral species were in thermal equilibrium with electrons even at early times, and hence, the electron temperature can be approximated by the excitation temperature. On the other hand, there was no convergence between experimental and theoretical curves for ionic lines except at delay times longer than 2 μs and significant overpopulation occurred at early times which implied that Saha equilibrium was not met. The authors asserted that this was because the plasma could be considered as stationary for the higher energy states.

Capitelli et al. [133] published an excellent treatise on equilibrium and non-equilibrium problems which occurred during the expansion of laser-induced plasmas. They discussed non-equilibrium plasmas in terms of the characteristic times of plasma expansion using fluid dynamics, deviation from Boltzmann distribution of excited state population using collisional radiative models and non-Maxwell behavior of the electron energy distribution function using the kinetic Boltzmann equation. On the other hand, equilibrium plasmas were discussed in terms of the challenges associated with partition function calculation, equilibrium composition and thermodynamic and transport properties of thermal plasmas. In brief, they have described the existence of a quasi-equilibrium state in which the Boltzmann relation was satisfied while the ionization equilibrium was violated either by predominance of the ionization process over recombination one or vice-versa. They also asserted that non-equilibrium conditions in a plasma near the surface was caused by the decrease in plasma temperature due to expansion and occurred whenever the following condition is satisfied:

$$t_{ion} \geq t_{exp} \tag{5-4}$$

where t_{ion} is the characteristic ionization time and t_{exp} is the characteristic time of plasma expansion. For typical plasma conditions, t_{ion} is in the range of 1-10 μs and is given by:

$$t_{ion} \approx \left(n_I k_{ion}\right)^{-1} \tag{5-5}$$

where n_I is the number density of neutral atoms in cm^{-3} and k_{ion} is the ionization rate coefficient with typical values of 10^{-11}-10^{-14} cm^3 s^{-1}. $t_{exp,}$ on the other hand, is given by:

$$t_{exp} = \frac{d}{\upsilon} \tag{5-6}$$

where d is the laser spot diameter in cm and υ is the plasma expansion velocity with values in the range of 10^5-10^6 cm s^{-1}.

Verification of the validity of local thermodynamic equilibrium in laser-induced plasmas using the line-to-continuum approach has also been recently proposed by Moon et al. [134]. The method is based on a similar research done by Sola et al. [135] in which the line-to-continuum intensity ratio method was used to determine the electron temperature in a high-pressure microwave discharge. The equation can be written as:

$$\frac{\bar{I}(\lambda)}{\varepsilon_{c,\lambda}} = 2.005\times10^{-5}\,\frac{A_{ki}g_k}{U(T)}\,\frac{\lambda}{T_e}\,\frac{\exp\left(\dfrac{-E_k}{k_B T_{exc}}\right)\exp\left(\dfrac{\chi-\Delta\chi}{k_B T_e}\right)}{\xi\left[1-\exp\left(\dfrac{-1}{T_e}\dfrac{hc}{k_B\lambda}\right)\right]+G\exp\left(\dfrac{-1}{T_e}\dfrac{hc}{k_B\lambda}\right)} \tag{5-7}$$

where $\bar{I}(\lambda)$ is the wavelength-integrated intensity of emitted light (W cm^{-3}), $\varepsilon_{c,\lambda}$ is the non-integrated continuum radiation intensity (W cm^{-3} nm^{-1}), ξ is the free-bound continuum correction factor, G is the free-free Gaunt factor and the other variables are defined in pp. 19-23. The main premise of this method is to compare the electron temperature, T_e, calculated using Eq. 5-7 with the excitation temperature, T_{exc}, determined using the Boltmann plot method at several delay times.

An excellent overview of the literature regarding the evaluation of local thermodynamic equilibrium in laser-induced plasmas is given in Ref. [124]. Tognoni et al. [124] concluded that it is evident from the results published in the literature that LTE is a good approximation in describing the plasma conditions usually at delays longer than 1 μs but that the reliability of the hypothesis is heavily dependent on various experimental parameters such as laser pulse energy, pulse width, ambient gas, temporal parameters, etc. The authors in Ref. [124] advise that it is necessary that all these parameters be reported as accurately as possible in order to determine the extent of the validity of the LTE condition and reproduce the exact experimental conditions, if necessary.

Optically thin plasma. In the CF-LIBS protocol, it is recommended that the spectral lines chosen for quantitative analysis do not suffer from self-absorption. In other words, the plasma must be optically thin. The measured intensities of lines which are possibly self-absorbed are lower than expected and have broader line widths, hence, resulting in an underestimation of the concentration of a sample component [54].

The radiation source is considered optically thin if all the emitted radiation reaches the detection system without re-absorption or if the product $n_i f_{ik} l$ approaches zero, where n_i is the number density (cm^{-3}) at lower level i, f_{ik} is the absorption oscillator strength (dimensionless) and l is the path length (cm) [106]. Although atoms at lower energy levels have a higher probability to re-absorb the radiation emitted by other atoms of the same elements in the plasma, it is less problematic in relatively small laser-induced plasmas where path lengths are short and for trace elements where there is only a small amount of analyte present in the plume.

The most recent version of the CF-LIBS approach does not have the exacting requirement of having an optically thin radiation source since the modified algorithm includes a method for

the correction of self-absorption as described in Refs. [54, 123, 125, 136]. However, it should be noted that this part of the algorithm underwent major revisions and improvements at the beginning of this research and a new method of correction was developed almost every year. For these reasons alone and for some limitations intrinsic to the methods of self-absorption correction, the CF-LIBS version that was used in the spectral data analysis does not include any form of self-absorption correction, hence, the necessity for optically thin spectral lines remains critical.

Measurement of Integrated Line Intensity

In the CF-LIBS routine, after the raw spectrum has been corrected for background and detector spectral efficiency, the peaks are manually labeled and identified by comparison of the approximate central wavelength with the NIST atomic spectra database [137]. Only the lines emitted by neutral (I) and singly-ionized species (II) are detected based on the experimental conditions of typical LIBS measurements [56]. The assigned peaks are fitted with an analytical approximation of the Voigt function which gives the measured central wavelengths, net line widths and the integrated line intensities as outputs [55, 56].

Under the assumption of local thermodynamic equilibrium, the integrated line intensity, I_{λ}^{ki}, in photons cm^{-3} s^{-1}, corresponding to the transition between upper energy level E_k and lower energy level E_i of an atomic species s can be expressed as [54, 56]:

$$I_{ki} = n_k^s A_{ki} = n_{tot}^s A_{ki} \frac{g_k \, \mathrm{e}^{-E_k / k_B T}}{U^s(T)} \tag{5-8}$$

where λ is the transition wavelength (nm), n_k^s is the number density (cm^{-3}) of species s at level k, n_{tot}^s is the total number density (cm^{-3}) of emitting atoms for each species, A_{ki} is the line transition probability for spontaneous emission (s^{-1}), g_k is the upper level degeneracy, k_B is the Boltzmann's

constant (J K^{-1}), T is the plasma temperature (K), and $U^s(T)$ is the partition function for the emitting species at the plasma temperature (dimensionless).

Spectral efficiency correction of the raw spectrum is not required at the beginning of the CF-LIBS analysis since it can be executed within the software as long the detector efficiency correction file is loaded into the program. This step is important because the measured integral line intensities, $I_{ki,meas}$, are affected by the optical efficiency of the collection system, $F_{det}(\lambda)$ which acts as a scale factor, as given in Eq. 5-9 and can be expressed as the product of the wavelength-dependent relative efficiency, $F_{rel}(\lambda)$, and the wavelength-independent absolute efficiency, F_{abs}, so that [138]:

$$I_{ki,meas} = F_{det}(\lambda) I_{ki} = F_{rel}(\lambda) F_{abs} I_{ki} \tag{5-9}$$

Rearrangement of Eq. 5-9 yields:

$$\overline{I_{ki}} = \frac{I_{ki,meas}}{F_{rel}(\lambda)} = F_{abs} I_{ki} \tag{5-10}$$

where $\overline{I_{ki}}$ is the measured integrated line intensity corrected for relative spectral efficiency. Also, in order to take into account the total particle number density of the plasma, n_{tot}, an overall experimental factor F is introduced:

$$F_{abs} n_{tot}^s = F_{abs} n_{tot} C^s = F C^s \tag{5-11}$$

where C^s refers to the relative number density of the species s in the sample. Combining Eqs. 5-8 to 5-11 yields the final expression for the measured integrated line intensity:

$$\overline{I_{ki}} = F C^s A_{ki} \frac{g_k \, e^{-E_k / k_B T}}{U^s(T)} \tag{5-12}$$

Determination of Electron Number Density

Knowledge of the electron number density is essential in describing the conditions of the plasma. In the CF-LIBS algorithm, there are three different approaches in determining electron number density and each method is described in detail in this section.

Saha-Boltzmann method. In this approach, the Boltzmann and Saha equations, given in Eqs. 5-1 and 5-2, respectively, are combined in order to describe the population ratio of two excited levels *k* and *m* of successive ionization stages of the same element, neutral and singly-ionized, respectively [124]. The resulting equation is given in Eq. 5-13:

$$n_e \frac{n_m^{II}}{n_k^I} = \frac{\left(2\pi m_e k_B T\right)^{3/2}}{h^3} \frac{g_m^{II}}{g_k^I} \exp\left(-\frac{E_m^{II} - E_k^I + \chi - \Delta\chi}{k_B T}\right) \tag{5-13}$$

where χ is the ionization potential (eV), $\Delta\chi$ is the lowering of the ionization potential (eV) and the rest of the parameters are defined in pp. 19-23. Substitution of Eq. 5-8 into Eq. 5-13 and simplification of variables yields the final expression:

$$n_e = 6.0 \times 10^{21} \left(\frac{\overline{I_{ki}^I}}{\overline{I_{ml}^{II}}}\right)\left(\frac{g_m^{II} A_{ki}^{II}}{g_k^I A_{ml}^I}\right)\left(T_{eV}^{3/2}\right)\exp\left(-\frac{E_m^{II} - E_k^I + \chi - \Delta\chi}{T_{eV}}\right) \tag{5-14}$$

This approach requires that the plasma must be sufficiently close to LTE conditions, otherwise, Eqs. 5-13 and 5-14 will not hold. Also, the use of Eq. 5-14 necessitates, in advance, the knowledge of the plasma temperature which usually presents a problem since methods of determining plasma temperature usually requires that electron number density is known as well.

Stark broadening method. As mentioned in Chapter 3, spectral line profiles are affected by different broadening effects and under typical experimental conditions employed in LIBS measurements, the main contribution to the spectral line width comes from Stark broadening. This type of broadening results from the interactions of the emitting atom with the electric field produced by the surrounding charged particles.

There are two computational methods based on the Stark effect which are incorporated into the CF-LIBS algorithm, one is based on the quadratic Stark effect of non-hydrogenic elements and the other is based on the Stark broadening of the Balmer hydrogen-alpha line, Hα, at 656.27 nm, which follows a linear Stark effect. Both methods have an advantage over the Saha-Boltzmann approach since they do not require the plasma to be in local thermodynamic equilibrium. However, knowledge of Stark broadening coefficients is required and most of them are scattered in the literature and some are not available.

Quadratic Stark effect. The electron number density calculation based on the quadratic Stark broadening of a line expressed as the FWHM in nanometers is given by [124]:

$$\Delta\lambda_{Stark} = 2w\left(\frac{n_e}{10^{16}}\right) + 3.5\alpha\left(\frac{n_e}{10^{16}}\right)^{1/4}\left[1-\beta n_D^{-1/3}\right]w\left(\frac{n_e}{10^{16}}\right) \quad (5\text{-}15)$$

$$n_D = 1.72\,\mathrm{x}\,10^{9}\,\frac{T_{eV}^{3/2}}{n_e^{1/2}} \quad (5\text{-}16)$$

where w is the electron-impact half-width in nm, α is the ion-broadening parameter, β is a coefficient equal to 0.75 or 1.2 for neutral and ionic lines, respectively, n_e is the electron number density in cm^{-3} and n_D is the number of particles in the Debye sphere in cm^{-3} (Eq. 5-16). Several Stark broadening parameters for different neutral and singly-charged ionic lines are tabulated in Refs. [131, 139] and excellent critical reviews of more recent calculated Stark coefficients are found in Refs. [140-143]. Furthermore, the second term in Eq. 5-15 is normally neglected due to the negligible contribution of ion-broadening under typical LIBS conditions, hence:

$$\Delta\lambda_{Stark} = 2w\left(\frac{n_e}{10^{16}}\right) \quad (5\text{-}17)$$

The Stark width, $\Delta\lambda_{Stark}$, which is Lorentzian in nature, can be estimated from the net line width, $\Delta\lambda_V$, of the resulting fit of the line which follows a Voigt function. Assuming that other

broadening mechanisms (e.g. natural, van der Waals, etc.) have negligible contribution to the line width, the Stark width can be calculated using Eq. 5-18:

$$\Delta\lambda_{Stark} = \frac{\Delta\lambda_V^2 + \Delta\lambda_G^2}{\Delta\lambda_V} \tag{5-18}$$

where $\Delta\lambda_G$ is the Gaussian line width determined from contribution of Doppler and instrumental broadening [54, 106]. In addition, it is crucial that lines chosen do not suffer from self-absorption since self-absorbed lines result in much broader line widths and an over-estimation of the electron number density.

Linear Stark Effect. The Stark broadening of hydrogen and hydrogenic ions is symmetric and is a linear function of the electric field strength. The use of hydrogen lines for electron number density determination, particularly, the lines in the Balmer series, is a well-established plasma diagnostic method. In brief, the Balmer series involves transitions with n = 2 as the lowest level, where n is the principal quantum number. The different lines in a particular series are ordered according to a change in n (Δn). Transition involving a Δn = 1 is called an α transition, a Δn = 2 is a β transition, and so on.

The Stark broadening of hydrogen lines have been effectively used in the past for diagnostics of several different kinds of plasmas. Escarguel et al. [144] observed and analyzed for the first time the emission from hydrogen lines in a plasma created with a single-pulse laser in bulk water. Ashkenazy et al. [145] measured the electron number density of plasma jets generated by a high-pressure capillary discharge capillary based on the Stark broadening of Hα and Hβ lines at various capillary currents and spatial positions. In astronomy, Hanaoka et al. [146] used high-cadence imaging, linear polarization and velocity field of Hα line to study the high energy aspect of the solar flares.

One of the very first studies that reported the use of Hα line at 656.272 nm for the determination of electron number density in laser-induced plasmas from solid targets in humid air was by El Sherbini et al. [147]. The Hα approach is based on the premise that plasmas produced in the presence of a very small concentration of water in the ambient atmosphere is optically thin and is, therefore, ideal for determining electron number density. Fig. 5-1 shows the temporal evolution of the Hα line and it can be observed that it is characterized by a relatively large signal-to-noise ratio and a broad line width. Experiments have also shown that the Hα line persists a long time after the termination of the laser pulse, up to about 10 μs [147]. In addition, any uncertainties on the spectral line fitting and on the estimation of instrumental broadening as well as Doppler broadening contributions can be considered less significant due to the relatively large line widths of the Hα lines, which are typically in the range of 0.5 to 3.0 nm [145].

The electron number density can be determined by using Eq. 5-19 [145, 147]:

$$n_e(\mathrm{cm}^{-3}) = 8.02 \times 10^{12} \left(\frac{\Delta\lambda_{H\alpha}}{\alpha_{1/2}} \right)^{3/2} \tag{5-19}$$

where $\Delta\lambda_{H\alpha}$ is the line width of the Hα line in nm and $\alpha_{1/2}$ is the FWHM of the reduced Stark profiles in nm per cgs field strength unit, which is weak function of temperature and electron number density through the ion-ion correlation and Debye shielding correction and the velocity dependence of the impact broadening [147]. A partial list of $\alpha_{1/2}$ values at selected temperatures and electron number densities are found in Table 5-1. More calculated $\alpha_{1/2}$ values can be found in Refs. [131, 139].

Determination of Laser-Induced Plasma Temperature

As discussed previously, under the assumption of local thermodynamic equilibrium, a single temperature describes the distribution of species in energy levels, the population of ionization states and kinetic energy of electrons, atoms and ions. Several techniques have been described in the literature for determining the plasma temperature and these include the line-pair ratio, line-to-continuum ratio, Boltzmann plot and Saha-Boltzmann plot. In the CF-LIBS algorithm, only the Boltzmann and the Saha-Boltzmann plots are included.

Boltzmann plot method. Evaluation of the laser-induced plasma temperature using the Boltzmann plot approach requires the measurement of intensities of a series of optically thin spectral lines from different excitation states of the same species on condition that transition probabilities, statistical weights and excitation energies are available. Linearization of the expression given in Eq. 5-12 yields the Boltzmann plot equation [55, 56]:

$$\ln\frac{\overline{I_{ki}}}{g_k A_{ki}} = -\frac{1}{k_B T}E_k + \ln\frac{FC^s}{U^s(T)} \tag{5-20}$$

Plotting the left-hand side of Eq. 5-20 against the upper energy level E_k in eV yields a slope equal to $-1/k_B T$. The Boltzmann plot method allows plasma temperature to be determined through a simple linear regression without knowledge of the concentration (or number densities) and the partition function, which is also a function of temperature. Although, it is important that the spectral lines chosen have excitation energies which are widely distributed in order to increase the accuracy of the determination. In addition, compared to the line-pair ratio method which is also based on the Boltzmann equation, the Boltzmann plot method leads to better precision in the plasma temperature calculation since a series of lines are used simultaneously, which in effect averages out any uncertainties inherent to the transition probabilities available in atomic spectra databases [124]. An example of a Boltzmann plot generated for neutral iron lines

in aluminum alloy sample is illustrated in Fig. 5-2. The calculated temperature from the slope is 10677 K.

Saha-Boltzmann plot method. The calculation of laser-induced plasma temperature based on the Saha-Boltzmann plot approach was first reported by Yalcin et al. [103]. The main difference between this method and the Boltzmann plot approach is that both neutral and singly-ionized species are placed on the same plot. This presents a huge advantage for this method since it provides a larger energy spread using the transitions from different ionization stages.

In brief, the *x*- and *y*-coordinates of neutral lines are exactly the same as those of the Boltzmann plot method. However, in the case of lines from singly-ionized species, adjustment of the *x*- and *y*-coordinates is required in order to place the ions on the same plot as the neutrals. The corrected *x*- and *y*-coordinate for the ionic lines can be obtained by linearization of Eq. 5-13 after substitution of Eq. 5-8, as shown in Eq. 5-21:

$$\ln\left(\frac{\overline{I_{ml}^{II}}}{g_m^{II}A_{ml}^{II}}\right)-\ln\left(\frac{2(2\pi m_e k_B)^{3/2}}{h^3}\frac{T^{3/2}}{n_e}\right)-\ln\left(\frac{\overline{I_{ki}^{I}}}{g_k^{I}A_{ki}^{I}}\right)=-\frac{E_m^{II}+\chi-\Delta\chi}{k_BT}-\frac{-E_k^{I}}{k_BT} \qquad (5\text{-}21)$$

For clarity on the transitions involved (and subscripts used), a schematic of the energy levels are illustrated in Fig. 5-3. The adjusted abscissa and ordinate points for the singly-ionized lines are shown in Eqs. 5-22 and 5-23, respectively.

$$x^{II}=E_m^{II}+\chi-\Delta\chi \qquad (5\text{-}22)$$

$$y^{II}=\ln\left(\frac{\overline{I_{ml}^{II}}}{g_m^{II}A_{ml}^{II}}\right)-\ln\left(\frac{2(2\pi m_e k_B)^{3/2}}{h^3}\frac{T^{3/2}}{n_e}\right) \qquad (5\text{-}23)$$

Similar to the Boltzmann plot, this method allows for the determination of temperature from the slope of the line ($-1/k_BT$). However, several iterations of y^{II} must be performed due to the $T^{3/2}$ term in the ordinate ion points and the Saha-Boltzmann plot method requires the electron number

density to be determined independently [103]. Examples of Saha-Boltzmann plots using neutral and singly-ionized lines of different elements are depicted in Fig. 5-4. The average temperature calculated from the slopes of the line is 11141 ± 600 K.

Determination of Relative Concentration and Experimental Factor

The final aspect of the CF-LIBS routine is the calculation of the elemental concentration using the Boltzmann plot equation given by Eq. 5-20, where each spectral line is represented as a point and the points from different species lie on several parallel lines under LTE condition [56]. The concentration parameter FC^s can be solved from the y-intercept, b^s, of the different lines in the Boltzmann plane (Eq. 5-24), but in order to determine the overall experimental factor F, it is essential to normalize to unity the sum of the species concentrations (Eq. 5-25) [56]. It is because of this simplification that only relative percentages of sample components are possible with CF-LIBS. Absolute measurement is possible only if the total particle number density, n_{tot}, which appears in Eq. 5-11 can be determined independently.

$$b^s = \ln \frac{FC^s}{U^s(T)} \tag{5-24}$$

$$\sum_s C^s = \frac{1}{F} \sum_s U^s(T) \mathrm{e}^{b^s} = 1 \tag{5-25}$$

Rearrangement of Eq. 5-25 gives the expression for the experimental factor F:

$$F = \sum_s U^s(T) \mathrm{e}^{b^s} \tag{5-26}$$

Therefore, the elemental species concentration can be determined by combining Eqs. 5-24 and 5-26, so that:

$$C^s = \frac{U^s(T) \mathrm{e}^{b^s}}{\sum_s U^s(T) \mathrm{e}^{b^s}} = \frac{U^s(T) \mathrm{e}^{b^s}}{F} \tag{5-27}$$

After obtaining all the relative species concentrations, addition of values corresponding to neutral and singly-ionized species for a given element *M* is required in order to determine the total elemental composition, as given by [55, 56]:

$$C_M^{TOT} = C_M^I + C_M^{II} \tag{5-28}$$

Monte Carlo Simulated Annealing Optimization Method for Laser-Induced Breakdown Spectroscopy (MC-LIBS)

The other key part of this research is the application of the semi-empirical radiative model developed by Gornushkin et al. [61-64]. The initial purpose of its formulation was the development of a radiation dynamic model for post-breakdown laser-induced plasma expansion in vacuum as applied to practical spectroscopy [61]. However, a distinct aspect of this modeling algorithm is that it is also possible to find a solution to the inverse problem of determining initial plasma conditions by a direct comparison of experimental with calculated spectra using an algorithm called the Monte Carlo simulated annealing optimization [62]. Complete theoretical information on the evolution and derivation of the model can be found in Refs. [61-64] and only the aspects analogous to the CF-LIBS algorithm will be described in detail.

Working Hypotheses and General Theoretical Considerations

The semi-empirical model, describes the expansion of a non-viscous and non-conducting plasma into vacuum at the end of the laser pulse when the laser-matter interaction has terminated (post-breakdown) and the plasma has thermalized (LTE is established). This time is taken as the starting point ($t = 0$) of the model. The algorithm is written in MATLAB 7.3.0 (R2006b) and the first version of the model assumes that the plasma acquires a spherical symmetry during expansion [61-63]. It is also assumed that the plasma composition remains constant in time (stoichiometric ablation) and that the species distribution is collision-dominated [61, 62].

In the model, the plasma is effectively described by a system of gas dynamic equations, in addition to the radiative transfer and state equations. There is also no limitation set on the character of atomic transitions; in other words, resonance or non-resonance lines can be used as long as the required spectroscopic parameters are available in atomic spectra databases [61]. In contrast with the CF-LIBS approach, higher ionization states can also be included in the simulations. The combination of all these factors yields an analytical expression for the radiation dynamics of the plasma and the structure of the plasma emission spectra.

A non-isothermal asymmetric laser-induced plasma expansion model was recently formulated by Gornushkin et al. [64] as a modification to the original version in order to eliminate the restrictive spherical symmetry assumption and to formally extend the plasma model to more realistic plasma shapes, specifically an ellipsoidal one [64]. The mathematical treatment of the asymmetric expansion of the radiative, thermally anisotropic plasma into vacuum has been extensively described in Ref. [64] and will not be discussed in this chapter due to the complexity of the equations and theories involved which are beyond the scope of this research. However, in order to understand the basic principles of the semi-empirical plasma radiative model as applied to analytical spectroscopy, the modeling of the expansion of spherically symmetrical laser-induced plasmas into vacuum will be described in detail in the succeeding sections. All variables used in the next sections are defined in pp. 19-23.

Calculation of Total Number Density, Temperature and Their Initial Distributions

The total number density of the *j*th constituent, $n^j(r,t)$, is a function of the radial coordinate *r* of particle in the plasma and time *t* and can be expressed as:

$$n^j(r,t) = \left(\frac{R(0)}{R(t)}\right)^3 g^j\left(r\frac{R(0)}{R(t)}\right) \tag{5-29}$$

where $R(t)$ is the radius of the outer boundary of the plasma at a particular time *t*, and $g^j(r)$ is the initial distribution of the number density of *j*th constituent at *t* = 0 or $n^j(r,0)$. In the model, $n^j(r,t)$ is calculated from the gas dynamic equation of conservation of mass which is given by:

$$\frac{\partial n^j}{\partial t} + \frac{1}{r^2}\frac{\partial}{\partial r}\left(r^2 u n^j\right) = 0 \tag{5-30}$$

The details of the derivation of Eq. 5-29 are given in Appendix B.

Solution of Eq. 5-30 requires knowledge of the radial expansion velocity, $u(r,t)$:

$$u(r,t) = \zeta(t) r = \frac{V(t)}{R(t)} r \tag{5-31}$$

where $V(t)$ is the velocity of the plasma boundary (cm s^{-1}), a measurable parameter initially introduced into the model. In the model it is assumed that the collective velocity of particles inside the plasma only has a radial component and depends linearly on the radial position of a particle where $0 \le r \le R(t)$. The plasma expansion speed, $u(r,t)$, can be determined once the proportionality coefficient between collective velocity of particles and radius, $\zeta(t)$, is solved from the momentum conservation equation (Eq. 5-32):

$$\frac{\partial}{\partial t}\left[u\sum_j \mu^j n^j\right] + \frac{1}{r^2}\frac{\partial}{\partial r}\left(r^2 u^2 \sum_j \mu^j n^j\right) = -\frac{\partial p}{\partial r} \tag{5-32}$$

where μ^j is the mass of *j*th constituen*t* (g) and *p* is the gas pressure (dyne cm^{-2}). The proportionality coefficient at *t* = 0, $\zeta(0)$ can be determined by:

$$\zeta^2(0) = \frac{p(0)}{\int_0^R \left(\sum_j \mu^j n^j(r,0)\right) r dr} \tag{5-33}$$

where $p(0)$ is the pressure at the plasma center. The values of the moving plasma boundary velocity, initial plasma radius, and gas pressure are essential input parameters in the

aforementioned calculations [61]. Typical values for these parameters are 10^5-10^6 cm s^{-1}, 0.1-0.5 cm and 0.01-0.1 Torr, respectively. The derivation of Eq. 5-33 can be found in Appendix A.

The laser-induced plasma temperature, *T*, can be determined using the energy conservation equation (Eq. 5-34) which considers only the contribution of plasma thermal energy and plasma expansion energy since the energy supplied by the photons is considered negligible:

$$\frac{\partial}{\partial t}\left(\rho\varepsilon+\frac{\rho u^2}{2}\right)=-\vec{\nabla}\left[\vec{u}\left(\rho\varepsilon+p_{total}+\frac{\rho u^2}{2}\right)\right]-q \tag{5-34}$$

where ρ is the gas density (cm^{-3}) and ε is the internal energy per unit mass (erg g^{-1}) of the gas species. The energy balance equation also includes a radiation loss term *q*, in erg cm^{-3} s^{-1}, which is particularly significant during the early hot stage of plasma evolution. Moreover, the plasma expansion energy, calculated from the plasma expansion speed, $u(r,t)$, is included as well because this energy is comparable to the thermal motion energy [61]. Taking into consideration all of the above points, the time derivative of temperature, given by Eq. 5-35, can be obtained by solving the energy balance equation [61] .

$$\frac{\partial T}{\partial t}=-\zeta\left[3T\frac{\sum_j n^j}{\sum_j \alpha^j n^j}+\left(\frac{\frac{5}{2}r^2\sum_j \mu^j n^j}{\sum_j \alpha^j n^j}\right)\left(\frac{T(0,t)\sum_j n^j(0,t)}{\int_0^R rdr\sum_j \mu^j n^j(r,t)}\right)+r\frac{\partial T}{\partial r}+\frac{r\frac{\partial}{\partial r}\left(T\sum_j n^j\right)}{\sum_j \alpha^j n^j}\right]s \tag{5-35}$$
$$-\frac{q}{k_B\sum_j \alpha^j n^j}$$

where α^j is ratio of specific heat capacities. The complete details of the derivation of the time derivative of plasma temperature *T* are found Appendix C.

Another important aspect included in the model is the parabolic initial distribution functions for both temperature (Eq. 5-36) and number density (Eq. 5-37):

$$T(r,0) = T_0\left(1 - k_1 r^2\right) \tag{5-36}$$

$$n^j(r,0) = n_0^j\left(1 - k_2 r^2\right) \tag{5-37}$$

where T_0 and n_0^j are the initial temperature and the initial number density, respectively, of the *j*th constituent at the plasma center, and k_1 and k_2 are numerical coefficients which are dependent on the gradient desired. It is also important to indicate the boundary conditions used to solve the system of equations described above [61]:

- the radius R(t) of the plasma after LTE has established (t = 0) is between 0.1 and 0.5 cm,
- the plasma expansion speed at the plasma center (r = 0) is zero, and
- the pressure as the radius of the plasma approaches the outer boundary R is equal to zero.

Calculation of Number Density of Atoms, Ions and Electrons

In the model, calculation of the number densities of electrons (Eq. 5-38), atoms (Eq. 5-39), and ions (Eq. 5-40) within the plasma are obtained by the use of the Saha ionization equation, the total mass conservation equation and the charge equilibrium equation, which are given by Eqs. 5-41, 5-42 and 5-43, respectively.

$$n_e = \sum_j \frac{n^j s^j(T)}{s^j(T) + n_e} \tag{5-38}$$

$$n_a^j = \frac{n^j n_e}{s^j(T) + n_e} \tag{5-39}$$

$$n_i^j = \frac{n^j s^j(T)}{s^j(T) + n_e} \tag{5-40}$$

$$\frac{n_i^j}{n_a^j} n_e = s^j(T) = 2\frac{U_i^j}{U_a^j}\left(\frac{2\pi m_e k_B T}{h^2}\right)^{3/2} \exp\left(-\frac{\chi^j - \Delta\chi}{k_B T}\right) \tag{5-41}$$

$$n_a^j + n_i^j = n^j \tag{5-42}$$

$$\sum_j n_i^j = n_e \tag{5-43}$$

Here, subscripts *a*, *i,* and *e* denote atoms, ions, and electrons, and all the other parameters are defined in pp. 19-23. Details of the derivation of Eqs. 5-38 through 5-40 are found in Appendix D.

Calculation of Emission Spectral Radiance and Line Profile

The radiative transfer equation, which describes the effect of radiation on the plasma, is given by the following equation, in spherical coordinates:

$$\varphi \frac{\partial I_\nu}{\partial r} + \frac{1-\varphi^2}{r}\frac{\partial I_\nu}{\partial \varphi} + \kappa'_\nu I_\nu = \kappa'_\nu I_\nu^b = K(r) \tag{5-44}$$

where $I_\nu = I_\nu(r, \varphi, \nu, t)$ is the emission spectral radiance (erg s^{-1} cm^{-2} Hz^{-1} sr^{-1}), $\kappa'_\nu = \kappa'_\nu(r, \nu, t)$ is the total absorption coefficient including stimulated emission (cm^{-1}) at any given point in the plasma, $I_\nu^b = I_\nu^{b'}(T)$ is the spectral radiance of blackbody radiation at temperature $T(r,t)$ (erg s^{-1} cm^{-2} Hz^{-1} sr^{-1}), φ is the angular factor cos θ and θ is the angle formed by the radius-vector *r* from the plasma center to an arbitrary point inside the plasma. An illustration of the spherical coordinate system used in the model is given in Fig. 5-5. In addition, it is assumed in the model that the rates of gas dynamic processes are much slower than the rates of radiative processes that only the stationary radiative transfer equation can be considered. The spectral radiance can be solved from Eq. 5-44 for any boundary condition in two ways in order to execute two computational routines.

Rough approximation. This approximation is used to calculate the radiation loss term in the energy equation. The spectral radiance inside the plasma sphere is calculated under the assumption that no radiation enters the plasma. The first order partial differential of Eq. 5-44 can be solved explicitly for any boundary conditions and can be expressed as:

$$I_\nu(r,\varphi) = \int_{-\sqrt{R^2-r^2(1-\varphi^2)}}^{r\varphi} dz K\left(\sqrt{z^2+r^2(1-\varphi^2)}\right) \exp\left[-\int_z^{r\varphi} ds \kappa'_\nu \left(\sqrt{s^2+r^2(1-\varphi^2)}\right)\right] \tag{5-45}$$

The calculations are carried out in a wide frequency range and require the use of the approximate expression for absorption coefficient given by the Planck mean absorption coefficient, κ^{Σ}_{mean}, as given by:

$$\kappa^{\Sigma}_{mean} = \left(\frac{128}{27} k_B\right)^{1/2} \left(\frac{\pi}{m_e}\right)^{3/2} \frac{z^2 e^6 G}{h\sigma c^3} \frac{n_e}{T^{7/2}} \sum_{j=1}^{N} n_i^j \tag{5-46}$$

which considers only the free-free and free-bound transitions. *G* in Eq. 5-46 is the dimensionless free-free Gaunt factor which is a weak function of temperature and electron number density and improves the theoretical description of the free-free continuum. However, precise quantum-mechanical calculation of Gaunt factors exist mostly for hydrogenic species and in most cases, the numerical value of *G* is approximately unity [148, 149]. The rest of the variables in Eq. 5-46 are defined in pp. 19-23. The use of the Planck mean absorption coefficient, κ^{Σ}_{mean}, also implies that that the line structure of the spectrum is not included since bound-bound transitions were neglected.

The spectral radiance given by Eq. 5-45 and the Planck mean absorption coefficient κ^{Σ}_{mean} are then used in the calculation of the radiation loss term *q* (Eq. 5-47) in the energy balance equation.

$$q = \int_0^{\infty} \mathrm{d}\nu \int \kappa'_\nu \left(I^b_\nu - I_\nu\right) \mathrm{d}\Omega \tag{5-47}$$

The use of κ^{Σ}_{mean} as an approximate expression for κ'_ν in the calculation of the radiation loss term *q* is valid and rationalizes the assumption of negligible bound-bound transitions since for the total energy emitted by the plasma, the radiation due to bound-bound transitions is a small

fraction of the total radiation energy. In other words, the line structure of the spectrum does not significantly affect the energy balance and is, therefore, omitted [61]. Also, as the plasma cools down and emits at frequencies of discrete atomic and ionic lines at later times, the radiation energy loss q becomes less significant [61].

Detailed approximation. The second solution to the radiative transfer equation allows the calculation of radiation emitted by the exterior of the plasma in a narrow frequency range in the vicinity of atomic or ionic transitions. The detailed approximation describes in detail the radiation emitted by the plasma. For the point on the sphere boundary where $r = R$, the spectral radiance can be written as:

$$I_\nu(R,\varphi) = \int_{-R\varphi}^{R\varphi} dz K\left(\sqrt{z^2 + R^2\left(1-\varphi^2\right)}\right) \exp\left[-\int_z^{R\varphi} ds\, \kappa'_\nu \left(\sqrt{s^2 + R^2\left(1-\varphi^2\right)}\right)\right] \tag{5-48}$$

The calculation requires the use of the exact absorption coefficient, κ'_ν, which now includes the contribution of all three dominant transitions, i.e., free-free, free-bound, and bound-bound, and can be expressed as:

$$\kappa'_\nu = \kappa^\Sigma_{ff} + \kappa^\Sigma_{fb} + \kappa^\Sigma_{bb} \tag{5-49}$$

Expressions for the free-free κ^Σ_{ff}, free-bound κ^Σ_{fb} and bound-bound κ^Σ_{bb} absorption coefficients are given in Eqs. 5-50, 5-51, and 5-52, respectively,

$$\begin{aligned} \kappa^\Sigma_{ff} &= \left(\frac{8\pi e^6}{3m_e hc\left(6\pi m_e k_B\right)^{1/2}}\right) \frac{n_e}{T^{1/2}} z^2 \frac{G}{\nu^3} e^{(h\nu/k_B T - 1)} \sum_{j=1}^{N} n_i^j \\ &= 3.7\times 10^8\, cgs\, \frac{n_e}{T^{1/2}} z^2 \frac{G}{\nu^3} e^{(h\nu/k_B T - 1)} \sum_{j=1}^{N} n_i^j \end{aligned} \tag{5-50}$$

$$\kappa_{fb}^{\Sigma} = \left(\frac{8\pi e^6}{3m_e hc\left(6\pi m_e k_B\right)^{1/2}} \right) \frac{n_e}{T^{1/2}} z^2 \frac{\xi_z}{\nu^3} e^{h\nu/k_B T} \left(1 - e^{-h\nu/k_B T}\right)^2 \sum_{j=1}^{N} n_i^j$$
$$= 3.7 \times 10^8 \, cgs \, \frac{n_e}{T^{1/2}} z^2 \frac{\xi_z}{\nu^3} e^{h\nu/k_B T} \left(1 - e^{-h\nu/k_B T}\right)^2 \sum_{j=1}^{N} n_i^j \tag{5-51}$$

$$\kappa_{bb}^{\Sigma} = \left[\frac{h\nu}{c} \sum_{j=1}^{N} \left(\sum_{l,u} B_{lu}^j n_s^j P_{lu}^j \left(\nu, r, t\right) \right) \right] \left(1 - e^{-h\nu/k_B T}\right) \tag{5-52}$$

where ξ is the dimensionless free-bound continuum correction factor that takes into account the electron structure of the atom and usually assumes a value of unity, B_{lu}^j is the Einstein coefficient for absorption transition *l* to *u* (in cm^3 erg^{-1} s^{-1} Hz), n_s^j is the number density of atoms or ions of constituent *j* which undergoes the transition from *l* to *u* (cm^{-3}) and P_{lu}^j is the normalized line profile expressed by the Voigt function.

Spectral line profile. The contribution of the line shape function, P_{lu}^j, in the bound-bound absorption coefficient, κ_{bb}^{Σ}, determines the appearance of the line spectrum. In the model, the line profile is described by a Voigt function under the assumption that the dominant line broadening mechanism is Stark broadening which competes with Doppler broadening as the plasma evolves in time. The Stark-shifted Voigt function in frequency terms is given by:

$$P_\nu = \frac{a\left(r,t\right)}{\pi\sqrt{\pi}} \int_{-\infty}^{\infty} \frac{e^{-y^2}}{\left[\Lambda\left(\nu,t\right) - y\right]^2 + a\left(r,t\right)^2} dy \tag{5-53}$$

where *y* is the integration parameter, $a\left(r,t\right)$ is radial and time dependent damping parameter, $\Lambda\left(\nu,t\right)$ is the line shift normalized by Doppler width, $\Delta\nu_D$ (Eq. 5-55).

$$\Lambda\left(\nu,t\right) = \frac{2\left[\nu - \nu_0 + \Delta\nu_{StarkShift}\left(r,t\right)\right]}{\Delta\nu_D\left(r,t\right)} \tag{5-54}$$

$$a(r,t)=\frac{\Delta\nu_{Stark}(r,t)\sqrt{\ln 2}}{\Delta\nu_{D}(r,t)} \tag{5-55}$$

The calculation of the Voigt function was performed using a modified Humlicek algorithm as proposed by Schreier [150].

Solution to the Inverse Problem

In order to extend the analytical applicability of the theoretical radiative model of the laser-induced plasma expansion in vacuum, an additional computational routine based on the Monte Carlo simulated annealing optimization was developed by Gornushkin et al. [62]. This method allows the determination of initial plasma parameters, such as temperature and particle number densities, by a direct comparison of an experimentally measured LIBS spectrum with a calculated synthetic emission spectrum obtained from the model [62]. In its simplest form, a simulated annealing algorithm can be generally used to search for the optimum solution to a variety of mathematical problems. It is analogous to the thermodynamic process involved in the cooling of glass where the atoms are initially heated to a very high temperature and then slowly cooled until the most stable system configuration is achieved. The simulated annealing algorithm is usually a part of a standard Monte Carlo (MC) simulation procedure which statistically samples all the possible states of a system by arbitrary selection of new parameters; in effect, the MC simulation represents a large number of random trials. However, not all changes are accepted since each MC step or attempt has to follow a certain probability criterion, known as the Metropolis criterion [151], defined by a particular cost function [152].

In the MC-LIBS approach, the necessary input parameters are the initial temperature and the initial number densities of plasma constituents. When the simulated annealing optimization method is applied to this initial set of data, the parameters are randomly varied within a given

range of values until the global maximum of the cost function is reached. In this case, the cost function is the linear correlation coefficient function given by Eq. 5-56:

$$R = \frac{\sum_i \left(x_i - \bar{x}\right)\left(y_i - \bar{y}\right)}{\sqrt{\sum_i \left(x_i - \bar{x}\right)^2}\sqrt{\sum_i \left(y_i - \bar{y}\right)^2}} \tag{5-56}$$

where x_i and y_i are the intensities of the experimental and theoretical spectra at the same wavelength λ_i, respectively, and $\bar{x}$ and $\bar{y}$ are the mean of the x_i's and y_i's, respectively [153]. The linear correlation provides a measure of the association between variables and, in this case, the value of the correlation coefficient R determines the similarity between the experimental and synthetic spectrum [62, 154]. Fig. 5-6 shows an example of the correlation between an experimental and a simulated spectrum of an Al alloy after multiple iterations. The R value obtained is 0.9913.

Ideally, the optimization undergoes several iterations of the initial parameters until the extreme maximum of the correlation coefficient is reached. However, realistically, a fixed value for the number of iterations is used to minimize the computer run time. In general, a shortfall of the maximization (or minimization in other cases) of a function is that the extremum point can be either global, which is truly the highest or lowest function value, or local, which is the highest or lowest in a finite neighborhood. These are illustrated in Fig. 5-7. Simulated annealing alleviates this difficulty, in most cases. A more extensive discussion of the Monte Carlo algorithm, as well as the simulated annealing process is found in Ref. [153].

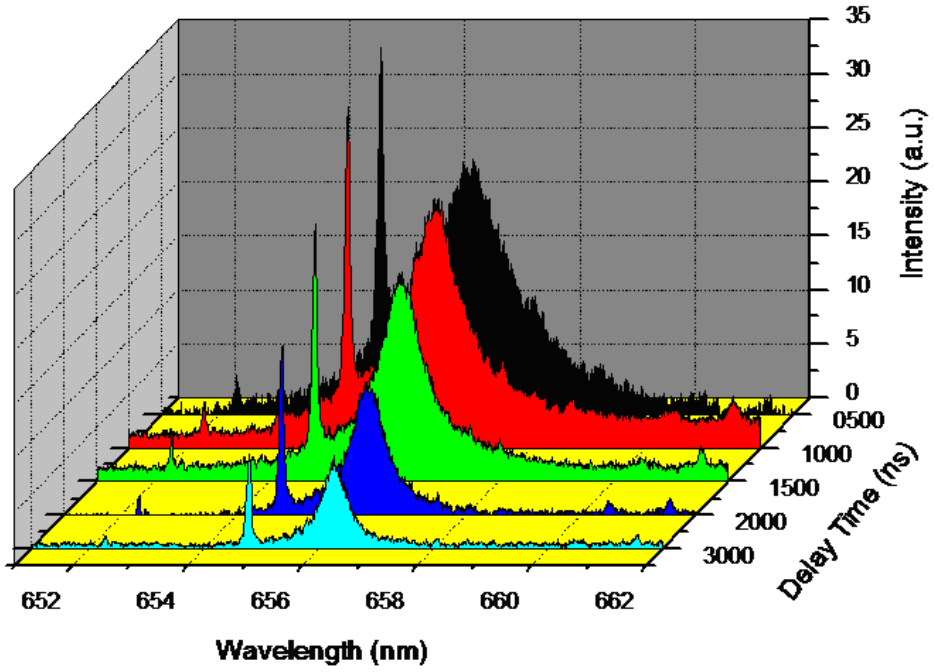

Figure 5-1. Temporal evolution of the Hα line at 656.272 nm. LIBS measurements were performed on an aluminum alloy sample using 5 different delay times and gate width of 500 ns at a pressure of 100 mbar in air.

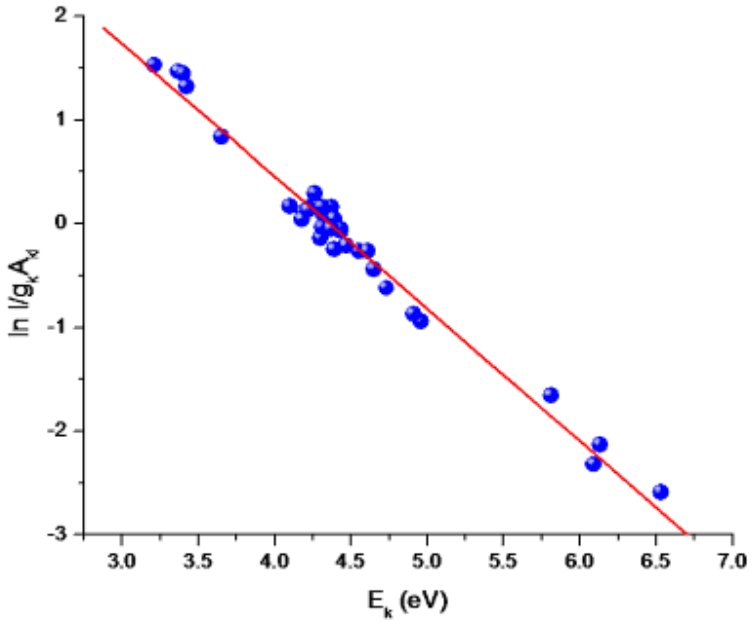

Figure 5-2. Boltzmann plot obtained using Fe I lines in an aluminum alloy sample. LIBS measurement was performed using a delay of 2.0 μs and a gate width of 0.5 μs under atmospheric conditions. The temperature calculated from the slope of the line is 10677 K.

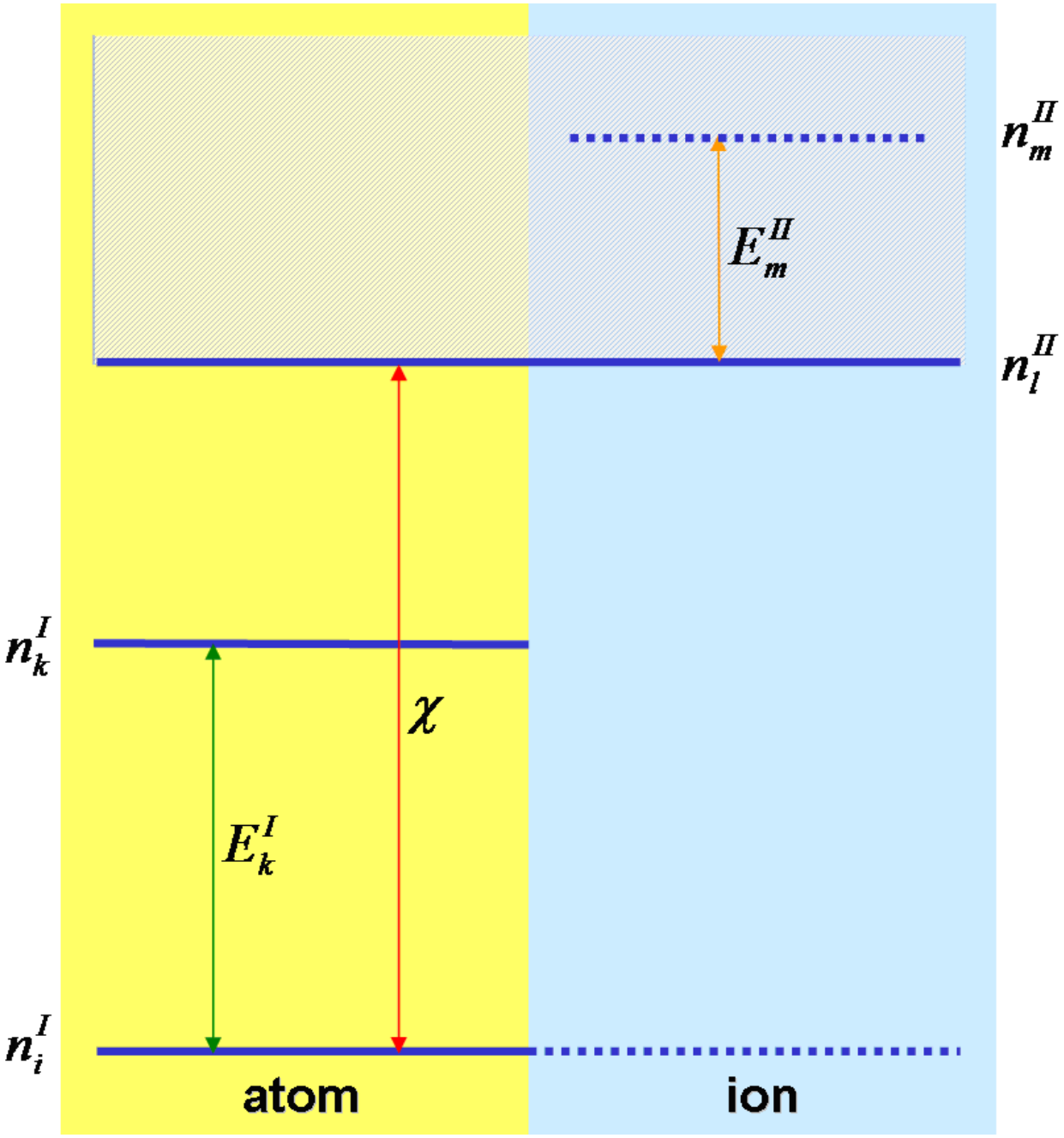

Figure 5-3. Energy levels of atomic (I) and ionic (II) species. E_k^I and E_m^{II} are the excitation energies of the atom and ion, respectively, χ is the ionization energy and n_i^I, n_k^I, n_l^{II} and n_m^{II} are the number densities for different levels and for different species. (Adapted from Ref. [25])

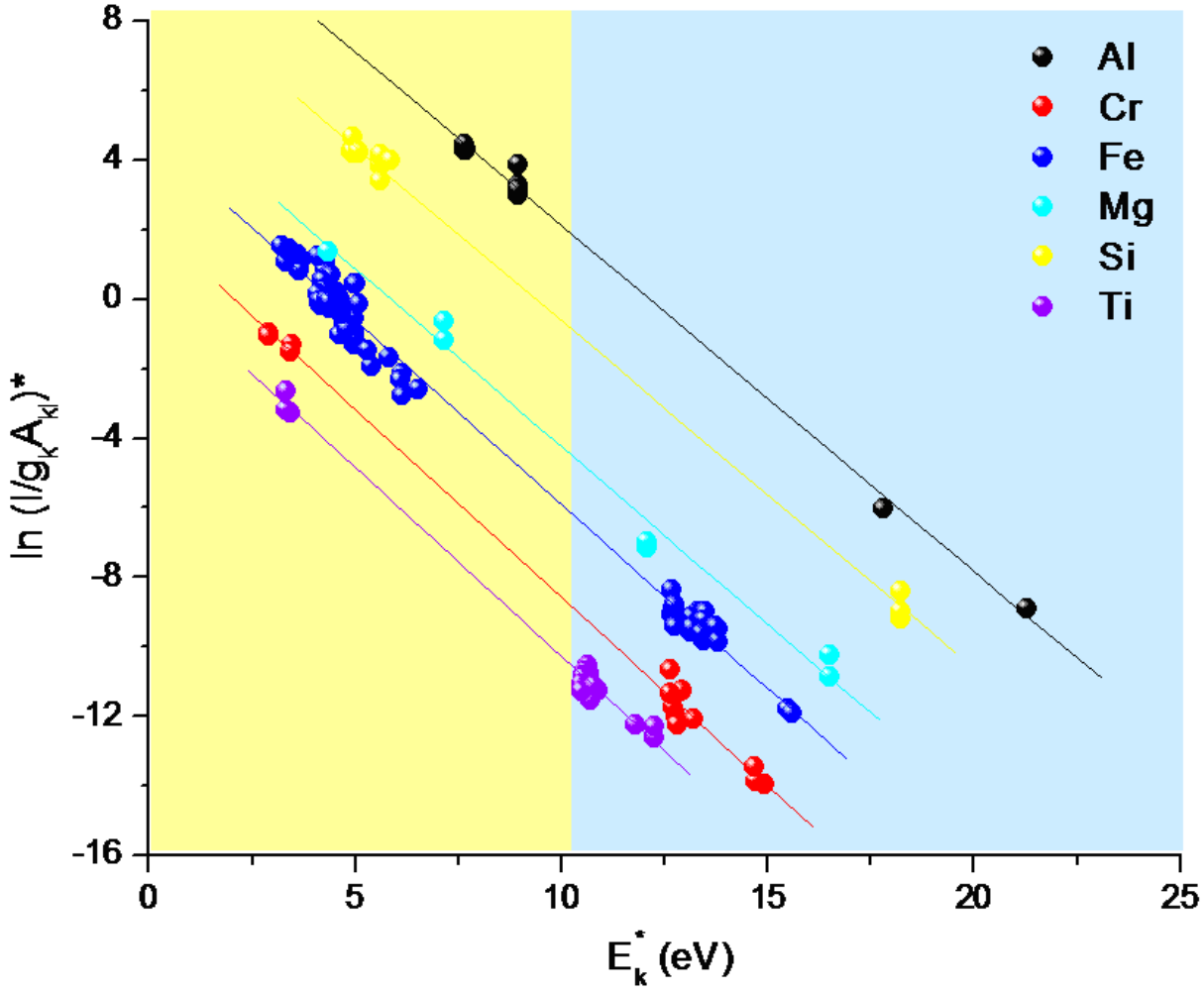

Figure 5-4. Saha-Boltzmann plots of different elements using neutral (points in yellow background) and singly-ionized (points in blue background) lines. LIBS measurements were performed using a delay of 2.0 μs and a gate width of 0.5 μs at atmospheric conditions. The average temperature calculated from the slopes of the line is 11141 ± 600 K.

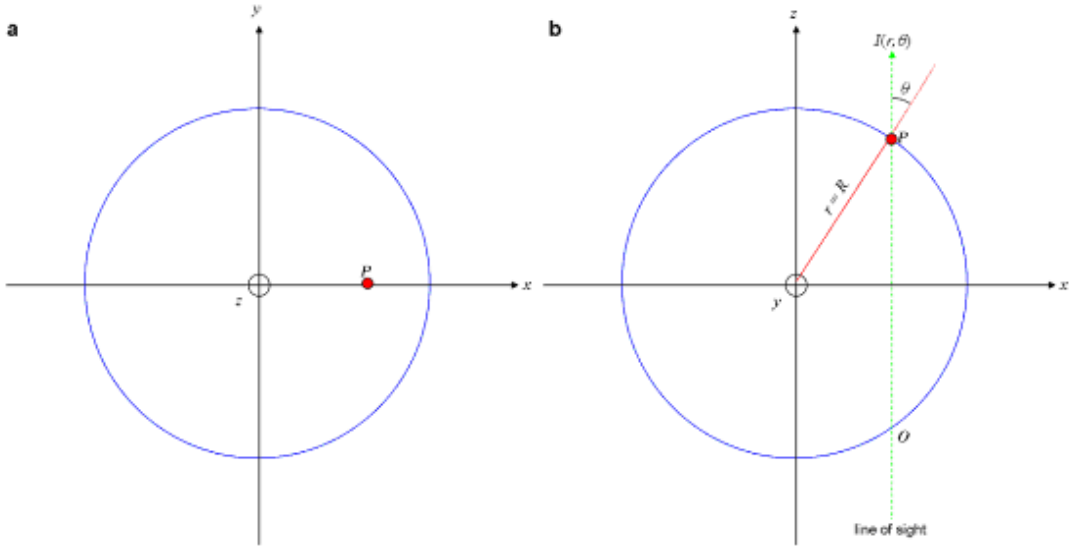

Figure 5-5. Illustration of the coordinate system used in the semi-empirical vacuum plasma expansion model. (a) Circular plasma projection viewed by an observer in the *z*-direction where *P* is a spatially-resolved observation point. (b) Circular plasma projection viewed by an observed in the *y*-direction; *OP* is the line of sight, $I(r,\theta)$ is the spectral radiance emitted along the line of sight and θ is the polar angle of the spherical coordinate system. (Adapted from Ref. [61])

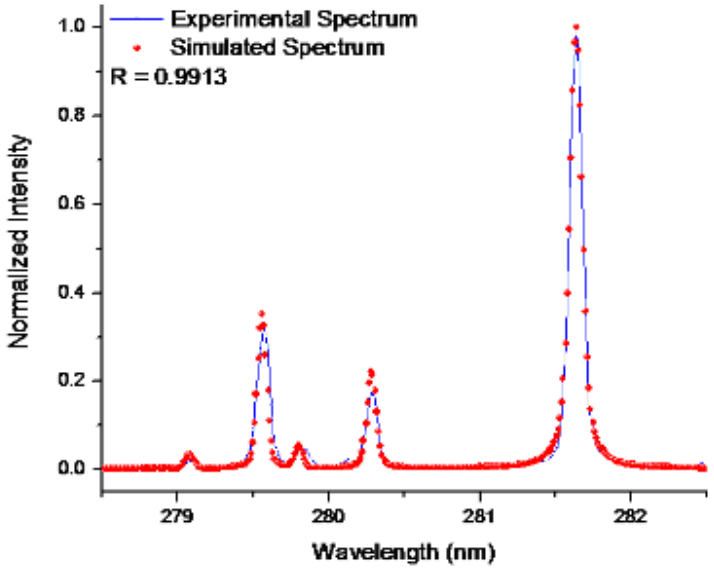

Figure 5-6. Correlation between the experimental (blue line) and simulated (red dots) spectrum. The correlation coefficient calculated from the MC-LIBS analysis is 0.9913. LIBS measurements were performed using a delay of 50 ns and a gate width of 100 ns at a pressure of 0.1 mbar.

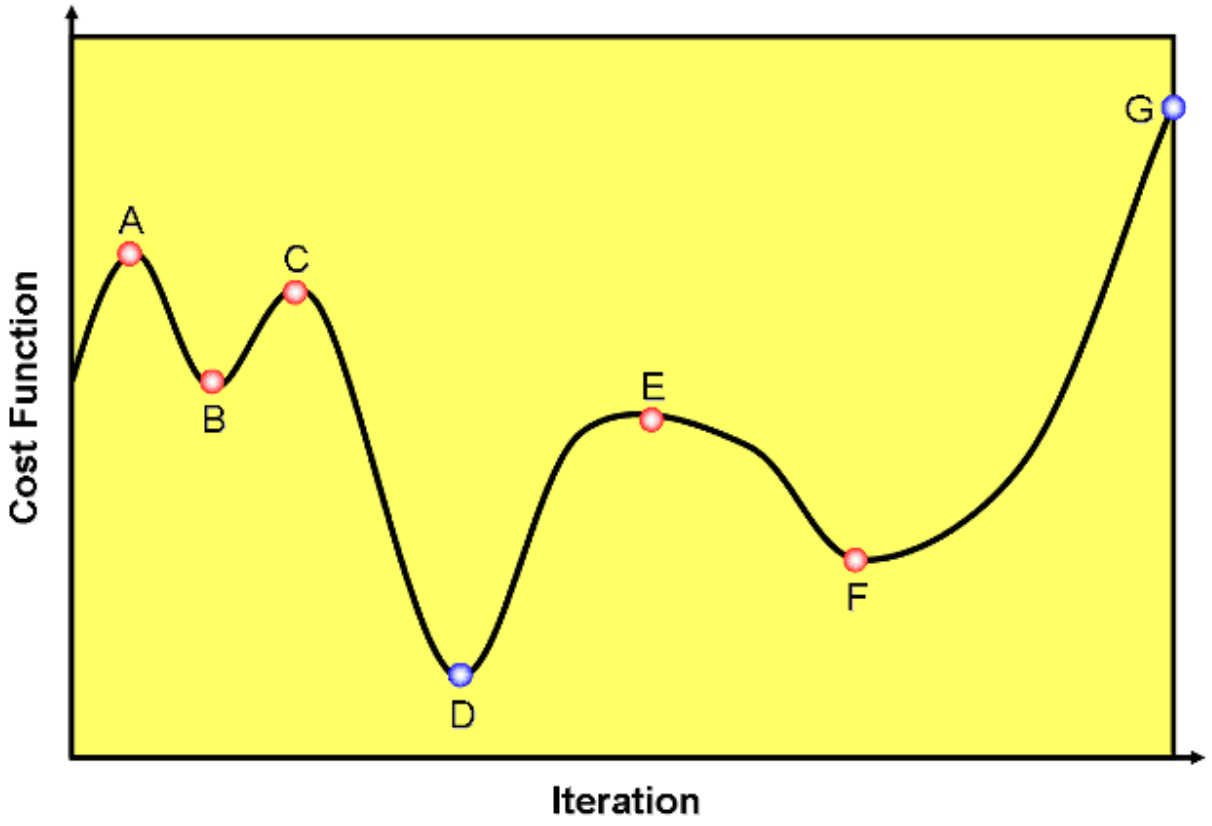

Figure 5-7. Extrema of a function in an interval. Points A, C and E are local but not global maxima. Points B and F are local but not global mimina. The global maximum occurs at G and the global minimum is at D. (Adapted from Ref. [153])

Table 5-1. Calculated FWHM of reduced Stark profiles in nm per cgs field strength unit.

Temperature (K)	Electron number density (cm^{-3})	$\alpha_{1/2}$ (nm)
10000	1×10^{15}	7.77×10^{-4}
	1×10^{16}	1.34×10^{-3}
	1×10^{17}	1.86×10^{-3}
	1×10^{18}	2.15×10^{-3}
20000	1×10^{15}	6.01×10^{-4}
	1×10^{16}	1.14×10^{-3}
	1×10^{17}	1.75×10^{-3}
	1×10^{18}	2.26×10^{-3}
	1×10^{19}	2.35×10^{-3}

CHAPTER 6
COMPARATIVE STUDY OF TWO STANDARD-FREE APPROACHES IN LASER-INDUCED BREAKDOWN SPECTROSCOPY

Introduction

In laser-induced breakdown spectroscopy (LIBS), quantitative information regarding the sample composition can be usually obtained by constructing several calibration curves for each component in the sample. This generally involves the requirement of matrix-matched standards which are very difficult to acquire, particularly in cases of highly variable or fully unknown matrices. The main challenge that has to be overcome in LIBS quantitative analysis is the occurrence of matrix effects which is characterized by the strong dependence of atomic emission spectra on relatively small variations in sample composition. Several studies on the various types of matrix effects [45, 46, 48, 49] have been carried out in order to fully develop the potential of LIBS for quantitative measurements. Matrix effects have been found to have a dependence on several factors which include particle size [45, 49], chemical speciation [46], amount of energy coupled to the plasma [48] and latent heat of vaporization [49].

Furthermore, numerous solutions to the matrix effects problem have been proposed in recent years [50, 51, 53]. The most common correction methods involve normalization of the analyte signal with a particular physical parameter, e.g. plasma temperature [50], ablated mass [50], sample surface density [53], and background signal [51]. Alternative analytical procedures based on chemometric methods have also been recently associated with LIBS in order to improve its analytical performance with respect to standard calibration curves. Among these are multivariate analysis [155-158], principal component analysis (PCA) [158-161], partial least squares (PLS) regression [158, 159, 162-164], and neural networks [161, 163, 165].

However, the aforementioned methods still require the use of standards followed by a certain type of correction or data treatment algorithm in order to extract useful quantitative

information from LIBS measurements. Several research groups have found an alternative route from sample to element composition which eliminates the use of matrix-matched standards for calibration purposes. Ciucci et al. [55, 56] pioneered the work on calibration-free LIBS analysis which is based on the Boltzmann plot approach and operates on the basic assumptions of stoichiometric ablation and local thermodynamic equilibrium. Gornushkin et al. [61, 62] modeled the expansion of laser-induced plasmas into vacuum which also solves the initial plasma conditions through a step-wise Monte Carlo optimization of calculated synthetic spectra in order to obtain a close correlation with experimentally measured ones. Yaroshchyk et al. [166] developed a fully automatic analytical software which uses a database of atomic emission lines to calculate a theoretical emission spectrum for selected elements using defined plasma parameters. The plasma temperature, which is the most important parameter in their model, is optimized using the "Golden Search in One Dimension" routine until the best least squares fit between theoretical and experimental spectrum is obtained. They obtained a 25% agreement between calculated and certified values for the major elements present in bauxites, brass, mineral samples and laboratory air. De Giacomo et al. [167] similarly proposed a self-calibrated LIBS (SC-LIBS) approach in which the analyte emission signals are normalized with respect to the blackbody emission. In their model, it is assumed that a partial LTE condition exists within the excitation energy range interval of 30,000 to 50,000 cm^{-1} included in the Boltzmann plot and that there is no appreciable ionization in the acquisition delay times used. The SC-LIBS was demonstrated to be applicable in the analysis of the minor components of copper-based alloys using fs and ns lasers.

The aim of this research is to evaluate the applicability of two standard-free approaches for LIBS quantitative analysis of different aluminum alloy samples: the calibration-free LIBS

approach and the Monte Carlo simulated annealing optimization method for LIBS. The two methods were applied to two types of measurements, spatially-integrated and spatially-resolved LIBS measurements, in order to characterize the laser-induced plasma and to determine the elemental composition of the samples under investigation without the use of calibration curves. The parameters determined in this study include temperature and electron number density of the plasma, the relative elemental composition of the sample and the percentage errors associated with the measurement.

Experimental

The LIBS experimental system and spectral data acquisition used in the measurements have already been described in detail in Chapter 4. All measurements in this study were carried out under vacuum conditions at a pressure of 0.1 mbar using a delay time of 50 ns and a gate width of 100 ns. The schematic of the set-up is illustrated in Fig. 4-3. The samples used were aluminum alloy standard disks (B8, D33, S4, SM10, V14 and Z8) from APEX Smelter Co. in South Africa. The elemental compositions are given in Table E-1 in Appendix E. No other sample pre-treatment, other than cleaning the sample surface with pure methanol prior to LIBS measurements, was necessary.

Two operational modes were used in this study: spectroscopy mode and imaging mode. In spectroscopy mode, the laser-induced breakdown spectra from 10 laser shots were summed up using the built-in accumulation function in the WinSpec32 software (Version 2.5.18.2; Princeton Instruments). In imaging mode, the spatial resolution was conserved since two-dimensional images of the spectral lines were recorded which were later on converted to spatially-resolved spectra using the binning and skipping function of the WinSpec32 program.

In both modes, ~10 nm wide spectral windows between 220 and 700 nm were consecutively recorded and the spectra in each region were measured in 3 successive runs. The

set of spectra obtained in each run were spliced together using a simple in-house program written in Q-Basic and the merged spectra were subsequently averaged. All merged spectra were corrected for background and relative detector spectral efficiency using in-house programs written in MATLAB before any standard-free spectral analyses were carried out.

Results and Discussion

Standard-Free Analysis of Aluminum Alloys

General assessment of procedure. The relatively high quality (in terms of the resolution and signal-to-noise ratio) of the laser-induced breakdown spectra measured in the current study is evident from the data shown in Fig. 6-1. CF-LIBS analysis required identification of several neutral and singly-ionized lines from the constituents present in the sample. The lines used for each sample are listed in Tables 6-1 to 6-6. It can be inferred from the tables that there are differences in the number of spectral lines used for each sample; this is a consequence of the variation in elemental composition. More lines can be identified and approximated with a fitting function if the concentration of the element is high and fewer lines if the concentration is low. Resonance lines of major elements in the alloy sample are usually not included in the calibration-free analysis as they are often self-absorbed. Use of resonance lines can lead to an underestimation of the relative concentration since there is no correction for self-absorption applied in the current study. However, it has to be remarked that the identification of lines in a wide spectral range data is not a trivial task especially when analyzing samples of unknown origin and composition. The process involves a great deal of decision-making and requires much knowledge and experience. Identification of the lines and the determination of integrated line intensities constitute the bulk of the work involved in the calibration-free procedure since both steps are user-dependent.

In the Monte Carlo LIBS simulated annealing optimizations, only 22 spectral lines from 6 different elements (Al, Cu, Fe, Mg, Mn and Si) found between the range of 270 and 335 nm were used in the simulated annealing optimization of Al alloys B8, D33, V14 and Z8. Two additional lines from Zn were used for Al alloys S4 and SM10. Table 6-7 lists the lines used in the Monte Carlo LIBS simulations. Both resonance and non-resonance emission lines were included in the simulation procedure since there is no limitation set on the character of atomic transitions as long as the required spectroscopic parameters are available in atomic spectra databases. Resonance lines of major sample components do not present any difficulty in this case since the modeling algorithm takes into account the occurrence of self-absorption or self-reversal of lines. Ideally, lines from both neutral and singly-ionized species must be used to improve the accuracy of the optimization procedure but the limitation was set on the spectral range to decrease computation time. The chosen range allowed the use of only neutral lines for Cu, Si and Zn. In general, the selection and number of lines included and the spectral range used in the optimization procedure is mainly limited by the computation time and the availability of atomic transition probabilities [137, 168], Stark broadening parameters [131, 139], and partition functions [130, 169, 170]. Other minor sample components such as Cr, Ni and Ti were excluded in the calculations for reasons described above.

Also, the MC-LIBS algorithm requires an initial guess for the temperature and number densities of sample constituents. In this study, the initial values used for the temperature and number densities were usually based on the values obtained with CF-LIBS. However, in cases where no references are available, typical plasma temperature values between 10000 and 20000 K and total number densities between 10^{16} and 10^{17} cm^{-3} can be used. The accuracy of the initial guess values is not essential because they are only used as starting parameters of the optimization

which are subsequently iterated in the algorithm. The only inconvenience of using values which are far from the true values is that the calculation will take longer before the values converge to optimal ones. The latter correspond to high correlation between the simulated spectra and the experimental spectra. The computation time depends on the number of parameters that need to be iterated, which includes the temperature and the number density of each sample component. The computation time also depends on the number of lines included in the simulations, the number of iterations and computer CPU speed. The symmetry of the plasma is also a required input parameter (although not iterated) and can be easily determined from images of the plasma (Fig. 6-2a). The axis *x* perpendicular to the image plane corresponds to the optical axis (line-of-sight direction) and the vertical axis *z* parallel to the image plane corresponds to the direction of the laser beam (axial direction), as illustrated in Fig. 6-2b. The dimensions of the laser-induced plasma in the *x* and *y* directions were the same and approximately equal to 0.24 cm and the height of the plasma in the axial direction was 0.29 cm.

As mentioned previously, the number of iterations is one of the factors which affects the computation time. It is a user-settable parameter which was initially optimized in order to determine the minimum number of iterations required to obtain a high correlation between the experimental spectrum and the synthetic spectrum calculated from the plasma expansion model. The optimization of the number of iterations per parameter, $N_{iteration}$, was performed using the experimental spectrum of Al alloy D33 and $N_{iteration}$ was varied as follows: 20, 35, 50, 75, 100, and 150. From the results of the simulations shown in Fig. 6-3, it can be observed that the correlation coefficient *R,* which determines the similarity between the experimental and synthetic spectrum, did not improve any further even after 150 $N_{iteration}$. In fact, *R* reaches a constant value at about 0.95 after 35 $N_{iteration}$ which is a huge advantage since the computer run time increases

linearly with the number of iterations. It should be noted that the number of iterations, $N_{iteration}$, is applied to each parameter to be optimized. In this case, there are seven parameters that need to be iterated; hence, the total number of iterations is $7 \times N_{iteration}$. The total number of iterations corresponds to the maximal abscissas of the correlation coefficient plots in Fig. 6-3. It is also evident from the correlation coefficient plots in Fig. 6-3 that at the beginning of the Monte Carlo simulated annealing procedure, the *R* values are highly dispersed. This is typical of Monte Carlo annealing simulations where extreme conditions are initially applied to the system and subsequently allowed to stabilize as signified by the almost constant correlation coefficient obtained after the 300^{th} iteration. Hence, for all the simulations carried out using Monte Carlo LIBS, the number of iterations was kept at 35 for each iterated parameter.

Determination of electron number density and temperature. In the CF-LIBS approach, the electron number density can be calculated in a number of ways, in this study, the electron number density was determined using the Stark width of the Hα line at 656.272 nm which was still very prominent under the experimental conditions applied (Fig. 6-4). The equation used in the calculations is given in Eq. 5-19. The electron number densities obtained are on the order of 10^{16} cm^{-3} (Table 6-8). The plasma temperatures were calculated by constructing several Saha-Boltzmann plots using lines from different elements present in the metallic alloy sample and the results were on the order of 9800 to 11000 K, similar to previously reported values in the literature [171, 172]. The Saha-Boltzmann plots of selected elements for each alloy sample are shown in Fig. 6-5. The parallelity exhibited by the Saha-Boltzmann plots of different sample constituents is a satisfactory indication of the existence of local thermodynamic equilibrium in the plasma. Furthermore, the parallel slopes obtained in the Saha-Boltzmann plots also verify that the effect of the shot-to-shot variability of the laser pulse is not very significant in this case

regardless of the sequential acquisitions that had to be performed to obtain spectral data from 220 to 700 nm for a single measurement. The negligible effect of laser fluctuations can be attributed to the statistical averaging of three measurements taken at different positions on the sample and due to the attention paid to maintain the optimum target surface conditions. The minimum electron number density required to further validate the existence of local thermodynamic equilibrium was also calculated using Eq. 5-19 and the results indicated that LTE condition was indeed satisfied in this particular analysis (Fig. 6-8).

In the Monte Carlo LIBS approach, the temporal evolution of temperature and electron number density at different spatial positions in the laser-induced plasma can be obtained and the three-dimensional plots are shown in Fig. 6-6 for the six alloy samples. The temporal window begins at the end of the laser pulse when the laser-matter interaction has terminated (post-breakdown) and local thermodynamic equilibrium is established. This time is taken as the starting point ($t = 0$) of the model. The spatial window, on the other hand, is related to the number of equipotential surfaces or subshells assigned to the plasma where each subshell is characterized by a single value for temperature, number density and pressure. Spatial position zero in Fig. 6-6 indicates the center of the plasma and the last spatial position indicates the outer plasma boundary [173].

During the onset of expansion ($t = 0$), the temperatures at the core ranged from 28000 to 33000 K and the electron number densities were between 4×10^{17} to 1×10^{18} cm^{-3} for the six samples analyzed. However, for the actual temporal window of observation used in the experiment, the spatial distribution of temperature and electron number density are shown in Fig. 6-7, where the values at each spatial position correspond to temporally-integrated measurements between 50 ns and 100 ns of plasma evolution. From the plots obtained (Figs. 6-6 and 6-7), it is

evident that both temperature and electron number density have a maximum at the center and decreases towards the plasma edge. A similar trend was experimentally obtained by Aguilera and Aragon [174] by deconvolution of spatially resolved spectra of laser-induced plasmas formed on an iron-nickel alloy under atmospheric conditions.

Furthermore, the temperature and electron number density values calculated using the CF-LIBS technique were spatially-integrated along the direction of line-of-sight and the full height of the plasma, in other words, the emission from the whole plasma was taken into consideration. In order to compare the values obtained with CF-LIBS with that of MC-LIBS, the average of the spatially resolved temperature and electron number density values in Fig. 6-7 was obtained for each alloy sample and the results are plotted in Fig. 6-8 and summarized in Table 6-8. The averaging resulted in large standard deviations for the MC-LIBS values (Table 6-8) due to the wide spatial distribution of electron number densities and temperatures over the whole plasma volume and over the whole duration of data acquisition (100 ns) as depicted in Figs. 6-6 and 6-7. Comparing the calculated temperature and electron number density values obtained using the two standard-free approaches, it can be concluded that spatially and temporally-integrated MC-LIBS temperatures are in close agreement with the temperatures obtained using the Saha-Boltzmann plot approach (CF-LIBS) for all six alloys investigated. The range of temperature values are between 9000 and 11000 K. However, the spatially and temporally-integrated electron number densities calculated using the Monte Carlo approach are about 3-8 times higher than the those determined using the linear Stark broadening of the hydrogen alpha line at 656.272 nm but the differences are within experimental and statistical errors of the measurement considering the widely distributed electron number density values in both spatial and temporal windows of observation obtained in the plasma modeling routine. However, it should be

emphasized that, theoretically, the average temperature and electron number density values reported for MC-LIBS do not exist since the model was principally built on the concept of non-uniform distribution in laser-induced plasmas [173]. The concept of inhomogeneity in temperature and number density distribution in laser-induced plasmas has been extensively studied and confirmed by nearly all experimental works [63, 172, 175-186]. The errors reported in Table 6-8 for temperature and electron number density values do not necessarily reflect uncertainties of the model but rather demonstrates the large spatial non-uniformity of plasma parameters which is particularly evident when spatially-integrated measurements are used to characterize laser-induced plasmas.

Determination of relative composition. In the CF-LIBS measurement protocol, several Boltzmann plots were constructed using the different species identified in the aluminum alloy sample in order to determine the relative elemental composition. The results of the calibration-free analysis are shown in Fig. 6-9 and summarized in Tables 6-9 to 6-11. There is close agreement between the CF-LIBS results and certified values only for the most abundant element present in the sample (Al). The analysis resulted in relative errors below 3% for Al. However, in the case of the other components of the metallic alloy sample, the analysis can be considered semi-quantitative only due to the large magnitude of errors that were calculated which ranged from 2-98% as illustrated in Fig. 6-10. The relatively large errors calculated can be attributed to the shot-to-shot intensity fluctuations, uncertainties related to the determination of temperature and non-uniformity of the temperature within the plasma. According to the numerical investigation carried out by Tognoni et al. [138] on the expected CF-LIBS precision and accuracy, the relative elemental compositions of sample components other than the most abundant element varied within ±150-200% under a simulation of broad temperature dispersion

and large intensity fluctuations which is similar to the results obtained in this study for most of the components present in the sample. On the other hand, in their simulations involving the most abundant element, the concentration only varied within ±1% even under the extreme conditions applied which is in agreement with the relative concentration values calculated for Al in this case.

In the MC-LIBS method, quantitative information was obtained through an extensive Monte Carlo simulated annealing optimization of the composite theoretical spectra to match them with experimental spectra. The process was carried out by varying seven parameters, the number densities of Al, Cu, Fe, Mg, Mn, Si and the initial plasma temperature, for Al alloys B8, D33, V14 and Z8. The number density of Zn was also iterated in the case of Al alloys S4 and SM10. The results of the optimization procedure are shown in Fig. 6-11 where the experimental spectra and the best-fit simulated spectra are shown in blue and red, respectively. Excellent correlation between the experimental and synthetic spectra was obtained after the simulated annealing optimization procedure, with correlation coefficients in the range of 0.93-0.96. Since only 35 iterations were used in the procedure, the optimization of a maximum of 8 parameters and 24 lines took about ~4 hours using well-tuned initial input parameters and a 3.1 GHz PC. The optimized number densities calculated for the elements that were iterated are listed in Table 6-12. The orders of magnitude obtained for the sample constituents are comparable to the results obtained by Gornushkin et al. [62] using a similar set of Al alloy standards for the initial verification of the plasma expansion model.

In order to compare the number densities obtained from the Monte Carlo optimizations alongside the relative elemental concentrations obtained with CF-LIBS and relative certified

values, the number densities were converted to relative mass concentrations using the simple equation given by:

$$\%C^j = \frac{n^j M^j}{\sum_{j=1}^{N}\left(n^j M^j\right)} \times 100 \qquad (6\text{-}1)$$

where C^j is the relative mass concentration of sample constituent j in %, n^j is the number density of j in cm^{-3}, M^j is the atomic mass of j in g mol^{-1} and N is the number of sample constituents iterated. The relative concentration values obtained using CF-LIBS and MC-LIBS are plotted in Fig. 6-12 are and tabulated in Tables 6-13 to 6-18. In all six alloys analyzed, the relative concentrations obtained for Al using the calibration-free technique were in much closer agreement with the certified values than those values obtained using the Monte Carlo optimization. CF-LIBS resulted in relative errors below 4% while MC-LIBS resulted in errors better than 20% for the major component in the sample (Fig. 6-13). However, for most of the other elements present in the sample, the uncertainties obtained using the MC-LIBS approach is usually below 50% except in the case of Si where relatively large errors (>100%) were determined for all six alloy samples as shown in Fig. 6-13. The poor accuracy obtained for Si can be attributed to the fact that only one Si line was used in the Monte Carlo optimizations. It could also explain the observed overestimation of the Si content in all six alloys under investigation as clearly depicted in Fig. 6-12. In a few cases, 200% relative errors were obtained for elements such as Fe in alloy sample S4, Cu in alloy sample SM10 and Mg in alloy samples SM10 and Z8 using the MC optimization procedure. On the other hand, relative concentration values calculated using the CF-LIBS method for elements besides Al exhibited errors better than 90%. From the determined relative errors in this particular study, the results from both approaches fall into the semi-quantitative category (30-200% error) as defined in Ref. [65]. A

plausible explanation regarding the semi-quantitative results obtained with the standard-free analysis of Al alloy samples is that the vapor composition of the plasma does not necessarily reflect the composition in the sample due to various thermal optical processes involved in laser ablation which may induce fractional vaporization [62]. It can be concluded that stoichiometric ablation, which is one of the main assumptions in the CF-LIBS measurement protocol, is not properly justified in this study and therefore requires further independent investigation which is beyond the scope of this research. It should also be noted that in the radiative model of plasma expansion into vacuum, the laser-material interaction is not taken into account since the model simulates the plasma expansion at the onset of the post-breakdown process after the laser pulse has terminated.

Spatially-Resolved Standard-Free Analysis of Aluminum Alloy

Spatially-resolved emission spectra. In this part of the study, spatially-resolved LIBS measurements were obtained by recording the plasma emission in imaging mode and binning the resulting image into 11 different spatial positions (A through K) along the axial direction as depicted in Fig. 6-14. Each binned region consisted of 11 vertical pixels which is equivalent to 0.02475 cm of the vertical plasma partition. However, it should be noted that the spectrum obtained for each spatial position was still spatially-integrated along the line-of-sight. The spatially-resolved spectra of Al alloy D33 at various spectral windows are shown in Fig. 6-15. The spatially-resolved analysis was carried out under the assumption that the laser-induced plasma is imaged with 1:1 magnification at the focal plane and that the detection system does not suffer from any significant optical aberrations such as astigmatism, coma, spherical aberration, etc.

A distinct trend in the intensities of neutral and singly-ionized lines can be observed in the spatially-resolved data shown in Fig. 6-15. The difference is clearly demonstrated in Fig. 6-16

where the spatial evolution of spectrally-integrated intensities of different neutral and singly-ionized lines of Al, Fe, Mg and Mn are plotted. It can be easily deduced from the spatial evolution plot of neutral line intensities (black bars) that a maximum value for the intensity is approached at approximately the same position, i.e., at positions close to the plasma center for all the neutral lines considered. A similar maximum along the axial and radial directions was observed by Aragon and Aguilera [177] in the spatial profiling of Fe I emission from a stainless steel plasma produced in air at atmospheric pressure using different laser irradiances (80-900 GW cm^{-2}).

However, a slightly different behavior was observed for singly-ionized lines (gray bars) of different elements. The intensities slowly increase as the plasma center is approached from the top portion of the plasma (spatial position A) unlike that of neutral lines where the increase is much sharper and the maximum intensity is very well-pronounced. It is also evident from the spatial profiles in Fig. 6-16 that the distribution of intensities along the axial direction is not symmetric with respect to the plasma center, particularly for the singly-ionized lines whose maximal intensities are reached at high axial distances from the surface of the sample. The position of the maximum intensity also varied depending on the emitting species. This implies that it is possible to minimize spectral interferences, if present, for certain elements by finding an optimum distance from the sample surface [5].

In the CF-LIBS approach, the number of lines identified for each sample component in the Al alloy sample vary as a function of the spatial position as illustrated in Fig. 6-17 and it is evident for elements such as Cu, Fe, Mn, and Ni that more neutral lines (blue squares) can be identified at distances closer to the surface of the sample. For ionic lines (red circles), on the other hand, the number of lines identified is usually constant, except in the case of Cr and Ti

where a certain maximum was reached at spatial position F, which corresponded to the center of the plasma. It should be emphasized that the number of lines chosen for the CF-LIBS algorithm at each point in space does not necessarily indicate that the line is not present at a particular spatial position due to the limited information available. The main reason a certain emission wavelength was omitted in the analysis is that the signal-to-noise ratio was too low which made it difficult to differentiate the line from the background and impossible to fit with an analytical function with high certainties. Spatial positions J and K were not included in Fig. 6-17 and in the calibration-free LIBS analysis for the same reason.

The aforementioned observations made on the spatially-resolved data can be related to a mass-dependent spatial dispersion of different species during the plasma expansion which was reported by Corsi et al. [187] in their study of the temporal and spatial evolution of laser-induced plasma from a steel target and by Di Palma et al. [188] in their investigation of the composition and gas dynamics of laser ablated AlN plumes for pulsed-laser deposition applications. At high laser irradiances (2.3×10^{11} W cm^{-2}), Corsi et al. [187] observed that all species in the plasma exhibited a maximum intensity at approximately the same time at a given distance from the sample and showed similar spatial evolution profile of line emissions. The authors explained this by the fact that the flow of all atomic species is characterized by a single streaming velocity which only occurs when collisions are significant during the plume expansion so that different species move as a single system. However, at lower laser irradiances (1.5×10^{9} W cm^{-2}) used in their study, they observed that the maximum intensity of Cr I occurred at a much earlier time than Fe I which they attributed to a much slower plume expansion and lower mass ablated which means less frequent collisions and possibly a non-stoichiometric plasma. The authors further

rationalized that the particles which are subjected to a lower collision rate move almost freely, this means that the heavier atoms (Fe I) move slower than lighter ones (Cr I).

Based on the above argument, it is a possibility that the apparent higher intensities of Cu I, Fe I, Ni I, and Mn I lines found at lower axial distances (close to the sample surface) are due to the relatively heavier masses of these atoms compared to the masses of Al, Cr, Mg, Si and Ti (Table 6-19). This implies that the species in the plasma do not move with a single streaming velocity as the plasma expands in the *z*-direction which results in more of the heavier neutrals close to the sample surface where the temperature is also lower as will be described in the next section.

Determination of electron number density and temperature. Similar to the CF-LIBS analysis of Al alloys previously discussed, the electron number density at each spatial position was estimated using the Stark width of the Hα line at 656.272 nm (Fig. 6-18a). The calculated values are plotted in the upper panel of Fig. 6-18b and the results show that the plasma electron number density has an approximately constant value of 1.9×10^{16} cm^{-3} from spatial positions B through G and decreases to about 1.1×10^{16} cm^{-3} towards the edges of the plasma (spatial positions A and I). The same behavior along the axial direction was reported by Aguilera and Aragon [174] in their characterization of a laser-induced plasma formed on an iron-nickel alloy in air at atmospheric pressure.

The laser-induced plasma temperature at each spatial position was calculated by constructing several Saha-Boltzmann plots using lines from different elements present in the alloys sample. Saha-Boltzmann plots of selected lines are shown in Fig. 6-19 and the averaged temperatures are summarized in Table 6- 20. From the results obtained, it is evident that there are no significant differences in the calculated temperature values from spatial positions A

through G which varied between 11000 and 12000 K but temperature values decrease as the sample surface is approached. A similar trend in plasma temperatures was reported in Ref. [174] along the axial direction, except that a decrease in temperature was also observed at higher axial distances.

The Monte Carlo simulated annealing optimization method was also applied to the different spatially-resolved spectra. The actual position of the recorded plasma emission was taken into account in the algorithm to simulate the correct experimental conditions and to minimize the errors of the calculations. However, it should be noted that the model still simulates and calculates the evolution of the whole plasma expansion at different space and time points and the corresponding spatial and temporal evolutions of the temperature and electron number density obtained using different spatial input parameters (denoted by letters A through K) are shown in Fig. 6-20. Ideally, all three-dimensional plots in Fig. 6-20 must be similar since the same expanding plasma is being simulated in each case and the only difference is the portion of the plasma where emission is being collected. The temperatures of the plasma at the core at the end of the laser pulse ranged from 20000 to 40000 K and the corresponding electron number densities calculated were between 8.0×10^{17} cm^{-3} and 2.3×10^{18} cm^{-3}. Since LIBS measurements are usually temporally-integrated, the three-dimensional plots can be transformed into a two-dimensional plot of the spatial evolution of temperature and electron number density at a delay time of 50 ns and gate width of 100 ns as shown in Fig. 6-21. The abscissa in this case are still in relative terms but directly proportional to the radius. Spatial position zero pertains to the center of the plasma and the last spatial position refers to the last subshell and the distance from the center to the outermost subshell is equal to the radius of the plasma.

In order to obtain local information regarding temperature and electron number density using the results of the optimization procedure, the curves in Fig. 6-21 were fitted with a sigmoidal function given by:

$$y = A_2 + \frac{A_1 - A_2}{1 + \exp\left(\frac{x - x_0}{dx}\right)} \tag{6-2}$$

The fitting parameters for the temperature and electron number density curves are given in Tables 6-21 and 6-22, respectively. The temperature and electron number density values at specific spatial positions corresponding to the experimentally-obtained spatially-resolved spectra were calculated by simple interpolation using Eq. 6-2. The interpolated temperature and electron number density values at the highlighted portion of Fig. 6-21 were averaged and summarized in Table 6-20 and Fig. 6-18c. From the results obtained, it is evident that the electron number density and temperature attain maximum values close to the center of the plasma and then decrease towards the edge, similar to the experimental results reported in Refs. [174, 177, 179]. Furthermore, it can be observed from Fig. 6-18c that the minimum electron number density for LTE is only slightly below the electron number density value found at the edges of the plasma (spatial points A and K), hence, measurements at these two extremes must be carried out with caution in order for the LTE assumption to remain valid.

The temperature and electron number density values obtained using the two standard-free approaches, although not equal in magnitude, demonstrated similar trends especially at lower axial distances which agree reasonably well with previous studies [174, 177, 179]. It is also quite interesting to note that the trend observed in the local temperature and electron number density values predicted by the plasma modeling algorithm and those obtained by the Saha-Boltzmann plot approach is reflected on the spatial evolution profiles of integrated emission

intensities of neutral and singly-ionized lines depicted in Fig. 6-16. The intensities of spectral lines also decrease as the edges of the plasma is approached. The lower temperatures obtained at distances closer to the sample surface may also explain the evident broadening due possible self-absorption of the four resonance lines of Al at 308.215 nm, 309.271 nm, 394.401 nm and 396.152 nm shown in Fig. 6-15a.

The temperatures obtained using the two standard-free approaches are clearly not comparable except at spatial positions close to the plasma center where the temperatures are between 11000 and 12000 K and it cannot be concluded with a high degree of certainty which temperature values are more accurate for each spatial position since the methods used in the determination are very much different in and of itself. In the Saha-Boltzmann plot approach, several lines from different elements contribute in the determination of the temperature and from previous discussion it is quite evident that some species are distributed unevenly in the axial direction. The apparent axial inhomogeneity of the plasma might be the cause of the slightly unparallel slopes of the Saha-Boltzmann plots constructed at spatial positions H and I where more neutral lines from heavier elements are more easily resolved which contributes to a much higher slope, hence, resulting in a fairly lower temperature compared to those predicted by the plasma model (Table 6-20). On the other hand, although the behavior of temperature and electron number density values determined using MC-LIBS at different spatial points is similar to those reported in the literature, their accuracy cannot be fully ascertained since only a relatively small spectral window was used compared to the much wider window with more spectral lines used in CF-LIBS method.

Determination of relative composition. The final step in the CF-LIBS measurement protocol is, of course, the determination of the relative elemental composition. The results are

summarized in Fig. 6-22 and Table 6-23. A noticeable trend in the concentration values can be deduced from Fig. 6-22 where the relative concentrations calculated for each sample constituent are shown as a function of spatial position. For Cr, Mg, Mn, Si, and Ti sample components, the relative concentration values calculated generally decrease towards the edges of the plasma (spatial positions A and K) and to some extent, a maximum value is attained around the center of the plasma. However, since Al is the predominant element in the alloy sample, no noticeable trend is observed and relatively satisfactory accuracy is obtained at any spatial position with errors better than 9% (Table 6-24). On the other hand, for Cu, Fe and Ni, there is an apparent decrease in the calculated concentration values towards spatial position I. However, it should be emphasized that the values obtained with CF-LIBS are only relative, which implies that overestimation of one component will lead to an underestimation of another. Hence, it is difficult to attach any physical meaning to the trend observed.

The experimentally obtained spatially-resolved spectra were also optimized using the Monte Carlo simulated annealing procedure and results of the simulations yield correlation coefficients in the range of 0.81-0.98 between the simulated and experimental spectra as illustrated in Fig. 6-23. The elemental number densities obtained in the optimization procedure are plotted in Fig. 6-24 as a function of spatial position and it is interesting to note that along the axial direction, the predicted number densities for most of the elements considered exhibited an almost Gaussian-like distribution around the center, particularly for Mg, Mn and Si. This also confirms the observed trend in the calculated relative elemental concentrations obtained with CF-LIBS as previously described since the values obtained in this case are absolute (in cm^{-3}). Several studies [174, 179-181] have already been carried out on the spatial distribution of the number densities of neutrals and ions along the axial direction but the values reported, which

were calculated through the Saha equation (Eq. 5-2), were only in relative terms. However, for comparative purposes, the total relative number densities also show a reduction in value towards the plasma edges [174].

Similar to the previous analysis of spatially-integrated measurements of different aluminum alloy samples, the total number densities obtained with MC-LIBS were converted to relative weight concentrations using Eq. 6-1 so that a comparison can be made between the calculated results and certified concentration values. The results are summarized in Fig. 6-25 and tabulated in Tables 6-25 to 6-35. The highest accuracies were obtained for the major component in the sample, which is Al, with relative errors of 20% or better for MC-LIBS-obtained values and 10% or better for CF-LIBS-obtained values at all spatial positions considered. Comparable errors were obtained for the other elements in the sample with errors as low as 20% and as high as 100%, except for Si where relatively higher errors were obtained for MC-LIBS-obtained concentration values (60-250%), similar to the results of previous measurements on different aluminum alloys. With respect to spatial positions, it can be observed that lower errors were obtained for most elements in both methods at positions closer to the center of the plasma (spatial position E, F and G). This can be attributed to the relatively higher temperatures and electron number densities at this region of the plasma, as predicted by the plasma modeling routine, which ensures the existence of local thermodynamic equilibrium, an assumption which is particularly significant in both standard-free approaches.

Conclusion

In this study, two techniques for quantitative LIBS analysis, which do not require the use calibration curves, were evaluated: the calibration-free LIBS (CF-LIBS) approach and the Monte Carlo simulated annealing optimization method for LIBS (MC-LIBS). Both methods were applied to LIBS measurements performed under vacuum condition (0.1 mbar pressure). The

spectral data acquisition method developed in this research proved to be suitable for both approaches, CF-LIBS in particular, for it allowed spectral data to be acquired over a wide wavelength range (200-700 nm). CF-LIBS required full characterization of the spectrum so that numerous lines from most, if not all, elements can be included in the analysis. This certainly improved the reliability of the method as a quantitative technique. However, the CF-LIBS approach is not a fully-automated algorithm, i.e., it is a highly user-dependent technique from start to finish, which also required proficiency in spectral line identification. The analysis may take from a few hours to a day depending on the sample and the number of lines included in the analysis. The MC-LIBS approach, on the other hand, although more complex in its formulation since it simulates the expansion of a laser-induced plasma into vacuum using several gas and fluid dynamic and radiative transfer equations, is relatively less user-involved compared to CF-LIBS. The only initial requirements are input files which contain relevant spectroscopic and physical parameters, partition functions and Stark broadening parameters of all the species included in the simulations. The Monte Carlo optimization procedure may take from a few hours to several days depending on the computer CPU speed, the number of iterations, the number of lines and the number of element number densities to be iterated.

The results of the analysis of the spatially-integrated spectra of six different aluminum alloy samples demonstrated that both methods are satisfactory semi-quantitative techniques for LIBS analysis of elements other than the most abundant component in the sample. Comparatively, concentration values obtained with CF-LIBS for the matrix element Al were much closer to the certified values than those obtained with MC-LIBS. This may be attributed to the larger amount of information used in CF-LIBS compared to the limited number of lines and elements as well as spectral window size used in the MC-LIBS analysis. However, regardless of

the limitations imposed on MC-LIBS, the relative concentration obtained for the remainder of the sample components resulted in lower relative errors compared to those determined with CF-LIBS. Plasma temperatures calculated using both approaches were between 9800-11000 K and electron number densities were on the order of 10^{16} cm^{-3}, comparable to results reported in the literature for vacuum LIBS measurements [171, 172].

Also, in this study, CF-LIBS and MC-LIBS approaches were applied for the first time to the analysis of spatially-resolved measurements taken at different points along the laser beam axis (axial direction). Plasma temperature and electron number density values obtained from both methods, although not equal magnitude, show similarities in behavior along the axial direction. The electron number density values calculated at different spatial positions using both approaches indicated a maximum around the center of the plasma, similar to the trend observed for the plasma temperatures calculated using the MC optimization routine. Temperatures calculated from the Saha-Boltzmann plot method only demonstrated a reduction in temperature towards the sample surface. Furthermore, element number densities obtained from the extensive MC optimization and relative concentration values obtained from the calibration-free analysis exhibited higher values around the plasma center which could be attributed to the higher temperatures and electron number densities in this region. Lower relative errors were also obtained for the calculated concentration values using either method at spatial positions close to the plasma center.

However, regardless of the type of measurement, spatially-integrated over the whole plasma emission or spatially-resolved at a specific position along the axial direction, it should be remarked that the plasma emission is still spatially-integrated along the line of sight (path-integrated) and could have contributed to the errors obtained with standard-free LIBS analysis.

Previous studies have already shown that radial inhomogeneity in the plasma is evident [174, 179-181] and should be taken into account. The contributions arising from regions with different electron number density and temperature values could be avoided by obtaining radially-resolved spectra using Abel inversion [103, 179, 184, 187].

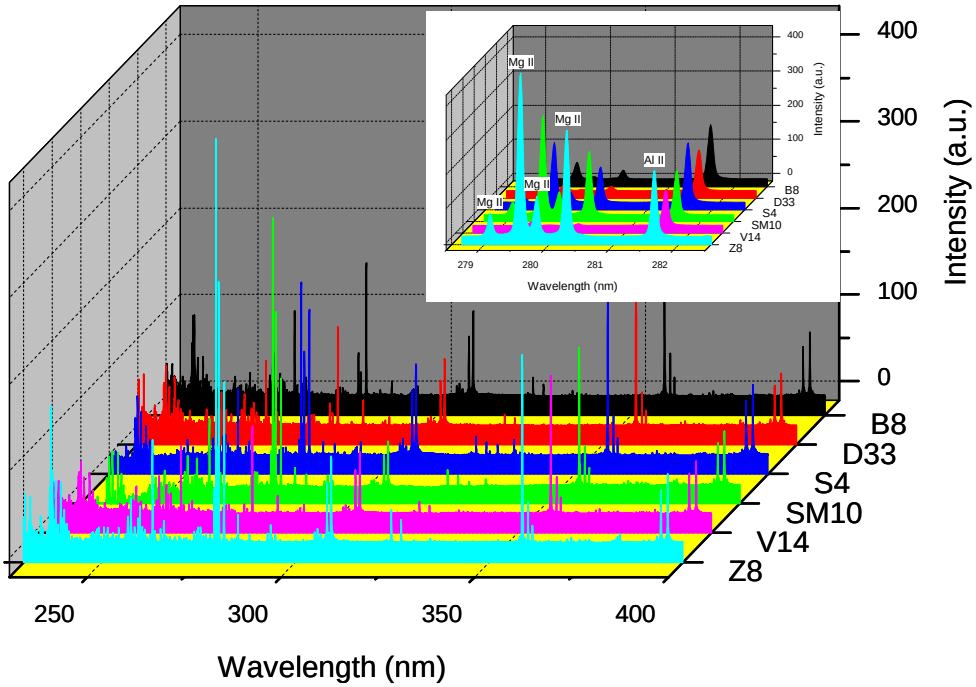

Figure 6-1. Section of laser-induced breakdown spectra of different aluminum alloys. The inset shows spectrally-resolved lines from singly-ionized Mg and Al.

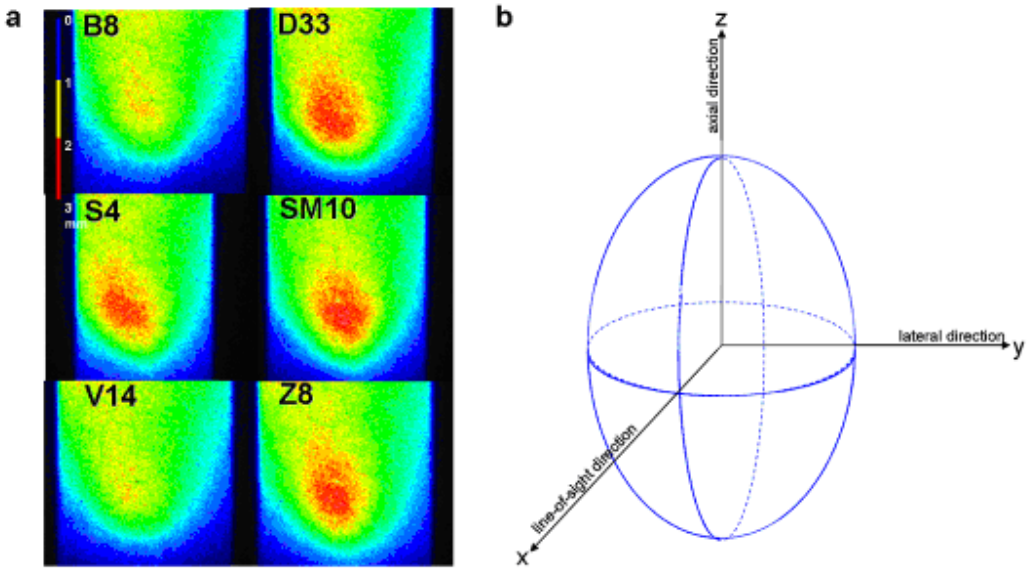

Figure 6-2. Images of laser-induced plasmas obtained from different aluminum alloy samples using a delay time of 50 ns and gate width of 100 ns. The images in (a) are the projections of the plasma on the *yz*-plane as defined in (b); the *z*-axis corresponds to the direction of the laser beam and the *x*-axis corresponds to the direction of line-of-sight.

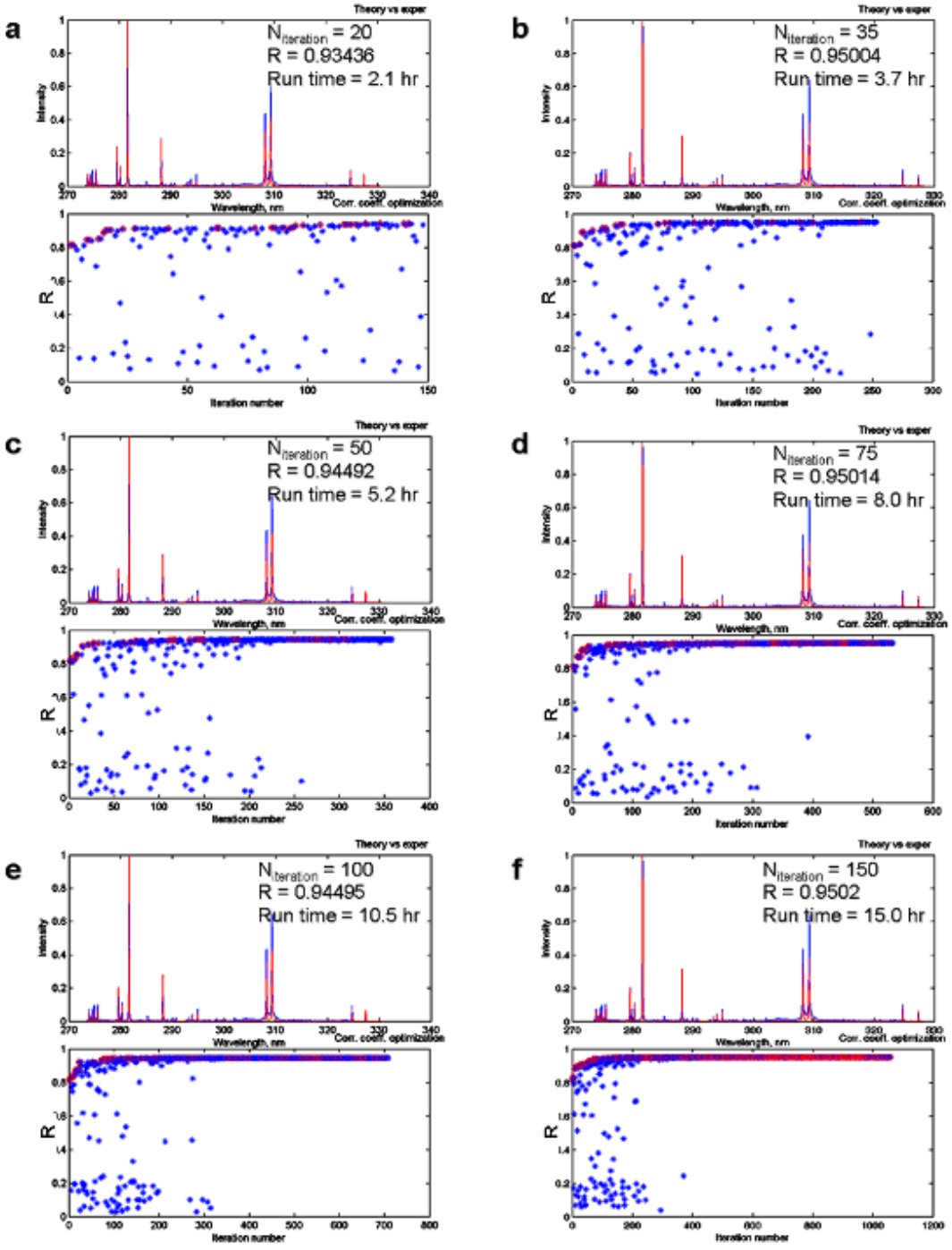

Figure 6-3. Effect of the number of iterations per parameter, $N_{iteration}$, (a) 20, (b) 35, (c) 50, (d) 75, (e) 100 and (f) 150, on the correlation coefficient R and computer run time of a 3.1 GHz PC. The upper panel shows the overlap of the experimental spectrum (blue) with the calculated synthetic spectrum (red). The lower panel shows plot of the correlation coefficient versus the iteration number. The total number of iterations is $7 \times N_{iteration}$, where 7 is the number of parameters iterated.

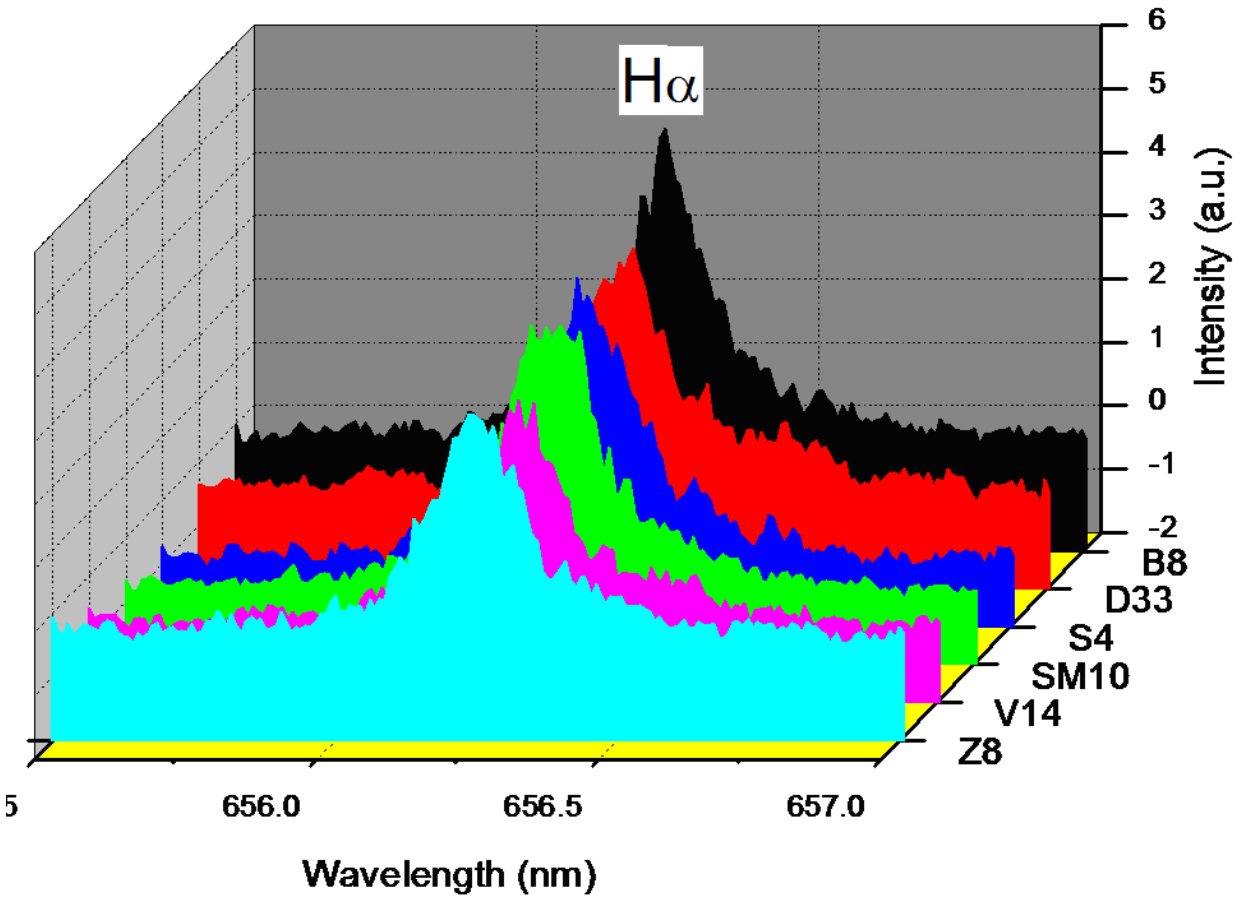

Figure 6-4. The Stark broadened hydrogen alpha line at 656.272 nm in the aluminum alloy spectra used for electron number density determination in CF-LIBS.

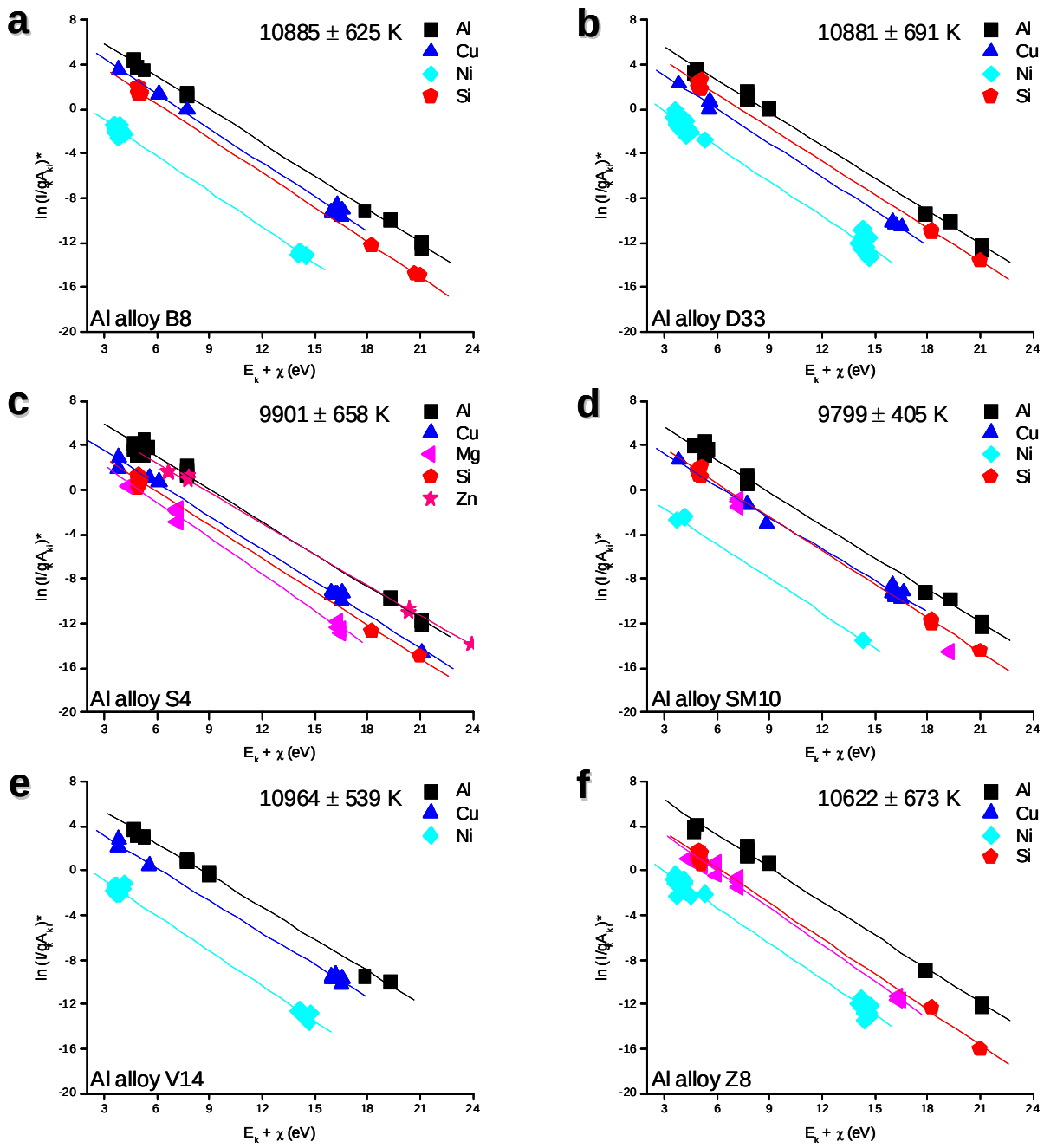

Figure 6-5. Saha-Boltzmann plots of selected elements in aluminum alloy sample (a) B8, (b) D33, (c) S4, (d) SM10, (e) V14 and (f) Z8.

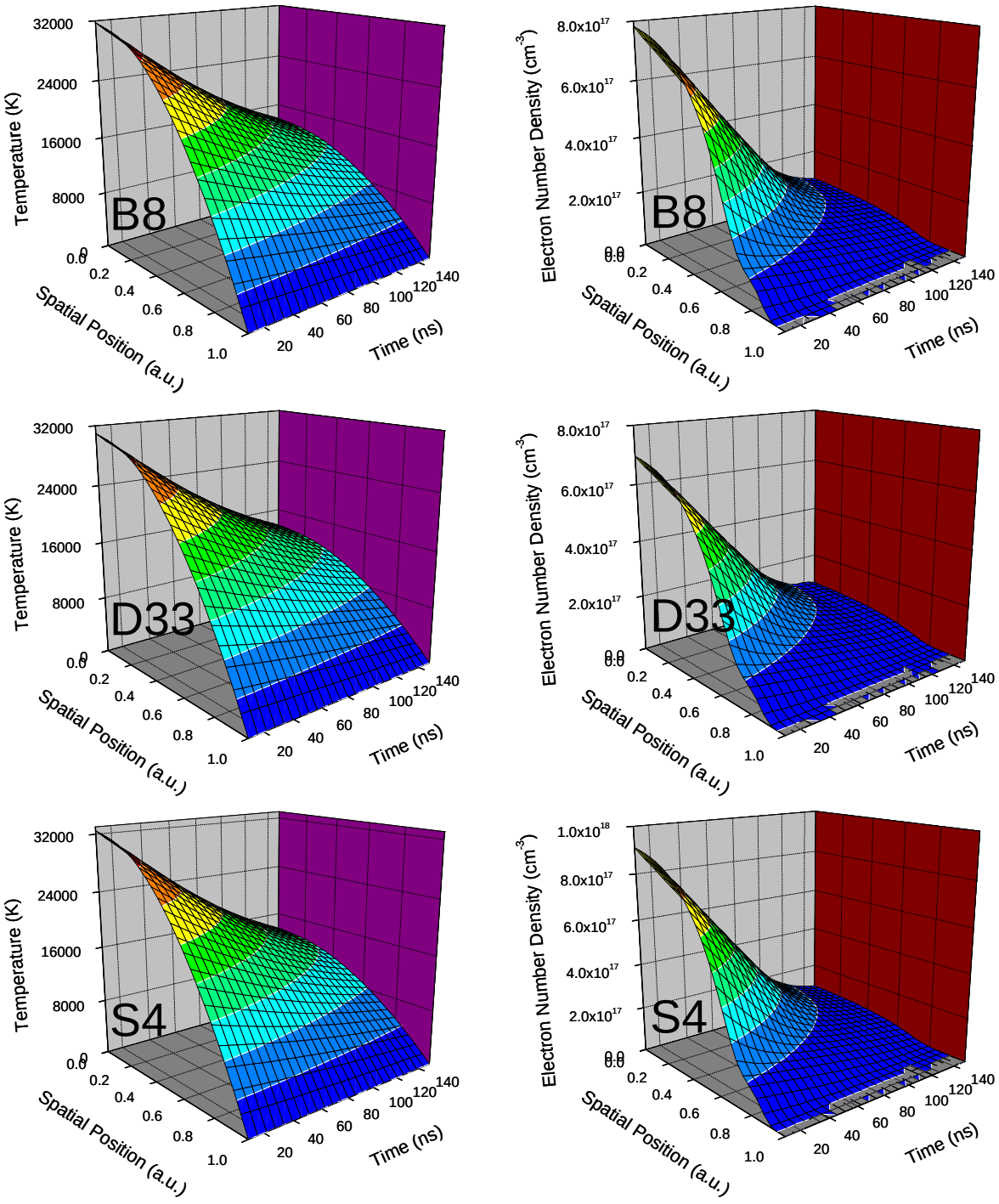

Figure 6-6. Spatial and temporal evolution of temperature (left) and electron number density (right) obtained using the MC-LIBS approach for aluminum alloy samples.

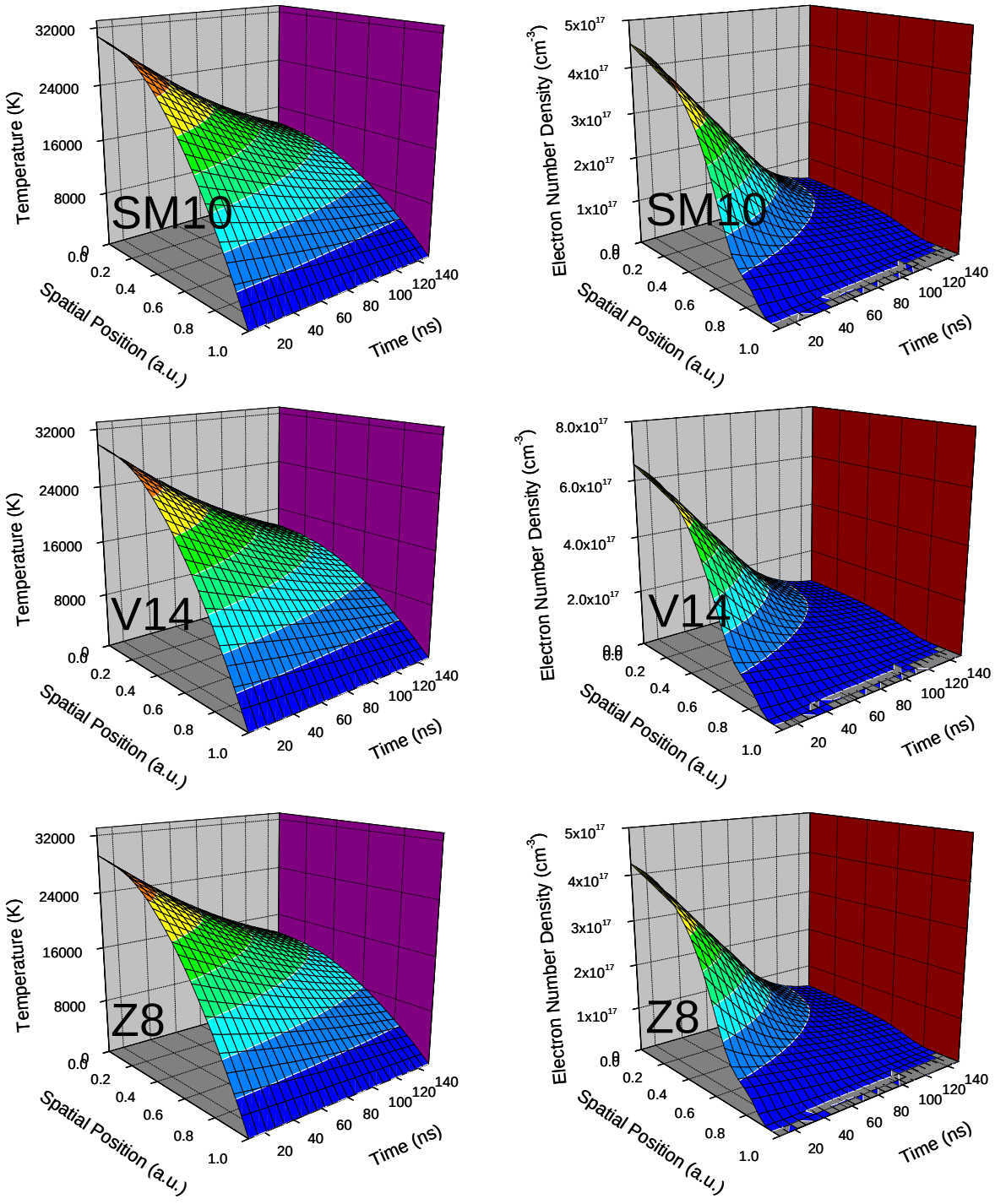

Figure 6-6. Continued.

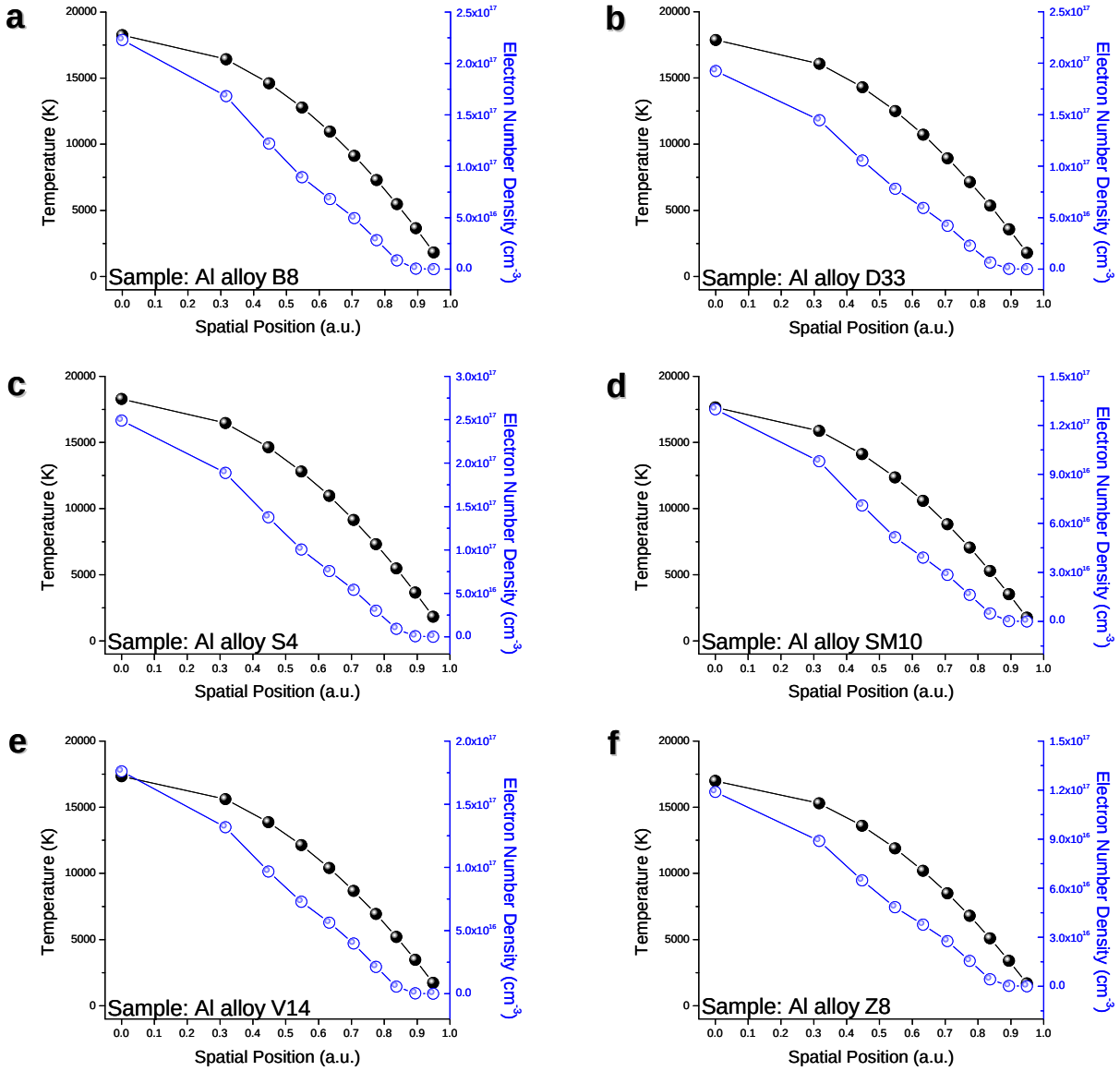

Figure 6-7. Spatial evolution of temporally-integrated temperature (black) and electron number density (blue) obtained using the MC-LIBS approach for aluminum alloy sample (a) B8, (b) D33, (c) S4, (d) SM10, (e) V14 and (f) Z8. The abscissa indicates relative spatial positions where spatial position zero indicates the first equipotential layer at the center of the plasma and the last spatial position indicates the outer layer of the plasma. There are no expected differences in the 6 plots since the samples are compositionally close.

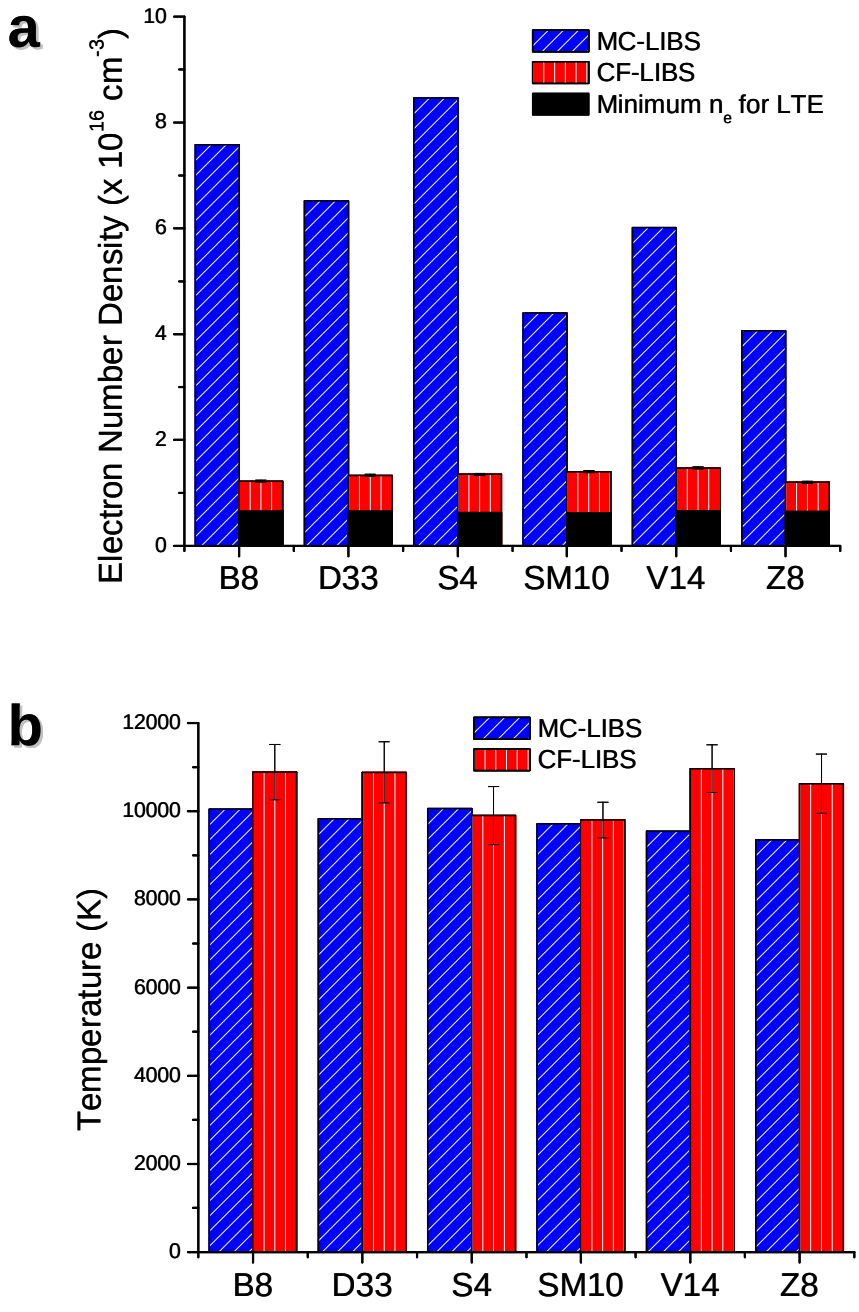

Figure 6-8. Comparison of (a) electron number densities and (b) plasma temperatures calculated using MC-LIBS (blue bars) and CF-LIBS approaches (red bars). The minimum electron number density values for LTE are shown as black bars in (a).

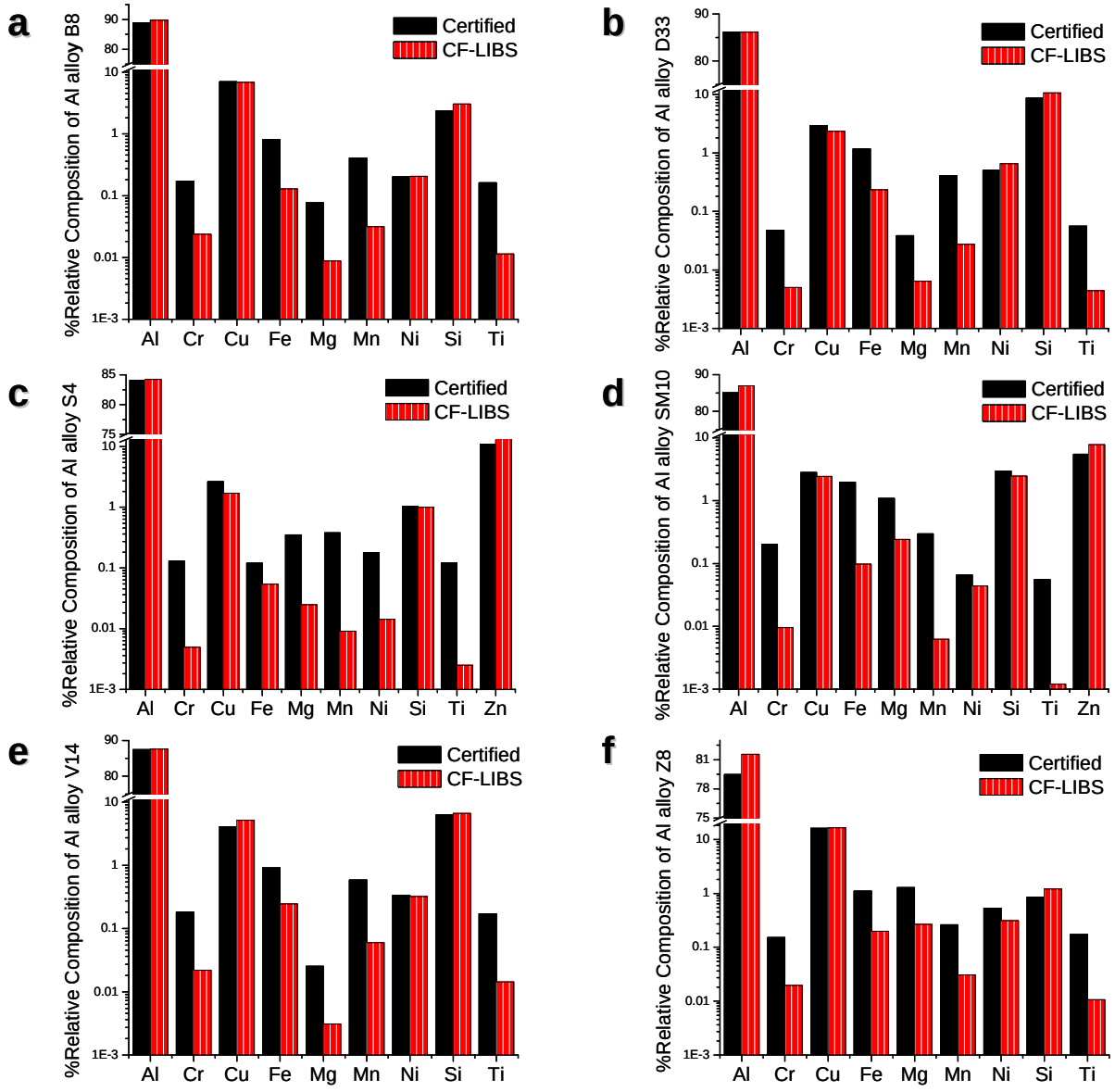

Figure 6-9. Relative elemental compositions of aluminum alloy samples (a) B8, (b) D33, (c) S4, (d) SM10, (e) V14 and (c) Z8 obtained with CF-LIBS compared with certified values (black bars).

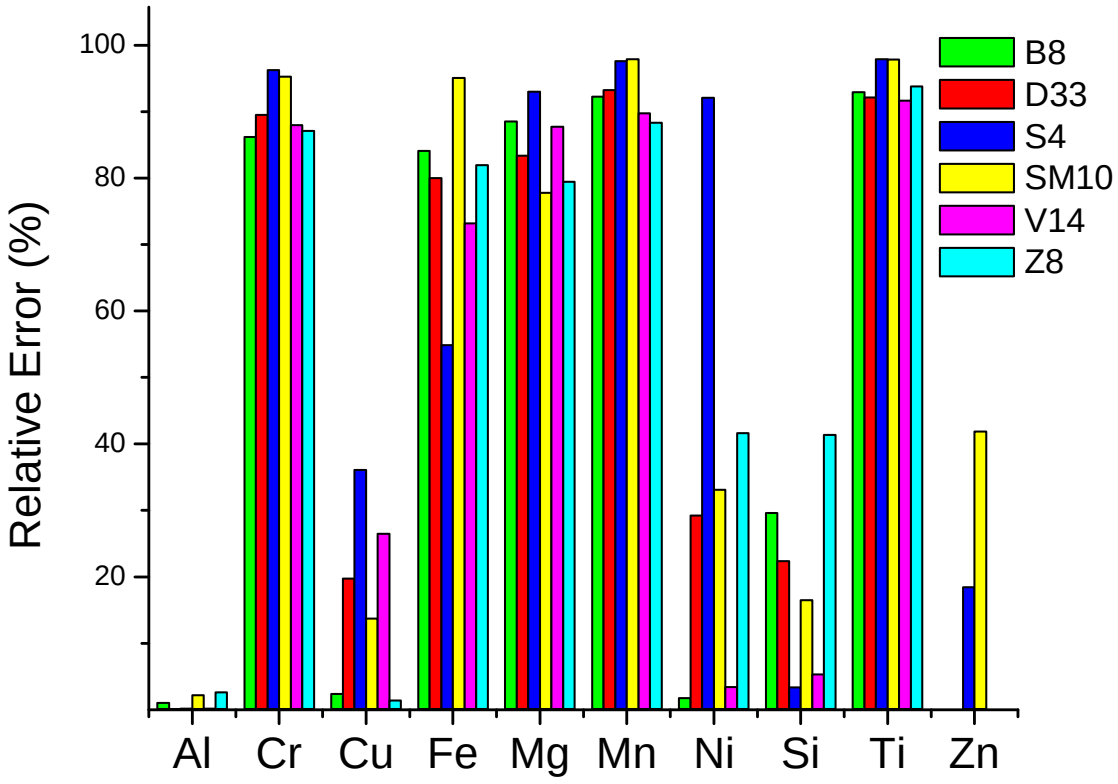

Figure 6-10. Relative percentage errors of the elemental composition calculated using CF-LIBS.

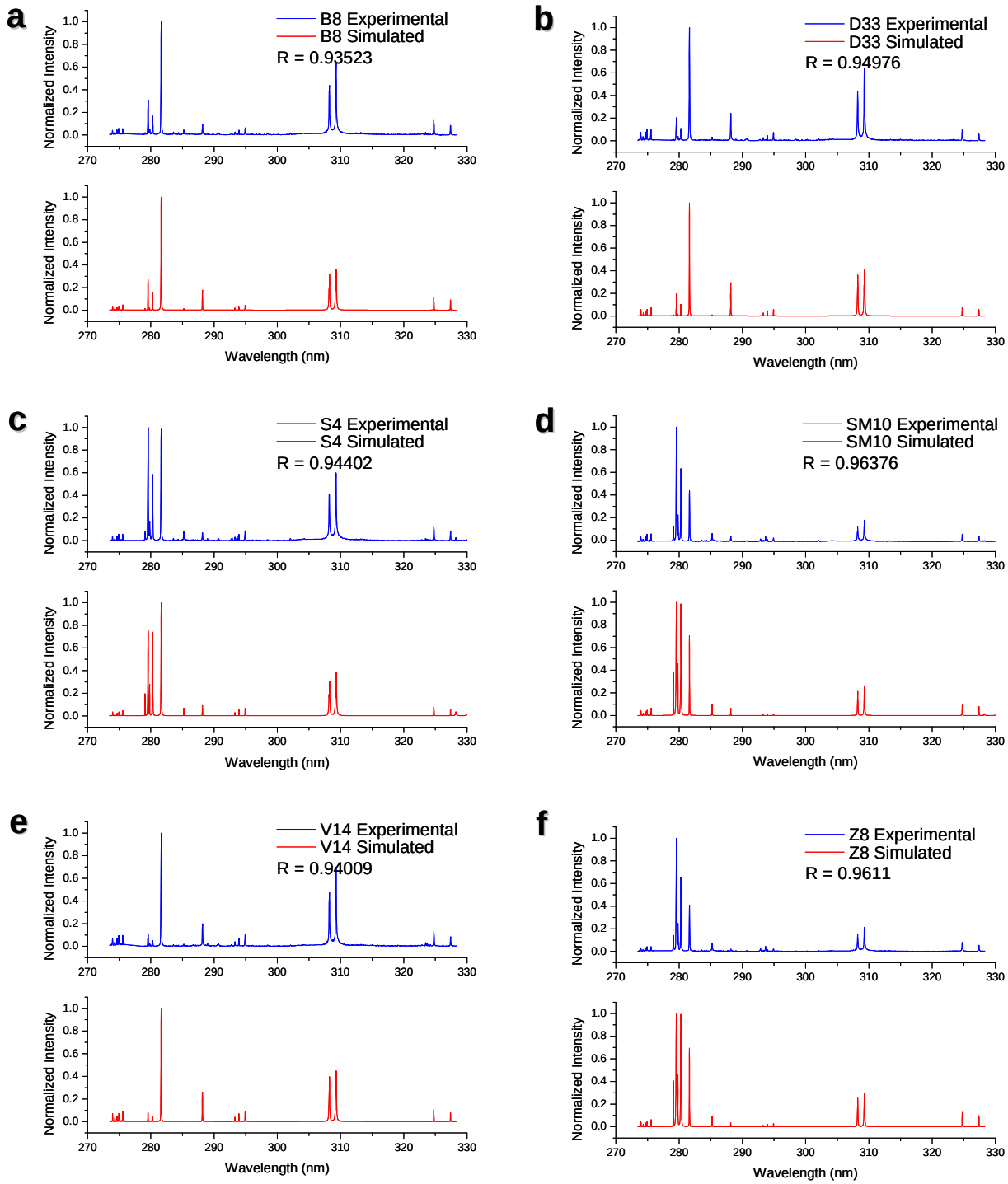

Figure 6-11. Comparison of experimental spectra of aluminum alloys (blue) and the best-fit simulated spectra (red) calculated with MC-LIBS. Maximized values of the cost function (correlation coefficient *R*) are also shown for each sample.

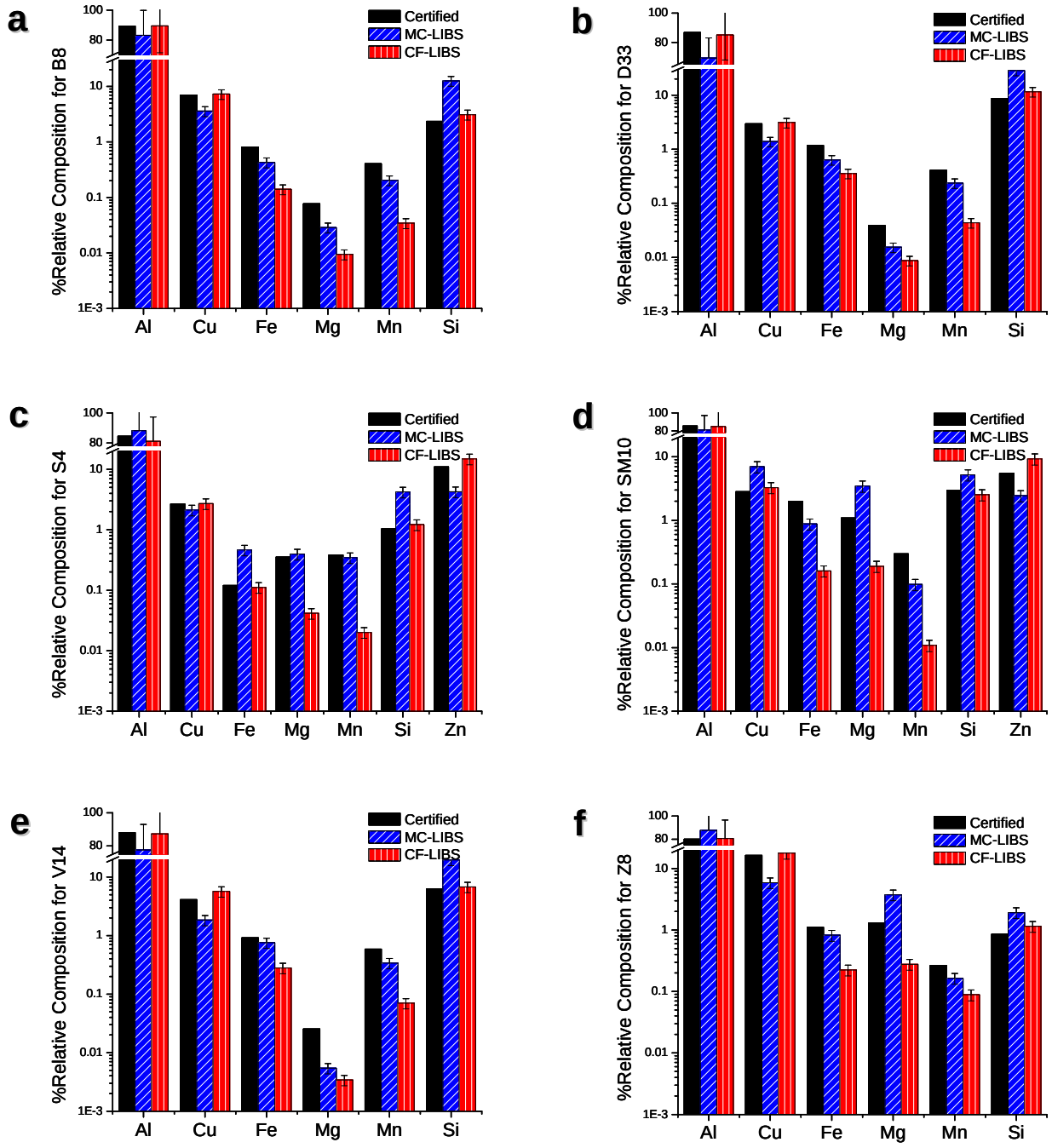

Figure 6-12. Relative concentration values obtained using MC-LIBS (blue bars) and CF-LIBS (red bars) compared with certified values (black bars).

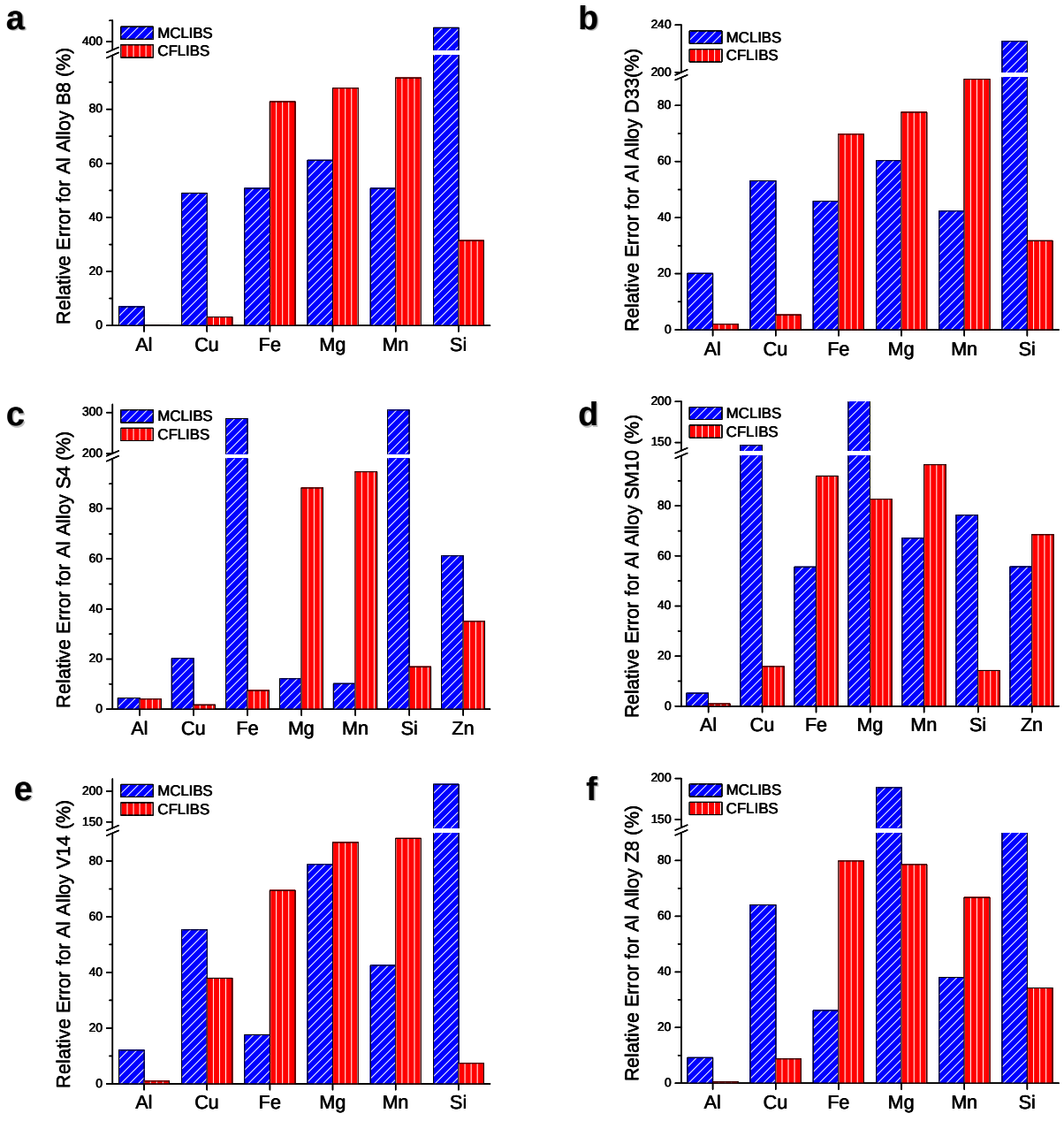

Figure 6-13. Relative errors of calculated concentration values obtained using MC-LIBS (blue bars) and CF-LIBS (red bars).

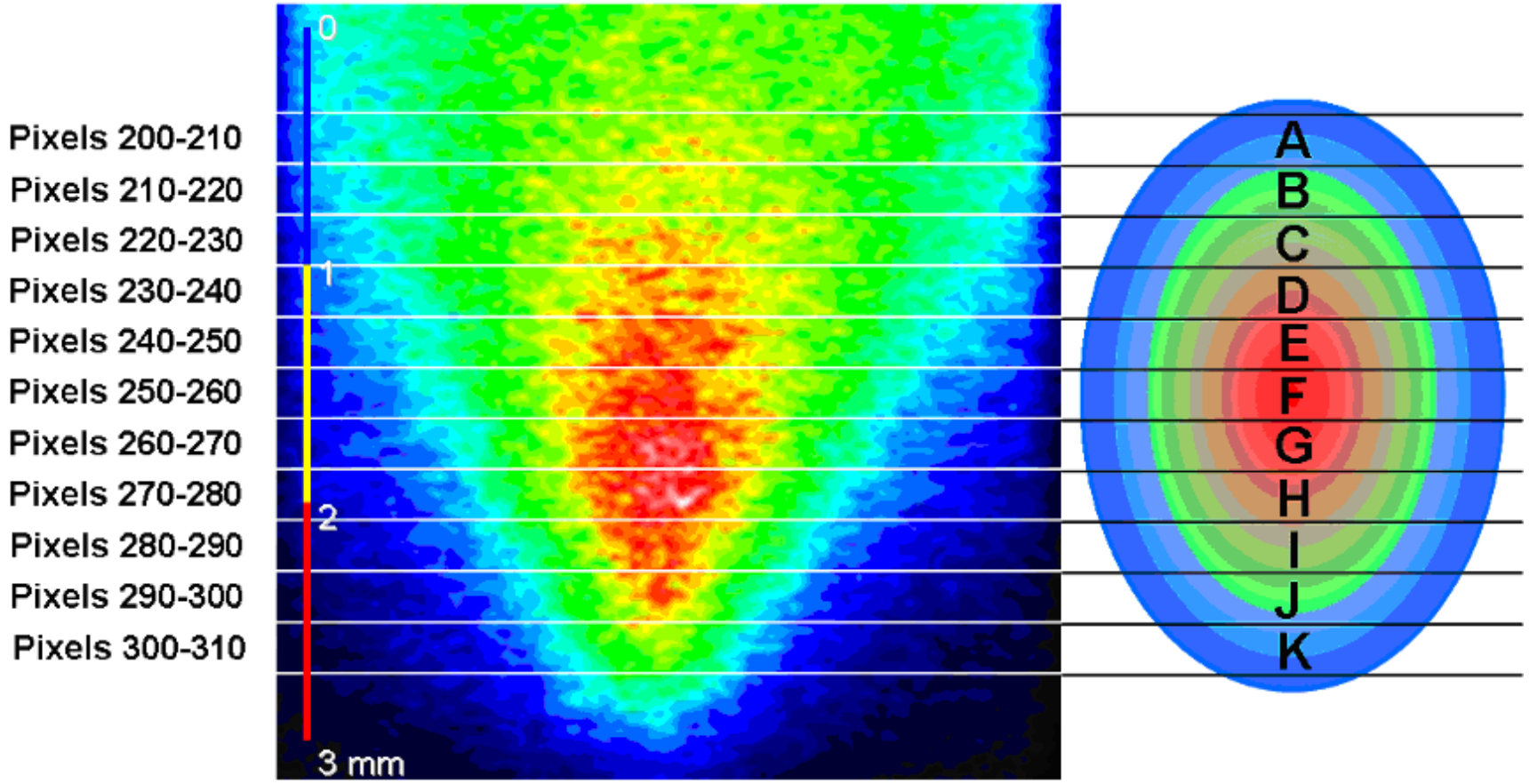

Figure 6-14. Image of the laser-induced plasma obtained from an Al alloy D33 using a delay time of 50 ns and gate width of 100 ns under 0.1 mbar pressure. Spatially-resolved measurements were obtained by binning the spectral emission images into 11 different spatial positions designated by letters A through K. The pixel numbers included in the binning process are shown on the left. Each binned region consists of 11 vertical pixels which is equal to 0.02475 cm.

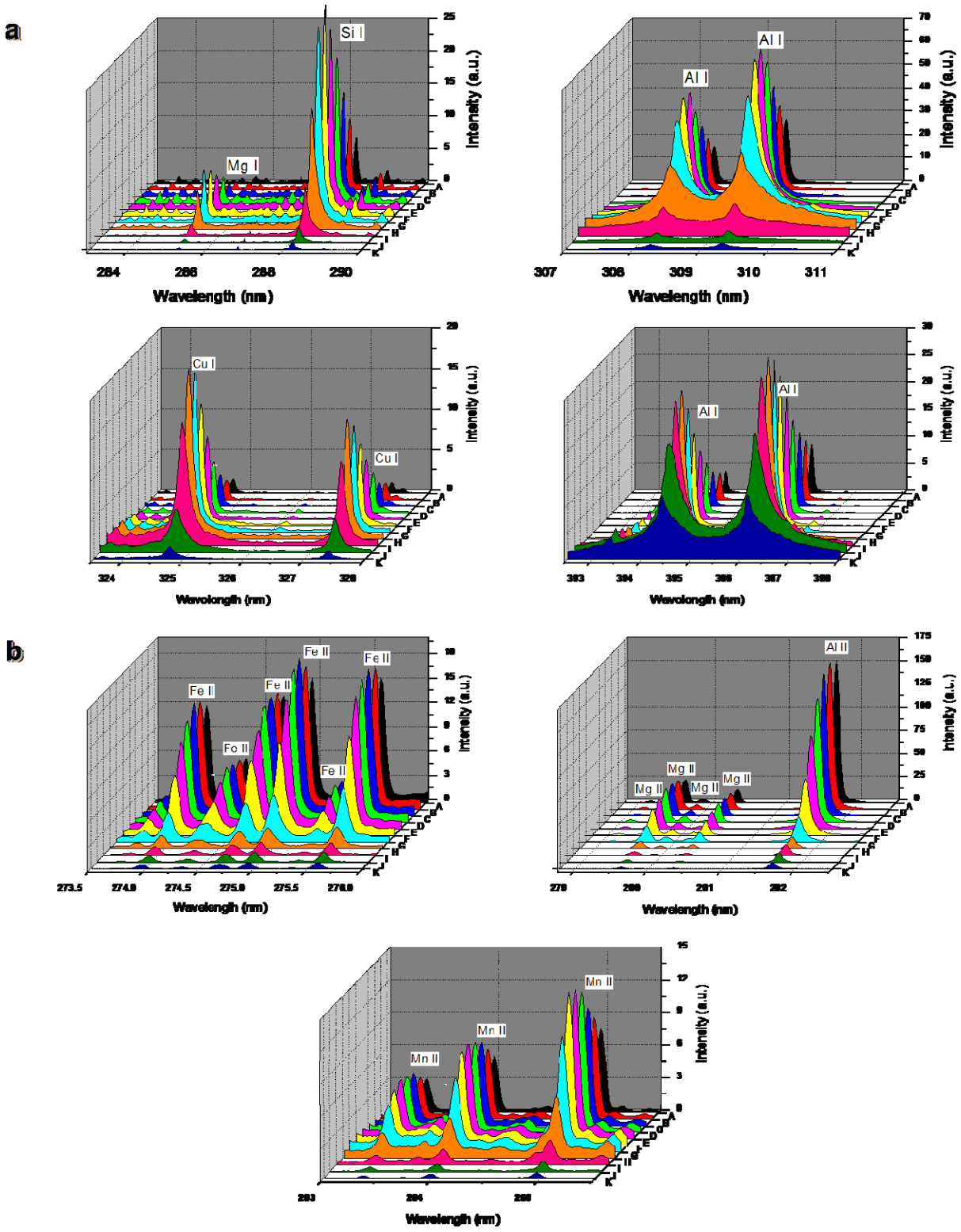

Figure 6-15. Spatially-resolved spectra of different (a) neutral and (b) singly-ionized lines.

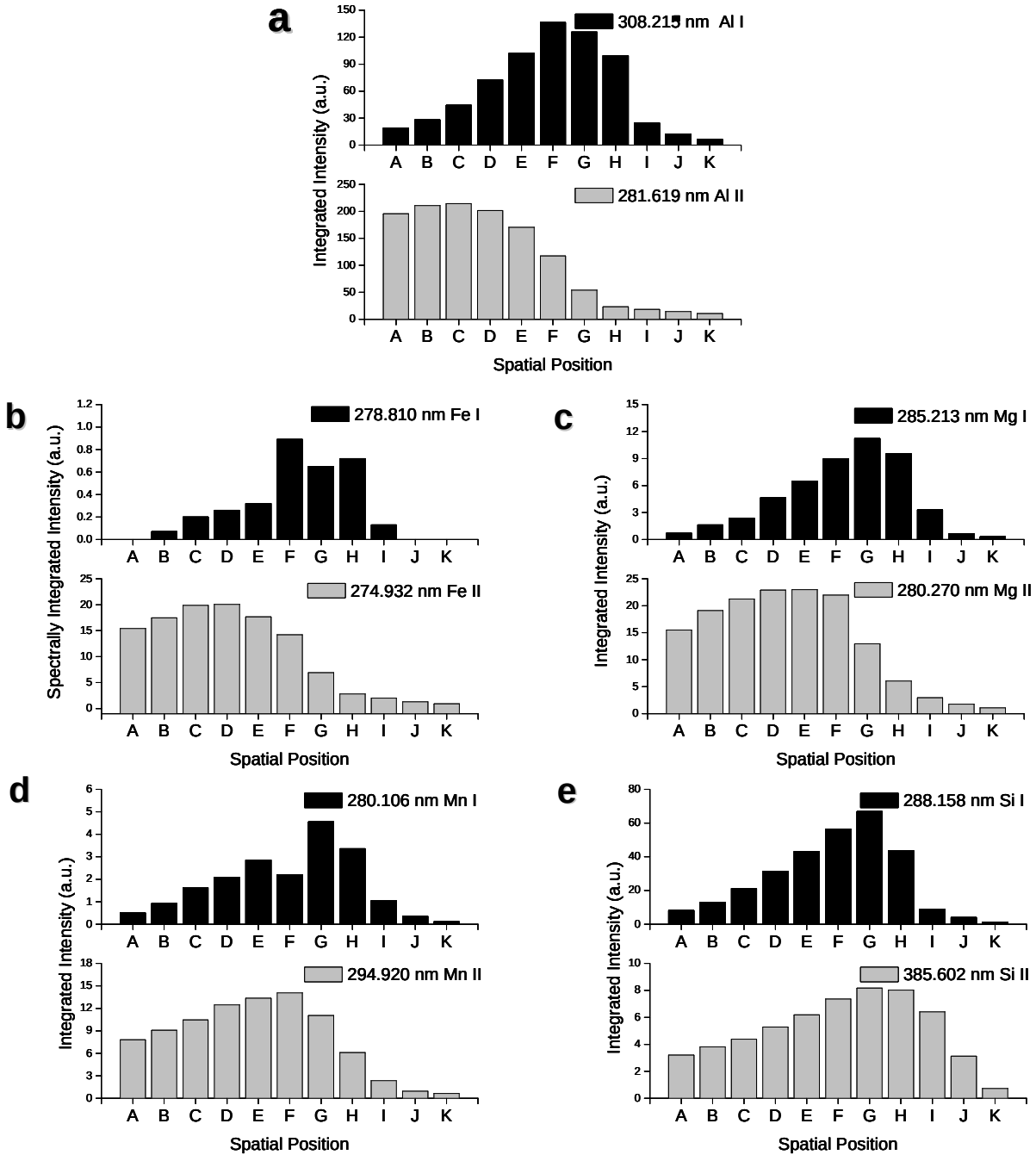

Figure 6-16. Spectrally-integrated intensities of different neutral (black bars) and singly-ionized (gray bars) lines of (a) Al, (b) Fe, (c) Mg, (d) Mn and (e) Si at various spatial positions.

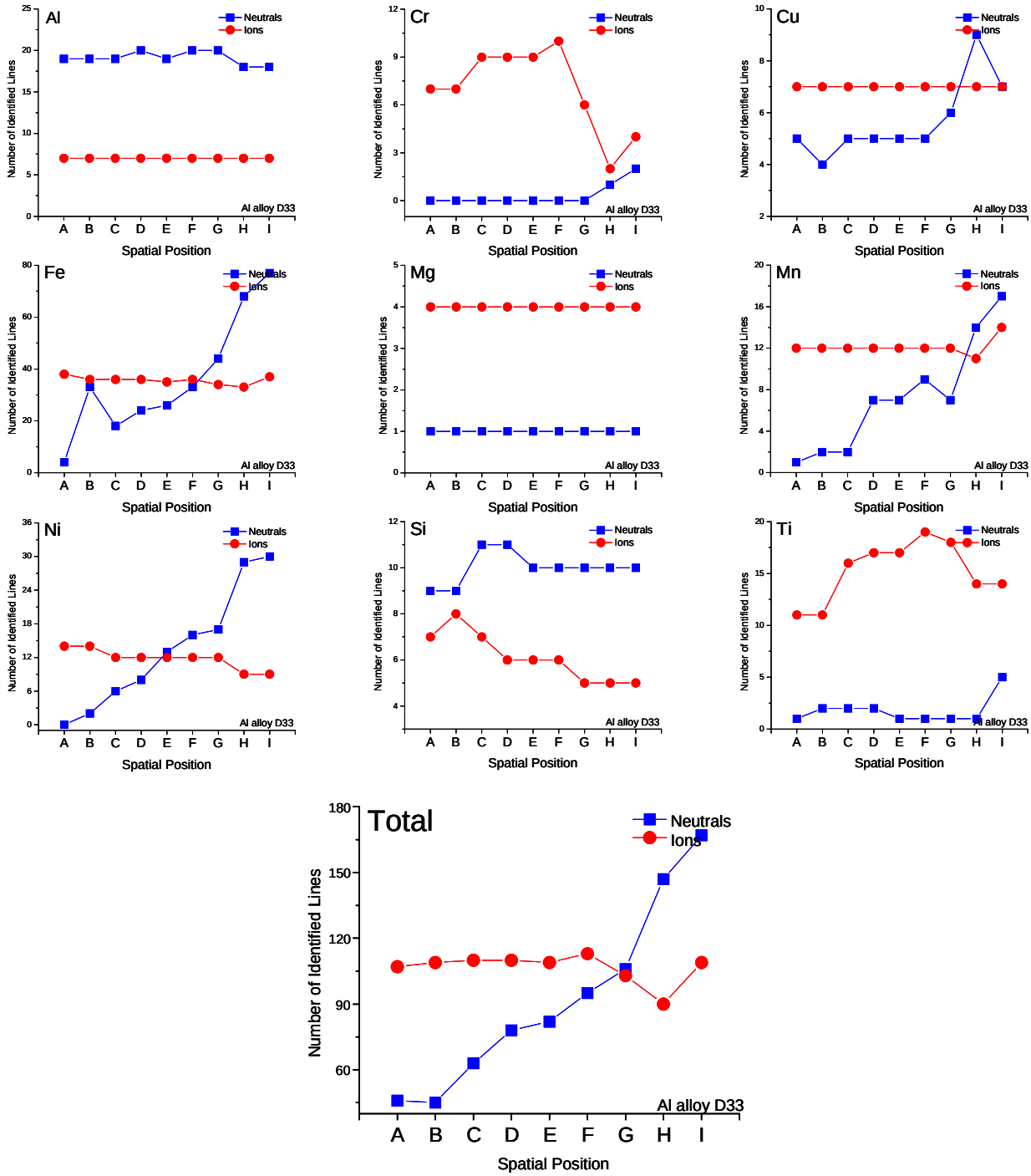

Figure 6-17. Spatial frequency distribution profile of different species in the aluminum alloy plasma.

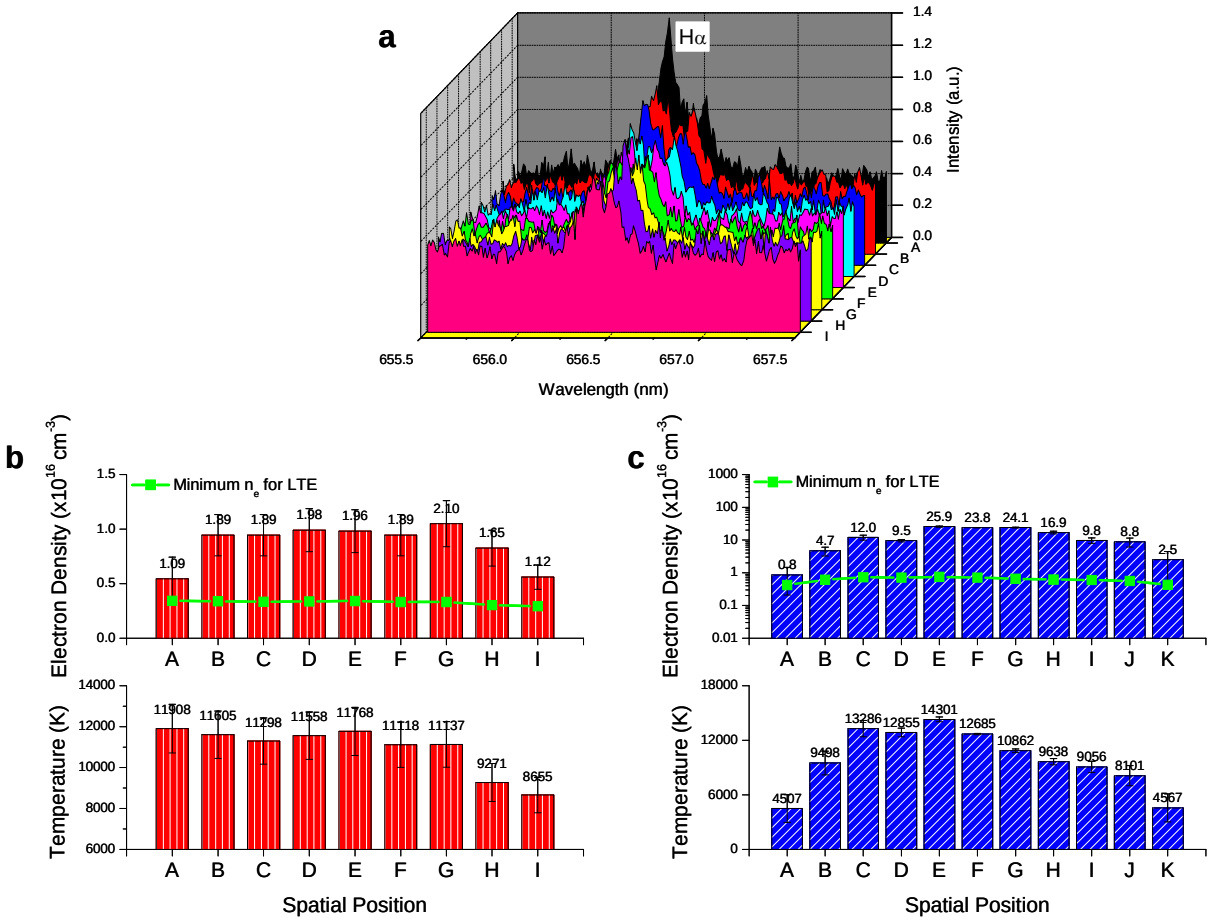

Figure 6-18. Electron number density and temperature values calculated at different spatial positions using (b) CF-LIBS and (c) MC-LIBS. The spectra in (a) shows the Hα line used to calculate the electron number density in CF-LIBS.

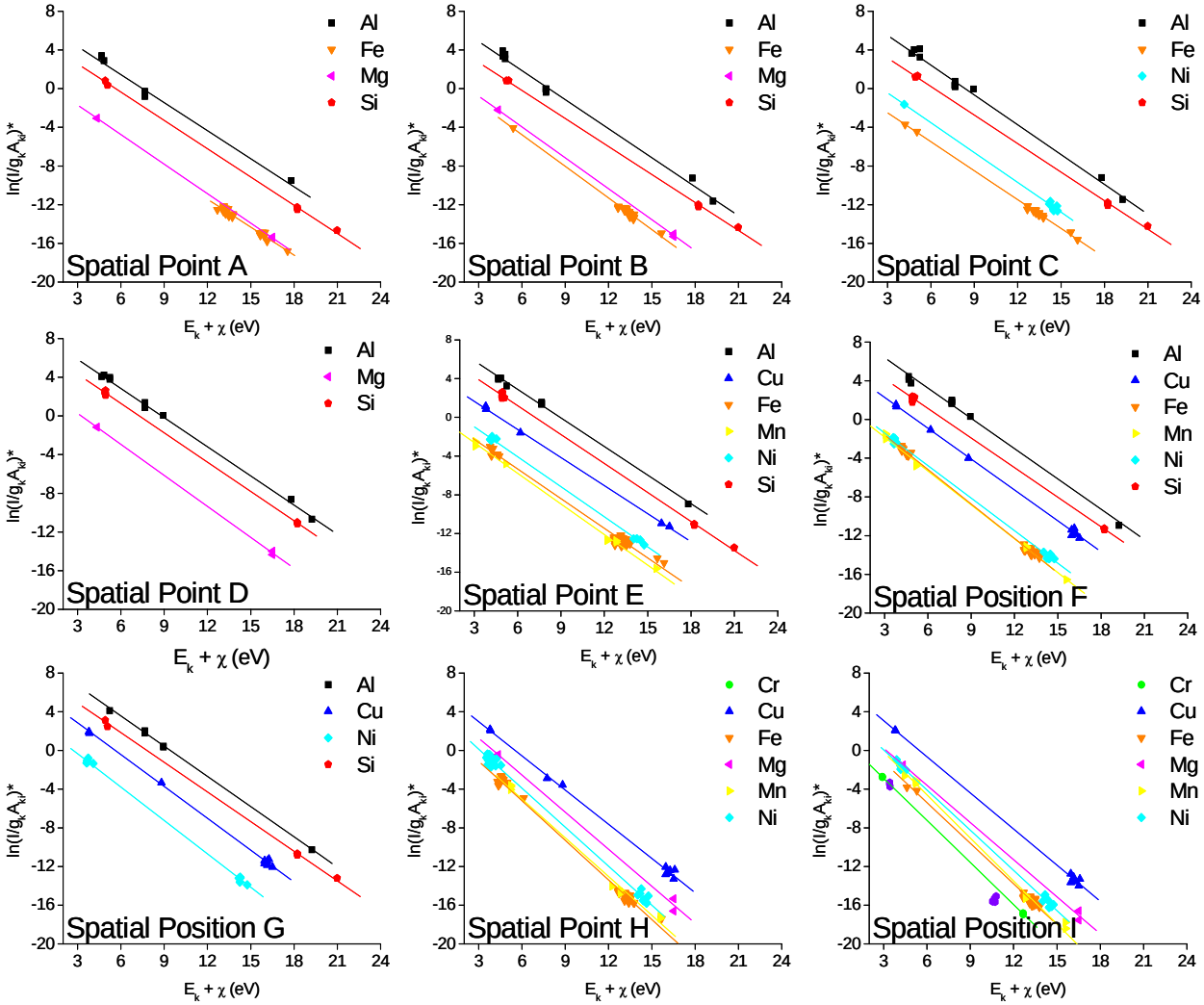

Figure 6-19. Saha-Boltzmann plots of selected elements in aluminum alloy sample D33 at different spatial positions (Left to right, top to bottom: spatial positions A through I).

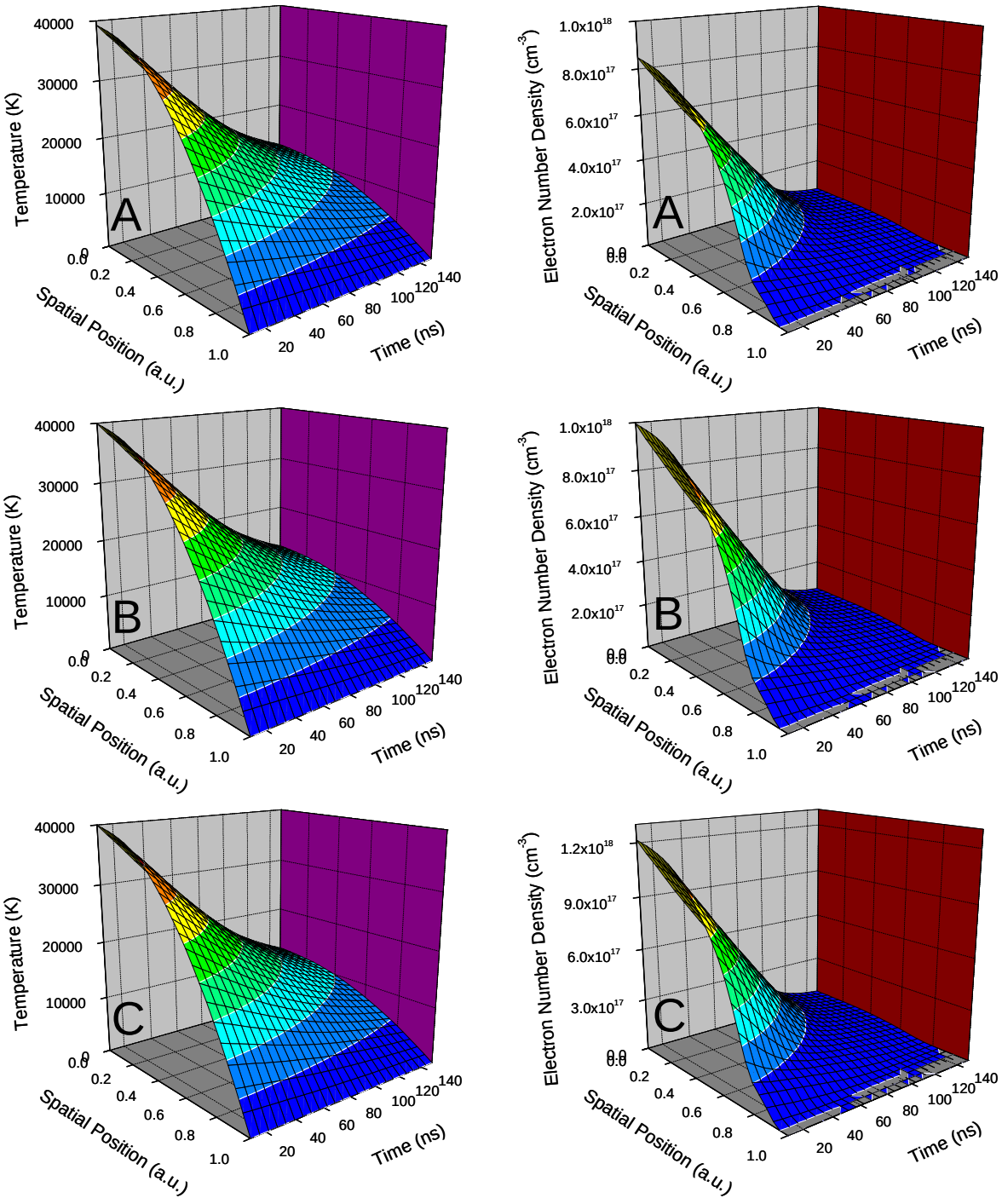

Figure 6-20. Spatial and temporal evolution of temperature (left) and electron number density (right) obtained using the MC-LIBS approach for aluminum alloy sample D33. The optimizations were carried out on spatially-resolved spectra denoted by letters A through K.

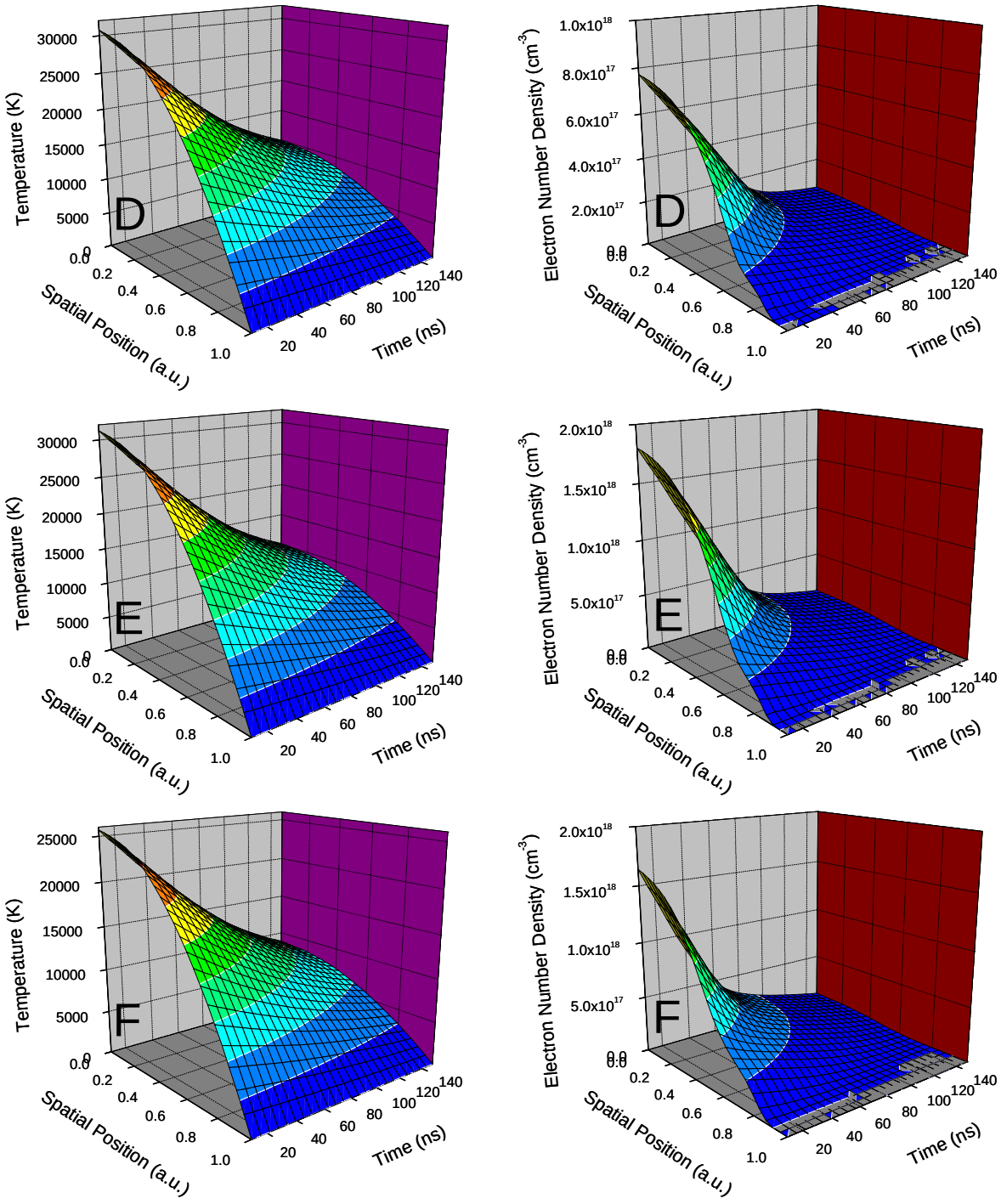

Figure 6-20. Continued.

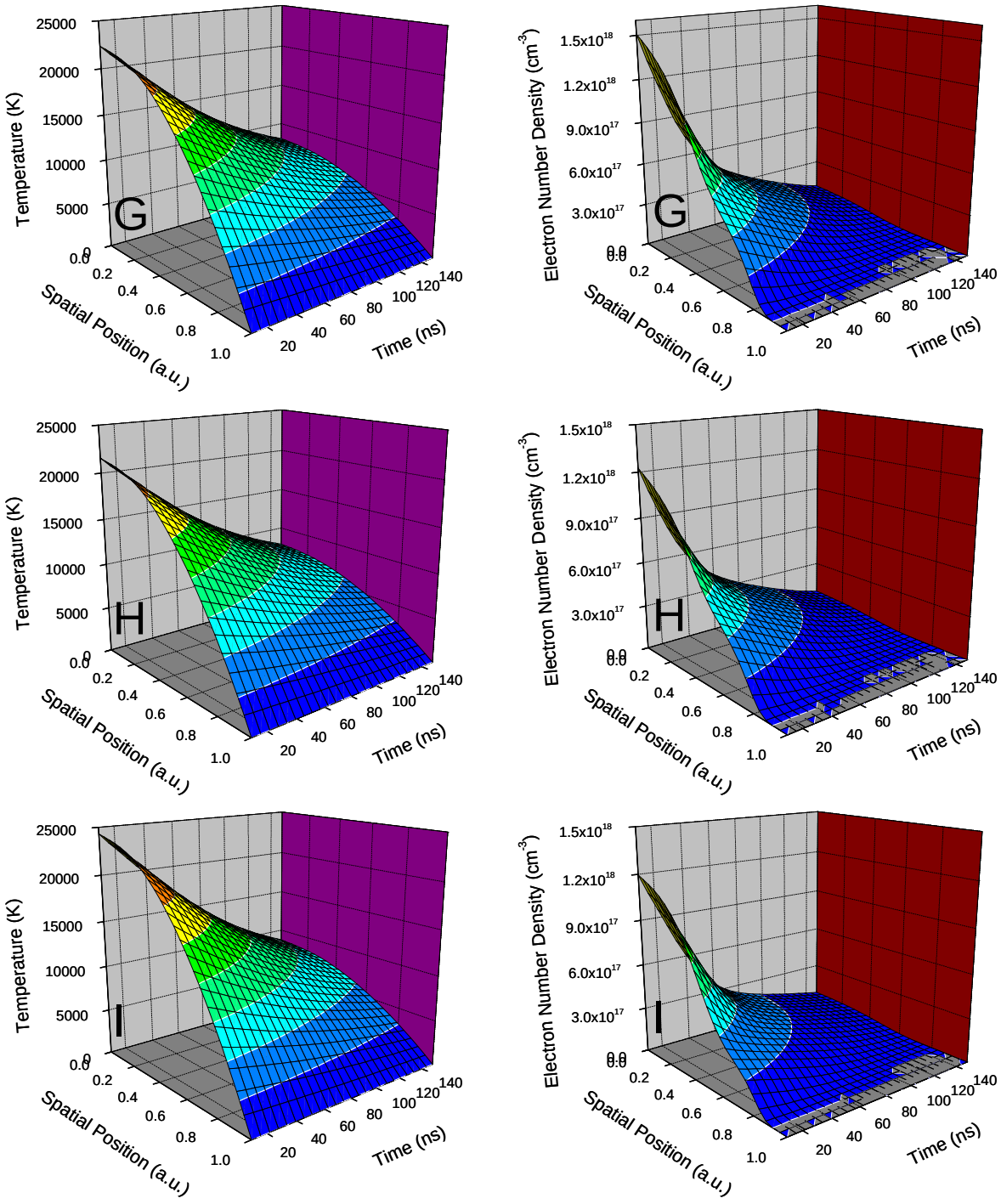

Figure 6-20. Continued.

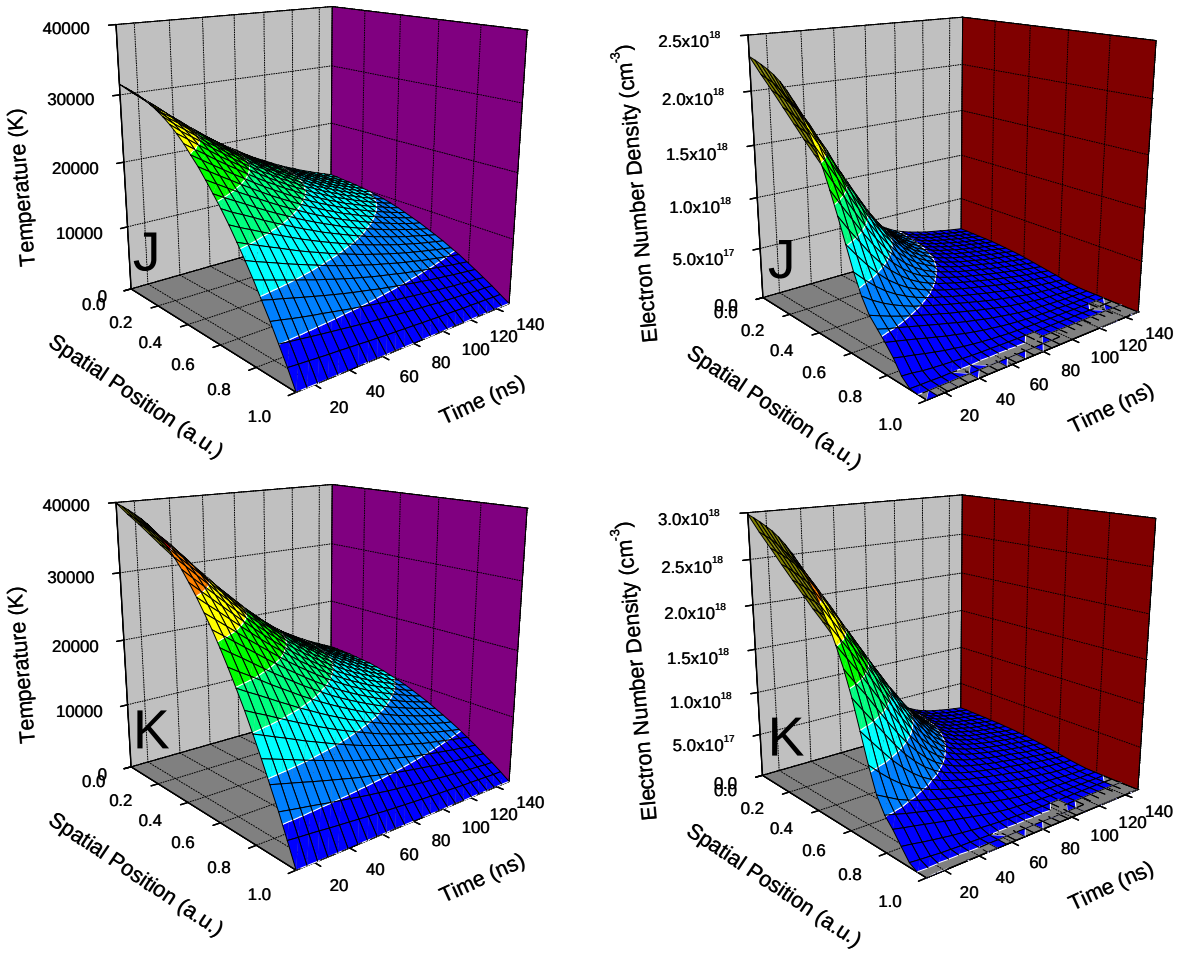

Figure 6-20. Continued.

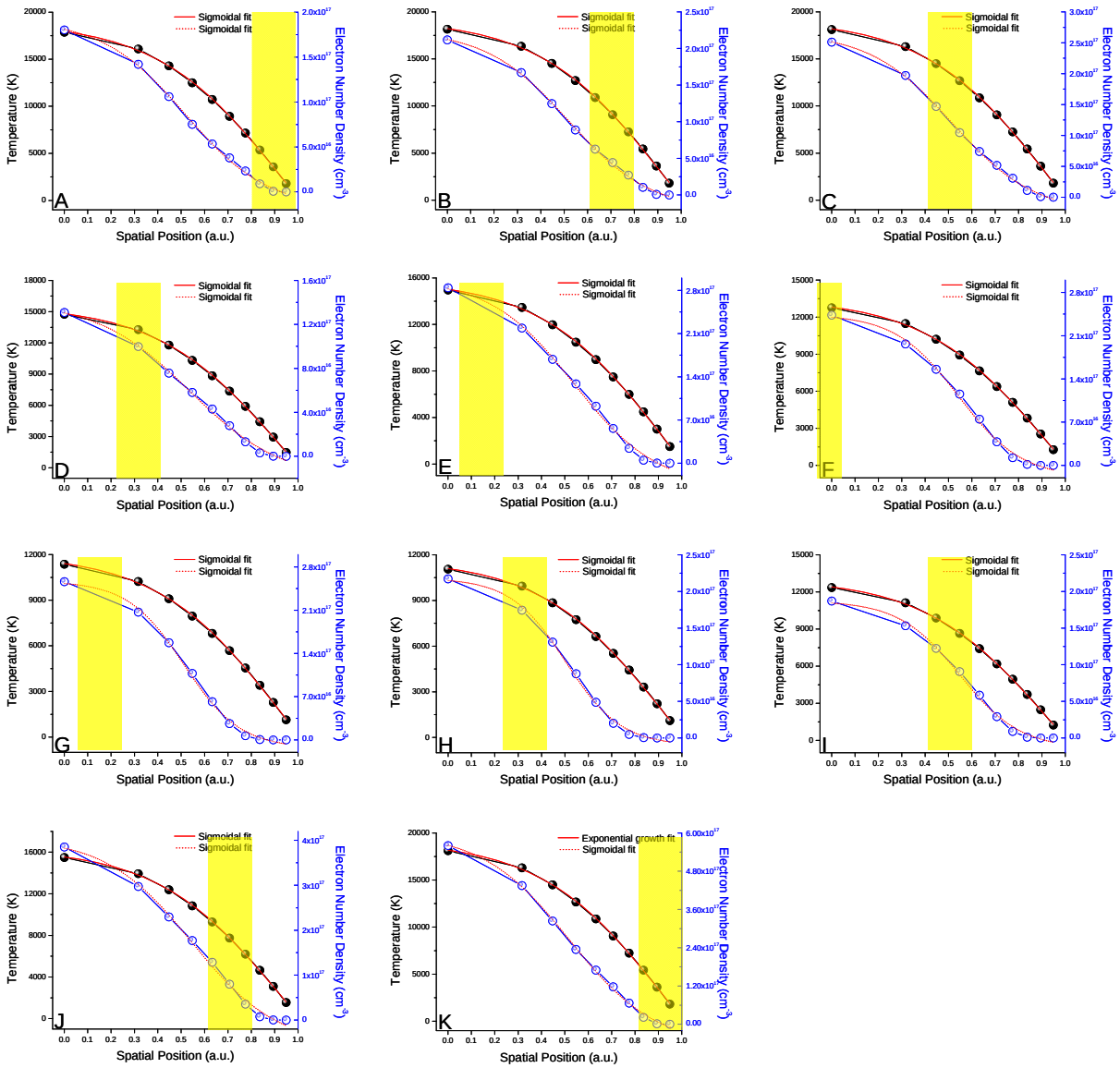

Figure 6-21. Spatial evolution of temporally-integrated temperature (black) and electron number density (blue) obtained using the MC-LIBS approach for aluminum alloy sample D33. The abscissa indicates relative spatial positions where spatial point zero indicates the first equipotential layer at the center of the plasma and the last spatial position indicates the outer layer of the plasma. The highlighted portion indicates the spatially-integrated portion of the plasma used to calculate the local temperatures at specific spatial positions (A through K). The solid and dotted red lines are the result of the curve fitting using a sigmoidal function.

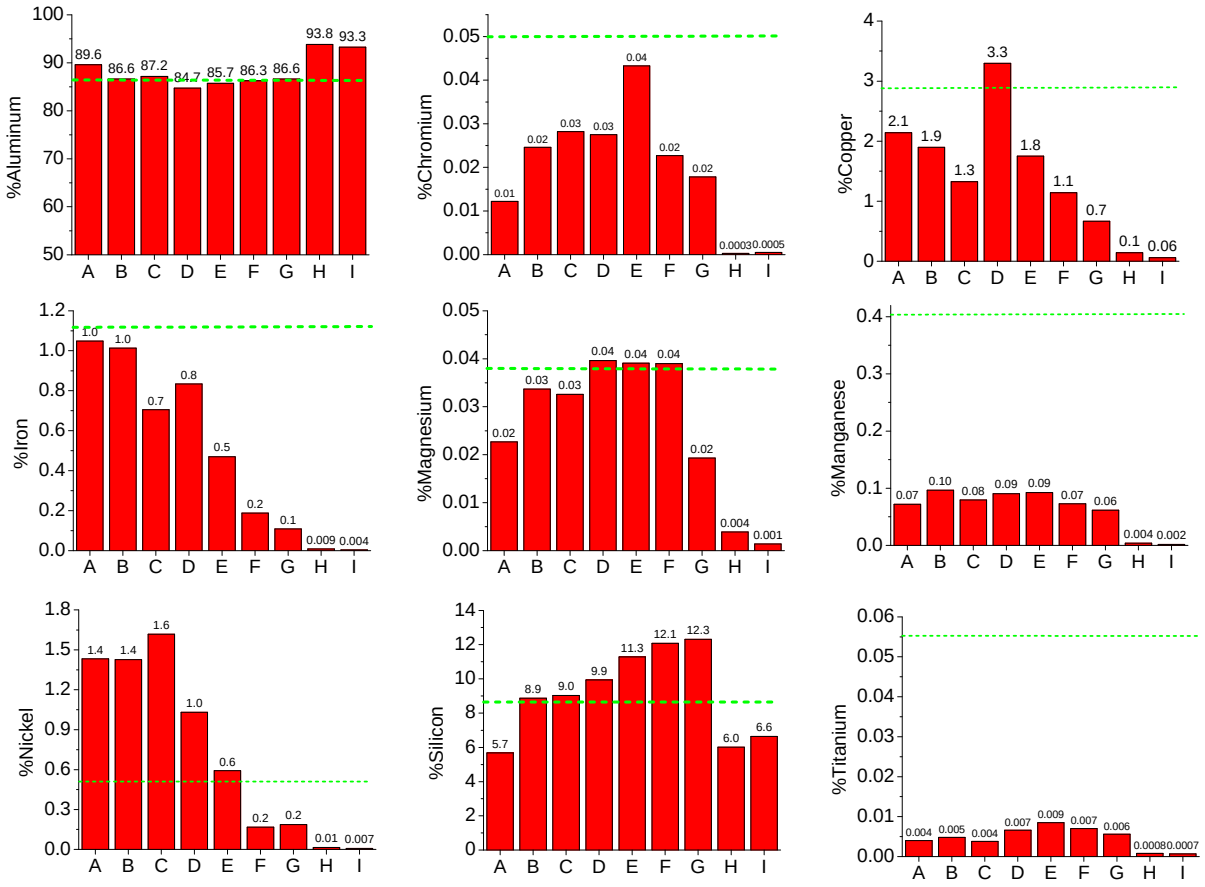

Figure 6-22. Relative concentration values at different spatial positions calculated with CF-LIBS. The dashed lines indicate the certified values.

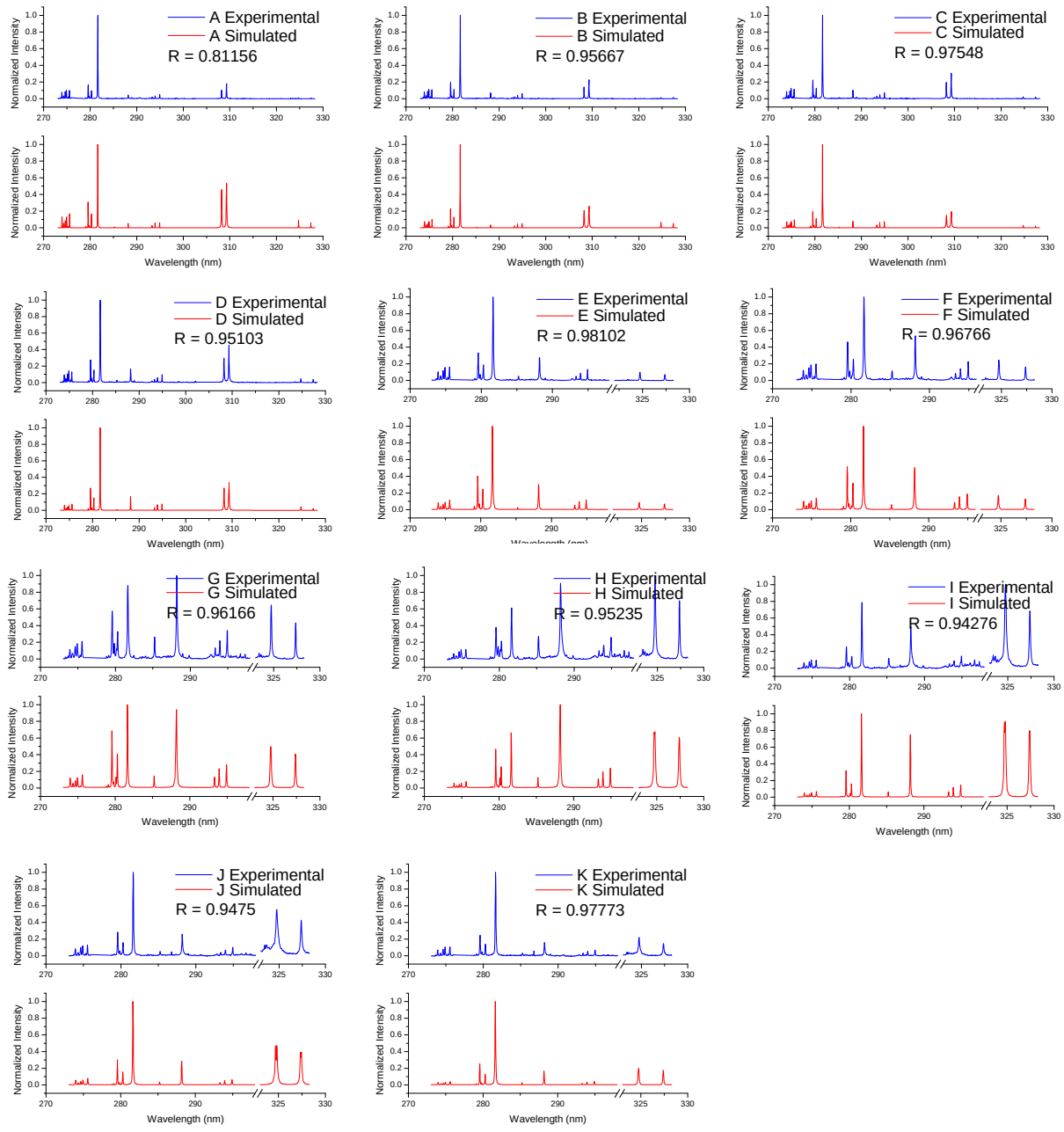

Figure 6-23. Comparison of experimental spectra of aluminum alloy D33 (blue) and the best-fit simulated spectra (red) calculated with MC-LIBS at different spatial positions (A through K). Maximized values of the cost function (correlation coefficient *R*) are also shown for each case.

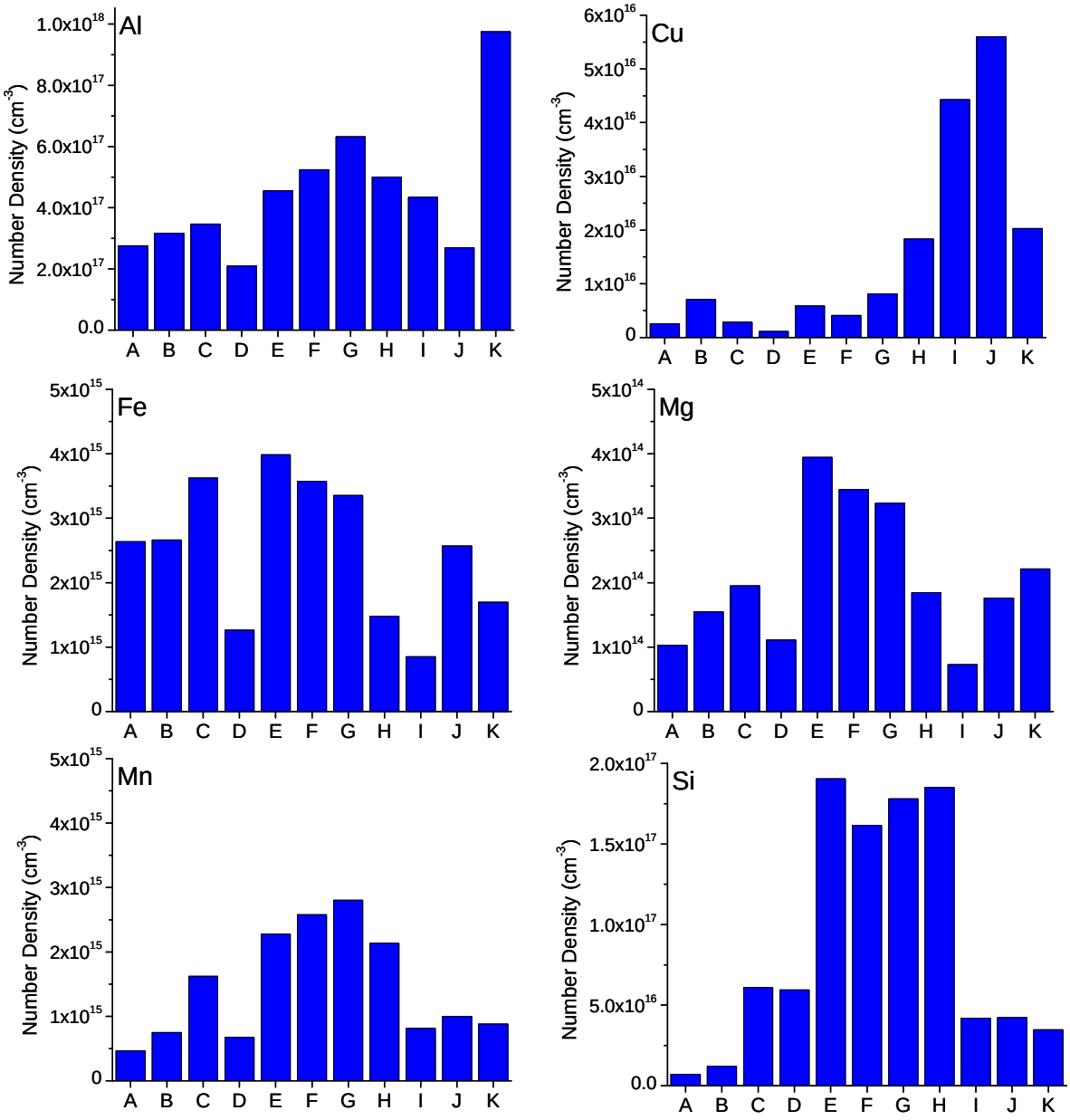

Figure 6-24. Number densities (cm^{-3}) of different elements in the alloy sample calculated at different spatial positions using MC-LIBS.

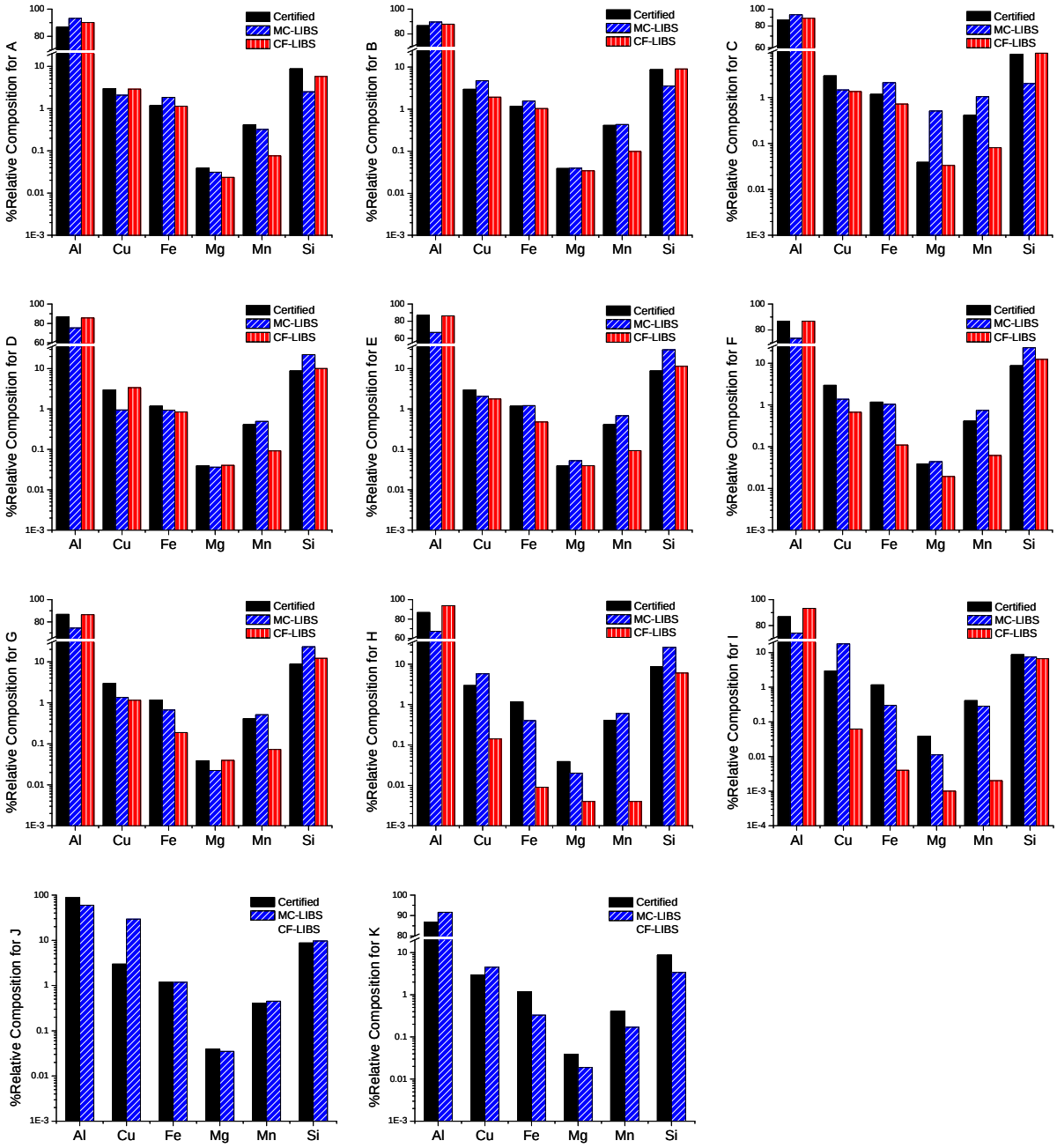

Figure 6-25. Relative concentration values calculated at different spatial positions (A through K) using MC-LIBS (blue bars) and CF-LIBS (red bars) compared with certified values (black bars).

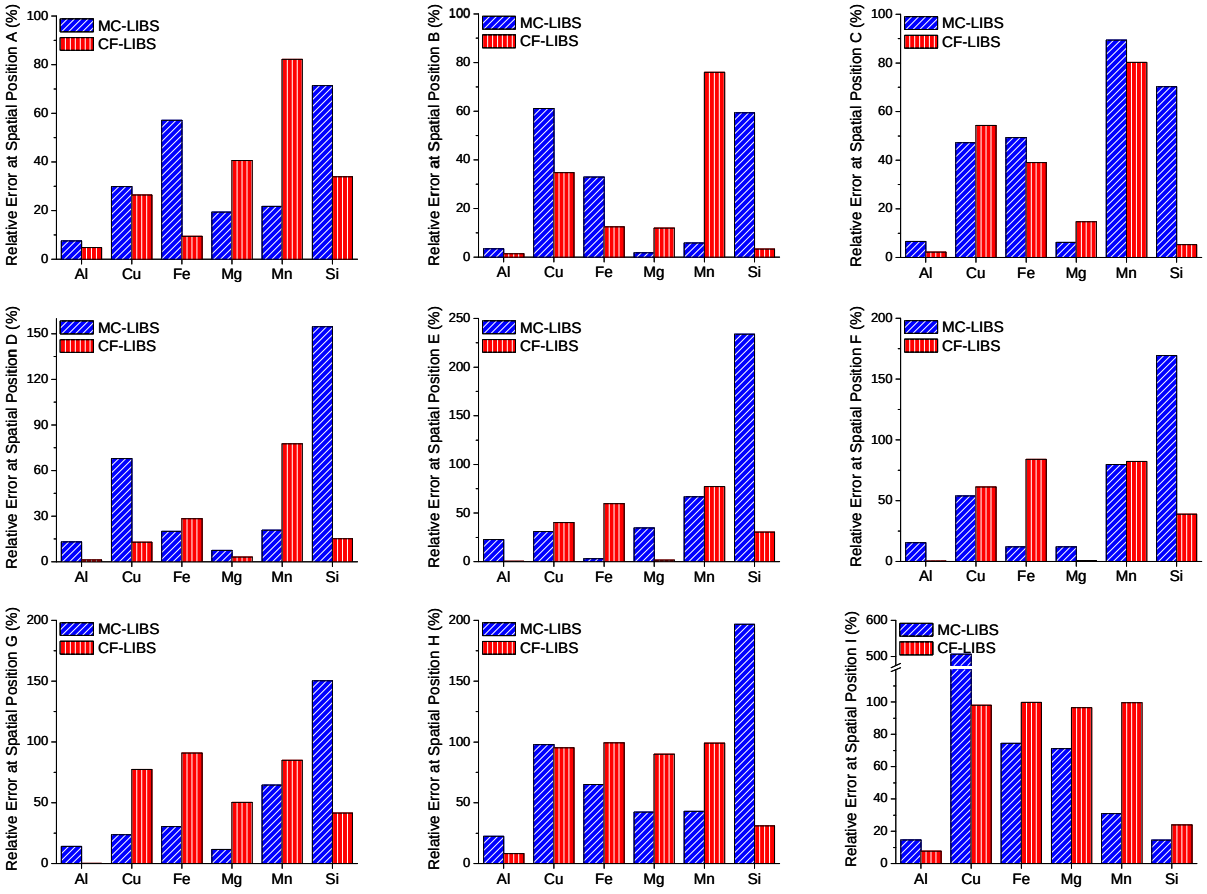

Figure 6-26. Relative errors of calculated concentration values at different spatial positions calculated using MC-LIBS (blue bars) and CF-LIBS (red bars).

Table 6-1. List of spectral lines used in the CF-LIBS analysis of Al alloy B8.

Al	I	236.705	Fe	II	262.567	Mn	I	405.893
Al	I	256.798	Fe	II	273.955	Ni	II	230.300
Al	I	265.248	Fe	II	274.320	Ni	II	239.452
Al	I	266.039	Fe	II	274.648	Ni	I	300.249
Al	II	281.619	Fe	II	275.329	Ni	I	341.476
Al	I	305.468	Fe	II	275.573	Ni	I	343.356
Al	I	305.714	Fe	I	296.689	Ni	I	345.847
Al	I	306.429	Fe	I	298.357	Ni	I	346.165
Al	I	306.614	Fe	I	364.784	Ni	I	351.505
Al	II	466.305	Fe	I	371.993	Ni	I	352.454
Al	II	622.618	Fe	I	373.486	Ni	I	361.939
Al	II	623.178	Fe	I	373.713	Si	I	250.690
Al	II	624.336	Fe	I	374.556	Si	I	251.432
Cr	II	283.563	Fe	I	374.948	Si	I	251.611
Cr	II	284.325	Fe	I	375.823	Si	I	251.920
Cr	II	284.984	Fe	I	376.378	Si	I	252.411
Cr	II	297.191	Fe	I	376.719	Si	I	252.851
Cr	II	297.974	Fe	I	382.042	Si	I	288.158
Cr	I	357.869	Fe	I	385.991	Si	II	385.602
Cr	I	359.349	Fe	I	404.581	Si	II	386.259
Cr	I	360.533	Fe	I	406.359	Si	I	390.552
Cr	I	520.604	Fe	I	407.173	Si	II	412.807
Cr	I	520.844	Fe	I	432.576	Si	II	505.598
Cu	II	221.027	Fe	I	438.354	Ti	II	323.452
Cu	II	221.810	Mg	II	279.078	Ti	II	332.294
Cu	II	222.886	Mg	II	279.800	Ti	II	332.946
Cu	II	224.261	Mg	I	285.213	Ti	II	333.520
Cu	II	224.700	Mn	II	259.373	Ti	II	334.034
Cu	II	227.625	Mn	II	260.569	Ti	II	334.941
Cu	II	229.436	Mn	II	261.020	Ti	I	335.464
Cu	II	240.012	Mn	II	293.306	Ti	II	336.121
Cu	I	261.837	Mn	II	293.930	Ti	II	337.280
Cu	I	427.511	Mn	II	294.920	Ti	I	363.546
Cu	I	510.554	Mn	II	344.199	Ti	I	365.350
Fe	II	238.204	Mn	II	348.291	Ti	II	375.930
Fe	II	256.253	Mn	I	356.949	Ti	II	376.132
Fe	II	258.588	Mn	I	380.672	Ti	I	498.173
Fe	II	259.837	Mn	I	403.076	Ti	I	499.107
Fe	II	259.940	Mn	I	403.307	Ti	I	499.951
Fe	II	260.709	Mn	I	403.449	Ti	I	500.721
Fe	II	261.187	Mn	I	403.573	Ti	I	501.424
Fe	II	261.382	Mn	I	404.136			

Table 6-2. List of spectral lines used in the CF-LIBS analysis of Al alloy D33.

Al	I	232.156	Fe	II	261.187	Fe	I	404.581	Ni	I	300.249
Al	I	256.798	Fe	II	261.382	Fe	I	406.359	Ni	I	300.363
Al	I	265.248	Fe	II	261.762	Fe	I	407.173	Ni	I	301.200
Al	I	266.039	Fe	II	262.167	Fe	I	427.175	Ni	I	313.411
Al	II	281.619	Fe	II	262.567	Fe	I	430.790	Ni	I	339.105
Al	I	305.007	Fe	II	262.829	Fe	I	432.576	Ni	I	339.299
Al	I	305.468	Fe	II	272.754	Fe	I	438.354	Ni	I	341.476
Al	I	305.714	Fe	II	273.697	Fe	I	440.475	Ni	I	342.371
Al	I	306.429	Fe	II	273.955	Mg	II	279.078	Ni	I	343.356
Al	I	306.614	Fe	I	274.240	Mg	II	279.553	Ni	I	343.728
Al	II	466.305	Fe	II	274.320	Mg	II	279.800	Ni	I	344.626
Al	II	622.621	Fe	II	274.648	Mg	II	280.270	Ni	I	345.289
Al	II	623.175	Fe	II	274.932	Mg	I	285.213	Ni	I	345.847
Al	II	624.337	Fe	II	275.329	Mn	II	259.373	Ni	I	346.165
Cr	II	297.974	Fe	II	275.573	Mn	II	260.569	Ni	I	349.296
Cr	II	342.273	Fe	I	296.689	Mn	II	261.814	Ni	I	351.505
Cr	I	427.480	Fe	I	297.313	Mn	I	280.106	Ni	I	352.454
Cu	II	224.261	Fe	I	298.357	Mn	II	293.305	Ni	I	356.637
Cu	II	224.700	Fe	II	298.482	Mn	II	293.931	Si	I	250.690
Cu	II	227.625	Fe	I	299.442	Mn	II	294.921	Si	I	251.432
Cu	I	296.116	Fe	I	300.094	Mn	II	344.199	Si	I	251.611
Cu	I	301.084	Fe	I	300.814	Mn	II	346.032	Si	I	251.920
Cu	I	510.554	Fe	I	300.956	Mn	I	403.076	Si	I	252.411
Fe	II	233.131	Fe	I	302.063	Mn	I	403.307	Si	I	252.851
Fe	II	233.280	Fe	I	346.586	Mn	I	403.449	Si	I	288.158
Fe	II	233.801	Fe	I	349.057	Mn	I	403.573	Si	I	298.764
Fe	II	234.349	Fe	I	351.381	Mn	I	404.136	Si	II	385.367
Fe	II	234.428	Fe	I	356.537	Mn	I	404.876	Si	II	385.602
Fe	II	234.830	Fe	I	357.009	Mn	I	405.554	Si	II	386.259
Fe	II	238.204	Fe	I	358.119	Ni	II	220.672	Si	I	390.552
Fe	II	238.863	Fe	I	361.876	Ni	II	221.648	Si	II	412.807
Fe	II	239.563	Fe	I	363.146	Ni	II	222.296	Ti	II	323.452
Fe	II	239.924	Fe	I	364.784	Ni	II	225.385	Ti	II	323.658
Fe	II	240.489	Fe	I	368.745	Ni	II	226.446	Ti	II	323.904
Fe	II	240.666	Fe	I	371.993	Ni	II	227.021	Ti	II	323.966
Fe	II	241.052	Fe	I	373.486	Ni	II	227.877	Ti	II	334.941
Fe	II	241.107	Fe	I	373.713	Ni	II	229.655	Ti	II	336.122
Fe	II	241.331	Fe	I	374.556	Ni	II	229.714	Ti	II	338.376
Fe	II	243.930	Fe	I	374.826	Ni	II	230.300	Ti	II	338.785
Fe	II	256.253	Fe	I	374.948	Ni	II	231.604	Ti	II	339.458
Fe	II	256.348	Fe	I	375.823	Ni	I	232.003	Ti	II	350.490
Fe	II	258.588	Fe	I	376.378	Ni	II	233.458	Ti	I	363.546
Fe	II	259.154	Fe	I	382.042	Ni	II	239.452	Ti	I	364.268
Fe	II	259.837	Fe	I	382.588	Ni	II	241.613	Ti	II	368.520
Fe	II	259.940	Fe	I	382.782	Ni	II	243.789	Ti	II	376.132
Fe	II	260.709	Fe	I	385.991	Ni	I	298.165			

Table 6-3. List of spectral lines used in the CF-LIBS analysis of Al alloy S4.

Al	I	226.910	Fe	II	239.562	Fe	I	374.826	Mn	I	405.554
Al	I	236.705	Fe	II	239.924	Fe	I	374.948	Ni	I	300.249
Al	I	237.312	Fe	II	240.488	Fe	I	375.823	Ni	I	336.957
Al	I	237.840	Fe	II	240.666	Fe	I	376.378	Ni	I	338.057
Al	I	256.798	Fe	II	241.052	Fe	I	376.554	Ni	I	339.299
Al	I	257.510	Fe	II	241.331	Fe	I	376.719	Ni	I	341.476
Al	I	265.248	Fe	II	249.326	Fe	I	382.042	Ni	I	344.626
Al	I	266.039	Fe	II	256.253	Fe	I	385.991	Ni	I	345.847
Al	I	305.007	Fe	II	256.348	Fe	I	388.628	Ni	I	346.165
Al	I	305.468	Fe	II	258.588	Fe	I	404.581	Ni	I	351.505
Al	I	305.714	Fe	II	259.837	Fe	I	406.359	Ni	I	352.454
Al	I	306.429	Fe	II	259.940	Fe	I	407.173	Si	I	250.690
Al	I	306.614	Fe	II	260.709	Fe	I	427.175	Si	I	251.432
Al	II	466.305	Fe	II	261.187	Fe	I	430.790	Si	I	251.611
Al	II	622.621	Fe	II	261.382	Fe	I	432.576	Si	I	251.920
Al	II	623.175	Fe	II	261.762	Fe	I	438.354	Si	I	252.411
Al	II	624.337	Fe	II	262.567	Fe	I	440.475	Si	I	252.851
Cr	II	283.563	Fe	II	262.829	Fe	I	441.512	Si	I	288.158
Cr	II	284.325	Fe	II	271.441	Mg	I	277.669	Si	II	385.602
Cr	II	284.984	Fe	I	271.902	Mg	I	277.827	Si	I	390.552
Cr	II	285.568	Fe	II	272.754	Mg	I	278.142	Si	II	412.807
Cr	I	300.089	Fe	II	273.697	Mg	I	278.297	Ti	II	323.452
Cr	II	313.206	Fe	II	273.955	Mg	II	279.078	Ti	II	323.657
Cr	I	360.533	Fe	II	274.320	Mg	II	279.553	Ti	II	323.904
Cr	I	425.433	Fe	II	274.648	Mg	II	279.800	Ti	II	324.199
Cr	I	427.480	Fe	II	275.329	Mg	II	280.270	Ti	II	332.294
Cr	I	428.972	Fe	II	275.574	Mg	I	285.213	Ti	II	334.941
Cu	II	221.027	Fe	II	278.369	Mg	II	292.863	Ti	II	336.121
Cu	II	221.810	Fe	I	296.689	Mg	II	293.651	Ti	II	337.280
Cu	II	222.886	Fe	I	297.313	Mn	II	257.610	Ti	II	338.376
Cu	II	224.261	Fe	I	298.357	Mn	II	259.373	Ti	II	338.784
Cu	II	224.700	Fe	I	299.442	Mn	II	260.569	Ti	II	339.458
Cu	II	227.625	Fe	I	302.063	Mn	II	261.020	Ti	I	363.546
Cu	II	229.436	Fe	I	344.060	Mn	I	280.106	Ti	I	364.268
Cu	II	240.333	Fe	I	346.586	Mn	II	293.306	Ti	I	365.350
Cu	I	276.637	Fe	I	356.537	Mn	II	293.930	Ti	II	368.520
Cu	I	296.116	Fe	I	357.009	Mn	II	294.920	Ti	II	375.930
Cu	I	327.396	Fe	I	360.885	Mn	II	344.199	Zn	II	250.199
Cu	I	510.554	Fe	I	361.876	Mn	II	346.033	Zn	II	255.795
Fe	II	233.131	Fe	I	363.146	Mn	I	380.672	Zn	I	328.233
Fe	II	233.280	Fe	I	364.784	Mn	I	403.076	Zn	I	330.258
Fe	II	233.801	Fe	I	371.993	Mn	I	403.307	Zn	I	334.502
Fe	II	234.349	Fe	I	372.761	Mn	I	403.449	Zn	I	468.014
Fe	II	234.830	Fe	I	373.486	Mn	I	403.573	Zn	I	472.215
Fe	II	238.204	Fe	I	373.713	Mn	I	404.136	Zn	I	481.053
Fe	II	238.863	Fe	I	374.556	Mn	I	404.876	Zn	II	491.162

Table 6-4. List of spectral lines used in the CF-LIBS analysis of Al alloy SM10.

Al	I	226.910	Fe	II	233.801	Fe	I	346.586	Mn	II	294.920
Al	I	236.705	Fe	II	234.349	Fe	I	356.537	Mn	II	344.199
Al	I	237.207	Fe	II	234.428	Fe	I	357.009	Mn	II	346.033
Al	I	237.312	Fe	II	234.830	Fe	I	358.119	Mn	I	380.672
Al	I	265.248	Fe	II	238.204	Fe	I	360.668	Mn	I	403.076
Al	I	266.039	Fe	II	238.863	Fe	I	360.885	Mn	I	403.307
Al	II	281.619	Fe	II	239.562	Fe	I	361.876	Mn	I	403.449
Al	I	305.007	Fe	II	239.924	Fe	I	363.146	Mn	I	403.573
Al	I	305.468	Fe	II	240.488	Fe	I	364.784	Mn	I	404.136
Al	I	305.714	Fe	II	240.666	Fe	I	371.993	Mn	I	404.876
Al	I	306.429	Fe	II	241.052	Fe	I	372.761	Mn	I	405.554
Al	I	306.614	Fe	II	241.107	Fe	I	373.486	Ni	II	221.648
Al	II	466.305	Fe	II	241.331	Fe	I	373.713	Ni	I	300.249
Al	II	622.621	Fe	I	252.284	Fe	I	374.556	Ni	I	344.626
Al	II	623.175	Fe	II	256.253	Fe	I	374.826	Si	I	250.690
Al	II	624.337	Fe	II	256.348	Fe	I	374.948	Si	I	251.432
Cr	II	283.563	Fe	II	258.588	Fe	I	375.823	Si	I	251.611
Cr	II	284.325	Fe	II	259.154	Fe	I	376.378	Si	I	251.920
Cr	II	284.984	Fe	II	259.837	Fe	I	376.554	Si	I	252.411
Cr	II	285.568	Fe	II	259.940	Fe	I	376.719	Si	I	252.851
Cr	II	297.974	Fe	II	260.709	Fe	I	381.584	Si	I	288.158
Cr	I	300.089	Fe	II	261.187	Fe	I	382.042	Si	II	385.602
Cr	II	313.206	Fe	II	261.382	Fe	I	385.991	Si	II	386.259
Cr	I	357.869	Fe	II	261.762	Fe	I	404.581	Si	I	390.552
Cr	I	359.349	Fe	II	262.567	Fe	I	406.359	Si	II	412.807
Cr	I	360.533	Fe	II	262.829	Fe	I	407.173	Ti	II	323.452
Cr	I	425.433	Fe	II	271.441	Fe	I	427.175	Ti	II	323.657
Cr	I	427.480	Fe	I	271.902	Fe	I	430.790	Ti	II	323.904
Cr	I	428.972	Fe	II	272.754	Fe	I	432.576	Ti	II	324.199
Cu	II	221.027	Fe	II	273.697	Fe	I	438.354	Ti	II	336.121
Cu	II	221.810	Fe	II	273.955	Fe	I	440.475	Ti	II	337.280
Cu	II	222.886	Fe	II	274.320	Fe	I	441.512	Ti	II	338.376
Cu	II	224.261	Fe	II	274.648	Mg	I	277.669	Ti	II	368.520
Cu	II	224.700	Fe	II	275.329	Mg	I	277.827	Ti	II	375.930
Cu	II	227.625	Fe	II	275.574	Mg	I	278.142	Ti	II	376.132
Cu	II	229.436	Fe	II	278.369	Mg	I	278.297	Zn	II	250.199
Cu	II	240.012	Fe	I	294.787	Mg	II	448.116	Zn	II	255.795
Cu	I	330.795	Fe	I	298.357	Mn	II	259.373	Zn	I	328.233
Cu	I	465.112	Fe	I	299.442	Mn	II	260.569	Zn	I	334.502
Cu	I	510.554	Fe	I	302.063	Mn	II	261.020	Zn	I	472.215
Fe	II	233.131	Fe	I	305.908	Mn	II	293.306	Zn	I	481.053
Fe	II	233.280	Fe	I	344.060	Mn	II	293.930			

Table 6-5. List of spectral lines used in the CF-LIBS analysis of Al alloy V14.

Al	I	231.249	Fe	II	241.052	Fe	I	382.043	Ni	I	349.296
Al	I	232.156	Fe	II	241.107	Fe	I	382.588	Ni	I	351.505
Al	I	236.705	Fe	II	241.331	Fe	I	382.782	Ni	I	352.454
Al	I	237.312	Fe	II	242.836	Fe	I	383.422	Ni	I	356.637
Al	I	256.798	Fe	II	243.930	Fe	I	385.991	Ni	I	361.939
Al	I	265.248	Fe	I	247.977	Fe	I	407.173	Si	I	221.089
Al	I	266.039	Fe	I	248.814	Fe	I	427.175	Si	I	243.515
Al	II	281.619	Fe	II	249.326	Fe	I	430.790	Si	I	250.690
Al	I	305.007	Fe	I	251.083	Fe	I	432.576	Si	I	251.432
Al	I	305.468	Fe	I	252.743	Fe	I	438.354	Si	I	251.611
Al	I	305.714	Fe	II	256.253	Fe	I	440.475	Si	I	251.920
Al	I	306.429	Fe	II	256.348	Mg	II	279.078	Si	I	252.411
Al	I	306.614	Fe	II	258.588	Mg	II	279.553	Si	I	252.851
Al	II	466.305	Fe	II	259.837	Mg	II	279.800	Si	I	288.158
Cr	II	266.602	Fe	II	259.940	Mg	II	280.270	Si	II	385.367
Cr	II	267.181	Fe	II	260.709	Mg	I	285.213	Si	II	385.602
Cr	II	283.563	Fe	II	261.187	Mn	II	257.610	Si	II	386.260
Cr	II	284.325	Fe	II	261.382	Mn	II	259.373	Si	I	390.552
Cr	II	284.984	Fe	II	261.762	Mn	II	260.569	Si	II	412.805
Cr	II	285.568	Fe	II	262.567	Mn	II	261.020	Ti	II	323.452
Cr	II	297.974	Fe	II	262.829	Mn	II	261.814	Ti	II	323.658
Cr	II	313.206	Fe	II	266.466	Mn	I	280.106	Ti	II	323.904
Cr	I	357.869	Fe	II	272.754	Mn	II	293.306	Ti	II	324.199
Cr	I	359.349	Fe	II	273.697	Mn	II	293.931	Ti	II	328.766
Cr	I	360.533	Fe	II	273.955	Mn	II	294.921	Ti	II	332.294
Cr	I	425.433	Fe	II	274.320	Mn	II	344.199	Ti	II	333.520
Cr	I	427.480	Fe	II	274.648	Mn	II	346.032	Ti	II	334.036
Cr	I	428.972	Fe	II	274.932	Mn	II	347.413	Ti	II	334.941
Cu	II	221.027	Fe	II	275.329	Mn	II	348.868	Ti	II	336.122
Cu	II	221.810	Fe	II	275.573	Mn	II	349.584	Ti	II	337.280
Cu	II	222.886	Fe	I	295.394	Mn	II	349.753	Ti	II	338.377
Cu	II	224.261	Fe	I	298.357	Mn	I	403.076	Ti	II	338.785
Cu	II	224.700	Fe	II	298.482	Mn	I	403.307	Ti	II	339.458
Cu	II	227.625	Fe	II	298.554	Mn	I	403.449	Ti	II	344.431
Cu	II	229.436	Fe	I	356.537	Mn	I	403.573	Ti	II	350.490
Cu	I	296.116	Fe	I	357.009	Mn	I	404.136	Ti	I	363.546
Cu	I	510.554	Fe	I	358.119	Ni	II	220.672	Ti	I	364.268
Cu	I	578.213	Fe	I	360.885	Ni	II	221.648	Ti	I	365.350
Fe	II	233.131	Fe	I	361.876	Ni	II	227.877	Ti	II	368.520
Fe	II	233.280	Fe	I	363.146	Ni	II	230.300	Ti	II	374.164
Fe	II	233.801	Fe	I	364.784	Ni	II	231.604	Ti	II	375.930
Fe	II	234.349	Fe	I	371.993	Ni	II	239.452	Ti	II	376.132
Fe	II	234.428	Fe	I	373.486	Ni	II	241.613	Ti	II	454.962
Fe	II	234.830	Fe	I	373.713	Ni	I	313.411	Ti	II	457.198
Fe	II	236.483	Fe	I	374.556	Ni	I	338.057	Ti	I	498.173
Fe	II	238.204	Fe	I	374.826	Ni	I	339.299	Ti	I	499.107
Fe	II	238.863	Fe	I	374.948	Ni	I	341.476	Ti	I	499.951
Fe	II	239.563	Fe	I	375.823	Ni	I	343.356	Ti	I	500.721
Fe	II	239.924	Fe	I	376.378	Ni	I	344.626			
Fe	II	240.489	Fe	I	376.719	Ni	I	345.847			
Fe	II	240.666	Fe	I	381.584	Ni	I	346.165			

Table 6-6. List of spectral lines used in the CF-LIBS analysis of Al alloy Z8.

Al	I	231.906	Cu	I	296.116	Fe	II	261.187
Al	I	232.156	Cu	I	301.084	Fe	II	261.382
Al	I	256.798	Cu	I	319.410	Fe	II	261.762
Al	I	265.248	Cu	I	328.271	Fe	II	262.167
Al	I	266.039	Cu	I	329.054	Fe	II	262.567
Al	II	281.619	Cu	I	333.784	Fe	II	262.829
Al	I	305.007	Cu	I	465.112	Fe	II	266.466
Al	I	305.468	Cu	I	510.554	Fe	II	271.441
Al	I	305.714	Cu	I	529.252	Fe	I	272.090
Al	I	306.429	Cu	I	578.213	Fe	II	272.754
Al	I	306.614	Fe	II	233.131	Fe	II	273.697
Al	II	622.621	Fe	II	233.280	Fe	II	273.955
Al	II	623.175	Fe	II	233.801	Fe	II	274.320
Al	II	624.337	Fe	II	234.349	Fe	II	274.648
Cr	II	276.259	Fe	II	234.428	Fe	II	274.932
Cr	II	282.238	Fe	II	234.830	Fe	II	275.329
Cr	II	283.563	Fe	II	238.204	Fe	II	275.573
Cr	II	284.001	Fe	II	238.863	Fe	II	278.369
Cr	II	284.325	Fe	II	239.563	Fe	I	294.787
Cr	II	284.984	Fe	II	239.924	Fe	I	296.689
Cr	II	285.568	Fe	II	240.489	Fe	I	297.313
Cr	II	285.890	Fe	II	240.666	Fe	I	299.442
Cr	II	286.257	Fe	II	241.052	Fe	I	299.951
Cr	II	297.190	Fe	II	241.107	Fe	I	300.094
Cr	II	311.865	Fe	II	241.331	Fe	I	300.814
Cr	II	312.036	Fe	II	243.930	Fe	I	341.313
Cr	II	312.869	Fe	I	247.977	Fe	I	356.537
Cr	II	313.206	Fe	I	248.327	Fe	I	358.119
Cr	II	313.668	Fe	I	248.814	Fe	I	360.885
Cr	I	357.869	Fe	II	249.326	Fe	I	361.876
Cr	I	359.349	Fe	I	251.083	Fe	I	363.146
Cr	I	360.533	Fe	I	252.284	Fe	I	364.784
Cr	I	425.433	Fe	I	252.743	Fe	I	375.823
Cr	I	427.480	Fe	II	253.363	Fe	I	376.378
Cr	I	428.972	Fe	II	253.442	Fe	I	376.719
Cu	II	221.027	Fe	I	253.560	Fe	I	381.584
Cu	II	221.810	Fe	II	253.820	Fe	I	382.042
Cu	II	222.886	Fe	II	253.899	Fe	I	385.991
Cu	II	224.261	Fe	II	256.253	Fe	I	404.581
Cu	II	224.700	Fe	II	256.348	Fe	I	406.359
Cu	II	227.625	Fe	II	258.588	Fe	I	407.173
Cu	II	229.436	Fe	II	259.154	Fe	I	427.175
Cu	II	260.027	Fe	II	259.837	Fe	I	430.790
Cu	I	282.437	Fe	II	260.709	Fe	I	432.576

Table 6-6. Continued.

Fe	I	438.354	Ni	II	231.604	Ti	II	322.860
Fe	I	440.475	Ni	I	232.003	Ti	II	322.860
Mg	I	277.669	Ni	II	233.458	Ti	II	323.452
Mg	I	277.827	Ni	II	239.452	Ti	II	323.658
Mg	I	278.142	Ni	II	241.613	Ti	II	323.904
Mg	I	278.297	Ni	II	243.789	Ti	II	323.966
Mg	II	279.078	Ni	I	300.249	Ti	II	333.520
Mg	II	279.800	Ni	I	300.363	Ti	II	334.036
Mg	I	285.213	Ni	I	301.200	Ti	I	334.188
Mg	II	292.863	Ni	I	313.411	Ti	II	334.941
Mg	II	293.651	Ni	I	338.057	Ti	II	336.122
Mg	I	382.930	Ni	I	339.105	Ti	II	337.280
Mg	I	383.230	Ni	I	339.299	Ti	II	338.377
Mg	I	383.829	Ni	I	341.476	Ti	II	338.785
Mg	I	516.733	Ni	I	343.356	Ti	II	344.431
Mg	I	517.268	Ni	I	344.626	Ti	II	350.490
Mg	I	518.361	Ni	I	345.847	Ti	II	362.482
Mn	II	257.610	Ni	I	346.165	Ti	I	363.546
Mn	II	259.373	Ni	I	349.296	Ti	II	364.133
Mn	II	260.569	Ni	I	351.505	Ti	I	364.268
Mn	II	261.020	Ni	I	352.454	Ti	I	365.350
Mn	II	261.814	Ni	I	356.637	Ti	II	368.520
Mn	II	293.305	Ni	I	361.939	Ti	II	374.164
Mn	II	293.931	Si	I	250.690	Ti	II	375.930
Mn	II	294.921	Si	I	251.432	Ti	II	376.132
Mn	I	322.809	Si	I	251.611	Ti	II	390.055
Mn	II	344.199	Si	I	251.920	Ti	II	391.347
Mn	II	346.032	Si	I	252.411	Ti	I	398.176
Mn	II	349.584	Si	I	252.851	Ti	I	398.976
Mn	II	349.753	Si	I	288.158	Ti	I	399.864
Mn	I	380.672	Si	II	385.602	Ti	II	429.410
Mn	I	403.076	Si	I	390.552	Ti	II	430.005
Mn	I	403.307	Si	II	412.805	Ti	II	439.503
Mn	I	403.449	Ti	II	315.226	Ti	II	444.379
Mn	I	403.573	Ti	II	315.421	Ti	II	446.850
Mn	I	404.136	Ti	II	315.568	Ti	II	450.127
Mn	I	404.876	Ti	II	316.122	Ti	II	454.962
Ni	II	220.672	Ti	II	316.177	Ti	II	457.198
Ni	II	221.648	Ti	II	316.257	Ti	I	498.173
Ni	II	222.296	Ti	II	316.853	Ti	I	499.107
Ni	II	226.446	Ti	II	319.088	Ti	I	499.951
Ni	II	227.021	Ti	II	320.254	Ti	I	500.721
Ni	II	227.877	Ti	II	321.706			
Ni	II	230.300	Ti	II	322.284			

Table 6-7. List of spectral lines used in the Monte Carlo LIBS simulations.

	Wavelength (nm)	Lower energy level (cm^{-1})	Upper energy level (cm^{-1})	Absorption oscillator strength, f	g_i	g_k
Al I	308.2151	0	32435	0.18	2	4
Al I	309.2708	112	32437	0.16	4	6
Al II	281.6185	59852	95351	0.15	3	1
Cu I	324.7540	0	30784	0.439	2	4
Cu I	327.3960	0	30535	0.22	2	2
Fe I	278.8105	6928	42784	0.087	11	13
Fe II	273.9548	7955	44447	0.217	8	8
Fe II	274.3197	8847	45290	0.406	2	4
Fe II	274.6484	8680	45080	0.33	4	6
Fe II	274.9321	8392	44754	0.318	6	8
Fe II	275.3288	26353	62662	0.162	10	12
Fe II	275.5737	7955	44233	0.3	8	10
Mg I	285.2126	0	35051	1.81	1	3
Mg II	279.0777	35669	71491	0.92	2	4
Mg II	279.5528	0	35761	0.627	2	4
Mg II	279.7998	35761	71490	0.828	4	6
Mg II	280.2705	0	35669	0.313	2	2
Mn I	280.1081	0	35690	0.29	6	4
Mn II	293.3055	9473	43557	0.15	5	3
Mn II	293.9308	9473	43485	0.25	5	5
Mn II	294.9200	9473	43371	0.35	5	7
Si I	288.1577	6299	40992	0.14	5	3
Zn I*	328.2328	32311	62769	0.44	1	3
Zn I*	330.2584	32501	62772	0.33	3	5

*Only used for Al alloys S4 and SM10.

Table 6-8. Electron number density (in cm^{-3}) and temperature (in K) values calculated using MC-LIBS and CF-LIBS for 6 Al alloy standards.

Al alloy sample	Electron number density, n_e ($\times 10^{16}$ cm^{-3})				Temperature, T ($\times 10^4$ K)			
	MC-LIBS*		CF-LIBS		MC-LIBS*		CF-LIBS	
B8	7.58	± 7.56	1.22	± 0.02	1.0	± 0.6	1.09	± 0.06
D33	6.52	± 6.55	1.33	± 0.02	1.0	± 0.5	1.09	± 0.07
S4	8.46	± 8.49	1.35	± 0.02	1.0	± 0.6	0.99	± 0.07
SM10	4.40	± 4.41	1.40	± 0.02	1.0	± 0.5	0.98	± 0.04
V14	6.01	± 5.98	1.47	± 0.02	1.0	± 0.5	1.10	± 0.05
Z8	4.06	± 4.02	1.20	± 0.02	0.9	± 0.5	1.06	± 0.07

*The temperature and electron number density reported is the average of temperatures at different spatial points.

Table 6-9. Relative concentration values and relative errors (in %) calculated from CF-LIBS analysis of aluminum alloys B8 and D33.

Element	Al alloy B8			Al alloy D33		
	Certified	CF-LIBS	Relative error	Certified	CF-LIBS	Relative error
Al	88.8095	89.7	1.0	86.1782	86.1	0.1
Cr	0.1716	0.02	86.2	0.04770	0.005	89.5
Cu	7.0155	6.8	2.4	2.9328	2.4	19.7
Fe	0.8075	0.1	84.1	1.1670	0.2	80.0
Mg	0.0767	0.009	88.5	0.0386	0.006	83.4
Mn	0.4038	0.03	92.3	0.4059	0.03	93.3
Ni	0.2019	0.2	1.7	0.5074	0.7	29.2
Si	2.3520	3.0	29.6	8.6665	10.6	22.4
Ti	0.1615	0.01	92.9	0.0558	0.004	92.1

Table 6-10. Relative concentration values and relative errors (in %) calculated from CF-LIBS analysis of aluminum alloys S4 and SM10.

Element	Al alloy S4			Al alloy SM10		
	Certified	CF-LIBS	Relative error	Certified	CF-LIBS	Relative error
Al	84.0937	84.2	0.2	85.0998	87.0	2.2
Cr	0.1305	0.005	96.2	0.2010	0.01	95.3
Cu	2.6495	1.7	36.1	2.8142	2.4	13.7
Fe	0.1194	0.05	54.9	1.9700	0.1	95.1
Mg	0.3513	0.03	93.0	1.0855	0.2	77.8
Mn	0.3814	0.009	97.6	0.2965	0.006	97.9
Ni	0.1807	0.01	92.1	0.0653	0.04	33.1
Si	1.0337	1.0	3.4	2.9348	2.5	16.5
Ti	0.1204	0.003	97.9	0.0553	0.001	97.8
Zn	10.9394	13.0	18.4	5.4777	7.8	41.9

Table 6-11. Relative concentration values and relative errors (in %) calculated from CF-LIBS analysis of aluminum alloys V14 and Z8.

Element	Al alloy V14			Al alloy Z8		
	Certified	CF-LIBS	Relative error	Certified	CF-LIBS	Relative error
Al	87.4618	87.6	0.1	79.4669	81.6	2.6
Cr	0.1815	0.02	88.0	0.1513	0.02	87.1
Cu	4.0836	5.2	26.4	16.1865	16.4	1.4
Fe	0.9075	0.2	73.2	1.0993	0.2	82.0
Mg	0.0252	0.003	87.7	1.2808	0.3	79.5
Mn	0.5848	0.06	89.8	0.2622	0.03	88.3
Ni	0.3327	0.3	3.4	0.5345	0.3	41.6
Si	6.2514	6.6	5.4	0.8471	1.2	41.4
Ti	0.1714	0.01	91.7	0.1714	0.01	93.8

Table 6-12. Number densities (in cm^{-3}) calculated from MC-LIBS analysis of six different aluminum alloys.

Element	Alloy B8	Alloy D33	Alloy S4	Alloy SM10	Alloy V14	Alloy Z8
Al	2.35×10^{17}	1.73×10^{17}	2.53×10^{17}	1.23×10^{17}	1.83×10^{17}	1.35×10^{17}
Cu	4.28×10^{15}	1.46×10^{15}	2.57×10^{15}	4.45×10^{15}	1.84×10^{15}	3.82×10^{15}
Fe	5.83×10^{14}	7.67×10^{14}	6.39×10^{14}	6.42×10^{14}	8.62×10^{14}	6.10×10^{14}
Mg	8.98×10^{13}	4.26×10^{13}	1.26×10^{15}	5.8×10^{15}	1.42×10^{13}	6.37×10^{15}
Mn	2.82×10^{14}	2.89×10^{14}	4.84×10^{14}	7.29×10^{13}	3.94×10^{14}	1.24×10^{14}
Si	3.42×10^{16}	6.83×10^{16}	1.16×10^{16}	7.55×10^{15}	4.46×10^{16}	2.83×10^{15}
Zn			5.01×10^{16}	1.52×10^{16}		

Table 6-13. Relative concentration values and relative errors (in %) calculated from MC-LIBS and CF-LIBS analysis of Al alloy B8.

Element	Relative concentration			Relative error	
	Certified	MC-LIBS	CF-LIBS	MC-LIBS	CF-LIBS
Al	89.2872	83.1	89.4	6.9	0.2
Cu	7.0533	3.6	7.3	49.0	3.1
Fe	0.8119	0.4	0.1	50.7	82.8
Mg	0.0771	0.03	0.009	61.1	87.8
Mn	0.4060	0.2	0.03	50.7	91.5
Si	2.3646	12.6	3.1	432.9	31.4

Table 6-14. Relative concentration values and relative errors (in %) calculated from MC-LIBS and CF-LIBS analysis of Al alloy D33.

Element	Relative concentration			Relative error	
	Certified	MC-LIBS	CF-LIBS	MC-LIBS	CF-LIBS
Al	86.7080	69.3	85.0	20.1	2.0
Cu	2.9508	1.4	3.1	53.1	5.3
Fe	1.1742	0.6	0.4	45.9	69.7
Mg	0.0388	0.02	0.009	60.3	77.6
Mn	0.4084	0.2	0.04	42.4	89.4
Si	8.7198	28.4	11.5	226.2	31.7

Table 6-15. Relative concentration values and relative errors (in %) calculated from MC-LIBS and CF-LIBS analysis of Al alloy S4.

Element	Relative concentration			Relative error	
	Certified	MC-LIBS	CF-LIBS	MC-LIBS	CF-LIBS
Al	84.4582	88.2	81.1	4.4	4.0
Cu	2.6610	2.1	2.7	20.3	1.7
Fe	0.1200	0.5	0.1	285.1	7.4
Mg	0.3528	0.4	0.04	12.2	88.3
Mn	0.3830	0.3	0.02	10.1	94.8
Si	1.0382	4.2	1.2	305.8	16.9
Zn	10.9868	4.3	14.8	61.3	35.0

Table 6-16. Relative concentration values and relative errors (in %) calculated from MC-LIBS and CF-LIBS analysis of Al alloy SM10.

Element	Relative concentration			Relative error	
	Certified	MC-LIBS	CF-LIBS	MC-LIBS	CF-LIBS
Al	85.3743	81.0	84.6	5.1	0.9
Cu	2.8233	7.0	3.3	146.4	15.9
Fe	1.9763	0.9	0.2	55.6	91.9
Mg	1.0890	3.5	0.2	217.1	82.6
Mn	0.2975	0.1	0.01	67.0	96.4
Si	2.9443	5.2	2.5	76.3	14.3
Zn	5.4953	2.4	9.3	55.6	68.4

Table 6-17. Relative concentration values and relative errors (in %) calculated from MC-LIBS and CF-LIBS analysis of Al alloy V14.

Element	Relative concentration			Relative error	
	Certified	MC-LIBS	CF-LIBS	MC-LIBS	CF-LIBS
Al	88.0656	77.5	87.2	12.0	1.0
Cu	4.1118	1.8	5.7	55.3	38.0
Fe	0.9137	0.8	0.3	17.6	69.4
Mg	0.0254	0.005	0.003	78.7	86.6
Mn	0.5889	0.3	0.07	42.5	88.1
Si	6.2946	19.6	6.8	211.2	7.4

Table 6-18. Relative concentration values and relative errors (in %) calculated from MC-LIBS and CF-LIBS analysis of Al alloy Z8.

Element	Relative concentration			Relative error	
	Certified	MC-LIBS	CF-LIBS	MC-LIBS	CF-LIBS
Al	80.1540	87.5	80.5	9.2	0.5
Cu	16.3264	5.9	17.7	64.0	8.7
Fe	1.1088	0.8	0.2	26.0	79.8
Mg	1.2919	3.7	0.3	188.8	78.6
Mn	0.2645	0.2	0.09	38.0	66.7
Si	0.8545	1.9	1.1	123.9	34.2

Table 6-19. Atomic masses (in g) of different elements in the aluminum alloy sample.

Element	Mass ($\times 10^{-23}$ g)
Mg	4.04
Al	4.48
Si	4.66
Ti	7.95
Cr	8.64
Mn	9.12
Fe	9.27
Ni	9.75
Cu	10.55

Table 6-20. Electron number density (in cm^{-3}) and temperature (in K) values calculated using MC-LIBS and CF-LIBS for Al alloy standard D33 at different spatial positions.

Spatial position	Electron number density, n_e ($\times 10^{16}$ cm^{-3})			Temperature, T ($\times 10^4$ K)		
	MC-LIBS		CF-LIBS	MC-LIBS		CF-LIBS
A	0.8	± 0.6	1.09	0.5	± 0.2	1.2
B	4.7	± 1.4	1.89	1.0	± 0.1	1.2
C	12.0	± 2.0	1.89	1.33	± 0.09	1.1
D	9.5	± 0.8	1.98	1.29	± 0.05	1.2
E	25.9	± 1.0	1.96	1.43	± 0.03	1.2
F	23.8	± 0.1	1.89	1.27	± 0.01	1.1
G	24.1	± 0.6	2.10	1.09	± 0.02	1.1
H	16.9	± 1.6	1.65	0.96	± 0.03	0.9
I	9.8	± 1.9	1.12	0.91	± 0.06	0.9
J	8.8	± 2.7		0.8	± 0.1	
K	2.5	± 2.0		0.5	± 0.2	

Table 6-21. Sigmoidal fitting parameters for the spatial evolution of temperature. (Equation: $y = A_2 + (A_1 - A_2) / (1 + \exp((x-x_0)/dx))$.

Spatial position	A_1 (K)	A_2 (K)	x_0	dx
A	18894.10	-13896.93	0.93	0.26
B	19196.56	-14126.06	0.93	0.27
C	19163.45	-14101.23	0.93	0.27
D	15590.02	-11471.51	0.93	0.27
E	15821.39	-11640.55	0.93	0.27
F	13490.44	-9926.33	0.93	0.27
G	12017.23	-8842.37	0.93	0.27
H	11688.34	-8599.35	0.93	0.27
I	13061.62	-9610.13	0.93	0.27
J	16371.27	-12047.07	0.93	0.27
K	19147.64	-14088.17	0.93	0.27

Table 6-22. Sigmoidal fitting parameters for the spatial evolution of electron number density. (Equation: $y = A_2 + (A_1 - A_2) / (1 + \exp((x-x_0)/dx))$.

Spatial position	A_1 ($\times 10^{17}$ cm^{-3})	A_2 ($\times 10^{16}$ cm^{-3})	x_0	dx
A	1.92	-1.93	0.52	0.18
B	2.25	-2.23	0.52	0.18
C	2.67	-2.67	0.52	0.18
D	1.40	-2.18	0.54	0.20
E	2.98	-3.99	0.54	0.18
F	2.45	-2.01	0.54	0.14
G	2.57	-1.34	0.51	0.12
H	2.18	-1.04	0.50	0.12
I	1.87	-1.46	0.55	0.13
J	4.06	-5.86	0.50	0.20
K	6.00	-7.05	0.52	0.19

Table 6-23. Relative concentration values (in %) calculated from CF-LIBS analysis of aluminum alloys D33 at different spatial positions.

	Al	Cr	Cu	Fe	Mg	Mn	Ni	Si	Ti
Certified	86.1782	0.0477	2.9328	1.167	0.0386	0.4059	0.5074	8.6665	0.0558
A	89.6	0.01	2.1	1.0	0.02	0.07	1.4	5.7	0.004
B	86.6	0.03	1.9	1.0	0.03	0.1	1.4	8.9	0.005
C	87.2	0.03	1.3	0.7	0.03	0.08	1.6	9.0	0.004
D	84.7	0.03	3.3	0.8	0.04	0.09	1.0	9.9	0.007
E	85.7	0.04	1.8	0.5	0.04	0.09	0.6	11.3	0.009
F	86.3	0.02	1.1	0.2	0.04	0.07	0.2	12.1	0.007
G	86.6	0.02	0.7	0.1	0.02	0.06	0.2	12.3	0.006
H	93.8	0.0003	0.1	0.009	0.004	0.004	0.01	6.0	0.0008
I	93.3	0.0005	0.06	0.004	0.001	0.002	0.007	6.62	0.0007

Table 6-24. Relative errors (in %) of calculated CF-LIBS concentration values at different spatial positions.

	Al	Cr	Cu	Fe	Mg	Mn	Ni	Si	Ti
A	4.0	74.4	27.0	10.2	41.2	82.3	182.3	34.5	92.8
B	0.5	48.4	35.3	13.2	12.7	76.2	181.2	2.4	91.4
C	1.2	40.9	54.8	39.6	15.5	80.4	218.8	4.2	93.2
D	1.7	42.3	12.4	28.6	2.6	77.7	103.2	14.6	88.2
E	0.5	9.2	40.2	59.7	1.3	77.2	16.8	30.3	84.8
F	0.1	52.4	61.1	83.9	1.0	82.1	66.9	39.4	87.5
G	0.5	62.7	77.3	90.7	50.0	84.9	63.1	42.0	90.0
H	8.9	99.4	95.2	99.2	89.9	99.0	97.2	30.6	98.6
I	8.2	99.0	97.9	99.7	96.4	99.6	98.6	23.4	98.7

Table 6-25. Relative concentration values, relative errors (in %) and number densities (in cm^{-3}) calculated from MC-LIBS and CF-LIBS analysis of Al alloy D33 at spatial position A.

	Relative concentration			Relative error		Number density (cm^{-3})
	Certified	MC-LIBS	CF-LIBS	MC-LIBS	CF-LIBS	MC-LIBS
Al	86.7080	93.2	90.9	7.5	4.8	2.76×10^{17}
Cu	2.9508	2.1	2.2	29.9	26.4	2.59×10^{15}
Fe	1.1742	1.8	1.1	57.1	9.4	2.64×10^{15}
Mg	0.0388	0.03	0.02	19.3	40.6	1.03×10^{14}
Mn	0.4084	0.3	0.07	21.7	82.2	4.65×10^{14}
Si	8.7198	2.5	5.8	71.4	33.9	7.08×10^{15}

Table 6-26. Relative concentration values, relative errors (in %) and number densities (in cm^{-3}) calculated from MC-LIBS and CF-LIBS analysis of Al alloy D33 at spatial position B.

	Relative concentration			Relative error		Number density (cm^{-3})
	Certified	MC-LIBS	CF-LIBS	MC-LIBS	CF-LIBS	MC-LIBS
Al	86.7080	89.7	87.9	3.4	1.4	3.16×10^{17}
Cu	2.9508	4.8	1.9	61.1	34.7	7.08×10^{15}
Fe	1.1742	1.6	1.03	32.9	12.4	2.66×10^{15}
Mg	0.0388	0.04	0.03	1.8	11.9	1.54×10^{14}
Mn	0.4084	0.4	0.1	5.8	76.0	7.48×10^{14}
Si	8.7198	3.5	9.0	59.3	3.3	1.20×10^{16}

Table 6-27. Relative concentration values, relative errors (in %) and number densities (in cm^{-3}) calculated from MC-LIBS and CF-LIBS analysis of Al alloy D33 at spatial position C.

	Relative concentration			Relative error		Number density (cm^{-3})
	Certified	MC-LIBS	CF-LIBS	MC-LIBS	CF-LIBS	MC-LIBS
Al	86.7080	81.0	88.6	6.6	2.2	3.46×10^{17}
Cu	2.9508	1.6	1.3	47.2	54.3	2.81×10^{15}
Fe	1.1742	1.8	0.7	49.3	39.0	3.62×10^{15}
Mg	0.0388	0.04	0.03	6.2	14.7	1.95×10^{14}
Mn	0.4084	0.8	0.08	89.4	80.2	1.62×10^{15}
Si	8.7198	14.8	9.2	70.2	5.3	6.10×10^{16}

Table 6-28. Relative concentration values, relative errors (in %) and number densities (in cm^{-3}) calculated from MC-LIBS and CF-LIBS analysis of Al alloy D33 at spatial position D.

	Relative concentration			Relative error		Number density (cm^{-3})
	Certified	MC-LIBS	CF-LIBS	MC-LIBS	CF-LIBS	MC-LIBS
Al	86.7080	75.4	85.7	13.1	1.2	2.10×10^{17}
Cu	2.9508	0.9	3.3	67.9	12.9	1.11×10^{15}
Fe	1.1742	0.9	0.8	20.1	28.3	1.26×10^{15}
Mg	0.0388	0.04	0.04	7.5	3.1	1.11×10^{14}
Mn	0.4084	0.5	0.09	20.7	77.6	6.74×10^{14}
Si	8.7198	22.2	10.0	154.6	15.2	5.94×10^{16}

Table 6-29. Relative concentration values, relative errors (in %) and number densities (in cm^{-3}) calculated from MC-LIBS and CF-LIBS analysis of Al alloy D33 at spatial position E.

	Relative concentration			Relative error		Number density (cm^{-3})
	Certified	MC-LIBS	CF-LIBS	MC-LIBS	CF-LIBS	MC-LIBS
Al	86.7080	66.9	86.3	22.8	0.5	4.55×10^{17}
Cu	2.9508	2.0	1.8	30.9	40.2	5.87×10^{15}
Fe	1.1742	1.2	0.5	3.1	59.7	3.98×10^{15}
Mg	0.0388	0.05	0.04	34.5	1.5	3.94×10^{14}
Mn	0.4084	0.7	0.09	66.8	77.2	2.28×10^{15}
Si	8.7198	29.1	11.4	233.7	30.3	1.90×10^{17}

Table 6-30. Relative concentration values, relative errors (in %) and number densities (in cm^{-3}) calculated from MC-LIBS and CF-LIBS analysis of Al alloy D33 at spatial position F.

	Relative concentration			Relative error		Number density (cm^{-3})
	Certified	MC-LIBS	CF-LIBS	MC-LIBS	CF-LIBS	MC-LIBS
Al	86.7080	73.3	86.5	15.4	0.3	5.24×10^{17}
Cu	2.9508	1.4	1.1	53.9	61.2	4.11×10^{15}
Fe	1.1742	1.0	0.2	11.9	83.9	3.57×10^{15}
Mg	0.0388	0.04	0.04	11.9	0.8	3.44×10^{14}
Mn	0.4084	0.7	0.07	79.8	82.2	2.58×10^{15}
Si	8.7198	23.5	12.1	169.3	38.8	1.61×10^{17}

Table 6-31. Relative concentration values, relative errors (in %) and number densities (in cm^{-3}) calculated from MC-LIBS and CF-LIBS analysis of Al alloy D33 at spatial position G.

	Relative concentration			Relative error		Number density (cm^{-3})
	Certified	MC-LIBS	CF-LIBS	MC-LIBS	CF-LIBS	MC-LIBS
Al	86.7080	74.4	86.8	14.2	0.1	6.32×10^{17}
Cu	2.9508	2.3	0.7	23.7	77.4	8.08×10^{15}
Fe	1.1742	0.8	0.1	30.4	90.8	3.35×10^{15}
Mg	0.0388	0.03	0.02	11.6	50.3	3.23×10^{14}
Mn	0.4084	0.7	0.06	64.5	84.9	2.80×10^{15}
Si	8.7198	21.8	12.3	150.2	41.4	1.78×10^{17}

Table 6-32. Relative concentration values, relative errors (in %) and number densities (in cm^{-3}) calculated from MC-LIBS and CF-LIBS analysis of Al alloy D33 at spatial position H.

	Relative concentration			Relative error		Number density (cm^{-3})
	Certified	MC-LIBS	CF-LIBS	MC-LIBS	CF-LIBS	MC-LIBS
Al	86.7080	67.3	93.8	22.4	8.2	5.00×10^{17}
Cu	2.9508	5.8	0.1	97.7	95.2	1.83×10^{16}
Fe	1.1742	0.4	0.009	65.0	99.2	1.48×10^{15}
Mg	0.0388	0.02	0.004	42.3	89.9	1.85×10^{14}
Mn	0.4084	0.6	0.004	43.0	99.0	2.13×10^{15}
Si	8.7198	25.9	6.0	196.8	31.0	1.85×10^{17}

Table 6-33. Relative concentration values, relative errors (in %) and number densities (in cm^{-3}) calculated from MC-LIBS and CF-LIBS analysis of Al alloy D33 at spatial position I.

	Relative concentration			Relative error		Number density (cm^{-3})
	Certified	MC-LIBS	CF-LIBS	MC-LIBS	CF-LIBS	MC-LIBS
Al	86.7080	74.1	93.3	14.6	7.6	4.34×10^{17}
Cu	2.9508	17.9	0.06	506.3	97.9	4.43×10^{16}
Fe	1.1742	0.3	0.004	74.4	99.7	8.49×10^{14}
Mg	0.0388	0.01	0.001	71.1	96.4	7.26×10^{13}
Mn	0.4084	0.3	0.002	30.9	99.6	8.12×10^{14}
Si	8.7198	7.5	6.6	14.5	23.8	4.20×10^{16}

Table 6-34. Relative concentration values, relative errors (in %) and number densities (in cm^{-3}) calculated from MC-LIBS and CF-LIBS analysis of Al alloy D33 at spatial position J.

	Certified	Relative concentration	Relative error	Number density (cm^{-3})
Al	86.7080	59.4	31.5	2.69×10^{17}
Cu	2.9508	29.2	890.8	5.60×10^{16}
Fe	1.1742	1.2	0.1	2.57×10^{15}
Mg	0.0388	0.04	9.6	1.76×10^{14}
Mn	0.4084	0.4	9.6	9.96×10^{14}
Si	8.7198	9.7	11.0	4.21×10^{16}

Table 6-35. Relative concentration values, relative errors (in %) and number densities (in cm^{-3}) calculated from MC-LIBS analysis of Al alloy D33 at spatial position K.

	Certified	Relative concentration	Relative error	Number density (cm^{-3})
Al	86.7080	91.6	5.6	9.75×10^{17}
Cu	2.9508	4.5	52.6	2.03×10^{16}
Fe	1.1742	0.3	71.9	1.69×10^{15}
Mg	0.0388	0.02	51.5	2.21×10^{14}
Mn	0.4084	0.2	58.8	8.81×10^{14}
Si	8.7198	3.4	61.1	3.47×10^{16}

CHAPTER 7
SEMI-QUANTITATIVE ANALYSIS OF DIFFERENT SAMPLES BY CALIBRATION-FREE LASER-INDUCED BREAKDOWN SPECTROSCOPY

Introduction

Since its inception, the calibration-free laser-induced breakdown spectroscopy (CF-LIBS) approach has been applied by several research groups to the analysis of different types of samples of varying degrees of complexities. One of the first applications of the CF-LIBS technique was on the analysis of aluminum alloys and ambient air [55, 56]. Ciucci et al. [55, 56] reported excellent agreement between the nominal composition of the untreated metallic alloy and CF-LIBS results. Moreover, all the elements in the alloy were detected and quantitatively determined in a wide dynamic range from 250 ppm Cu up to 96% Al. In the CF-LIBS analysis of ambient air, the results reported for Ar, C, N, O and H were also in good agreement with standard atmospheric composition data.

CF-LIBS has also been applied in the field of cultural heritage conservation where the samples are very precious, irreplaceable and have to be analyzed in situ and in a non-destructive manner. Borgia et al. [189] obtained quantitative stratigraphic results in the analysis of ancient Roman fresco samples. Two iron-based fresco fragments were analyzed and results showed that although the spectra are similar qualitatively, the pigments can be differentiated quantitatively. Stratigraphic analysis also shows the variation in elemental composition for each layer of sample probed by a single laser shot. The CF-LIBS approach demonstrated, in this case, the feasibility of its use in real-time for in situ stratigraphic analysis of pigment composition without substrate contamination or destruction.

Corsi et al. [190] demonstrated the applicability of CF-LIBS in the determination of caratage of precious ternary and quaternary alloys. The errors reported on the concentration values calculated with CF-LIBS were below 1%. Four hypothetical calibration curves were also

constructed using neutral Au lines at 267.5 nm, 274.8 nm, 312.2 nm and 627.8 nm but the experimental data were highly scattered which led the authors to conclude that CF-LIBS in this case is evidently superior compared to conventional calibration methods since large dispersion in calibration points greatly affects the precision and accuracy of calculated elemental composition. In addition, the LIBS signal corresponding to the same gold caratage for ternary and quaternary alloys did not coincide at all in the calibration plots constructed which demonstrates that calibration curves for gold caratage determination are highly affected by matrix effects.

The CF-LIBS protocol has also been applied to continuous in situ monitoring of metal smoke emissions from industrial plants [191]. A micro-plasma was generated in a flue duct of a 150 MW oil-fired power plant and the spectra taken showed elemental emissions from Ni, V, Ti, Mg, Fe, etc. The results obtained with CF-LIBS were confirmed by analyzing a sample of combustion products with ICP-MS.

Corsi et al. [192] also studied the feasibility of the CF-LIBS technique for hair tissue mineral analysis (HTMA) which is a useful medical diagnostic tool for detecting mineral deficiencies or imbalances in patients. CF-LIBS allowed for the measurement of relative concentrations of Mg, K, Ca, Na, and Al at the level of few milligrams per 100 grams of sample and the determination of their ratios. Although the potential of CF-LIBS for hair analysis was not fully exploited in this work, the authors concluded that the advantage provided by CF-LIBS in alleviating the requirement for reference standards and calibration curves is the most crucial part due to the high variability of different hair types.

Colao et al. [193] attempted to quantitatively determine the elemental composition of ancient Roman bronze coins. However, because of the intrinsic difficulties related to the quantitative analysis of Cu based alloys due to large differences in the physical properties of

metal constituents, the authors proposed two data reduction algorithms, one was based on the calibration-free approach and the other on calibration curves. The authors modified the CF-LIBS approach by considering that the plasma was a super-position of two non- or weakly interacting plumes described by two temperatures to account for inhomogeneity. Two normalization procedures were also used in the calibration method to minimize statistical fluctuations in both background level and spectrum intensity. The authors reported that there was only a partial agreement between the CF-LIBS and calibration results for the bronze coins due to possible inhomogeneity in the coin alloy, surface oxidation and preferential evaporation.

Burakov and Raikov [194] carried out a quantitative determination of different samples of bronze, brass and gold alloys, and glass samples using the calibration-free technique. A close agreement between CF-LIBS results and reference data was demonstrated for most of the constituents in the analyzed samples. The authors also reported that absolute errors in the determined concentration values were generally larger for the glass samples compared to the metal alloys which they attributed to the higher transparency and melting temperatures of glass targets, as well as the lower efficiency of the laser-to-sample interaction. They also investigated the effect of uncertainties in temperature determinations on CF-LIBS quantitative results and found out that in order to achieve accuracy better than 1% for elemental concentration, the precision of temperature measurements must also be better than 1%.

The main objective of this study is the further evaluation of CF-LIBS under various experimental working conditions using the spectral acquisition method described in Chapter 4. The capabilities and limitations of laser-induced breakdown spectroscopy as a calibration-free approach are investigated by analyzing different samples of metallic alloys (Al, Ti, Cu, Zn, Ni) and soil samples.

Experimental

The experimental system and spectral data acquisition used in all measurements have already been described in detail in Chapter 4. The schematic of the set-up is illustrated in Fig. 4-1 for experiments under atmospheric conditions and in Fig. 4-3 for vacuum measurements. The samples used in this study were aluminum alloy standard disks (B8, D33, S4, SM10, V14 and Z8) from APEX Smelter Co. in South Africa, standard reference materials of Zn alloy (SRM 627 and 629), Cu-Ni alloy (SRM 1276a), Ti alloy (SRM 654b), Ni alloy powder (SRM 882), Cu-Zn alloy (SRM 1107, 1108, 1110 to 1117) and soil (SRM 1646, 2704, 2710 and 2711) from NIST, Ti alloy powder (SRM 88395) from Alfa Aesar and soil standards (CAN SO-2 and SO-3) from Canadian Certified Reference Materials Project. The elemental compositions are given in Appendix E.

The alloys in powder form were mixed in a 1:4 ratio with Licowax C micropowder amide binder (Clariant). The mixing was accomplished by ball milling each sample for 20 minutes in a mixer (8000M; SPEX SamplePrep) to ensure that the samples are homogeneously mixed. All samples in powder form were placed in aluminum sample discs (Spec-Cap 3619; SPEX SamplePrep) and pressed into pellets using a manual hydraulic steel pump (P-39, Enerpac) under a pressure of 5000 psi. The size of the resulting pellet was 31 mm in diameter and 5 mm in thickness. The pellets that were prepared were stored in a desiccator to prevent surface contamination and minimize moisture absorption.

Spectra from 10 laser shots were summed up using the accumulation mode that is incorporated in the WinSpec32 software (Version 2.5.18.2; Princeton Instruments). A total of 67 spectral windows between 220 and 700 nm were recorded and each region was measured in 3 consecutive runs. Each set of recorded laser-induced breakdown spectra were merged together using an in-house program written in Q-Basic. The set of 3 merged spectra were subsequently

averaged and the resulting spectrum was corrected for background and relative detector spectral efficiency using in-house programs written in MATLAB.

Imaging of the laser-induced plasmas were also carried out prior to LIBS measurements to determine the size of the plasma in the axial direction (laser beam axis) since it is the full plasma height that dictates the number of vertical pixels to be included in the binning process. The plasma image was recorded by setting the diffraction grating to zero order (mirror reflection) and opening the entrance slit of the spectrometer close to its maximum width (3 mm).

Results and Discussion

Temporally-Resolved Analysis of Aluminum Alloys

The wide wavelength range spectra from 220 to 700 nm of two aluminum alloy samples, B8 and SM10, were recorded at different delay times starting from 0.5 μs until 3.0 μs at a gate width of 0.5 μs. The experiments were carried out under a pressure of 100 mbar. A small section of the wide spectral range data for each delay time are shown in Fig. 7-1a and 7-1b for Al alloy B8 and SM10, respectively, which contains singly-ionized lines of Mg and Al. As expected, the continuum radiation and line intensities decrease as the plasma evolves.

In addition, the number of neutral and singly-ionized lines for every element identified in Al alloy B8 and Al alloy SM10 are plotted against delay time as well as the total number of neutral and ionic lines (Figs. 7-2a and 7-2b). It can be observed that the number of neutral lines (blue squares) increase at longer delays while the number of singly-ionized lines (red circles) generally decrease as the delay time is increased. This is, of course, due to electron-ion radiative recombination which occurs when an ion captures an electron and causes a radiative transition to a bound state, a so-called free-bound transition, as the plasma expands and evolves in time.

The corresponding images of the laser-induced plasma obtained at different delay times were recorded for the two samples analyzed and are shown in Fig. 7-3. The plasma size is about 2.5 cm in diameter and the symmetry is approximately spherical at all conditions considered. By vertically binning the pixels over the full height of the plasma, approximately 120 pixels, the values calculated for electron number density and temperature are regarded as spatially-averaged since spatial information is lost when applying the CCD pixel binning clocking scheme. It can also be observed from Fig. 7-3 that the plasma moves away from the sample surface as the plasma expands and evolves with time. According to Wen et al. [95], this phenomenon is due to the vortex ring which is formed immediately after the internal shockwave reaches the sample surface which then causes the vapor plume to be propelled away from the target.

The electron number density was determined using the Stark width of the hydrogen-alpha (Hα) line at 656.272 nm. The equation used in the calculation is given in Eq. 5-19. The temporal evolution of the Hα line and the calculated electron number densities for the alloys B8 and SM10 are shown in Figs. 7-4a and 7-4b, respectively. For Al alloy B8, the electron number density values ranged from $3.6 \pm 0.1 \times 10^{17}$ cm^{-3} to $0.37 \pm 0.02 \times 10^{17}$ cm^{-3} and for Al alloy SM10, the electron number densities are between $2.7 \pm 0.2 \times 10^{17}$ cm^{-3} and $0.32 \pm 0.02 \times 10^{17}$ cm^{-3}. The minimum value for electron number density in order to satisfy local thermodynamic equilibrium (LTE) conditions were also calculated using Eq. 5-3 and are plotted against the delay time (blue squares). It is apparent that at delays longer than 2.0 μs, the minimum criterion is not reached in both samples. The calculated temperature and electron number density values for alloys B8 and SM10 are also summarized in Tables 7-1 and 7-2, respectively. The precision of the calculated electron number densities using the Hα approach is 8% or better depending on the

delay time, which is within the typical uncertainties (~10%) associated with the use of the Hα line for electron number density measurements [138].

The temperature of the plasma was determined using the Saha-Boltzmann plot approach described in Chapter 5 and the plots for selected elements in samples B8 and SM10 at different delay times are shown in Figs. 7-5a and 7-5b, respectively. The parallelity of the slopes obtained for different elements at the delay times considered in this study is a satisfactory demonstration of the existence of local thermodynamic equilibrium. The goodness of the agreement between temperature values obtained for the different sample constituents also verifies, to some extent, the gross effect of any shot-to-shot variability of the laser pulse which in this case is not as severe regardless of the fact that multiple acquisitions have to be carried out in order to obtain spectral information from 220 to 700 nm for a single measurement. The temperature values (in eV) calculated from the slope of the Saha-Boltzmann plots for each constituent of the sample are also plotted against the delay time and are shown in Figs. 7-6a and 7-6b for alloys B8 and SM10, respectively. For all elements considered, the temperature decreases as the plasma expands and evolves in time. The temporal evolution of the averaged temperatures (in K) with the corresponding error bars are shown in Figs. 7-7a and 7-7b. The error bars were obtained by averaging the temperature values calculated from the atomic constituents of the target. The highest RSD calculated from the measurements is 12%. The precision obtained for the temperatures calculated at different delay times are summarized in Tables 7-1 and 7-2.

The results of the calibration-free analysis of Al alloys B8 and SM10 at different delays are reported in Tables 7-3 and 7-4, respectively. The relative concentration values for each element identified in the two Al alloys are plotted against delay time and are illustrated in Figs. 7-8a and 7-8b. The certified concentration value in each case is depicted as a dashed line. In general, the

results obtained from CF-LIBS agree well with the certified value for the major component in the sample only, in this case, Al of which the accuracy of the determination is in the range of 1-6% for sample B8 and 0.3-2% for sample SM10. For the other constituents present in the sample, the calculated relative errors at different delays, which are listed in Tables 7-5 and 7-6 and plotted in Figs. 7-9a and 7-9b, are within the accuracy range for a semi-quantitative analysis only (30-200% error) as defined in Ref. [65]. The relatively large errors calculated can be attributed to the uncertainties associated with temperature determination as well as intensity fluctuations. This conclusion is based on the results of the numerical study carried out by Tognoni et al. [138] regarding the expected precision and accuracy in CF-LIBS, wherein under a simulation of broad temperature dispersion and large intensity fluctuations, the relative concentrations of the elements other than the most abundant element varied within ±150-200%, similar to the results obtained in the CF-LIBS analysis of the two Al alloy samples carried out in this study. In the case of the most abundant element, even under the extreme conditions applied in their simulations, the concentration only varied within ±1%, which agrees to some extent with the relative concentration values calculated for Al. In addition, for moderate intensity fluctuations and temperature dispersion simulations carried out in Ref. [138], the calculated concentration of minor elements varied within ±20%. However, their simulations on the effect of a 10% variation in electron number density values resulted in about 1-2% uncertainty in the concentrations of the most abundant element and about 10% in the concentration of minor components. Therefore, based on the aforementioned discussion, it can be concluded that for the most abundant element present in the samples used in this study, quantitative analysis is possible within ±5% accuracy, with relative errors due to the contributions from electron number density and temperature determinations and intensity fluctuations. On the other hand, the relatively large

errors calculated for the other sample constituents can be attributed to moderate to extreme fluctuation in intensities and dispersion in temperatures for which the composition of most elements in the sample can be determined to within a factor of 2 to 3.

Quantitative Analysis of Brass

Calibration-free LIBS. For the CF-LIBS analysis of brass, 10 NIST standards were used and the measurements were carried out using a delay time of 2.0 μs and a gate width of 0.5 μs. The elemental composition is summarized in Table E-2 in Appendix E. All of the Cu-Zn alloys used in this study were considered as binary compounds since the concentrations of the constituents other than Cu and Zn are well below 0.1%.

A narrow region of the wide spectral range data obtained for each brass sample are shown in Fig. 7-10a. The spectra are arranged in order of decreasing Zn concentration (or increasing Cu concentration) starting from sample 1107 (black fill). The narrow spectral region shown in Fig. 7-10a contains six resonance lines of Cu and Zn and it is evident that the intensities of Zn I at 328.23 nm and 330.26 nm decrease with concentration. However, it can be observed that the intensities of the 4 Cu I lines do not increase with concentration due to the possible occurrence of self-absorption in the plasma. The corresponding images of the laser-induced plasma obtained from brass samples are depicted in Fig. 7-10b and the images clearly indicate the spherically symmetrical shape of the plasmas formed which were about 2.5 cm in diameter.

The application of CF-LIBS algorithm to different lines of Cu and Zn identified in the brass standards resulted in a very good agreement between calculated and certified values for both elements. The results are summarized in Table 7-7 and are plotted in Figs. 7-11a and 7-11b. The corresponding relative errors calculated are also listed in Table 7-7 and are plotted in Fig. 7-11d. The highest relative error obtained is 1.25% for Cu and 12.78% for Zn. The results in this

case can be considered quantitative, particularly for the major element which is Cu due to the relatively low relative errors calculated. However, in 9 out of 10 brass standards analyzed, the concentration of Zn is always much higher than the nominal Zn concentration (Fig. 7-11b) which means that the vapor plume from the ablated brass contains increased amounts of Zn. Baldwin [195] attributed the Zn enrichment in the ablated mass to the lower vaporization temperature of Zn, which is 906°C as compared to the 2595°C vaporization temperature of Cu.

The goodness of the agreement between CF-LIBS and the certified values are quite unexpected due to the nature of the samples used. Several works have shown that brass samples suffer significantly from fractionation and numerous studies have already been carried out to understand the mechanisms behind the fractional ablation using a variety of laser and sample conditions [129, 195-199]. The main factors which influence fractionation in brass are the laser wavelength, pulse duration and irradiance. Mao et al. [196] indicated that at low irradiances (<0.3 GW cm^{-2}) and long pulse durations (>30 ns), the mechanism involved is thermal vaporization and at higher irradiances (>1 GW cm^{-2}) and shorter pulse durations (~3 ns), the mechanism is governed by both thermal and non-thermal processes and the Zn/Cu ratio approaches stoichiometry but the ablated mass always remains enriched in Zn. On the other hand, use of lasers with short pulse durations (35 ps) appears to shift the mechanism to a non-thermal nature and the vapor plume is more enriched with Cu [129]. Hence, the choice of the appropriate laser parameters is critical in obtaining accurate and stoichiometric ratios. In this case, the experimental parameters used seem suitable in the analysis of brass since stoichiometric ablation is apparent from the results obtained with CF-LIBS.

The calculated plasma temperatures and electron number densities are summarized and plotted in Table 7-8 and Fig. 7-11c. The plasma temperature was calculated by constructing

Saha-Boltzmann plots for Cu and Zn lines. There is no significant difference in the temperatures obtained for the different brass standards used and the average temperature for all 10 samples is 13900 ± 200 K. The electron number density was estimated using the Stark broadening of 510.554 nm Cu I line instead of the 656.272 nm Hα line since the latter has a spectral interference with the second order wavelength of 328.233 nm Zn I line. There is also no significant difference in the electron number densities calculated which averages to about $1.4 \pm 0.1 \times 10^{17}$ cm^{-3}. In addition, the calculated electron number densities are all well above the minimum electron number density values required for local thermodynamic equilibrium.

CF-LIBS versus conventional LIBS. In order to extend the experimental evaluation of the CF-LIBS approach, the results for selected brass standards were compared to those obtained by using the conventional analytical calibration procedure. Three calibration curves were constructed using the lines listed in Table 7-9. Plots of integrated intensity against certified Zn concentration are shown in Fig. 7-12. Excellent linear calibration curves were obtained using the three Zn lines with correlation coefficients greater than 0.99 in all cases (Table 7-10). For each set of calibration plots constructed, several brass standards were chosen to serve as 'unknown' samples for comparison with CF-LIBS and the spectra of these selected standards are shown with white fill background in Fig. 7-12. In Fig. 7-12a, a singly-ionized Zn line at 255.795 nm was used in the calibration and two neutral Zn lines at 328. 233 nm and 330.258 nm were used to construct the plots in Fig. 7-12b and 7-12c, respectively. The calibration graphs exhibited a relatively wide dynamic range particularly the calibration plot constructed using the 255.795 nm Zn II line (Fig. 7-12a).

Comparison of the Zn concentration values calculated via the CF-LIBS and calibration curve approach are tabulated in Table 7-11 and the corresponding relative errors of the analysis

are listed in Table 7-12. In general, the results of the CF-LIBS and calibration techniques agree well with certified values. In addition, the CF-LIBS technique resulted in lower relative errors (5-8%) compared to the calibration curve method (10-27%), except in the case of brass 1112 where the calibration plot using the 330.258 nm Zn I yield a relative error of ~2% and CF-LIBS yield a higher relative error of ~12%.

The corresponding limits of detection, c_L, of the Zn content were also calculated using the expression [106]:

$$c_L = \frac{3s_{blank}}{m} \tag{7-1}$$

where s_{blank} is the standard deviation of blank measurements and m is the slope of the calibration curve. The calculated limits of detection for each calibration plot and the resulting parameters of the linear regression are summarized in Table 7-10. The best detection limit obtained based the three calibration curves constructed for Zn was 0.084%.

Quantitative Analysis of Aluminum Alloys

Calibration-free LIBS. The analysis of metallic samples has very important industrial applications which include production process and quality assurance monitoring. In this study, six different aluminum alloy standards from South Africa were used. The elemental composition is summarized in Table E-1 in Appendix E. Analysis of Al alloys B8 and SM10 were carried out at three different ambient pressures: 1000, 100 and 0.1 mbar and analysis of Al alloys D33, S4, V14 and Z8 were carried out at two different pressures: 1000 and 0.1 mbar. LIBS experiments at pressures of 1000 and 100 mbar were performed using a delay time of 2.0 μs and a gate width of 0.5 μs and experiments at a pressure of 0.1 mbar were performed using a delay time of 50 ns and gate width of 100 ns. The delay times and gate widths were selected by considering the significantly different evolution dynamics of the plasma at different ambient pressures. In fact,

under atmospheric conditions, the acquisition delay time must be long enough to allow the decay of continuum emission due to bremsstrahlung radiation and free-bound electronic radiative recombination, which is very intense at higher pressures; then again, under vacuum conditions, the rapid evolution of the laser-induced plasma requires that the delay time is not too long in order that the emission signal coming from both neutral and singly-ionized species still reaches the detector.

The rapid expansion of the plasma as the pressure is decreased can be observed from the images of the laser-induced plasmas shown in Fig. 7-13. The plasma sizes at 1000 mbar and 0.1 mbar pressures are not exactly comparable due to the difference in the delay times and gate widths used in the measurements. However, it can be clearly observed that under similar gating conditions, the plasmas formed at 1000 mbar have a smaller diameter (~2.0 cm) than the plasma formed at 100 mbar (~2.5 cm) and that in both cases, the plasmas are approximately spherical in shape. Furthermore, it is evident that at early delays, the plasmas formed under vacuum conditions are not spherically symmetrical but acquires an ellipsoidal shape which agrees with the initial growth of the plasma emission in the direction of the laser beam. Aragon and Aguilera [172] reported a similar observation regarding the shape of the laser-induced plasmas generated with an iron sample at different gas pressures.

The line intensities also decrease as the pressure is reduced as can be observed in Fig. 7-14 where a narrow portion of the Al alloy spectra under different ambient conditions are shown. This observation is contrary to the results reported in previous studies [171, 200, 201] where the intensities increase significantly when the pressure is reduced to an optimum value, usually between 50 and 350 Torr depending on the experimental conditions, and then decreases when the pressure is further reduced. However, there were only 2-3 pressure conditions that were used in

this particular study, hence the apparent increase in intensity was not observed when the pressure approached low vacuum conditions. The observed behavior of emission intensities at various air pressures, as shown and explained in previous studies [171, 200, 201], can be attributed primarily to the plasma shielding effect which is particularly crucial when using infrared lasers because the absorption of the laser energy is caused by the inverse bremsstrahlung processes in the plasma whose absorption cross-section is proportional to λ^3 [171]. Under atmospheric conditions, the laser energy absorbed by the plasma is rapidly converted into kinetic energy and causes ionization which translates into high temperatures and high electron number densities in the plasma. This is confirmed by the electron number density and temperature values calculated at 1000 mbar air pressure.

In this study, the electron number densities at different pressures were determined using the Hα line at 656.272 nm and the results are plotted and tabulated in Fig. 7-15a and Table 7-13. The calculated values agree well with electron number densities reported in the literature under similar ambient conditions [171, 172]. There is an order of magnitude difference between the electron number densities calculated at 1000 mbar (10^{17} cm^{-3}) and at 0.1 mbar (10^{16} cm^{-3}). The temperatures were calculated using the Saha-Boltzmann plot approach and the results are shown in Fig. 7-15b and summarized in Table 7-14. The temperatures obtained under atmospheric conditions are about 12000 K which is ~1000 K higher than the temperatures obtained under low pressure conditions. Furthermore, under vacuum conditions, despite the increase in mass removal due to the reduction in plasma shielding [202], lower emission is still generated by the plasma due to its lower temperature [171]. Iida [200] also indicated that besides plasma shielding, the confinement of the plasma under different ambient pressures plays a major role as well. Under atmospheric conditions, the plasma expansion is significantly confined by the

surrounding background gas and the resultant plasma usually produces an intense background continuum instead of a strong analytical emission lines. On the other hand, at reduced pressures, the rapidly expanding plasma causes a decrease in emission intensity due to the rapid escape of emissive species from the temporal and spatial window of observation.

The results of the CF-LIBS analysis of the Al alloys at different pressures are summarized in Figs. 7-16 and 7-17 and are tabulated in Tables 7-15 to 7-20. In general, it can be observed that the calculated concentration values for Al, which is the most predominant element in the sample, agree very well with certified values and therefore, resulted in very low relative errors (0.08-6%). However, for the remainder of the elements present in the alloy samples, the results are semi-quantitative only due to the relatively high relative errors obtained in the calculations for which the sample components can be determined within a factor of 2 except for Fe which can be determined within a factor of 3.

CF-LIBS versus conventional LIBS. Similar to the analysis of brass, calibration curves were constructed for a few elements in the Al alloy samples for comparison with CF-LIBS results. Only the measurements under atmospheric conditions (1000 mbar) were used in this part of the study. The lines used to generate the calibration graphs are: 229.436 nm Cu II, 327.396 nm Cu I and 288.158 nm Si I. The pertinent spectroscopic parameters are listed in Table 7-21. Linear calibration curves with correlation coefficients greater than 0.99 were obtained using some of the Al alloy standards while the rest serve as 'unknown' samples for comparison with CF-LIBS. The resulting calibration plots and the spectra of the lines used are shown in Fig, 7-18. The Cu and Si content in the 'unknown' samples were calculated using the linear regression parameters tabulated in Table 7-22 and the results are summarized in Tables 7-23 and 7-25 for Cu and Si concentration values, respectively. The limits of detection were also calculated using

Eq. 7-1 and the results are shown in Fig. 7-18. The lowest detection limit obtained was 0.0084% using the 229.436 nm Cu II line. Sabsabi and Cielo [24] reported detection limits of 10 ppm for Cu and 14 ppm for Si using the lines at 327.393 nm Cu I and 251.611 nm Si I, respectively. Although, the detection limits calculated in this study are about two orders of magnitude higher than those reported in the literature, a wider dynamic range was obtained for Cu and Si despite the limited number of standards used in the construction of the calibration curves. The calibration curve reported in Ref. [24] for Cu start to deviate from linearity at about 1%.

The accuracy of the two techniques used in this study was evaluated by determining the relative errors of the measurement. Although, in general, the CF-LIBS results were closer to the certified values than those calculated using the calibration curve approach, the relative errors were still in the semi-quantitative category (≥30%) specifically the errors obtained for Cu which are better than 50% (Table 7-24). On the other hand, the accuracy of the calculated Si content using the CF-LIBS method is better than that for Cu since the errors are in the range of 2-20% (Table 7-25).

Quantitative Analysis of Soils

Application of laser-induced breakdown spectroscopy to quantitative analysis of soils has been demonstrated to have a significant potential for remote and in situ terrestrial and extraterrestrial applications [28-30, 119, 203-207]. In this part of the study, the calibration-free LIBS approach was applied to six different types of soil standards from NIST [208] and Natural Resources Canada [209]. The elemental composition of the standards used is listed in Table E-3 in Appendix E. The soil samples were made into pressed pellets as previously described in the experimental section. LIBS measurements were carried out using a delay time of 1.2 μs and a gate width of 0.1 μs. A small portion of the soil spectra are shown in Fig. 7-19a and the images

of the laser-induced plasmas obtained from the soil samples are illustrated in Fig. 7-19b. The plasmas formed were approximately 2.0 cm diameter in size.

Due to the complexity of the soil matrix, only major and minor elements have been identified and used in the analysis. The CF-LIBS results for each soil standard analyzed are shown in Fig. 7-20 and tabulated in Tables 7-26 to 7-28. The results are in relative terms and are dependent on the number of species included in the CF-LIBS analysis. Approximately 50-60% of the soil composition remained undetermined in this case which includes organic compounds and other minor constituents, e.g. barium, phosphorus, potassium, sodium, sulfur, etc.

From the CF-LIBS results, the highest accuracy (≤2%) was obtained for Si which is the most abundant element in the soil standards (Fig. 7-21a). However, a 13-14% relative error was obtained for the same element in the Canadian soil standards. The slight difference obtained between the two soil 'types' may be attributed to factors such as provenance, sample preparation, texture and particle size. Moreover, several works have already shown that soil samples are strongly affected by matrix effects and different approaches have been used in order to correct or overcome these effects [26, 160, 210-212]. Chemometric methods such as principal components analysis (PCA) [160] and multivariate analysis [212] are the most recent techniques applied to soil analysis. For the remainder of the elements determined with CF-LIBS, the relative errors were randomly distributed within the range of 20-120% which makes the analysis of soil matrices semi-quantitative. Corsi et al. [213] recently applied double-pulse LIBS in the analysis of soils and sediment and found enhancements on the LIBS signal of the order of 5-10 times depending on the upper energy level of the transition which may be particularly advantageous to standard-free techniques such as CF-LIBS.

The electron number density of the laser-induced plasma was calculated using the Stark width of the Hα line and the temperature was determined by generating Saha-Boltzmann plots using lines from different elements identified from the soil spectrum. The plasmas formed are in local thermodynamic equilibrium since the calculated electron number densities are all above the minimum value required for LTE (Fig. 7-21b and Table 7-29). The measured plasma temperatures for different samples were between 11000 and 12500 K, while the estimated electron number density was on the order of 10^{17} cm^{-3}.

Quantitative Analysis of Different Types of Alloys

The calibration-free LIBS approach was also applied to Ti alloys, Zn alloys, Ni alloy and Cu-Ni alloy. The elemental composition of the samples used is listed in Table E-4 in Appendix E. Some of the samples were in powder form and were made into pressed pellets before analysis as described previously in the experimental section. The LIBS measurements of metal alloys were carried out in atmospheric conditions using a delay time of 2.0 μs and a gate width of 0.5 μs while the pelletized samples were measured using a delay time of 1.2 μs and a gate width of 0.1 μs.

A section of the wide spectral range data for each alloy sample analyzed are shown in Fig. 7-22a. The images of the laser-induced plasmas obtained from different alloy samples show a distinct difference in the plasma symmetry (Fig. 7-22b). The plasmas formed on the Ni alloy pellet and Ti alloy samples in both metal and pellet forms were flattened in the radial direction while the plasmas formed on the Zn and Cu-Ni alloys were elongated in the direction of the laser beam. The difference can be attributed generally to the samples used and not to the form of samples, i.e., pellet or metal form, since the plasmas formed on two different forms of Ti alloys acquired a similar shape.

The results of the CF-LIBS analysis of the six alloys are shown Fig. 7-23 and the corresponding accuracy of the measurement are summarized in Fig. 7-24a-d. The Ti content of the ternary Ti alloy sample in both pellet and metal forms agree well with certified values and the relative errors obtained are below 7% (Table 7-30). The Al and V content, on the other hand, resulted in relative errors between 14-120%. The Zn concentration of the NIST Zn alloys calculated with CF-LIBS gave the highest accuracy with relative percentage errors which are below 1% (Table 7-31). Also, for the remainder of the elements present in the Zn alloy sample (Al, Cu and Fe) semi-quantitative results were obtained with errors in the range of 2-60%. Excellent results were obtained for both Ni and Cu in the Ni alloy pellet and the Cu alloy metal with errors below 4% (Table 7-32). On the other hand, 30-120% errors were obtained for the other elements present in the alloy standards.

The electron number density of the laser-induced plasma was determined using the Stark widths of different lines: the Hα line for the Ti and Ni alloy, the Ni I line at 361.939 nm for the Cu-Ni alloy and the Al I line at 394.401 nm for the Zn alloys. The Ni I line was used to determine the electron number density of the Cu-Ni alloy plasma instead of the Hα line since the latter was very weak and cannot be fitted with relatively high accuracy. Conversely, the Al I line was used for electron number density determination since one of the second order wavelengths of Zn interferes with the Hα line. The electron number density values calculated for the six alloys analyzed are within the range of 2.2×10^{17} to 3.7×10^{17} cm^{-3} (Table 7-33). Furthermore, the plasma temperature was determined using the Saha-Boltzmann plot approach and the results are plotted in Fig. 7-24e and tabulated in Table 7-33. The measured plasma temperatures for different alloy samples were of the order of 12500 to 14600 K.

Conclusion

In this study, calibration-free LIBS was applied to the analysis of different samples of varying degrees of complexities. Temporally-resolved measurements of Al alloy samples have demonstrated the importance of optimization of gating parameters to ascertain that the minimum value of electron number density for local thermodynamic equilibrium condition is achieved. As far as the experiments carried out under different ambient pressures, no significant effect has been observed on the calculated accuracy of the relative elemental composition of the alloy samples analyzed. Also, in the analysis of Al alloy and brass samples, the results obtained with CF-LIBS are generally in closer agreement with nominal values compared to those obtained with conventional analytical calibration methods.

In general, quantitative results with accuracy better than 5% were obtained for the most abundant constituent in the sample. However, for the remainder of the components of the sample, the results are semi-quantitative, with relative errors between 30 and 200% in most of the samples that were analyzed. The relatively large errors obtained particularly for minor and trace elements can be attributed to uncertainties associated mainly with the determination of temperature, as well as uncertainties in the fitting of spectral lines and the transition probabilities used in the calculations. There are other minor contributing factors that affect the accuracy of the final elemental concentration values calculated with CF-LIBS and numerical simulations of the effect of each parameter on CF-LIBS results have already been undertaken and described succinctly in Ref. [138]. There is no correction for self-absorption considered in this study but resonance lines of major elements were not used in the CF-LIBS analysis, whenever possible, in order to avoid underestimation of the element composition.

Analysis of samples in the form of pressed pellets also did not show any significant influence on the accuracy of the results obtained, positive or otherwise. However, CF-LIBS

analysis of soil matrices proved to be more complicated than alloy matrices and only about 40-50% of the total sample composition was determined which excludes organic compounds and other minor constituents such as barium, phosphorus, potassium, sodium, sulfur, etc.

The spectral acquisition method developed in this research proved effective for CF-LIBS analysis due to the large spectral window it offered along with the moderately high-resolution provided by the detection system. Hundreds of emission lines were resolved within the spectral range from 220 to 700 nm which were certainly necessary in improving the accuracy and precision of the Boltzmann and Saha-Boltzmann plots generated, which are the framework of the CF-LIBS protocol.

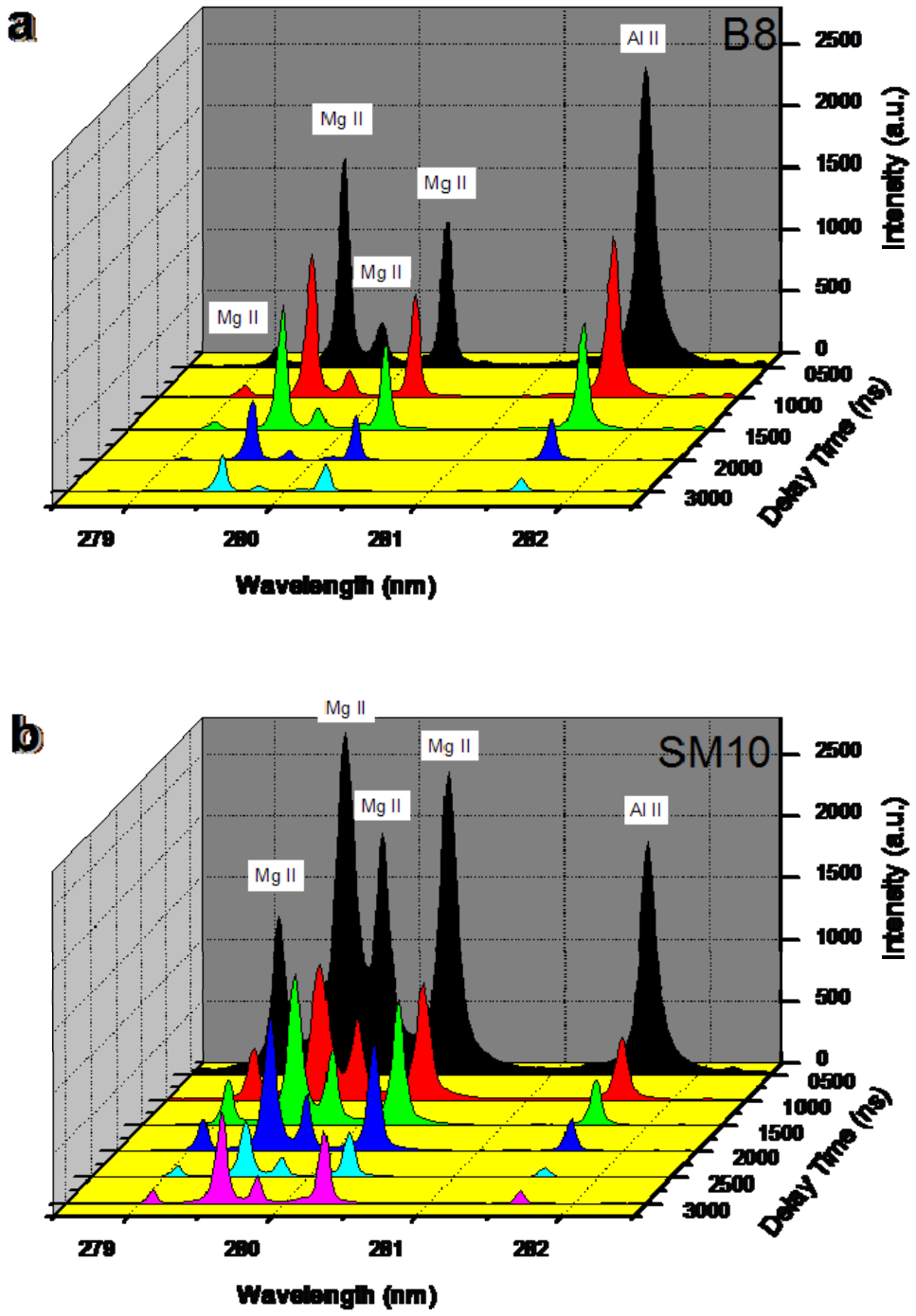

Figure 7-1. Section of the wide spectral range data of aluminum alloy sample (a) B8 and (b) SM10 at different delay times.

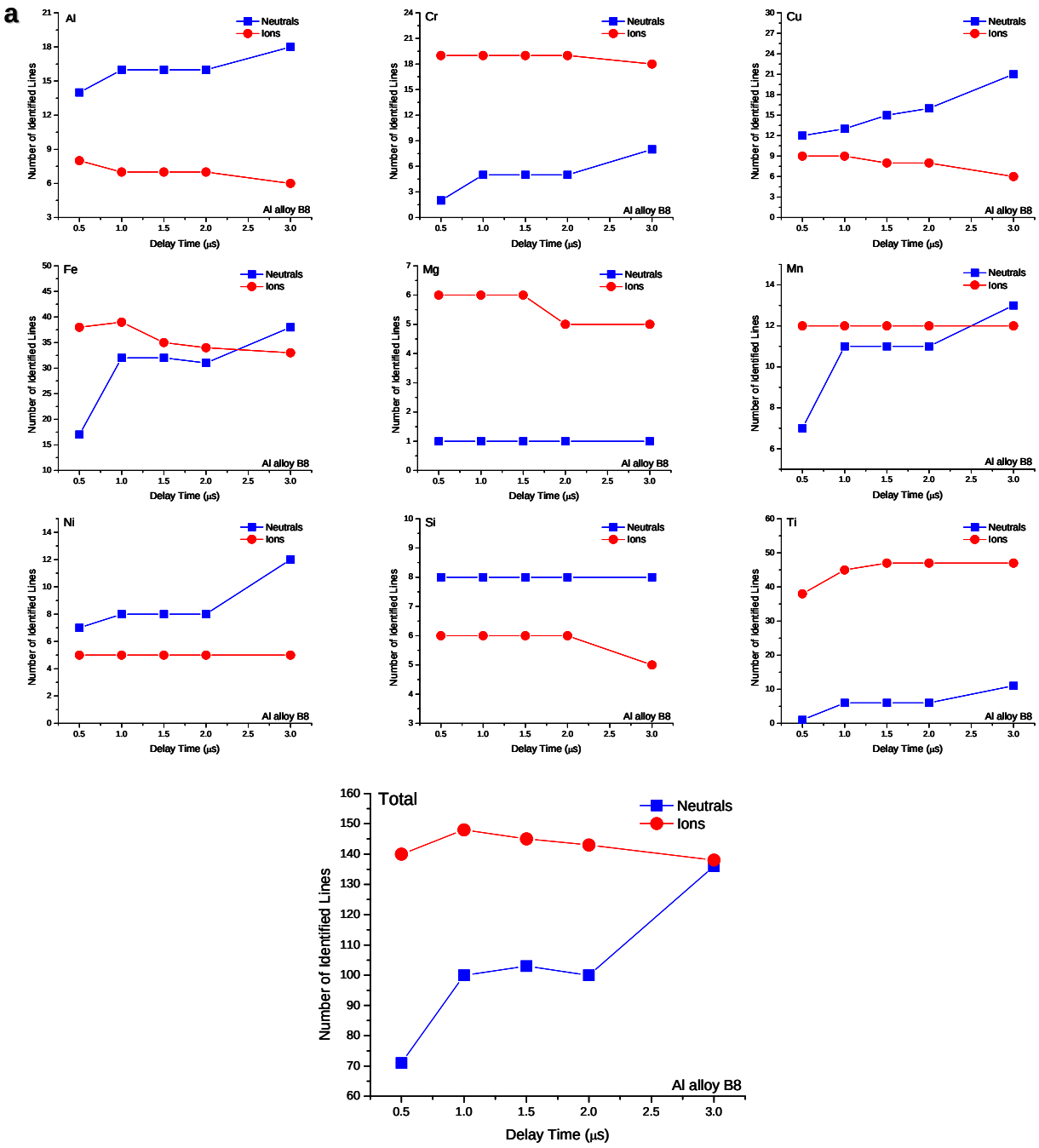

Figure 7-2. Temporal evolution of the number of identified neutral lines (blue squares) and singly-ionized lines (red circles) for the different elements present in (a) Al alloy B8 and (b) Al alloy SM10. The number of neutral lines increases with delay time while the number of singly-ionized lines decreases with delay time due to electron-ion radiative recombination. (Left to right, top to bottom: (a) Al, Cr, Cu, Fe, Mg, Mn, Ni, Si, Ti and total and (b) Al, Cr, Cu, Fe, Mg, Mn, Ni, Si, Ti, Zn and total)

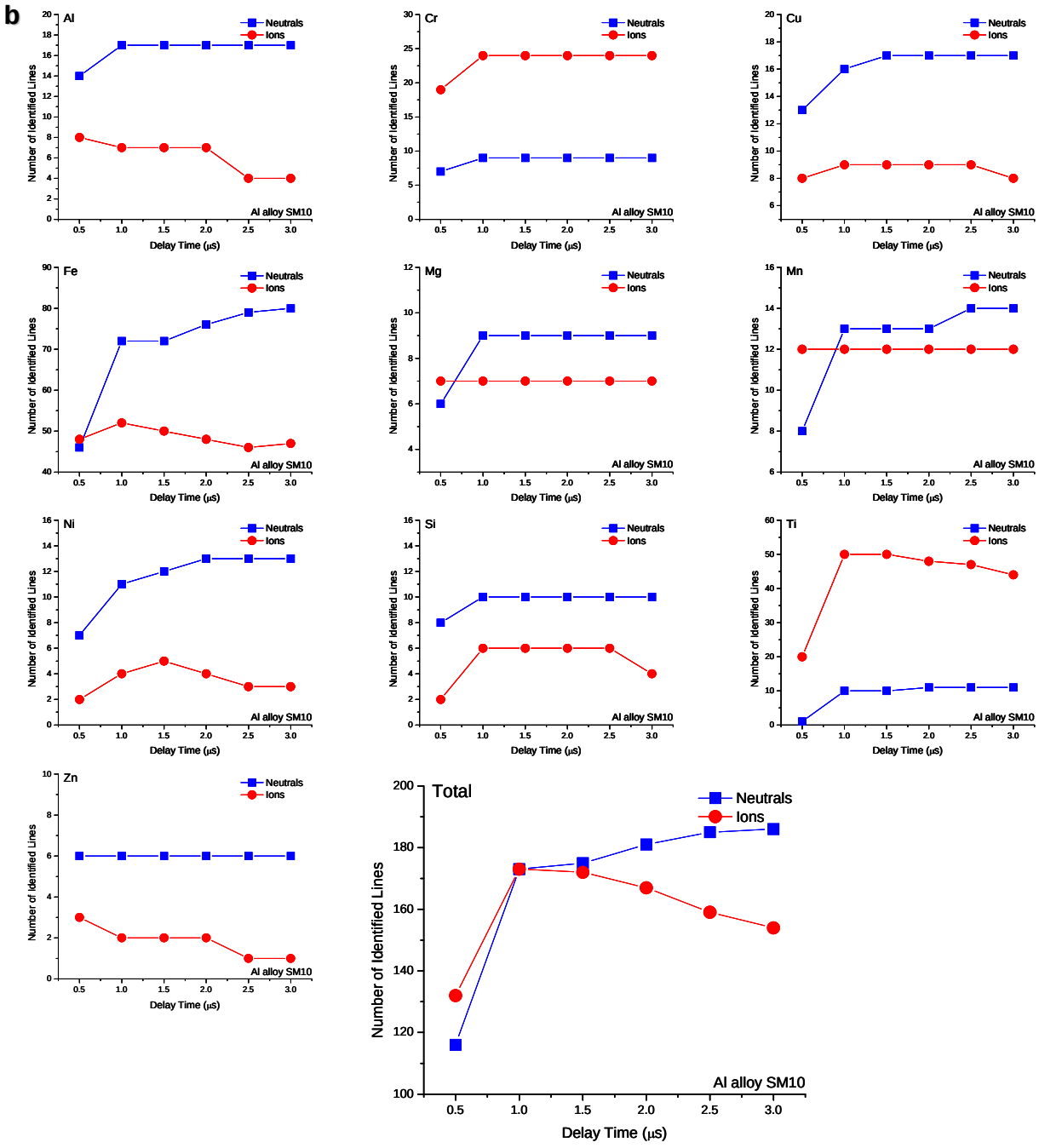

Figure 7-2. Continued.

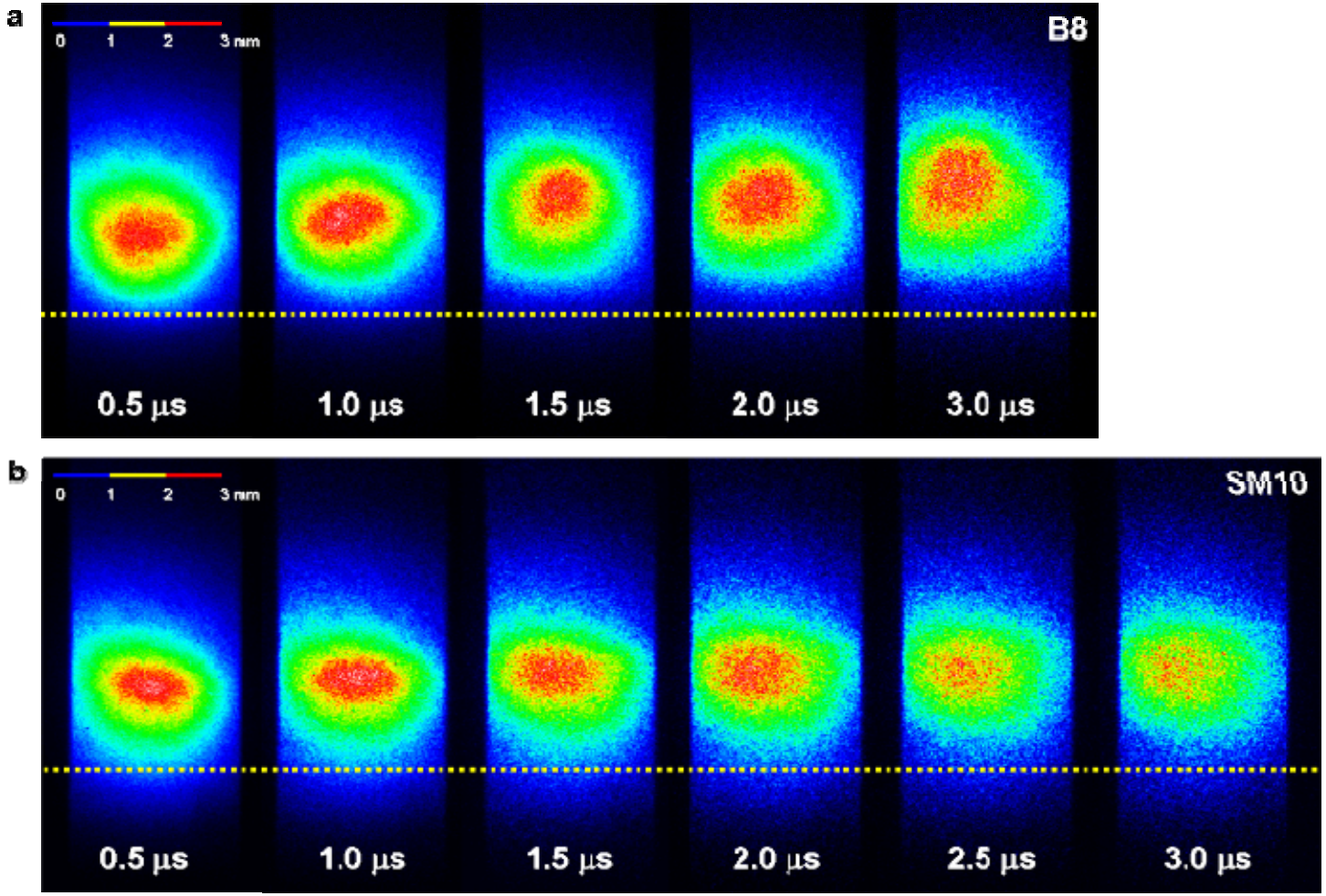

Figure 7-3. Temporal evolution of laser-induced plasmas obtained from (a) Al alloy B8 and (b) Al alloy SM10. The plasma is propelled away from the target surface indicated by the dashed yellow line. This is due to the vortex ring formed immediately after the internal shockwave reaches the sample surface which then causes the vapor plume to be propelled away from the target.

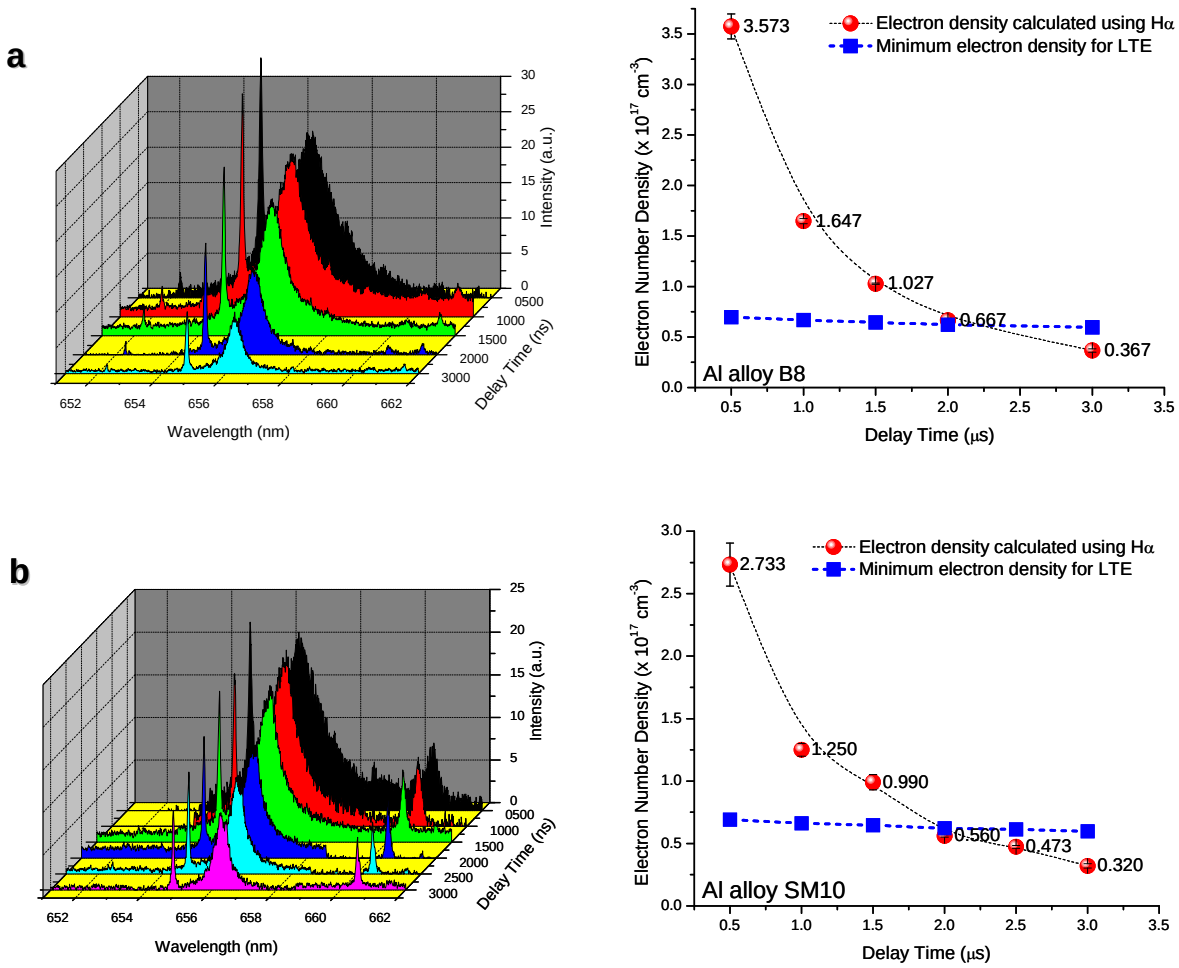

Figure 7-4. Temporal evolution of the electron number density calculated using the Hα line at 656.272 nm (shown on the left) for (a) Al alloy B8 and (b) Al alloy SM10. The blue squares indicate the minimum electron number density for the plasma to be in LTE at different delay times.

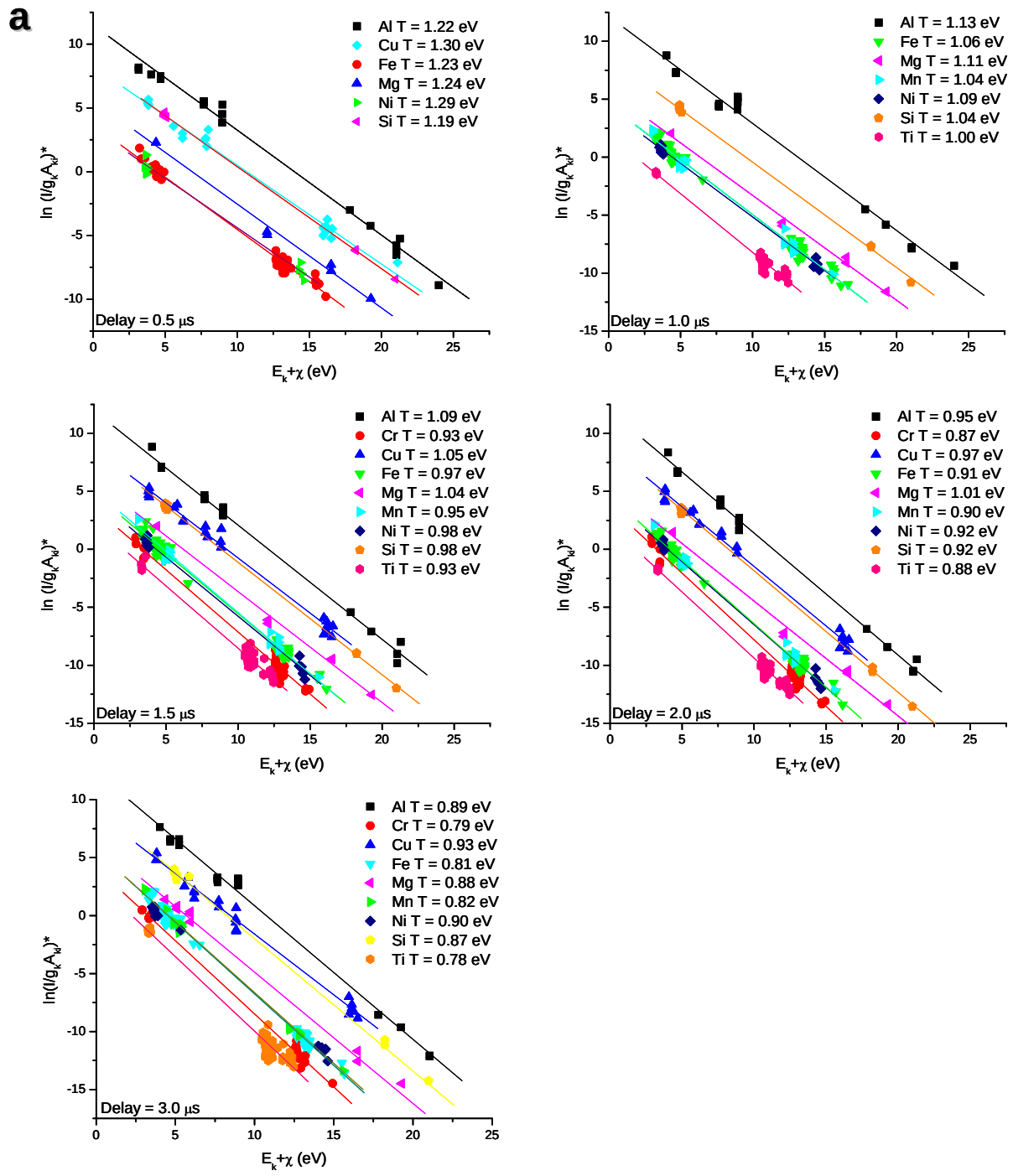

Figure 7-5. Saha-Boltzmann plots of selected lines at different delay times. The temperature values obtained are given in eV where 1 eV is equivalent to 11605 K. (Left to right, top to bottom: (a) 0.5, 1.0, 1.5, 2.0 and 3.0 µs and (b) 0.5, 1.0, 1.5, 2.0, 2.5 and 3.0 µs).

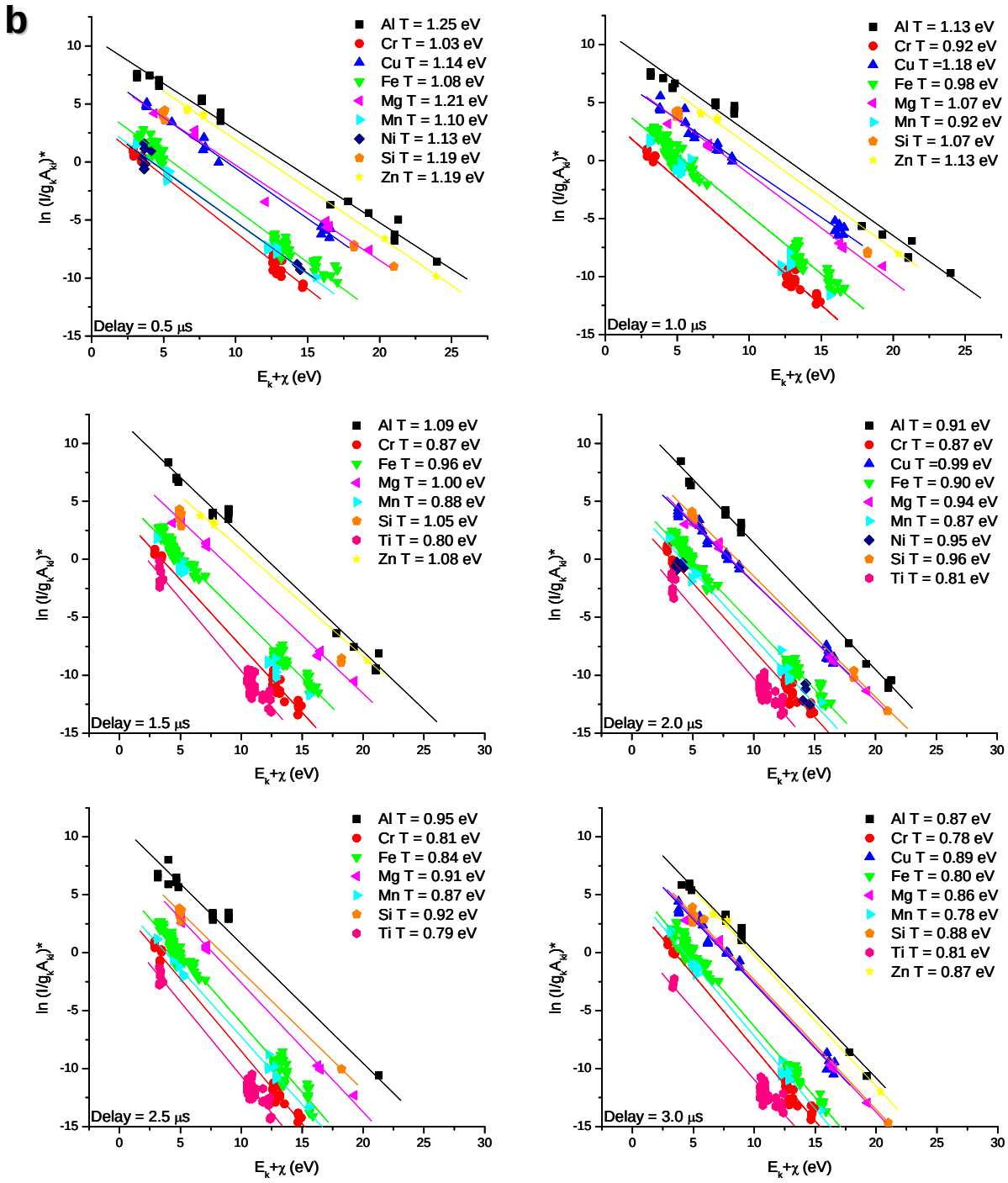

Figure 7-5. Continued.

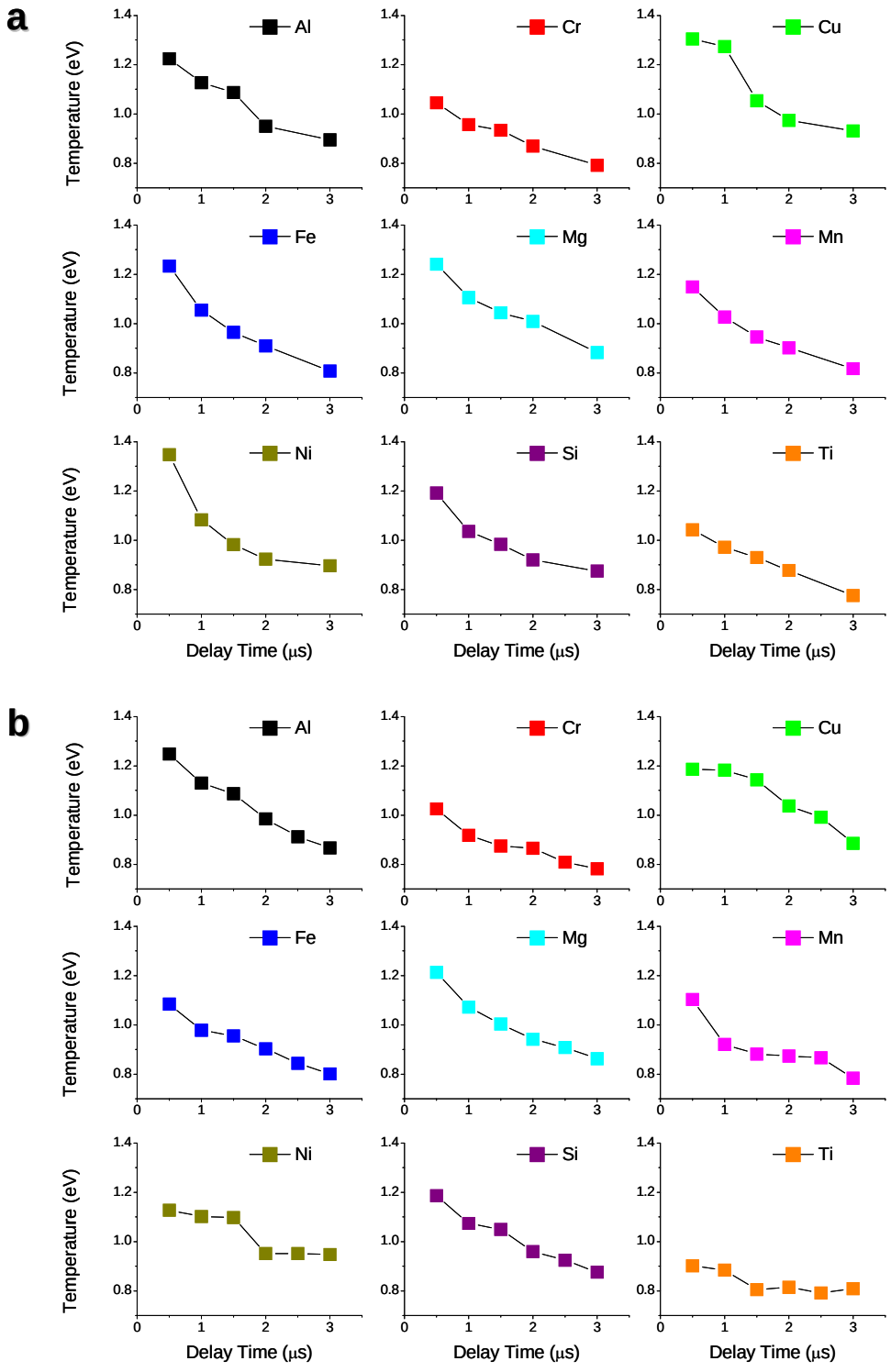

Figure 7-6. Temporal evolution of temperature calculated for selected elements in (a) Al alloy B8 and (b) Al alloy SM10.

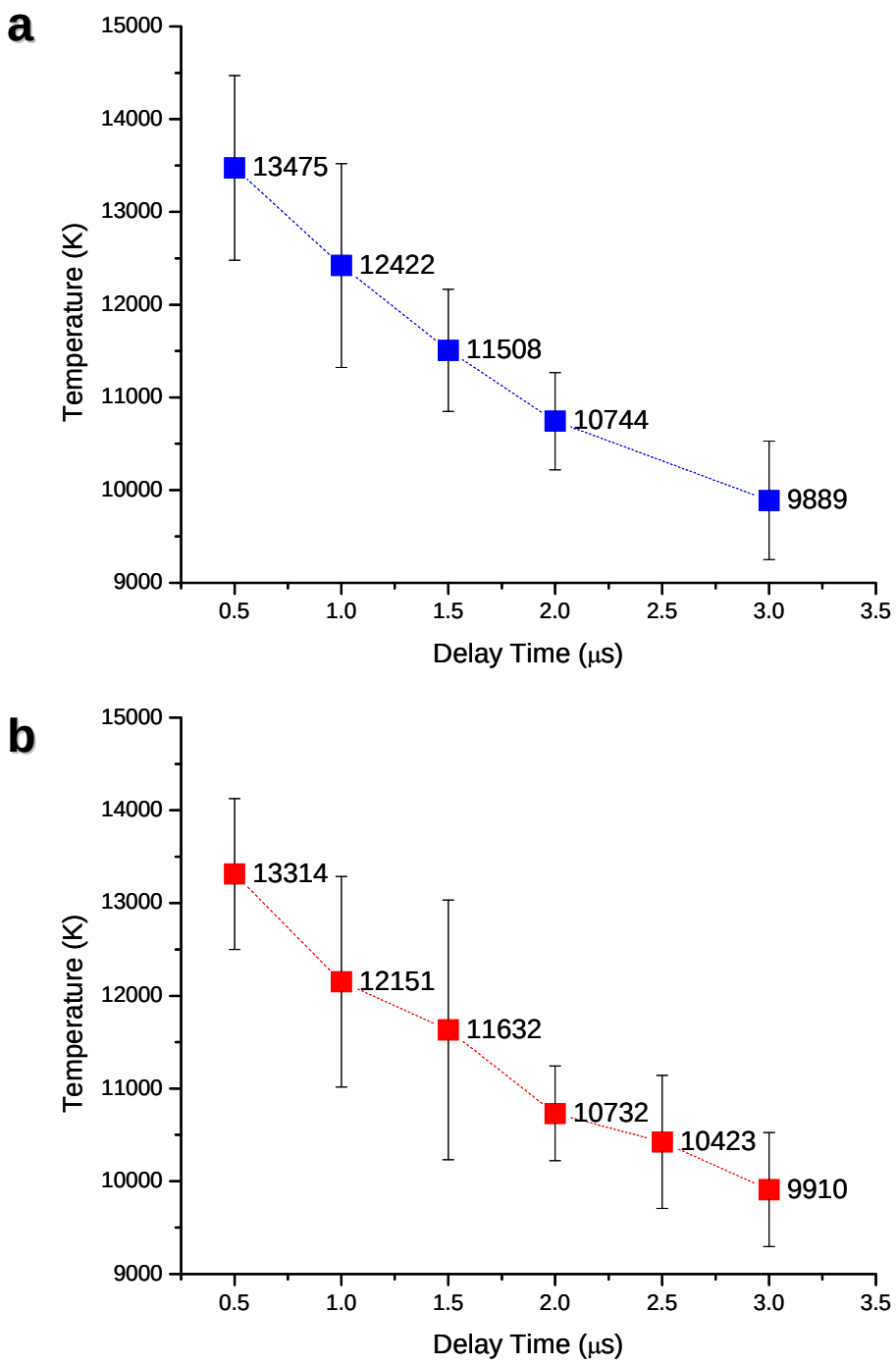

Figure 7-7. Temporal evolution of averaged plasma temperature of (a) Al alloy B8 and (b) Al alloy SM10.

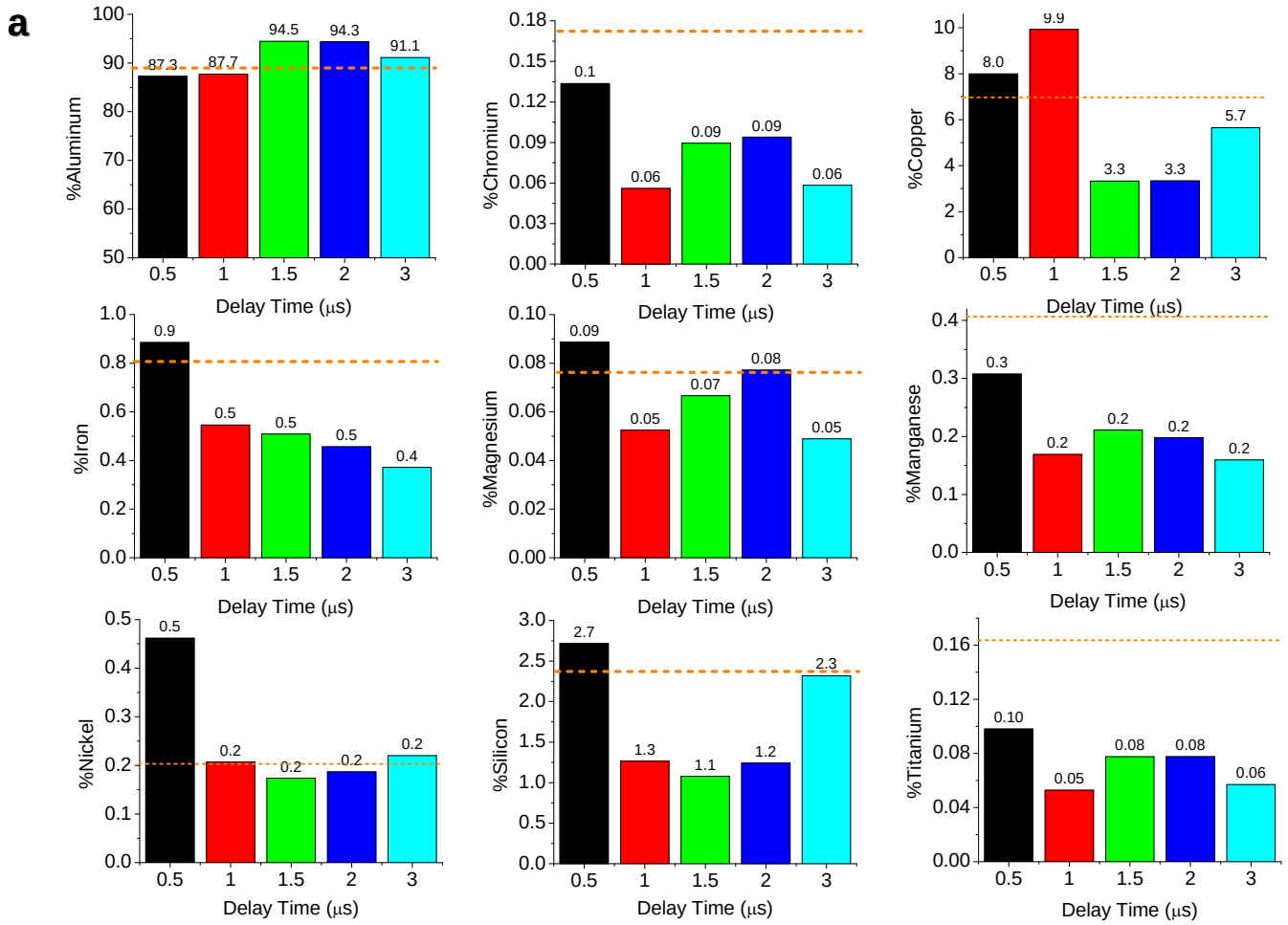

Figure 7-8. Elemental concentrations of (a) Al alloy B8 and (b) Al alloy SM10 calculated from CF-LIBS at different delay times. The dashed lines indicate the nominal concentration value. (Left to right, top to bottom: (a) Al, Cr, Cu, Fe, Mg, Mn, Ni, Si, and Ti and (b) Al, Cr, Cu, Fe, Mg, Mn, Ni, Si, Ti and Zn).

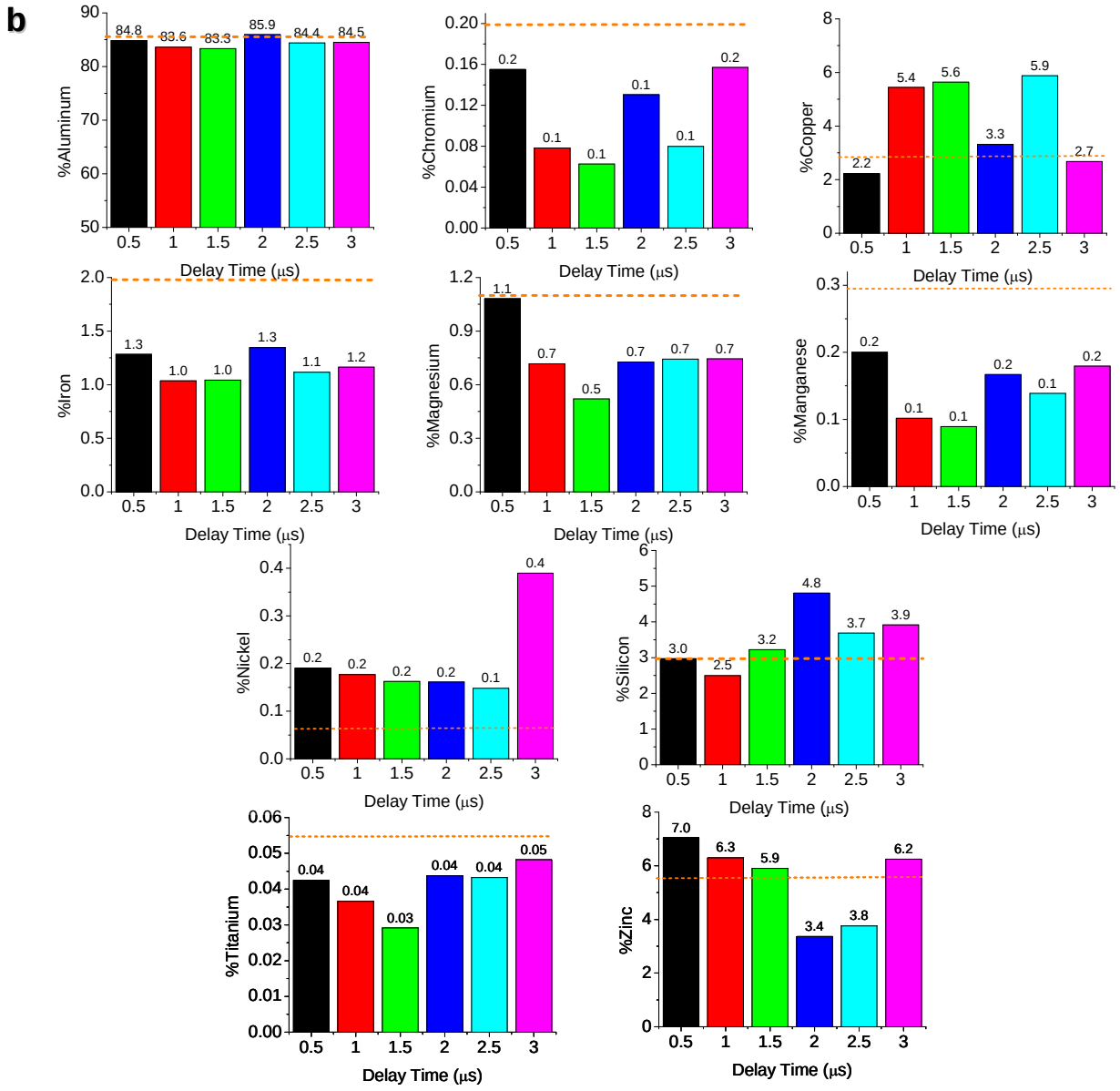

Figure 7-8. Continued.

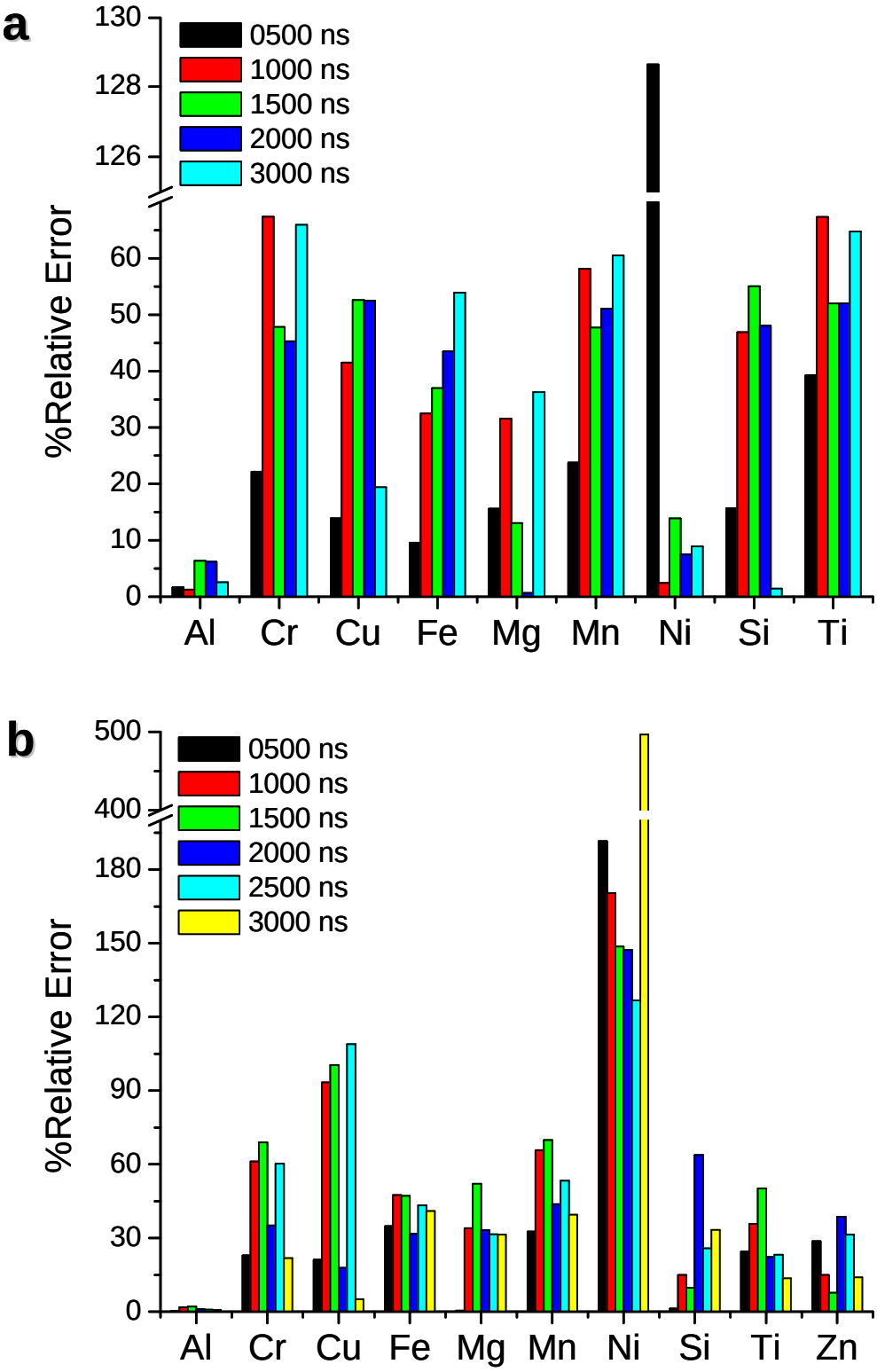

Figure 7-9. Relative errors calculated from CF-LIBS results of (a) Al alloy B8 and (b) Al alloy SM10.

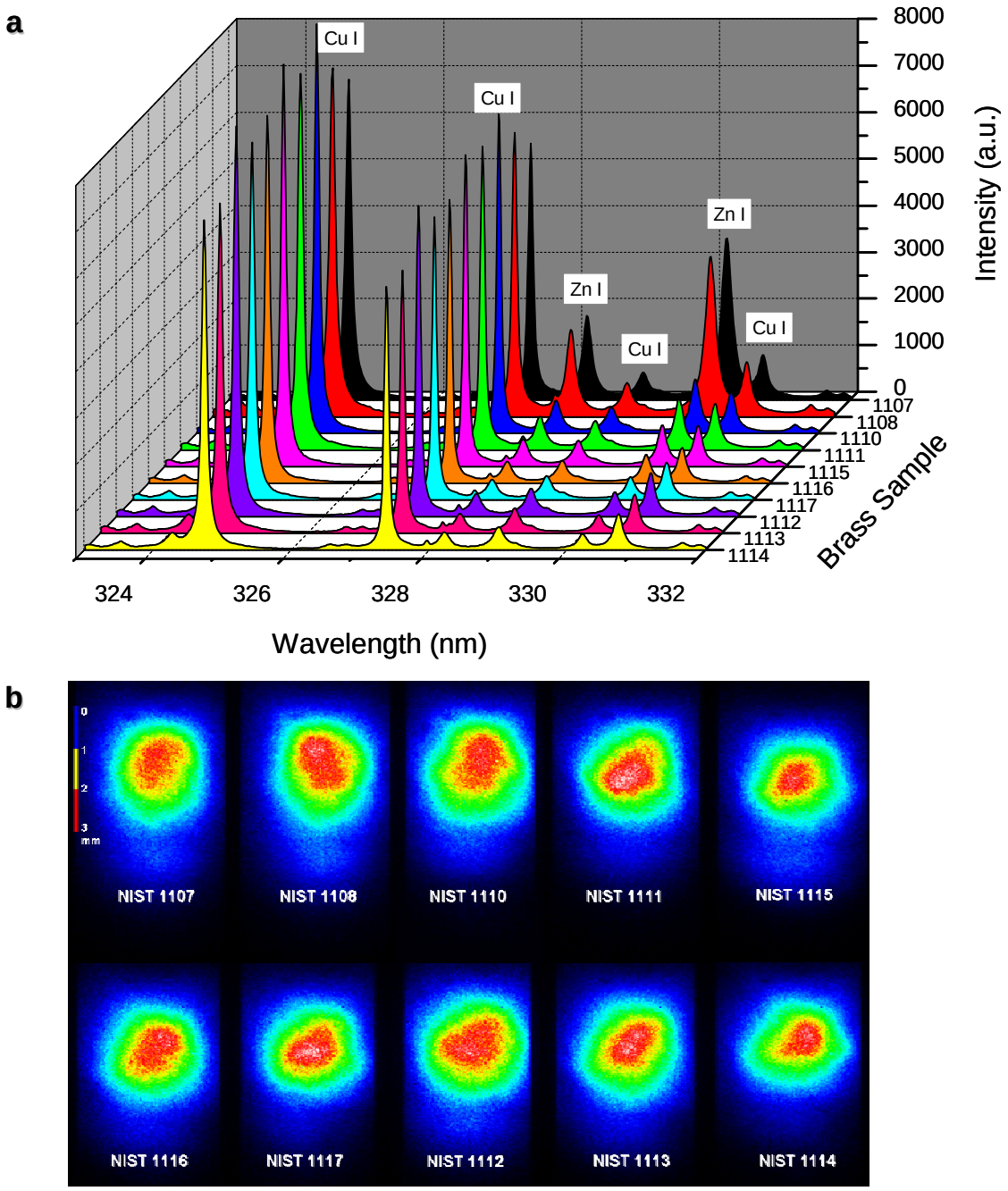

Figure 7-10. LIBS measurements of 10 NIST brass standards. A section of the laser-induced breakdown spectra of brass showing selected Cu I and Zn I lines are shown in (a) and the corresponding images of the laser-induced plasma obtained at 2.0 μs delay time and 0.5 μs gate width are illustrated in (b).

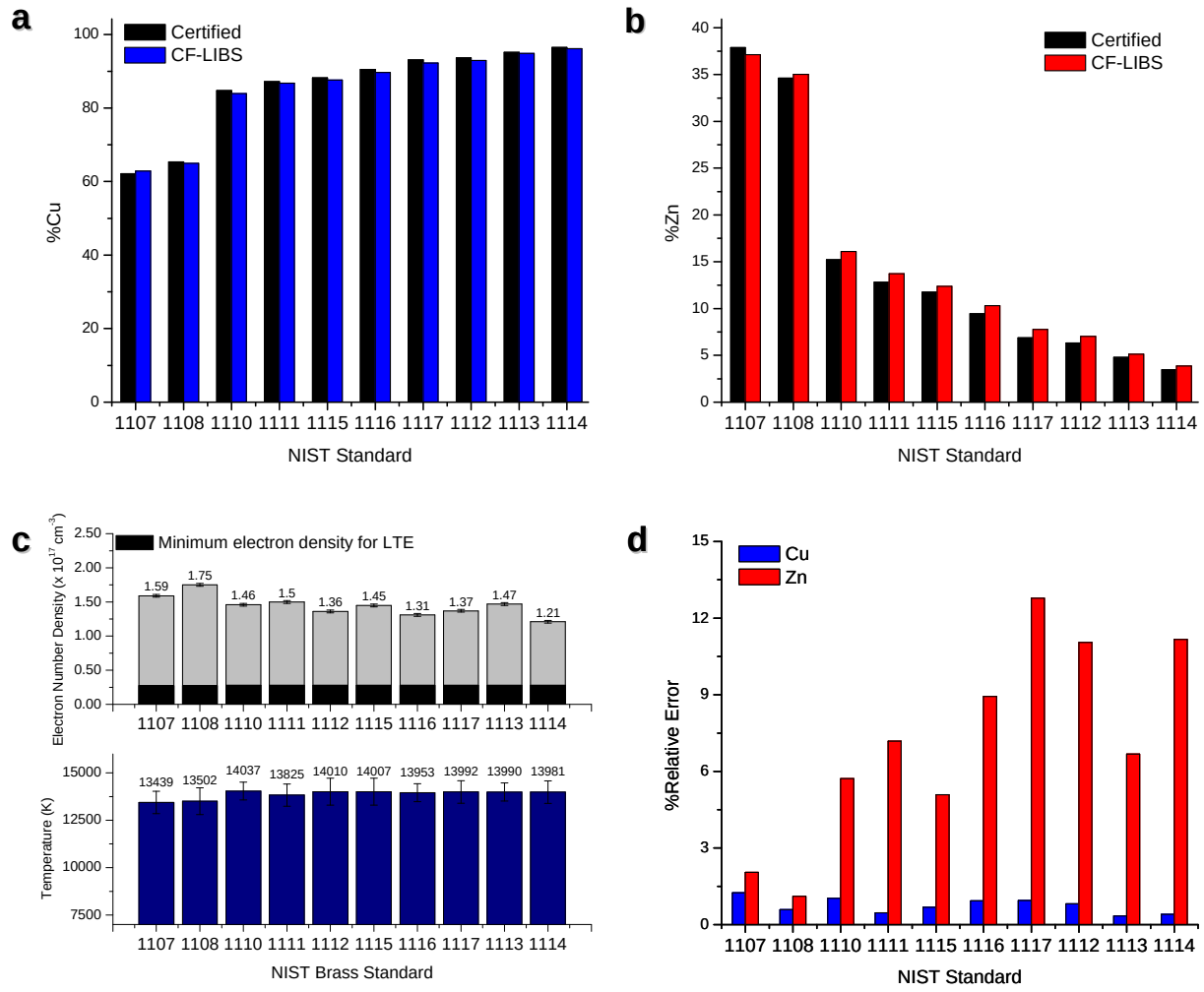

Figure 7-11. Results of the CF-LIBS analysis of 10 NIST brass standards. The relative elemental concentrations of (a) Cu and (b) Zn are shown in blue and red bars, respectively. The certified values are depicted by the black bars. The calculated electron number densities and temperatures are shown in (c) and the relative percentage errors of the CF-LIBS concentration results are summarized in (d).

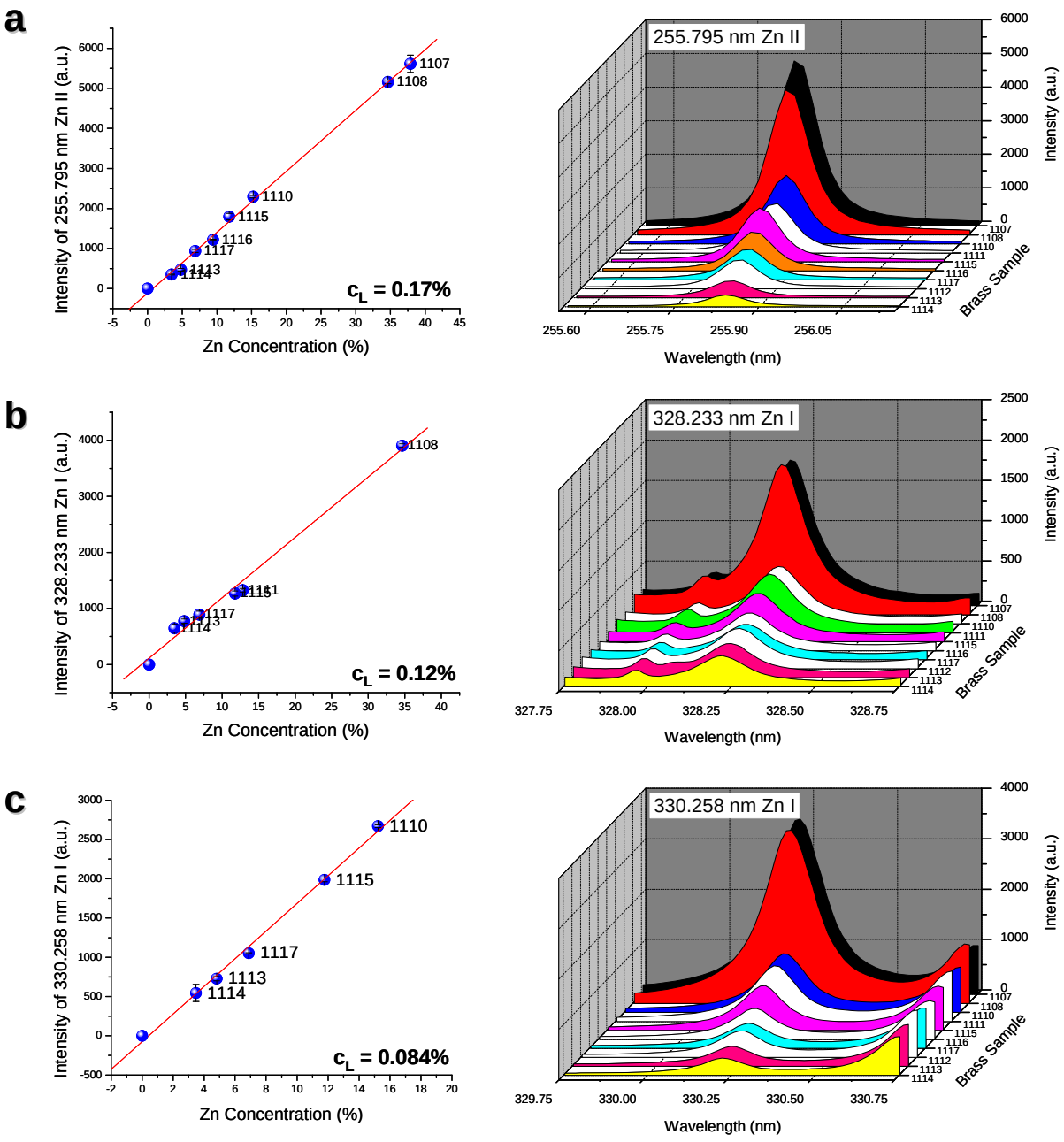

Figure 7-12. Calibration curves constructed for the quantitative analysis of Zn in brass samples using (a) 255.795 nm Zn II, (b) 328. 233 nm Zn I and (c) 330.258 nm Zn I lines.

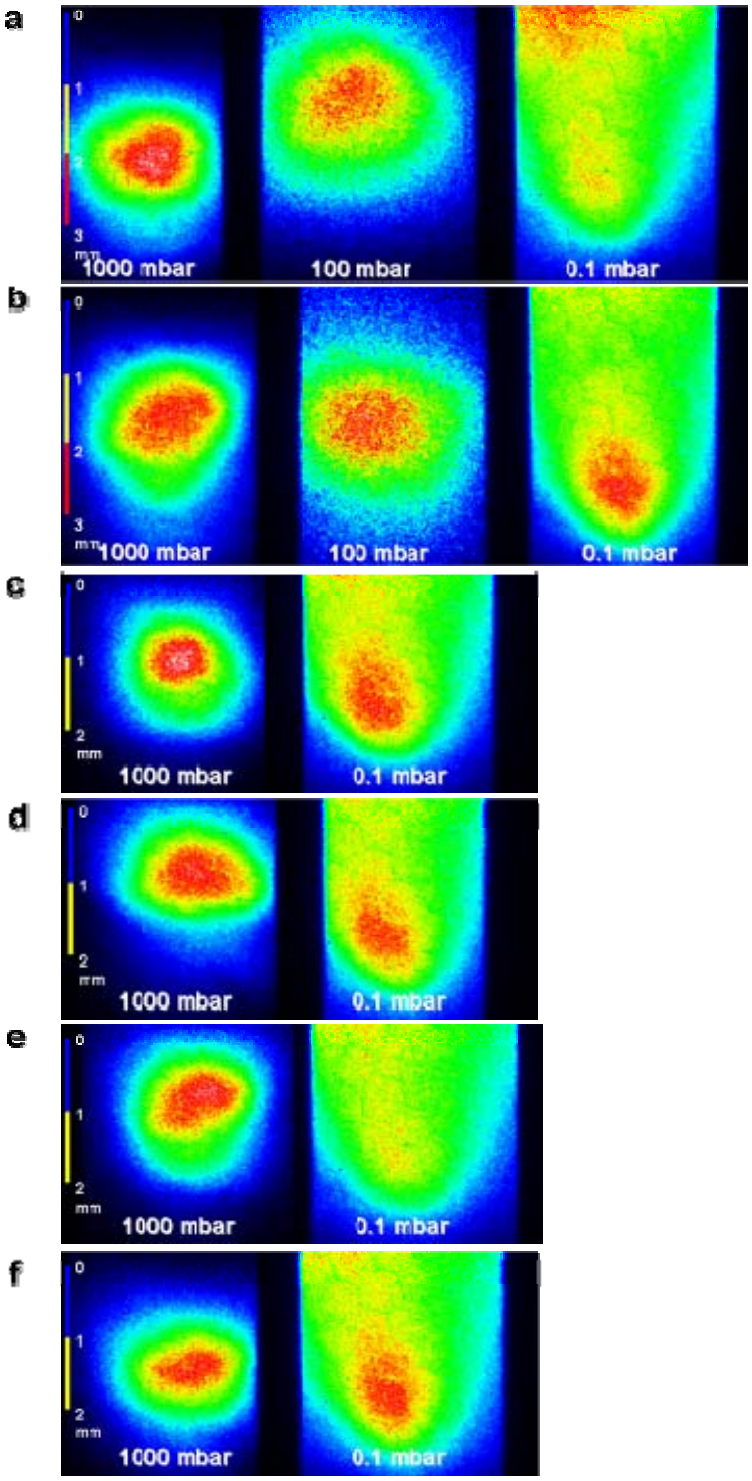

Figure 7-13. Images of the laser-induced plasma obtained from Al alloy (a) B8, (b) SM10, (c) D33, (d) S4, (e) V14 and (f) Z8 at different ambient pressures.

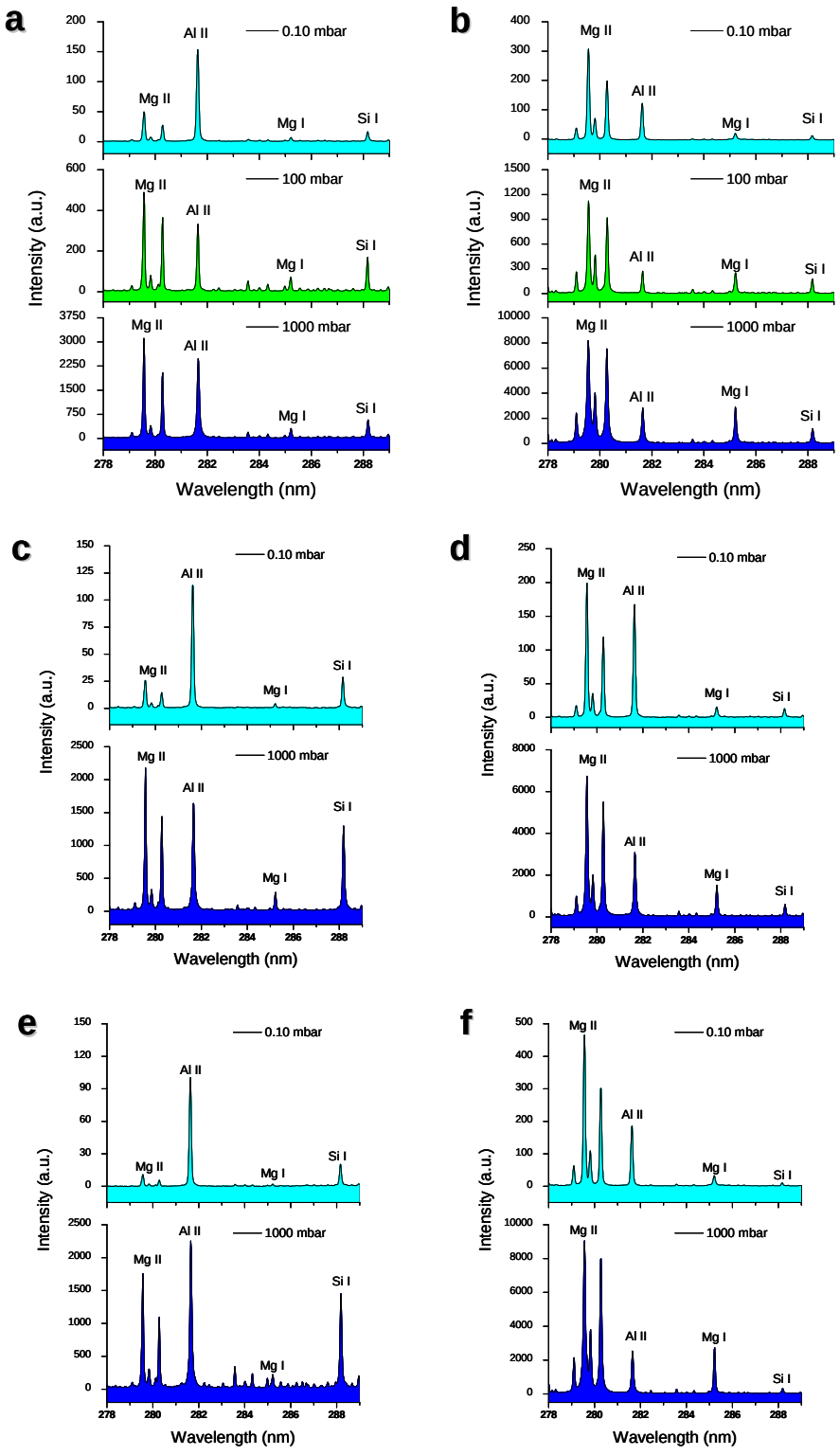

Figure 7-14. Section of laser-induced breakdown spectra of Al alloy (a) B8, (b) SM10, (c) D33, (d) S4, (e) V14 and (f) Z8 at different ambient pressures (cyan: 0.1 mbar, green: 100 mbar, blue: 1000 mbar).

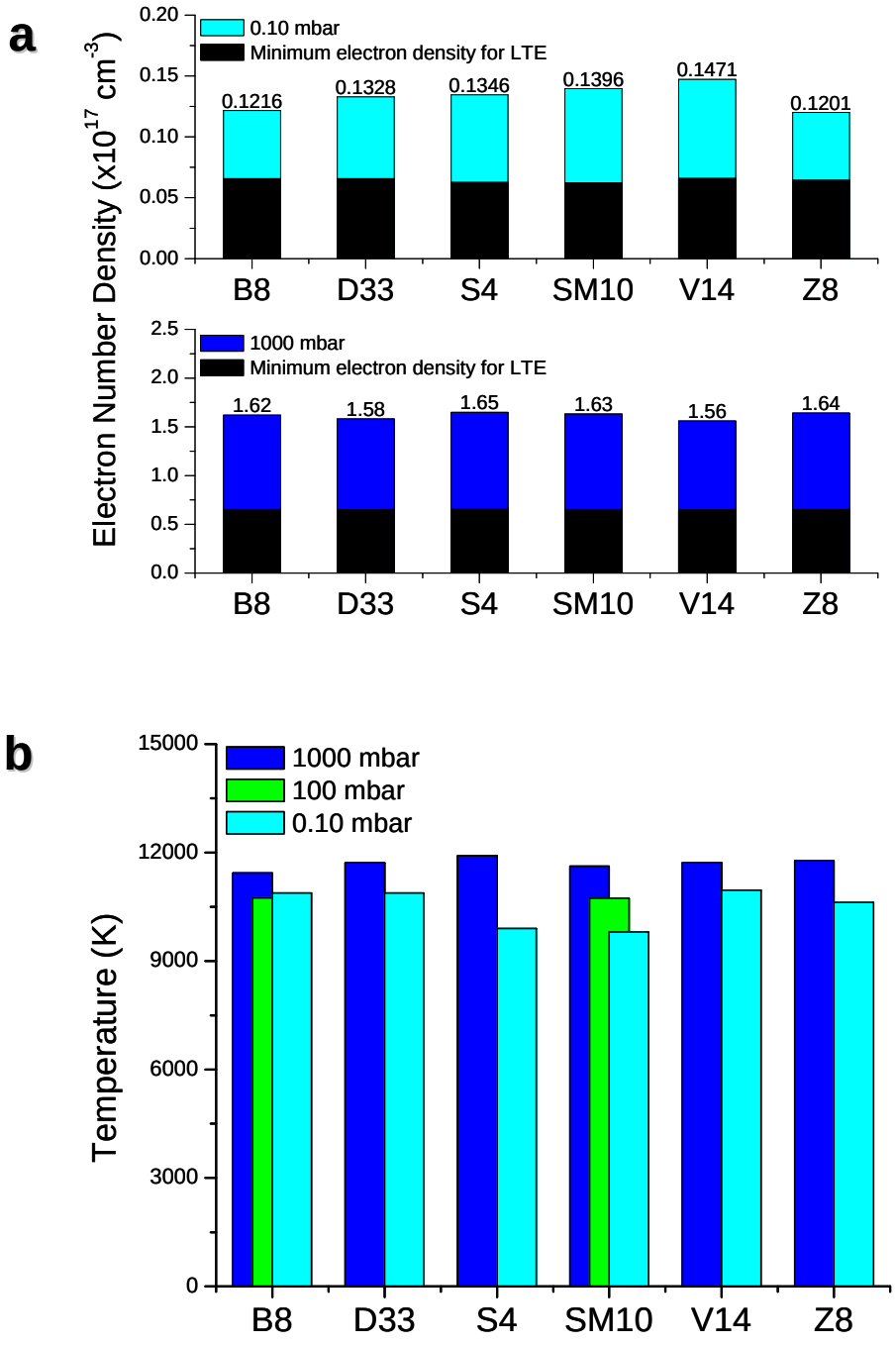

Figure 7-15. Calculated (a) electron number density and (b) temperature values for different Al alloys under different ambient pressures.

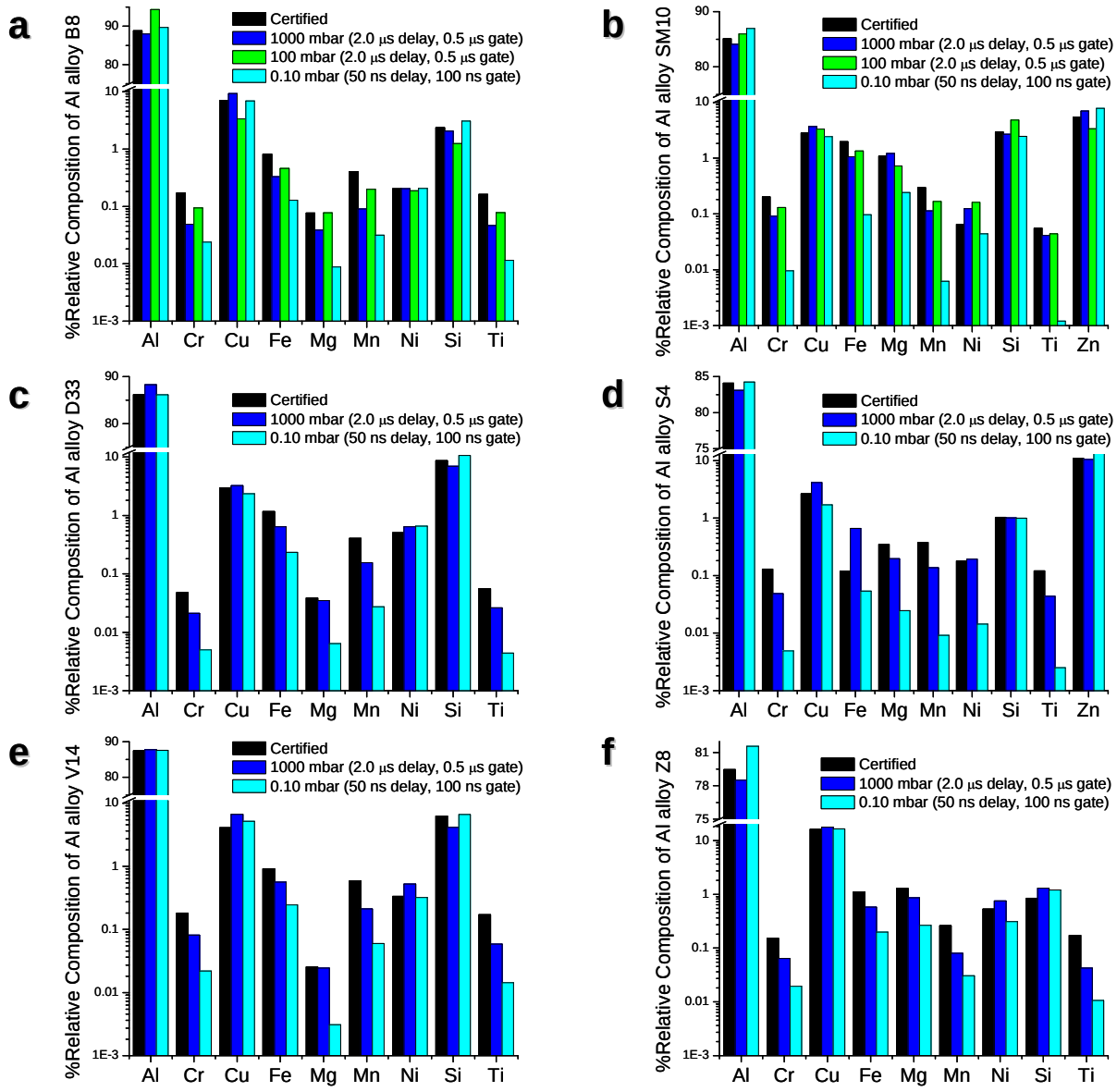

Figure 7-16. Relative elemental concentrations of Al alloy (a) B8, (b) SM10, (c) D33, (d) S4, (e) V14 and (f) Z8 at different ambient pressures (cyan: 0.1 mbar, green: 100 mbar, blue: 1000 mbar, black: certified).

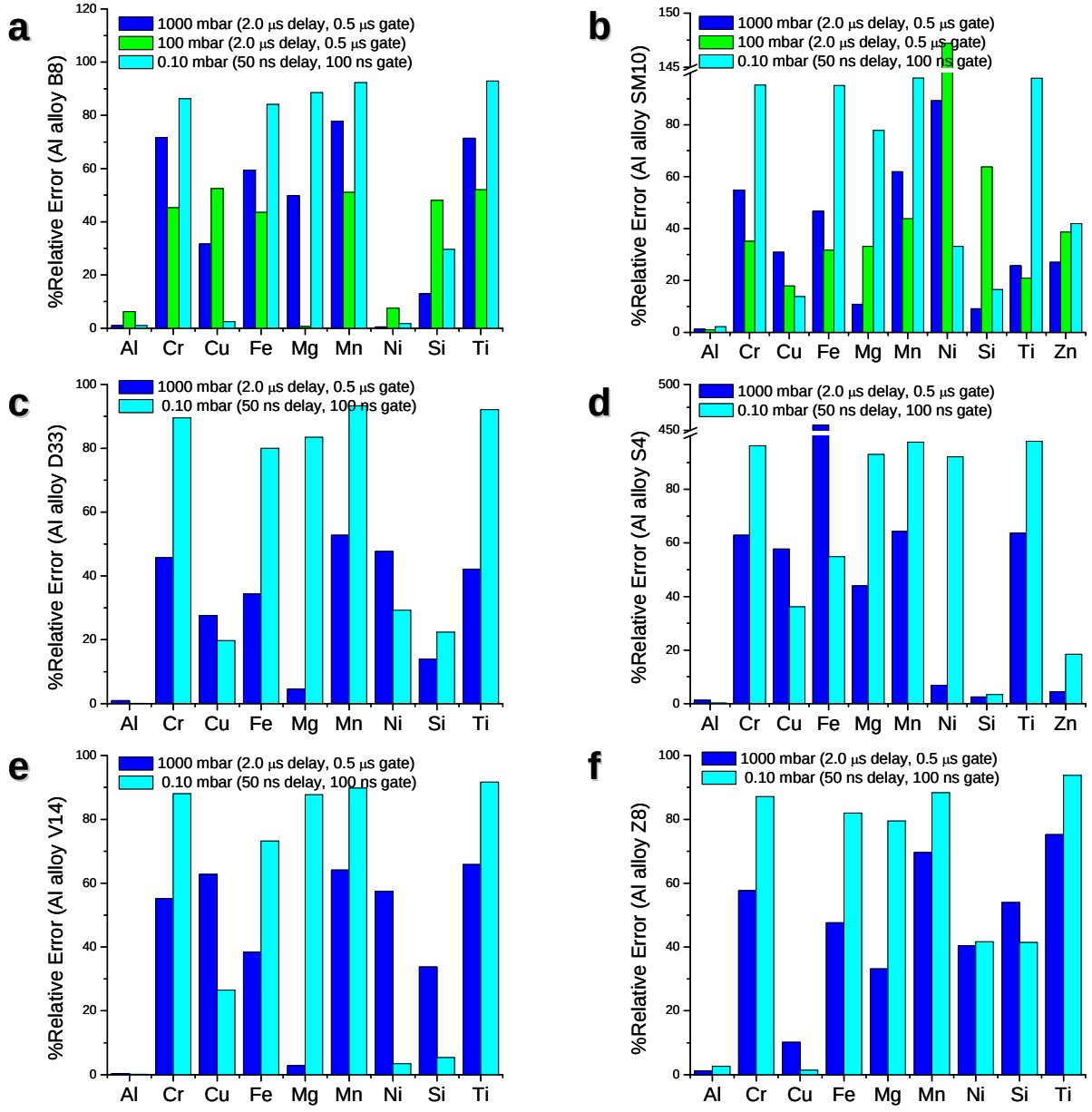

Figure 7-17. Relative errors of calculated elemental concentrations of Al alloy (a) B8, (b) SM10, (c) D33, (d) S4, (e) V14 and (f) Z8 at different ambient pressures (cyan: 0.1 mbar, green: 100 mbar, blue: 1000 mbar).

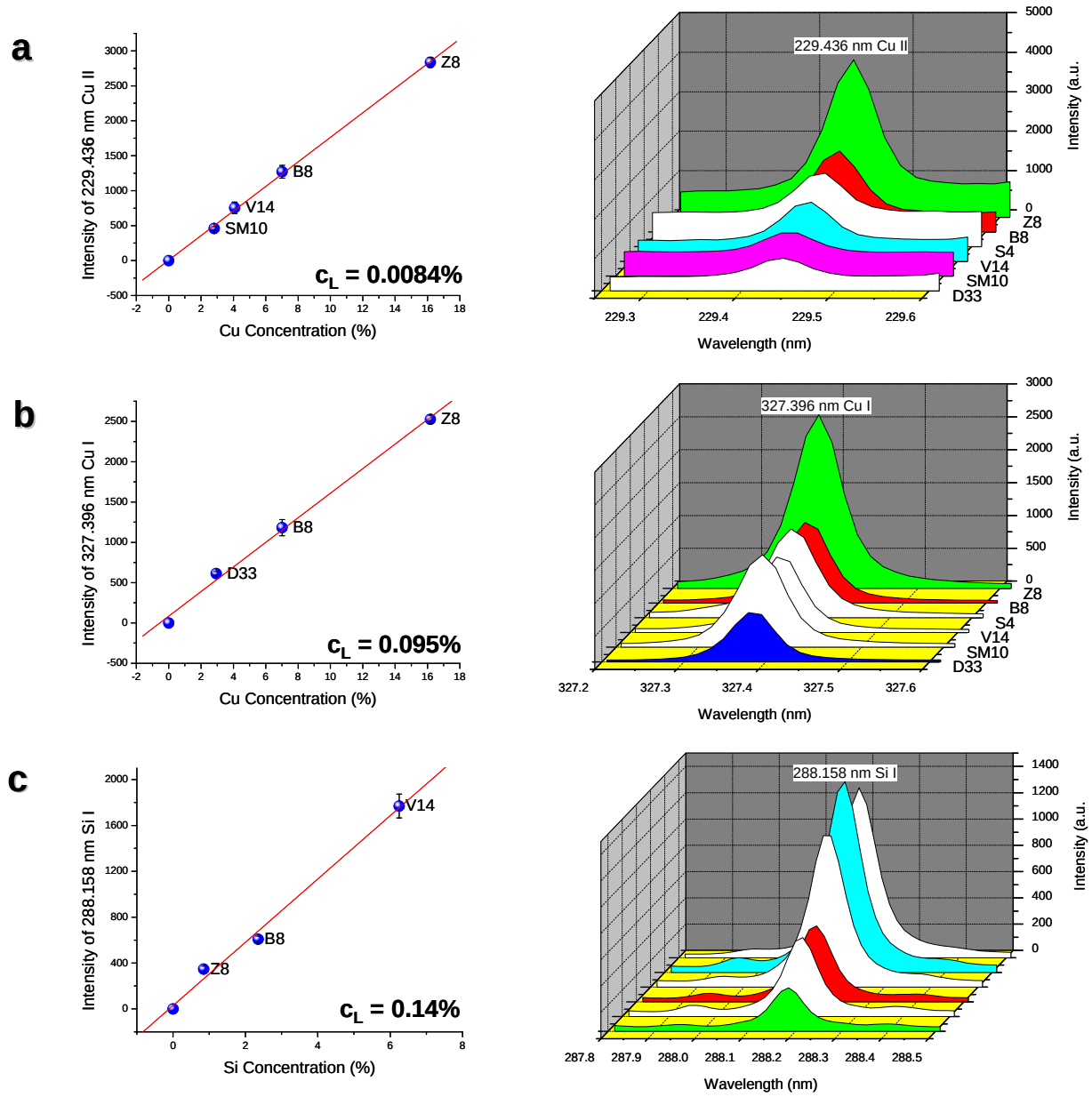

Figure 7-18. Calibration curves constructed for the quantitative analysis of Cu and Si in the Al alloy samples using (a) 229.436 nm Cu II, (b) 327.396 nm Cu I and (c) 288.158 nm Si I.

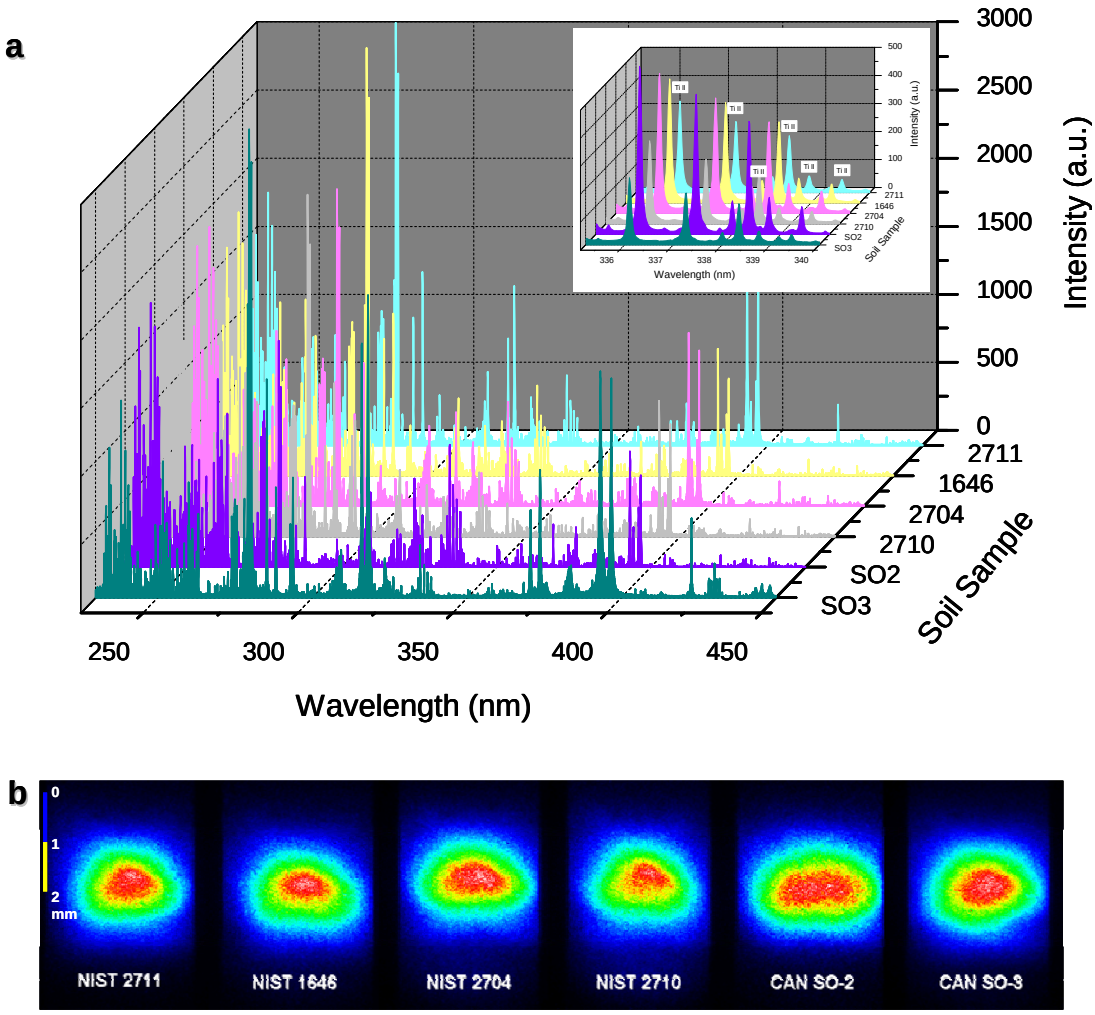

Figure 7-19. LIBS measurements of 6 soil standards. A section of the laser-induced breakdown spectra of soil samples showing selected Ti I lines are shown in (a) and the corresponding images of the laser-induced plasma obtained at 1.2 μs delay time and 0.1 μs gate width are illustrated in (b).

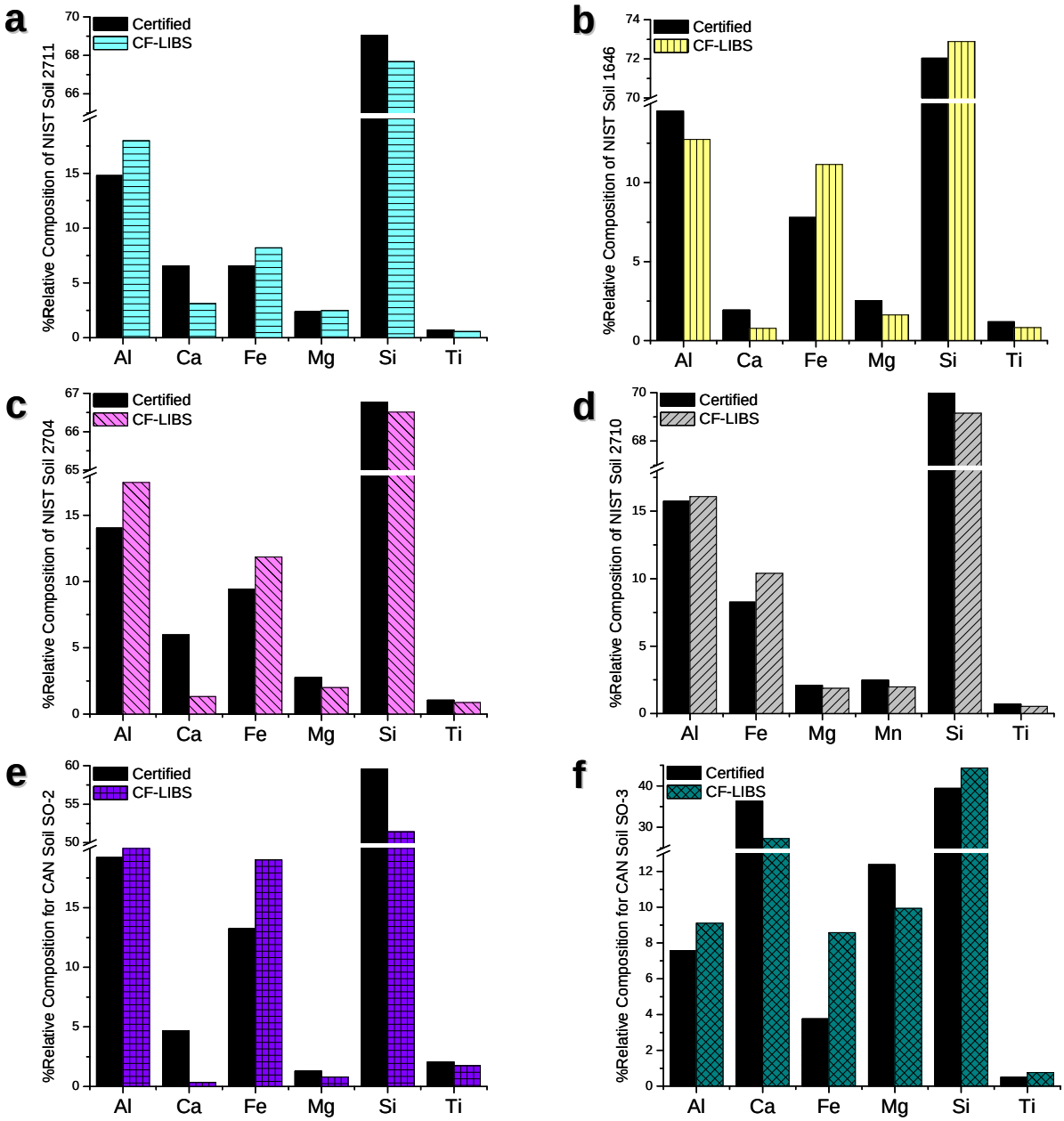

Figure 7-20. Relative elemental concentrations of soil standards (a) NIST SRM 2711, (b) NIST SRM 1646, (c) NIST SRM 2704, (d) NIST SRM 2710, (e) CAN SO-2 and (f) CAN SO-3 calculated from CF-LIBS.

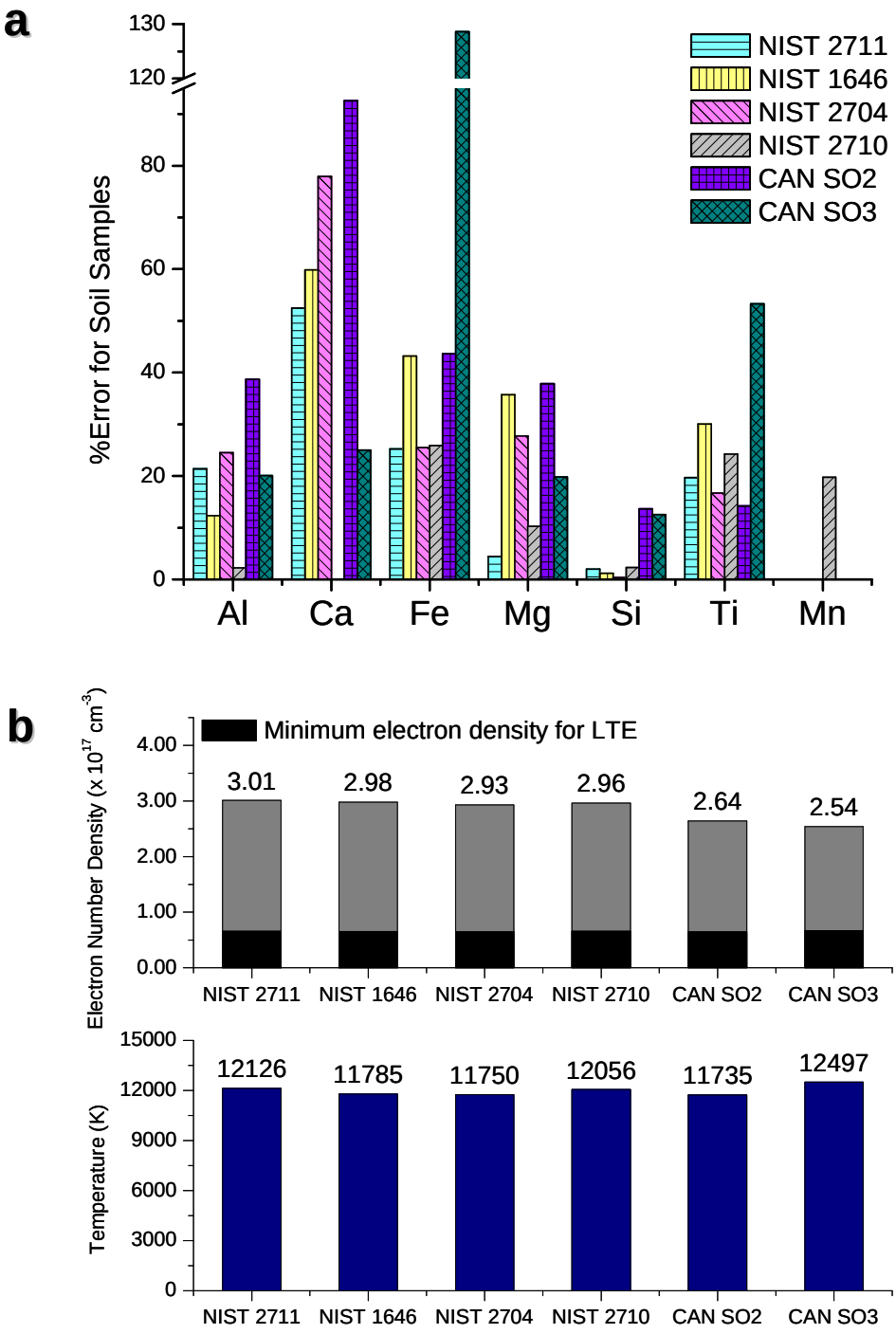

Figure 7-21. The relative errors of calculated elemental concentrations of soil standards are shown in (a) while the electron number density and temperature values of the laser-induced plasmas are shown in (b).

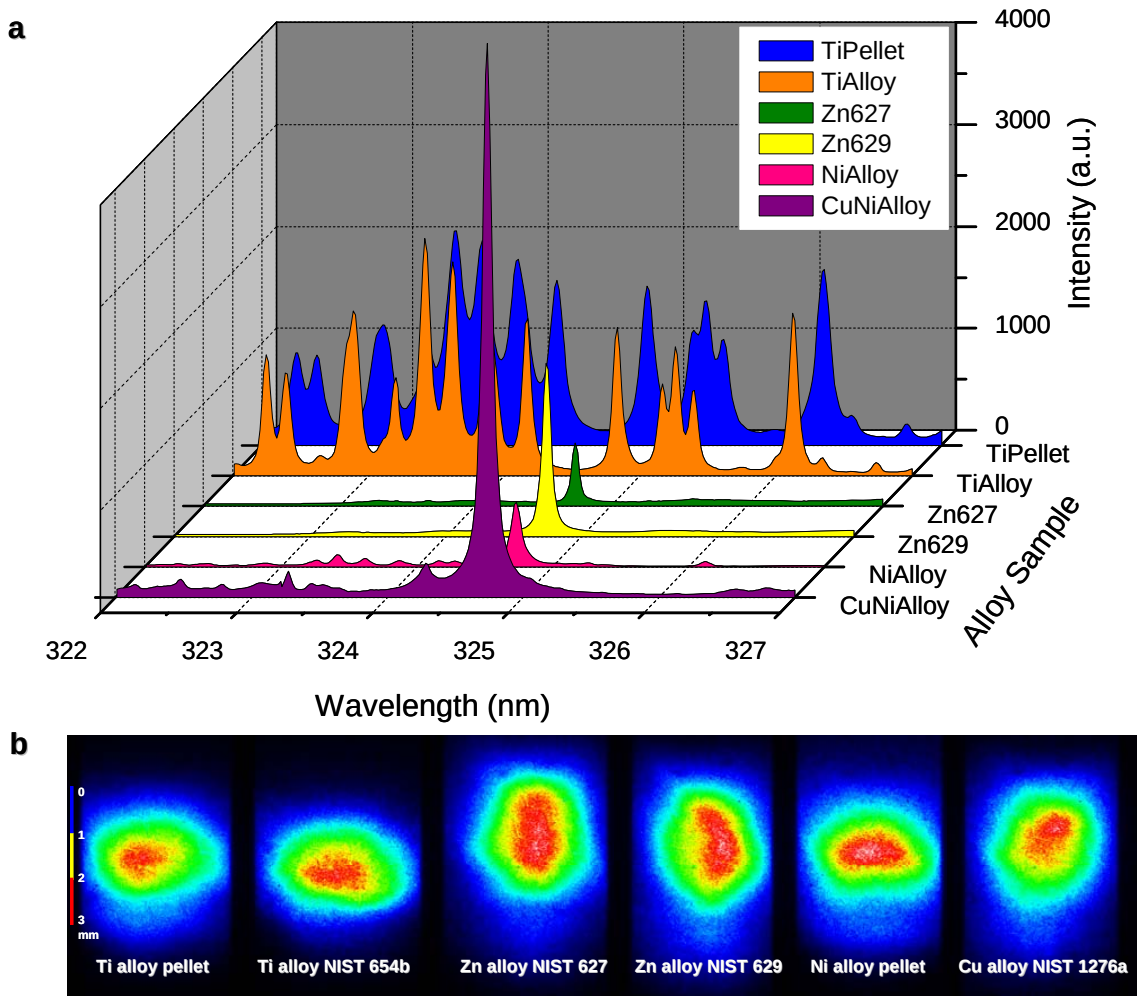

Figure 7-22. LIBS measurements of 6 different alloy standards. A section of the laser-induced breakdown spectra of alloy samples are shown in (a) and the corresponding images of the laser-induced plasma obtained are illustrated in (b).

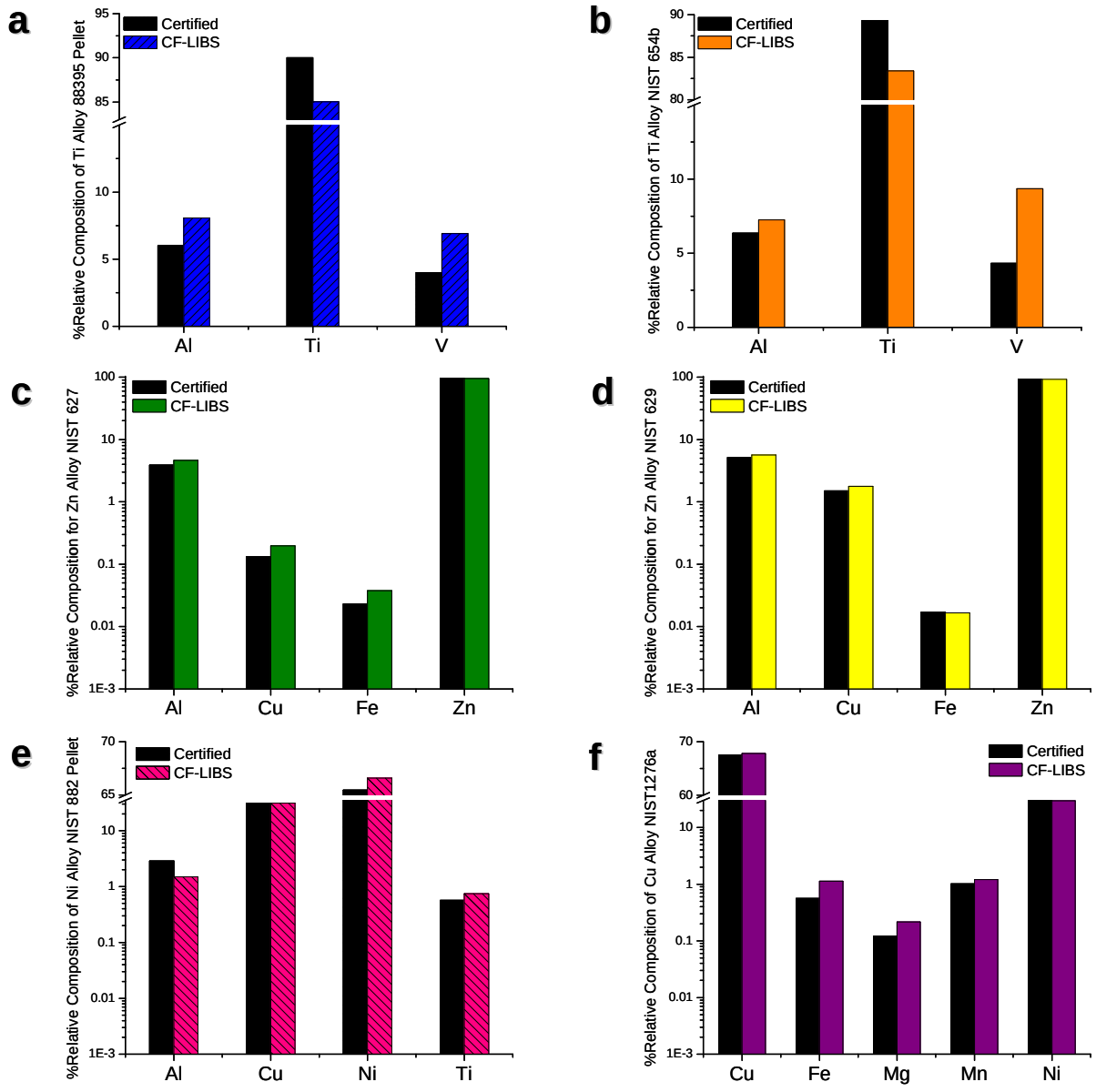

Figure 7-23. Relative elemental concentrations of alloy standards (a) Alfa Aesar 88395 Ti alloy pellet, (b) NIST SRM 654b Ti alloy, (c) NIST SRM 627 Zn alloy, (d) NIST SRM 629 Zn alloy, (e) NIST SRM 882 Ni alloy pellet and (f) NIST SRM 1276a Cu-Ni alloy calculated from CF-LIBS.

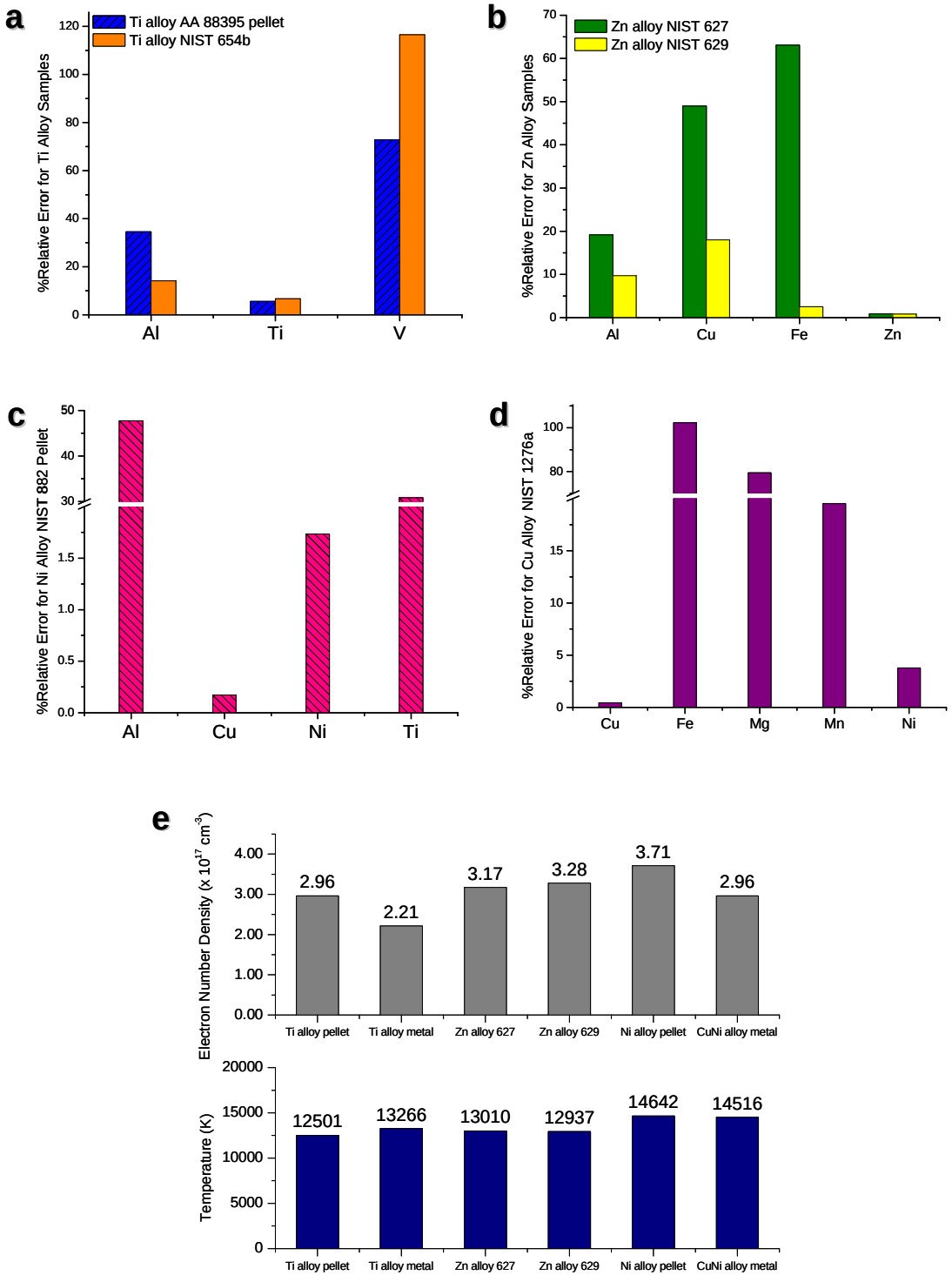

Figure 7-24. The relative errors of calculated elemental concentrations of alloy standards are shown in (a)-(d) while the electron number density and temperature values of the laser-induced plasmas are shown in (e).

Table 7-1. Electron number density, temperature and relative standard deviation calculated for aluminum alloy B8 at 5 different delay times.

Delay time (μs)	Electron density, n_e ($\times 10^{17}$ cm^{-3})	Minimum n_e for LTE ($\times 10^{17}$ cm^{-3})	RSD in n_e (%)	Temperature, T ($\times 10^4$ K)	RSD in T (%)
0.5	3.6 ± 0.1	0.696	2.8	1.4 ± 0.1	7.4
1.0	1.65 ± 0.03	0.668	1.8	1.2 ± 0.1	8.9
1.5	1.027 ± 0.006	0.643	0.6	1.15 ± 0.07	5.7
2.0	0.67 ± 0.02	0.622	3.0	1.07 ± 0.05	4.9
3.0	0.37 ± 0.02	0.596	5.4	0.99 ± 0.06	6.5

Table 7-2. Electron number density, temperature and relative standard deviation calculated for aluminum alloy SM10 at 6 different delay times.

Delay time (μs)	Electron density, n_e ($\times 10^{17}$ cm^{-3})	Minimum n_e for LTE ($\times 10^{17}$ cm^{-3})	RSD in n_e (%)	Temperature, T ($\times 10^4$ K)	RSD in T (%)
0.5	2.7 ± 0.2	0.692	7.4	1.33 ± 0.08	6.1
1.0	1.25 ± 0.05	0.661	4.0	1.2 ± 0.1	9.3
1.5	0.99 ± 0.06	0.647	6.1	1.2 ± 0.1	12.0
2.0	0.56 ± 0.01	0.621	1.8	1.07 ± 0.05	4.8
2.5	0.47 ± 0.01	0.612	2.1	1.04 ± 0.07	6.9
3.0	0.32 ± 0.02	0.597	6.3	0.99 ± 0.06	6.2

Table 7-3. Relative concentration values (in %) calculated from CF-LIBS analysis of aluminum alloy B8 at 5 different delay times.

Element	0.5 μs	1.0 μs	1.5 μs	2.0 μs	3.0 μs	Certified
Al	87.3	87.7	94.5	94.3	91.1	88.8095
Cr	0.1	0.06	0.09	0.09	0.06	0.1716
Cu	8.0	9.9	3.3	3.3	5.7	7.0155
Fe	0.9	0.5	0.5	0.5	0.4	0.8075
Mg	0.09	0.1	0.07	0.08	0.05	0.0767
Mn	0.3	0.2	0.2	0.2	0.2	0.4038
Ni	0.5	0.2	0.2	0.2	0.2	0.2019
Si	2.7	1.3	1.1	1.2	2.3	2.3520
Ti	0.1	0.05	0.08	0.08	0.06	0.1615

Table 7-4. Relative concentration values (in %) calculated from CF-LIBS analysis of aluminum alloy SM10 at 6 different delay times.

Element	0.5 μs	1.0 μs	1.5 μs	2.0 μs	2.5 μs	3.0 μs	Certified
Al	84.8	83.6	83.3	85.9	84.4	84.5	85.0998
Cr	0.2	0.08	0.06	0.1	0.08	0.2	0.2010
Cu	2.2	5.4	5.6	3.3	5.9	2.7	2.8142
Fe	1.3	1.0	1.0	1.3	1.1	1.2	1.9700
Mg	1.1	0.7	0.5	0.7	0.7	0.7	1.0855
Mn	0.2	0.1	0.09	0.2	0.1	0.2	0.2965
Ni	0.2	0.2	0.2	0.2	0.1	0.4	0.0653
Si	3.0	2.5	3.2	4.8	3.7	3.9	2.9348
Ti	0.04	0.04	0.03	0.04	0.04	0.05	0.0553
Zn	7.0	6.3	5.9	3.4	3.8	6.2	5.4777

Table 7-5. Relative errors (in %) calculated from CF-LIBS analysis of aluminum alloy B8 at 5 different delay times.

Element	0.5 μs	1.0 μs	1.5 μs	2.0 μs	3.0 μs
Al	1.7	1.2	6.4	6.2	2.6
Cr	22.1	67.4	47.8	45.3	66.0
Cu	13.9	41.5	52.6	52.5	19.4
Fe	9.6	32.5	37.0	43.5	53.9
Mg	15.6	31.6	13.1	0.6	36.3
Mn	23.8	58.1	47.7	51.0	60.5
Ni	128.6	2.4	13.9	7.5	8.9
Si	15.7	46.9	55.1	48.0	1.4
Ti	39.3	67.3	52.0	52.0	64.8

Table 7-6. Relative errors (in %) calculated from CF-LIBS analysis of aluminum alloy SM10 at 6 different delay times.

Element	0.5 μs	1.0 μs	1.5 μs	2.0 μs	2.5 μs	3.0 μs
Al	0.3	1.7	2.1	1.0	0.8	0.7
Cr	22.8	61.1	68.9	35.1	60.3	21.9
Cu	21.2	93.3	100.4	17.8	108.8	5.1
Fe	34.8	47.4	47.1	31.7	43.3	41.0
Mg	0.4	33.9	52.1	33.1	31.5	31.4
Mn	32.6	65.7	69.9	43.7	53.2	39.5
Ni	191.4	170.5	148.6	147.2	126.7	496.7
Si	1.2	14.9	9.8	63.7	25.7	33.3
Ti	24.4	35.7	50.1	22.2	23.1	13.5
Zn	28.6	15.0	7.7	38.6	31.4	14.0

Table 7-7. Relative concentration values and relative errors (in %) calculated from CF-LIBS analysis of 10 NIST brass standards.

NIST Standard	Relative Concentration of Cu (%)		Relative Concentration of Zn (%)		Relative Error (%)	
	Certified	CF-LIBS	Certified	CF-LIBS	Cu	Zn
1107	62.111	62.9	37.889	37.1	1.3	2.0
1108	65.362	65.0	34.638	35.0	0.6	1.1
1110	84.768	83.9	15.232	16.1	1.0	5.7
1111	87.184	86.8	12.816	13.7	0.5	7.2
1115	88.234	87.6	11.766	12.4	0.7	5.1
1116	90.542	89.7	9.458	10.3	0.9	8.9
1117	93.122	92.2	6.878	7.8	0.9	12.8
1112	93.680	92.9	6.320	7.0	0.8	11.1
1113	95.192	94.9	4.808	5.1	0.3	6.7
1114	96.527	96.1	3.473	3.9	0.4	11.2

Table 7-8. Temperature, electron number density and minimum electron number density for LTE calculated from CF-LIBS analysis 10 NIST brass standards.

NIST Standard	Temperature, T ($\times 10^4$ K)	Electron density, n_e ($\times 10^{17}$ cm^{-3})	Minimum n_e for LTE ($\times 10^{17}$ cm^{-3})
1107	1.34 $\pm$ 0.06	1.59 $\pm$ 0.02	0.275
1108	1.35 $\pm$ 0.07	1.75 $\pm$ 0.02	0.275
1110	1.40 $\pm$ 0.05	1.46 $\pm$ 0.02	0.281
1111	1.38 $\pm$ 0.06	1.50 $\pm$ 0.02	0.279
1115	1.40 $\pm$ 0.07	1.36 $\pm$ 0.02	0.280
1116	1.40 $\pm$ 0.07	1.45 $\pm$ 0.02	0.280
1117	1.40 $\pm$ 0.05	1.31 $\pm$ 0.02	0.280
1112	1.40 $\pm$ 0.06	1.37 $\pm$ 0.02	0.280
1113	1.40 $\pm$ 0.05	1.47 $\pm$ 0.02	0.280
1114	1.40 $\pm$ 0.06	1.21 $\pm$ 0.02	0.280

Table 7-9. Spectroscopic parameters of Zn spectral lines used in the calibration curves for brass analysis.

Specie	Zn II	Zn I	Zn I
Wavelength, λ (nm)	255.795	328.233	330.258
Lower energy level, E_i (cm^{-1})	49355	32311	32501
Upper energy level, E_k (cm^{-1})	88437	62769	62772
Transition probability, A_{ki} (s^{-1})	3.26×10^8	0.87×10^8	1.07×10^8
Lower level degeneracy, g_i	4	1	3
Upper level degeneracy, g_k	2	3	5

Table 7-10. Zn calibration curve parameters and limits of detection.

Specie	255. 795 nm Zn II	328.233 nm Zn I	330.258 nm Zn I
Slope, m	152.1 ± 2.7	107.8 ± 5.2	176.2 ± 5.5
Intercept, b (%)	-115.8 ± 50.5	113.2 ± 77.7	-75.0 ± 47.8
Correlation coefficient, R	0.99782	0.99432	0.99612
Limit of detection, c_L (%)	0.17	0.12	0.084

Table 7-11. Relative concentration of Zn (in %) calculated using CF-LIBS and conventional LIBS approaches.

Sample	Certified	CF-LIBS	Calibration curve		
			255.795 nm Zn II	328.233 nm Zn I	330.258 nm Zn I
1110	15.232	16.1		11.9 ± 1.0	
1111	12.816	13.7	11.3 ± 0.5		14.0 ± 0.9
1112	6.320	7.1	7.0 ± 0.4	8.0 ± 1.0	6.5 ± 0.4
1116	9.458	10.3		7.6 ± 1.0	7.8 ± 0.4

Table 7-12. Relative errors (in %) in calculated Zn concentration.

Sample	CF-LIBS	Calibration curve		
		255.795 nm Zn II	328.233 nm Zn I	330.258 nm Zn I
1110	5.7		22.0	
1111	7.2	12.2		9.1
1112	12.0	10.4	26.7	2.3
1116	8.9		20.2	17.8

Table 7-13. Electron number density and minimum electron number density for LTE calculated for 6 Al alloy standards at different ambient pressures.

Al alloy sample	Electron density, n_e ($\times 10^{17}$ cm^{-3})			Minimum n_e for LTE ($\times 10^{17}$ cm^{-3})		
	1000 mbar	100 mbar	0.10 mbar	1000 mbar	100 mbar	0.10 mbar
B8	1.62	0.667	0.122	0.646	0.622	0.0656
D33	1.58		0.133	0.649		0.0656
S4	1.65		0.135	0.655		0.0626
SM10	1.63	0.560	0.140	0.647	0.621	0.0623
V14	1.56		0.147	0.649		0.0659
Z8	1.64		0.120	0.651		0.0648

Table 7-14. Laser-induced plasma temperatures calculated for 6 Al alloy standards at different ambient pressures.

Al alloy sample	Temperature, T ($\times 10^4$ K)		
	1000 mbar	100 mbar	0.10 mbar
B8	1.14	1.07	1.09
D33	1.17		1.09
S4	1.19		0.99
SM10	1.16	1.07	0.98
V14	1.17		1.10
Z8	1.18		1.06

Table 7-15. Relative concentration values and relative errors (in %) calculated from CF-LIBS analysis of aluminum alloy B8 at 3 different pressures.

Element	Certified	Relative concentration			Relative error		
		1000 mbar	100 mbar	0.1 mbar	1000 mbar	100 mbar	0.1 mbar
Al	88.8095	88.0	94.3	89.7	1.0	6.2	1.0
Cr	0.1716	0.05	0.09	0.02	71.6	45.3	86.2
Cu	7.0155	9.2	3.3	6.8	31.6	52.5	2.4
Fe	0.8075	0.3	0.5	0.1	59.4	43.5	84.1
Mg	0.0767	0.04	0.08	0.009	49.8	0.6	88.5
Mn	0.4038	0.09	0.2	0.03	77.8	51.0	92.3
Ni	0.2019	0.2	0.2	0.2	0.5	7.5	1.7
Si	2.3520	2.0	1.2	3.0	12.9	48.0	29.6
Ti	0.1615	0.05	0.08	0.01	71.4	52.0	92.9

Table 7-16. Relative concentration values and relative errors (in %) calculated from CF-LIBS analysis of aluminum alloy SM10 at 3 different pressures.

Element	Certified	Relative concentration			Relative error		
		1000 mbar	100 mbar	0.1 mbar	1000 mbar	100 mbar	0.1 mbar
Al	85.0998	84.1	85.9	87.0	1.2	1.0	2.2
Cr	0.2010	0.09	0.1	0.01	54.8	35.1	95.3
Cu	2.8142	3.7	3.3	2.4	30.8	17.8	13.7
Fe	1.9700	1.1	1.3	0.1	46.7	31.7	95.1
Mg	1.0855	1.2	0.7	0.2	10.8	33.1	77.8
Mn	0.2965	0.1	0.2	0.006	61.9	43.7	97.9
Ni	0.0653	0.1	0.2	0.04	89.2	147.2	33.1
Si	2.9348	2.7	4.8	2.5	9.1	63.7	16.5
Ti	0.0553	0.04	0.04	0.001	25.7	21.0	97.8
Zn	5.4777	7.0	3.4	7.8	27.0	38.6	41.9

Table 7-17. Relative concentration values and relative errors (in %) calculated from CF-LIBS analysis of aluminum alloy D33 at 2 different pressures.

Element	Certified	Relative concentration		Relative error	
		1000 mbar	0.1 mbar	1000 mbar	0.1 mbar
Al	86.1782	88.3	86.1	1.0	0.1
Cr	0.04770	0.02	0.005	45.7	89.5
Cu	2.9328	3.3	2.4	27.6	19.7
Fe	1.1670	0.6	0.2	34.3	80.0
Mg	0.0386	0.03	0.006	4.5	83.4
Mn	0.4059	0.2	0.03	52.7	93.3
Ni	0.5074	0.6	0.7	47.7	29.2
Si	8.6665	7.0	10.6	14.0	22.4
Ti	0.0558	0.03	0.004	42.1	92.1

Table 7-18. Relative concentration values and relative errors (in %) calculated from CF-LIBS analysis of aluminum alloy S4 at 2 different pressures.

Element	Certified	Relative concentration		Relative error	
		1000 mbar	0.1 mbar	1000 mbar	0.1 mbar
Al	84.0937	83.1	84.2	1.2	0.2
Cr	0.1305	0.05	0.005	62.8	96.2
Cu	2.6495	4.2	1.7	57.7	36.1
Fe	0.1194	0.7	0.05	455.6	54.9
Mg	0.3513	0.2	0.03	44.0	93.0
Mn	0.3814	0.1	0.009	64.2	97.6
Ni	0.1807	0.2	0.01	6.8	92.1
Si	1.0337	1.0	1.0	2.5	3.4
Ti	0.1204	0.04	0.003	63.6	97.9
Zn	10.9394	10.5	13.0	4.4	18.4

Table 7-19. Relative concentration values and relative errors (in %) calculated from CF-LIBS analysis of aluminum alloy V14 at 2 different pressures.

Element	Certified	Relative concentration		Relative error	
		1000 mbar	0.1 mbar	1000 mbar	0.1 mbar
Al	87.4618	87.8	87.6	0.3	0.1
Cr	0.1815	0.08	0.02	55.2	88.0
Cu	4.0836	6.6	5.2	62.7	26.4
Fe	0.9075	0.6	0.2	38.3	73.2
Mg	0.0252	0.02	0.003	2.8	87.7
Mn	0.5848	0.2	0.06	64.1	89.8
Ni	0.3327	0.5	0.3	57.5	3.4
Si	6.2514	4.1	6.6	33.7	5.4
Ti	0.1714	0.06	0.01	65.8	91.7

Table 7-20. Relative concentration values and relative errors (in %) calculated from CF-LIBS analysis of aluminum alloy Z8 at 2 different pressures.

Element	Certified	Relative concentration		Relative error	
		1000 mbar	0.1 mbar	1000 mbar	0.1 mbar
Al	79.4669	78.5	81.6	1.2	2.6
Cr	0.1513	0.06	0.02	57.6	87.1
Cu	16.1865	17.8	16.4	10.1	1.4
Fe	1.0993	0.6	0.2	47.6	82.0
Mg	1.2808	0.9	0.3	33.1	79.5
Mn	0.2622	0.08	0.03	69.6	88.3
Ni	0.5345	0.8	0.3	40.5	41.6
Si	0.8471	1.3	1.2	53.9	41.4
Ti	0.1714	0.04	0.01	75.2	93.8

Table 7-21. Spectroscopic parameters of spectral lines used in the calibration curves for Al alloy analysis.

Specie	Cu II	Cu I	Si I
Wavelength, λ (nm)	229.436	327.396	288.158
Lower energy level, E_i (cm^{-1})	22847	0	6299
Upper energy level, E_k (cm^{-1})	66419	30535	40992
Transition probability, A_{ki} (s^{-1})	0.25×10^8	1.36×10^8	1.89×10^8
Lower level degeneracy, g_i	5	2	5
Upper level degeneracy, g_k	5	2	3

Table 7-22. Cu and Si calibration curve parameters and limits of detection.

Specie	229.436 nm Cu II	327.396 nm Cu I	288.158 nm Si I
Slope, m	175.7 ± 2.9	152.6 ± 7.2	275.8 ± 16.9
Intercept, b (%)	6.7 ± 24.0	83.6 ± 64.2	28.8 ± 56.9
Correlation coefficient, R	0.99916	0.99559	0.99627
Limit of detection, c_L (%)	0.0084	0.095	0.14

Table 7-23. Relative concentration of Cu (in %) calculated using CF-LIBS and conventional LIBS approaches.

Sample	Certified	CF-LIBS	Calibration curve	
			229.436 nm Cu II	327.396 nm Cu I
D33	2.9328	3.7	2.2 ± 0.3	
S4	2.6495	3.8	5.4 ± 0.2	8.2 ± 0.6
SM10	2.8142	3.5		7.5 ± 0.8
V14	4.0836	6.2		5.9 ± 0.7

Table 7-24. Relative errors (in %) in calculated Cu concentration.

Sample	CF-LIBS	Calibration curve	
		229.436 nm Cu II	327.396 nm Cu I
D33	27.60	23.5	
S4	42.02	102.6	210.5
SM10	23.15		165.3
V14	52.67		43.7

Table 7-25. Relative concentration of Si and relative errors (in %) calculated using CF-LIBS and conventional LIBS approaches.

Sample	Certified	CF-LIBS	Calibration curve	Relative error	
			288.158 nm Si I	CF-LIBS	Calibration curve
D33	8.6665	7.0	5.8 ± 0.4	19.6	33.0
S4	1.0337	1.0	2.4 ± 0.3	2.5	132.0
SM10	2.9348	2.7	5.2 ± 0.4	9.1	76.2

Table 7-26. Relative concentration values and relative errors (in %) calculated from CF-LIBS analysis of Montana soil NIST SRM 2711 and Estuarine sediment NIST SRM 1646.

Element	NIST SRM 2711			NIST SRM 1646		
	Certified	CF-LIBS	Relative error	Certified	CF-LIBS	Relative error
Al	14.8086	18.0	21.4	14.5248	12.7	12.3
Ca	6.5312	3.1	52.5	1.9289	0.8	59.8
Fe	6.5539	8.2	25.3	7.7853	11.1	43.2
Mg	2.3812	2.5	4.4	2.5331	1.6	35.7
Si	69.0312	67.7	2.0	72.0428	72.9	1.2
Ti	0.6939	0.6	19.7	1.1852	0.8	30.1

Table 7-27. Relative concentration values and relative errors (in %) calculated from CF-LIBS analysis of Buffalo River sediment NIST SRM 2704 and Montana soil NIST SRM 2710.

Element	NIST SRM 2704			NIST SRM 2710		
	Certified	CF-LIBS	Relative error	Certified	CF-LIBS	Relative error
Al	14.0276	17.5	24.5	15.7319	16.1	2.3
Ca	5.9692	1.3	77.9			
Fe	9.4359	11.8	25.5	8.2568	10.4	25.8
Mg	2.7550	2.0	27.7	2.0837	1.9	10.3
Mn				2.4673	2.0	19.8
Si	66.7631	66.5	0.4	70.7690	69.2	2.3
Ti	1.0492	0.9	16.7	0.6913	0.5	24.3

Table 7-28. Relative concentration values and relative errors (in %) calculated from CF-LIBS analysis of Canadian soils SO-2 and SO-3.

Element	CAN SO-2			CAN SO-3		
	Certified	CF-LIBS	Relative error	Certified	CF-LIBS	Relative error
Al	19.2234	26.7	38.7	7.5814	9.1	20.1
Ca	4.6689	0.3	92.6	36.3659	27.3	25.0
Fe	13.2444	19.0	43.7	3.7534	8.6	128.6
Mg	1.2863	0.8	37.8	12.3788	9.9	19.8
Si	59.5284	51.4	13.6	39.4233	44.4	12.5
Ti	2.0486	1.8	14.2	0.4971	0.8	53.3

Table 7-29. Temperature, electron number density and minimum electron number density for LTE calculated from CF-LIBS analysis of 6 soil standards.

Soil Standard	Temperature, T ($\times 10^4$ K)	Electron number density, n_e ($\times 10^{17}$ cm^{-3})	Minimum n_e for LTE ($\times 10^{17}$ cm^{-3})
NIST 2711	1.21	3.01	0.660
NIST 1646	1.18	2.98	0.651
NIST 2704	1.18	2.93	0.650
NIST 2710	1.21	2.96	0.658
CAN SO-2	1.17	2.64	0.650
CAN SO-3	1.25	2.54	0.670

Table 7-30. Relative concentration values and relative errors (in %) calculated from CF-LIBS analysis of Ti alloy pellet Alfa Aesar 88395 and Ti alloy metal NIST SRM 654b.

Element	Alfa Aesar 88395 Ti alloy pellet			NIST SRM 654b Ti alloy metal		
	Certified	CF-LIBS	Relative error	Certified	CF-LIBS	Relative error
Al	6	8.1	34.6	6.3546	7.3	14.2
Ti	90	85.0	5.5	89.3255	83.4	6.7
V	4	6.9	72.8	4.3199	9.4	116.6

Table 7-31. Relative concentration values and relative errors (in %) calculated from CF-LIBS analysis of Zn alloys NIST SRM 627 and 629.

Element	Zn alloy NIST SRM 627			Zn alloy NIST SRM 629		
	Certified	CF-LIBS	Relative error	Certified	CF-LIBS	Relative error
Al	3.8800	4.6	19.2	5.1589	5.7	9.7
Cu	0.1320	0.2	48.9	1.5026	1.8	18.0
Fe	0.0230	0.04	63.0	0.0170	0.02	2.5
Zn	95.9650	95.1	0.9	93.3215	92.6	0.8

Table 7-32. Relative concentration values and relative errors (in %) calculated from CF-LIBS analysis of Ni alloy pellet NIST SRM 882 and Cu-Ni alloy metal NIST SRM 1276a.

Element	Ni alloy pellet NIST SRM 882			Cu-Ni alloy metal NIST SRM 1276a		
	Certified	CF-LIBS	Relative error	Certified	CF-LIBS	Relative error
Al	2.8589	1.5	47.7			
Cu	31.1165	31.2	0.2	67.5068	67.8	0.4
Fe				0.5601	1.1	102.3
Mg				0.1200	0.2	79.4
Mn				1.0101	1.2	19.5
Ni	65.4529	66.6	1.7	30.8031	29.6	3.8
Ti	0.5718	0.7	30.8			

Table 7-33. Temperature and electron number density calculated from CF-LIBS analysis of 6 alloy standards.

Soil Standard	Temperature, T ($\times 10^4$ K)	Electron number density, n_e ($\times 10^{17}$ cm^{-3})
Ti alloy pellet	1.25	2.96
Ti alloy metal	1.33	2.21
Zn alloy 627	1.30	3.17
Zn alloy 629	1.29	3.28
Ni alloy pellet	1.46	3.71
Cu-Ni alloy	1.45	2.96

CHAPTER 8
CONCLUSION AND FUTURE WORK

Summary and Concluding Remarks

An extensive experimental evaluation of two existing standard-free techniques for laser-induced breakdown spectroscopy (LIBS) was carried out in this research. The calibration-free LIBS (CF-LIBS) approach and the Monte Carlo simulated annealing optimization for LIBS both have capabilities to perform semi-quantitative analysis and provide elemental sample composition without the need for analytical calibration curves. The two techniques have basic assumptions which are similar but the formulations of the algorithm are inherently different. CF-LIBS and MC-LIBS both assume that local thermodynamic equilibrium (LTE) exists in the spatial and temporal window of observation and that the plasma composition is representative of actual material composition prior to laser ablation. In terms of experimental flexibility and practicality, CF-LIBS prevails over MC-LIBS since the algorithm can be applied to any type of spectral data taken either under atmospheric or vacuum conditions. MC-LIBS, on the other hand, can only be applied to experiments performed under reduced pressures since part of the algorithm is currently a model which simulates the radiative expansion of a laser-induced plasma into vacuum. However, the calibration-free method usually requires the use of an echelle spectrometer because a large spectral range is required in order to fully characterize the plasma and extract quantitative information. In this research, it was demonstrated that a non-echelle, gated detection system with moderate resolution was feasible for obtaining multiple narrow spectral windows for use with CF-LIBS as long as the careful attention is paid to the spectral data acquisition and an intensive investigation of the instrumental function and detector spectral efficiency is carried out prior to LIBS measurement. The Monte Carlo optimization procedure has the advantage in this aspect since it can still be applied even if only a few lines are present in

a particular spectral window, although accuracy is guaranteed to improve significantly if more lines from all components in the sample are included.

CF-LIBS is also restricted to the use of neutral and singly-ionized lines while species of higher ionization stages can be included in MC-LIBS optimizations. Another requirement for CF-LIBS is that the plasma has to be optically thin. Resonance lines of major elements, which are usually self-absorbed, are simply excluded in the CF-LIBS analysis to avoid underestimation of the elemental concentration. On the other hand, the use of resonance lines in MC-LIBS does not present any difficulty since the modeling algorithm takes into account the occurrence of self-absorption or self-reversal of lines. While only spatially-integrated temperatures and electron number densities can be calculated with the CF-LIBS method based on the experimental used in this research, MC-LIBS can provide spatial and temporal evolution of temperature and electron number densities. In terms of the final output, CF-LIBS can only provide relative information, i.e., all concentration values determined are relative with respect to the number of elements included in the analysis, which is, of course, dependent on the lines present within the spectral window of observation. MC-LIBS has the advantage in this regard since it is capable of predicting absolute number densities (in cm^{-3}) for each element included in the optimization procedure.

The CF-LIBS and MC-LIBS approaches were both applied to the analysis of certified aluminum alloy samples using spatially-integrated and spatially-resolved LIBS measurements carried out under vacuum conditions. The CF-LIBS technique was further evaluated under different delay times and different ambient pressures. Different types of samples were also used, from brass to powdered soil and alloy samples. Furthermore, standard calibration curves were constructed for a few elements for comparison with CF-LIBS analysis. Laser-induced plasma

parameters, such temperature and electron number densities, were reported for each sample and for every spatial position analyzed. The accuracy of the quantitative results obtained was evaluated using relative percentage errors. Generally, for the major element present in the sample, CF-LIBS resulted in errors better than 10% while MC-LIBS resulted in errors better than 20% despite the relatively high correlation between experimental and simulated spectra ($R >$ 0.9). However, in the case of the other elements present in the sample, both methods only proved to be suitable for a semi-quantitative analysis with relative errors between 30-200%.

The errors can be due to the contributions of several factors: uncertainties in the atomic transition probabilities, uncertainties in the Stark broadening coefficients which are scattered in the literature, uncertainties in the spectral line integration for CF-LIBS and unavailability of calculated partition functions which takes into account all the bound quantum states of an atom or ion for some elements considered in the present study, and uncertainties in the temperature and electron number density determination. Experimental variables, e.g. laser fluctuations, crater formation, aerosol formation, etc., also affect the results of the analysis; however, these are controllable parameters which can be improved so that their effects can be minimized. In order to illustrate how these factors influence the calculated elemental concentration, a simple general schematic diagram is presented in Figs. 8-1a and 8-1b for CF-LIBS and MC-LIBS analysis, respectively. It is evident from Fig. 8-1 that the route to quantitative analysis, from sample to signal, is indeed a complex one [124]. However, the major factor which truly affects the calculated results and is related to most of the factors described previously is the validity of the assumptions imposed on the two algorithms, particularly, stoichiometric ablation and local thermodynamic equilibrium (LTE). If LTE condition fails, it implies that Saha, Boltzmann and Maxwell relationships cannot be used to describe the laser-induced plasma, and therefore, the

calculated plasma temperature is affected and everything else that is related to it. Stoichiometric ablation is also very important, perhaps even more important than LTE, since this is the basis of a standard-free quantitative analysis using LIBS. Even if the influences of the other variables are minimized or eliminated, if the gaseous composition of the plasma does not reflect the composition in solid phase, then the whole scheme fails. An independent investigation (see Future Research Directions) of the assumptions made in the two approaches is crucial if standard-free LIBS analysis is to compete with conventional atomic spectroscopic methods.

The experimental assessment of CF-LIBS and MC-LIBS carried out in this research is a step towards the ultimate goal of absolute analysis in analytical spectroscopy. Although further investigation is still required in order to improve the accuracy of the calculated results, it can be concluded that standard-free techniques, such as CF-LIBS and MC-LIBS, have found a niche in the matrix-effect-ridden world of laser-induced breakdown spectroscopy. This definitely opens up several avenues for the applicability of LIBS in different analytical situations.

Future Research Directions

As an addendum to the research carried out in this dissertation, independent investigations of the assumptions imposed on both approaches are required in order to determine the ideal working conditions for an accurate standard-free quantitative LIBS analysis. The verification of the existence of local thermodynamic equilibrium in laser-induced plasma has recently been proposed by Moon et al. [134] using the line-to-continuum approach which is based on a similar research done by Sola et al. [135] in which the line-to-continuum intensity ratio method was used to determine the electron temperature in a high-pressure microwave discharge. It is ideal if the LTE verification will involve experiments carried out under vacuum conditions as well. Furthermore, it is important to determine whether the elemental components of the sample enter the plasma in proportion to their solid phase concentrations. In close relation is the independent

determination of absolute number densities by scanning over absorption profiles in the plasma. This may aid in improving the accuracy of calculated results since the value obtained in the absorption experiment can be used as an initial estimate of the number densities in the Monte Carlo simulations, especially for unknown samples. An extension of the radiative post-breakdown model to plasma expansion under atmospheric conditions also needs to be carried out so that the problems inherent to vacuum experiments can be further eliminated. Initial work on this aspect has already been started by Kazakov et al. [214]. Use of an auxiliary technique which checks for self-absorption of emission lines is also ideal particularly for CF-LIBS so that lines can be excluded or included properly in the analysis on the basis of the presence or absence of self-absorption, respectively. This can be straightforwardly achieved by performing LIBS measurements with and without a concave or spherical mirror placed at the radius of curvature (Fig. 3-4) [110]. Moreover, with the advent of faster computers, the number of lines and elements included in the MC optimization procedure can be increased, as well the length of the spectral range used.

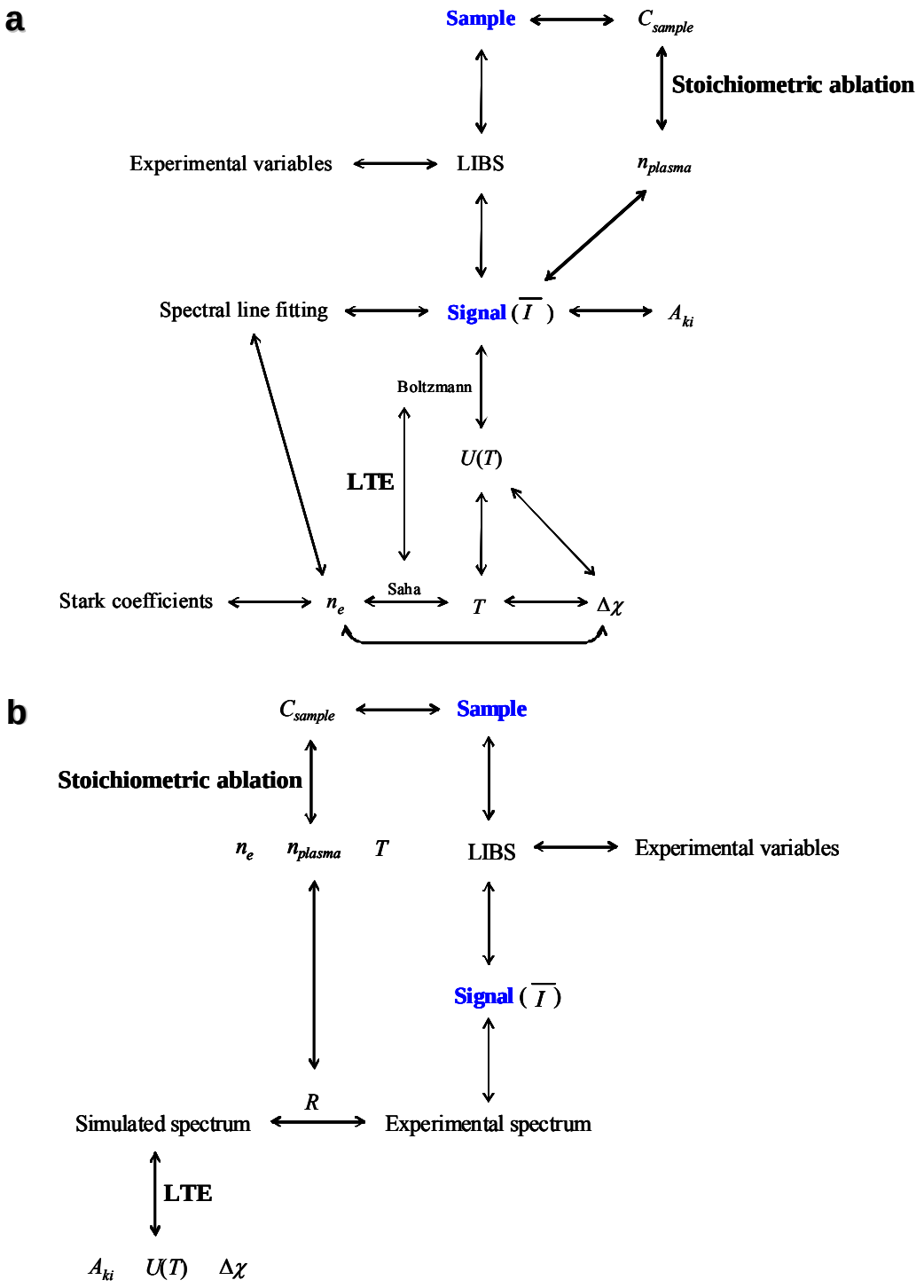

Figure 8-1. A general schematic diagram of (a) CF-LIBS and (b) MC-LIBS analysis from sample to signal. (See pp. 19-23 for the definitions of the symbols used in the scheme.)

APPENDIX A
CALCULATION OF RADIAL EXPANSION VELOCITY PROPORTIONALITY CONSTANT IN MC-LIBS

The conservation of momentum equation is given by:

$$\frac{\partial}{\partial t}\left[u\sum_j \mu^j n^j\right]+\frac{1}{r^2}\frac{\partial}{\partial r}\left(r^2u^2\sum_j \mu^j n^j\right)=-\frac{\partial p}{\partial r} \tag{A-1}$$

where μ^j is the mass of *j*th constituen*t* (g) and *p* is the gas pressure (dyne cm^{-2}). Integrating Eq. A-1 along the plasma radius *r* from 0 to *R* yields:

$$\int_0^R\left[\frac{\partial}{\partial t}\left(u\sum_j \mu^j n^j\right)+\frac{1}{r^2}\frac{\partial}{\partial r}\left(r^2u^2\sum_j \mu^j n^j\right)\right]dr=\int_0^R-\frac{\partial p}{\partial r}dr \tag{A-2}$$

Simplifying the right-hand side of Eq. A-2 yields:

$$\int_0^R\left[\frac{\partial}{\partial t}\left(u\sum_j \mu^j n^j\right)+\frac{1}{r^2}\frac{\partial}{\partial r}\left(r^2u^2\sum_j \mu^j n^j\right)\right]dr = p(0)-p(R) \tag{A-3}$$

where $p(0)$ is the pressure at the plasma center and $p(R)$ is the pressure at the outer plasma boundary which is assumed zero (vacuum). Note that the radial expansion velocity is given by:

$$u(r,t)=\zeta(t)r \tag{A-4}$$

Substituting Eq. A-4 and $p(R) = 0$ into Eq. A-3 yields:

$$\int_0^R\left[\frac{\partial}{\partial t}\left(\zeta(t)r\sum_j \mu^j n^j\right)+\frac{1}{r^2}\frac{\partial}{\partial r}\left(r^2(\zeta(t)r)^2\sum_j \mu^j n^j\right)\right]dr = p(0) \tag{A-5}$$

Expanding the integral in Eq. A-5 and simplifying some of the terms yields:

$$\int_0^R\frac{\partial}{\partial t}\left(\zeta(t)r\sum_j \mu^j n^j\right)dr+\int_0^R\frac{1}{r^2}\frac{\partial}{\partial r}\left(\zeta^2(t)r^4\sum_j \mu^j n^j\right)dr = p(0) \tag{A-6a}$$

$$\frac{\partial}{\partial t}\zeta(t)\int_0^R r\left(\sum_j \mu^j n^j\right)dr+\zeta^2(t)\int_0^R\frac{1}{r^2}\left(\frac{\partial}{\partial r}r^4\right)\left(\sum_j \mu^j n^j\right)dr = p(0) \tag{A-6b}$$

$$\frac{\partial}{\partial t}\zeta(t)\int_0^R r\left(\sum_j \mu^j n^j\right)dr + \zeta^2(t)\int_0^R \frac{1}{r^2}\left(4r^3\right)\left(\sum_j \mu^j n^j\right)dr = p(0) \tag{A-6c}$$

$$\frac{\partial}{\partial t}\zeta(t)\int_0^R r\left(\sum_j \mu^j n^j\right)dr + \zeta^2(t)\int_0^R 4r\left(\sum_j \mu^j n^j\right)dr = p(0) \tag{A-6d}$$

Further simplification of Eq. A-6d yields:

$$\left[\frac{d}{dt}\zeta(t) + 4\zeta^2(t)\right]\int_0^R\left(\sum_j \mu^j n^j\right)rdr = p(0) \tag{A-7}$$

Note that the pressure at the plasma center, $p(0)$, can be calculated using the ideal gas equation:

$$p(0) = k_B T_0 \sum_j n_0^j \tag{A-8}$$

where T_0 is the temperature in the plasma center ($r = 0$), in K, and is also the initial guess for T provided in the simulation and n_0^j is the initial guess for the total number density for the jth constituent. Recall that the initial distribution function for temperature and number density are given by

$$T(r,0) = T_0\left(1 - k_1 r^2\right) \tag{A-9}$$

and

$$n^j(r,0) = n_0^j\left(1 - k_2 r^2\right) = g^j(r), \tag{A-10}$$

respectively, where k_1 and k_2 are numerical coefficients used for setting the boundary conditions. Substituting Eq. A-8 into Eq. A-7 yields:

$$\left[\frac{d}{dt}\zeta(t) + \zeta^2(t)\right]\int_0^R\left(\sum_j \mu^j n^j\right)rdr = k_B T_0 \sum_j n_0^j \tag{A-11}$$

Recall that the derivative of a constant is zero, therefore, the proportionality constant ζ(t) at $t = 0$ or the time when the laser pulse is terminated, LTE has established and the plasma has acquired a spherical symmetry is given by:

$$\zeta^2(0) = \frac{p(0)}{\int_0^R \left(\sum_j \mu^j n^j(r,0) \right) r dr} \tag{A-12}$$

APPENDIX B
CALCULATION OF THE TOTAL ELEMENT NUMBER DENSITY IN MC-LIBS

The conservation of mass or continuity equation in spherical coordinates is given by:

$$\frac{\partial n^j}{\partial t} + \frac{1}{r^2}\frac{\partial}{\partial r}\left(r^2 u n^j\right) = 0 \tag{B-1}$$

where $j = 1,2,\ldots,N$. It is assumed that all constituents occur as two components—atomic and ionic so that the total number density $n^j(r,t) = n_a^j(r,t) + n_i^j(r,t)$, where $n_a^j(r,t)$ and $n_i^j(r,t)$ are number densities of atoms and ions, respectively.

Note that the radial expansion velocity is given by:

$$u(r,t) = \zeta(t) r \tag{B-2}$$

where $\zeta(t)$ is the proportionality coefficient between the collective velocity of particles and the radius and r is the radial coordinate of the particle in the plasma. Substituting Eq. B-2 in Eq. B-1 yields:

$$\frac{\partial n^j}{\partial t} + \frac{1}{r^2}\frac{\partial}{\partial r}\left[\left(r^2 n^j\right)\left(\zeta(t) r\right)\right] = 0 \tag{B-3a}$$

$$\frac{\partial n^j}{\partial t} + \frac{1}{r^2}\zeta(t)\frac{\partial}{\partial r}\left(r^3 n^j\right) = 0 \tag{B-3b}$$

Multiplying both sides of Eq. B-3b by r^3 yields:

$$\frac{\partial}{\partial t}\left(r^3 n^j\right) + \frac{r^3}{r^2}\zeta(t)\frac{\partial}{\partial r}\left(r^3 n^j\right) = 0 \tag{B-4a}$$

$$\frac{\partial}{\partial t}\left(r^3 n^j\right) + r\zeta(t)\frac{\partial}{\partial r}\left(r^3 n^j\right) = 0 \tag{B-4b}$$

Eq. B-4b above is a first-order partial differential equation. A partial differential equation (PDE) is an equation relating a function of two or more independent variables and its partial derivatives. Considering the general equation:

$$a\frac{\partial^2 u}{\partial x^2}+b\frac{\partial^2 u}{\partial x\partial t}+c\frac{\partial^2 u}{\partial t^2}+d\frac{\partial u}{\partial x}+e\frac{\partial u}{\partial t}+fu=g \tag{B-5}$$

where a, b, c, d, e and f may be functions of x, t and even u. The order of the equation is given by the order of the highest derivative. Thus, if one of the functions a, b or c are non-zero, then the PDE is second order. If $a = b = c = 0$ but d or e are non-zero, then the PDE is first order. If the functions a, b, c, d, e and f do not depend on the dependent variable u, then Eq. B-5 is linear otherwise it is non-linear. If $g = 0$, then Eq. B-5 is homogeneous, otherwise it is inhomogeneous.

The general solution of B-4b is given by:

$$r^3 n^j(r,t)=Q^j\left(\frac{r}{R(t)}\right) \tag{B-6}$$

where $Q^j(r/R(t))$ is some function of the argument $r/R(t)$ derived in the course of the solution of Eq. B-4b after multiple renaming of variables. Note that the initial distribution of the number density of jth constituent in the plasma is given by:

$$n^j(r,0)=n_0^j\left(1-k_2 r^2\right)=g^j(r) \tag{B-7}$$

where n_0^j is the initial number density of the jth constituent at the plasma center and k_2 is numerical coefficient which is dependent on the spatial resolution and distribution gradient desired. At $t = 0$, Eq. B-6 becomes:

$$r^3 n^j(r,0)=Q^j\left(\frac{r}{R(0)}\right) \tag{B-8a}$$

$$r^3=Q^j\left(\frac{r}{R(0)}\right)\frac{1}{g^j(r)} \tag{B-8b}$$

After substitution of Eq. B-8b into Eq. B-6 and solving the function Q^j, one can obtain the number density of constituent j as a function of the radial coordinate r of particle in the plasma and time t:

$$n^j(r,t) = \left(\frac{R(0)}{R(t)}\right)^3 g^j\left(r\frac{R(0)}{R(t)}\right) \tag{B-9}$$

APPENDIX C
CALCULATION OF PLASMA TEMPERATURE IN MC-LIBS

The conservation of energy equation is given by:

$$\frac{\partial}{\partial t}\left(\rho\varepsilon+\frac{\rho u^2}{2}\right)=-\vec{\nabla}\left[\vec{u}\left(\rho\varepsilon+p_{total}+\frac{\rho u^2}{2}\right)\right]-q \tag{C-1}$$

where ρ is the gas density and is given by:

$$\rho=\sum_j \mu^j n^j \tag{C-2}$$

ε is the internal energy per unit mass of the gas species and q is the energy loss due to radiation.

Note that the internal energy relation is given by:

$$\rho\varepsilon=k_B T\sum_j \alpha^j n^j \tag{C-3}$$

where α^j is ratio of specific heat capacities. Dalton's law of partial pressures is given by:

$$p_{total}=\sum_j p^j=\sum_j n^j k_B T=k_B T\sum_j n^j \tag{C-4}$$

Substituting Eqs. C-2, C-3 and C-4 into Eq. C-1 yields:

$$\frac{\partial}{\partial t}\left(k_B T\sum_j \alpha^j n^j+\frac{u^2}{2}\sum_j \mu^j n^j\right)=-\vec{\nabla}\left[\vec{u}\left(k_B T\sum_j \alpha^j n^j+k_B T\sum_j n^j+\frac{u^2}{2}\sum_j \mu^j n^j\right)\right]-q \tag{C-5a}$$

$$\frac{\partial}{\partial t}\left(k_B T\sum_j \alpha^j n^j+\frac{u^2}{2}\sum_j \mu^j n^j\right)=-\vec{\nabla}\left[\vec{u}\left(k_B T\sum_j (\alpha^j+1) n^j+\frac{u^2}{2}\sum_j \mu^j n^j\right)\right]-q \tag{C-5b}$$

Recall that the ∇ operator is given by:

$$\nabla^2=\frac{1}{r^2}\frac{\partial}{\partial r}\left(r^2\frac{\partial}{\partial r}\right) \tag{C-6}$$

Substituting Eq. C-6 into Eq. C-5 yields:

$$\frac{\partial}{\partial t}\left(k_B T\sum_j \alpha^j n^j+\frac{u^2}{2}\sum_j \mu^j n^j\right)=-\frac{1}{r^2}\frac{\partial}{\partial r}\left[r^2 u\left(k_B T\sum_j (\alpha^j+1) n^j+\frac{u^2}{2}\sum_j \mu^j n^j\right)\right]-q \tag{C-7}$$

Distributing the partial derivatives on the left-hand side and r^2u on the right-hand side yields:

$$\frac{\partial}{\partial t}k_BT\sum_j \alpha^j n^j + \frac{\partial}{\partial t}\frac{u^2}{2}\sum_j \mu^j n^j = -\frac{1}{r^2}\frac{\partial}{\partial r}\left(r^2 u k_B T\sum_j (\alpha^j + 1)n^j + r^2 u\frac{u^2}{2}\sum_j \mu^j n^j \right) - q \quad \text{(C-8a)}$$

$$\frac{\partial}{\partial t}k_BT\sum_j \alpha^j n^j + \frac{\partial}{\partial t}\frac{u^2}{2}\sum_j \mu^j n^j = -\frac{1}{r^2}\frac{\partial}{\partial r}\left(r^2 u k_B T\sum_j (\alpha^j + 1)n^j + \frac{1}{2}r^2 u^3\sum_j \mu^j n^j \right) - q \quad \text{(C-8b)}$$

Distributing the partial derivatives on the right-hand side yields:

$$\frac{\partial}{\partial t}k_BT\sum_j \alpha^j n^j + \frac{\partial}{\partial t}\frac{u^2}{2}\sum_j \mu^j n^j = -\frac{1}{r^2}\frac{\partial}{\partial r}\left(r^2 u k_B T\sum_j (\alpha^j + 1)n^j \right) - \frac{1}{r^2}\frac{\partial}{\partial r}\left(\frac{1}{2}r^2 u^3\sum_j \mu^j n^j \right) - q \quad \text{(C-9)}$$

Excluding partial time derivatives of u and n^j yields:

$$k_B\sum_j \alpha^j n^j \frac{\partial T}{\partial t} + \frac{u^2}{2}\sum_j \mu^j \frac{\partial n^j}{\partial t} = -uk_B\frac{\partial T}{\partial r}\sum_j (\alpha^j + 1)n^j - \frac{1}{2r^2}\frac{\partial}{\partial r}\left(r^2 u^3\sum_j \mu^j n^j \right) - q \quad \text{(C-10)}$$

With the use of the conservation of mass equation:

$$\frac{\partial n^j}{\partial t} + \frac{1}{r^2}\frac{\partial}{\partial r}\left(r^2 u n^j \right) = 0 \quad \text{(C-11)}$$

and radial expansion velocity equations:

$$u(r,t) = \zeta(t)r \quad \text{(C-12)}$$

Eq. C-10 becomes

$$k_B\sum_j \alpha^j n^j \frac{\partial T}{\partial t} + \frac{u^2}{2}\sum_j \mu^j \frac{\partial n^j}{\partial t} + r^2\zeta\dot{\zeta}\sum_j \mu^j n^j = -\frac{k_BT}{r^2}\frac{\partial}{\partial r}\left(r^2 u^2 T\sum_j n^j \right) - uk_B\frac{\partial T}{\partial r}\sum_j (\alpha^j + 1)n^j - \frac{1}{2r^2}\frac{\partial}{\partial r}\left(r^2 u^3\sum_j \mu^j n^j \right) - q \quad \text{(C-13)}$$

Dividing Eq. C-13 by k_B yields:

$$\sum_j \alpha^j n^j \frac{\partial T}{\partial t} + \frac{u^2}{2k_B}\sum_j \mu^j \frac{\partial n^j}{\partial t} + \frac{r^2\zeta\dot{\zeta}}{k_B}\sum_j \mu^j n^j = -\frac{T}{r^2}\frac{\partial}{\partial r}\left(r^2 u^2 T\sum_j n^j \right) - u\frac{\partial T}{\partial r}\sum_j (\alpha^j + 1)n^j - \frac{1}{2k_B r^2}\frac{\partial}{\partial r}\left(r^2 u^3\sum_j \mu^j n^j \right) - \frac{q}{k_B} \quad \text{(C-14)}$$

Solving Eq. C-14 for $\partial T/\partial t$ yields:

$$\sum_j \alpha^j n^j \frac{\partial T}{\partial t} = -\frac{u^2}{2k_B}\sum_j \mu^j \frac{\partial n^j}{\partial t} - \frac{r^2\zeta\dot{\zeta}}{k}\sum_j \mu^j n^j - \frac{T}{r^2}\frac{\partial}{\partial r}\left(r^2u^2T\sum_j n^j\right) - u\frac{\partial T}{\partial r}\sum_j\left(\alpha^j+1\right)n^j - \frac{1}{2k_Br^2}\frac{\partial}{\partial r}\left(r^2u^3\sum_j \mu^j n^j\right) - \frac{q}{k_B}$$

(C-15)

Dividing both sides of the equation by $\sum(\alpha^j n^j)$ yields:

$$\frac{\partial T}{\partial t} = -\frac{\frac{u^2}{2k_B}\sum_j \mu^j \frac{\partial n^j}{\partial t}}{\sum_j \alpha^j n^j} - \frac{\frac{r^2\zeta\dot{\zeta}}{k_B}\sum_j \mu^j n^j}{\sum_j \alpha^j n^j} - \frac{\frac{T}{r^2}\frac{\partial}{\partial r}\left(r^2u^2T\sum_j n^j\right)}{\sum_j \alpha^j n^j} - \frac{u\frac{\partial T}{\partial r}\sum_j\left(\alpha^j+1\right)n^j}{\sum_j \alpha^j n^j} - \frac{\frac{1}{2k_Br^2}\frac{\partial}{\partial r}\left(r^2u^3\sum_j \mu^j n^j\right)}{\sum_j \alpha^j n^j} - \frac{q}{k_B\sum_j \alpha^j n^j}$$

(C-16)

Simplifying the 4th term on the right-hand side of Eq. C-16 yields:

$$\frac{\partial T}{\partial t} = -\frac{\frac{u^2}{2k_B}\sum_j \mu^j \frac{\partial n^j}{\partial t}}{\sum_j \alpha^j n^j} - \frac{\frac{r^2\zeta\dot{\zeta}}{k_B}\sum_j \mu^j n^j}{\sum_j \alpha^j n^j} - \frac{\frac{T}{r^2}\frac{\partial}{\partial r}\left(r^2u^2T\sum_j n^j\right)}{\sum_j \alpha^j n^j} - \frac{u\frac{\partial T}{\partial r}\left(\sum_j\left(\alpha^j n^j\right)+\sum_j n^j\right)}{\sum_j \alpha^j n^j} - \frac{\frac{1}{2k_Br^2}\frac{\partial}{\partial r}\left(r^2u^3\sum_j \mu^j n^j\right)}{\sum_j \alpha^j n^j} - \frac{q}{k_B\sum_j \alpha^j n^j}$$

$$\frac{\partial T}{\partial t} = -\frac{\frac{u^2}{2k_B}\sum_j \mu^j \frac{\partial n^j}{\partial t}}{\sum_j \alpha^j n^j} - \frac{\frac{r^2\zeta\dot{\zeta}}{k_B}\sum_j \mu^j n^j}{\sum_j \alpha^j n^j} - \frac{\frac{T}{r^2}\frac{\partial}{\partial r}\left(r^2u^2T\sum_j n^j\right)}{\sum_j \alpha^j n^j} - \frac{u\frac{\partial T}{\partial r}\sum_j \alpha^j n^j}{\sum_j \alpha^j n^j} - \frac{u\frac{\partial T}{\partial r}\sum_j n^j}{\sum_j \alpha^j n^j} - \frac{\frac{1}{2k_Br^2}\frac{\partial}{\partial r}\left(r^2u^3\sum_j \mu^j n^j\right)}{\sum_j \alpha^j n^j} - \frac{q}{k_B\sum_j \alpha^j n^j}$$

$$\frac{\partial T}{\partial t} = -\frac{\frac{u^2}{2k_B}\sum_j \mu^j \frac{\partial n^j}{\partial t}}{\sum_j \alpha^j n^j} - \frac{\frac{r^2\zeta\dot{\zeta}}{k_B}\sum_j \mu^j n^j}{\sum_j \alpha^j n^j} - \frac{\frac{T}{r^2}\frac{\partial}{\partial r}\left(r^2u^2T\sum_j n^j\right)}{\sum_j \alpha^j n^j} - \frac{\frac{1}{2k_Br^2}\frac{\partial}{\partial r}\left(r^2u^3\sum_j \mu^j n^j\right)}{\sum_j \alpha^j n^j} - u\frac{\partial T}{\partial r} - \frac{u\frac{\partial}{\partial r}\left(T\sum_j n^j\right)}{\sum_j \alpha^j n^j} - \frac{q}{k_B\sum_j \alpha^j n^j}$$

(C-17)

Substituting $u(r,t)=\zeta(t)r$ into the 4th term of Eq. C-17 yields:

$$\frac{\partial T}{\partial t} = -\frac{\frac{u^2}{2k_B}\sum_j \mu^j \frac{\partial n^j}{\partial t}}{\sum_j \alpha^j n^j} - \frac{\frac{r^2\zeta\dot{\zeta}}{k_B}\sum_j \mu^j n^j}{\sum_j \alpha^j n^j} - \frac{\frac{T}{r^2}\frac{\partial}{\partial r}\left(r^2u^2T\sum_j n^j\right)}{\sum_j \alpha^j n^j} - \frac{\frac{1}{2k_Br^2}\sum_j \mu^j n^j \frac{\partial}{\partial r}\left(r^2\zeta^3r^3\right)}{\sum_j \alpha^j n^j} - u\frac{\partial T}{\partial r} - \frac{u\frac{\partial}{\partial r}\left(T\sum_j n^j\right)}{\sum_j \alpha^j n^j} - \frac{q}{k_B\sum_j \alpha^j n^j}$$

$$\frac{\partial T}{\partial t} = -\frac{\frac{u^2}{2k_B}\sum_j \mu^j \frac{\partial n^j}{\partial t}}{\sum_j \alpha^j n^j} - \frac{\frac{r^2\zeta\dot{\zeta}}{k_B}\sum_j \mu^j n^j}{\sum_j \alpha^j n^j} - \frac{\frac{T}{r^2}\frac{\partial}{\partial r}\left(r^2u^2T\sum_j n^j\right)}{\sum_j \alpha^j n^j} - \frac{\frac{5r^4\zeta^3}{2k_Br^2}\sum_j \mu^j n^j}{\sum_j \alpha^j n^j} - u\frac{\partial T}{\partial r} - \frac{u\frac{\partial}{\partial r}\left(T\sum_j n^j\right)}{\sum_j \alpha^j n^j} - \frac{q}{k_B\sum_j \alpha^j n^j}$$

$$\frac{\partial T}{\partial t} = -\frac{\frac{u^2}{2k_B}\sum_j \mu^j \frac{\partial n^j}{\partial t}}{\sum_j \alpha^j n^j} - \frac{\frac{r^2\zeta\dot{\zeta}}{k_B}\sum_j \mu^j n^j}{\sum_j \alpha^j n^j} - \frac{\frac{T}{r^2}\frac{\partial}{\partial r}\left(r^2u^2T\sum_j n^j\right)}{\sum_j \alpha^j n^j} - \frac{\frac{5r^2\zeta^3}{2k_B}\sum_j \mu^j n^j}{\sum_j \alpha^j n^j} - u\frac{\partial T}{\partial r} - \frac{u\frac{\partial}{\partial r}\left(T\sum_j n^j\right)}{\sum_j \alpha^j n^j} - \frac{q}{k_B\sum_j \alpha^j n^j}$$

(C-18)

Recall that the equation for the radial expansion proportionality constant is given by:

$$\zeta^2(t) = \frac{k_B T(0,t)\sum_j n^j(0,t)}{\int_0^R rdr \sum_j \mu^j n^j(r,t)} \tag{C-19}$$

Substituting Eq. C-19 into the 4th term of Eq. C-18 yields:

$$\frac{\partial T}{\partial t} = -\frac{\frac{u^2}{2k_B}\sum_j \mu^j \frac{\partial n^j}{\partial t}}{\sum_j \alpha^j n^j} - \frac{\frac{r^2 \zeta\dot{\zeta}}{k_B}\sum_j \mu^j n^j}{\sum_j \alpha^j n^j} - \frac{\frac{T}{r^2}\frac{\partial}{\partial r}\left(r^2 u^2 T \sum_j n^j\right)}{\sum_j \alpha^j n^j} - \left(\frac{\frac{5r^2\zeta}{2k_B}\sum_j \mu^j n^j}{\sum_j \alpha^j n^j}\right)\left(\frac{k_B T(0,t)\sum_j n^j(0,t)}{\int_0^R rdr \sum_j \mu^j n^j(r,t)}\right) - u\frac{\partial T}{\partial r} - \frac{u\frac{\partial}{\partial r}\left(T\sum_j n^j\right)}{\sum_j \alpha^j n^j} - \frac{q}{k_B \sum_j \alpha^j n^j}$$

$$\frac{\partial T}{\partial t} = -\frac{\frac{u^2}{2k_B}\sum_j \mu^j \frac{\partial n^j}{\partial t}}{\sum_j \alpha^j n^j} - \frac{\frac{r^2 \zeta\dot{\zeta}}{k_B}\sum_j \mu^j n^j}{\sum_j \alpha^j n^j} - \frac{\frac{T}{r^2}\frac{\partial}{\partial r}\left(r^2 u^2 T \sum_j n^j\right)}{\sum_j \alpha^j n^j} - \left(\frac{\frac{5}{2}r^2\zeta\sum_j \mu^j n^j}{\sum_j \alpha^j n^j}\right)\left(\frac{T(0,t)\sum_j n^j(0,t)}{\int_0^R rdr \sum_j \mu^j n^j(r,t)}\right) - u\frac{\partial T}{\partial r} - \frac{u\frac{\partial}{\partial r}\left(T\sum_j n^j\right)}{\sum_j \alpha^j n^j} - \frac{q}{k_B \sum_j \alpha^j n^j}$$

(C-20)

After further simplification, one can obtain:

$$\frac{\partial T}{\partial t} = -3T\zeta\frac{\sum_j n^j}{\sum_j \alpha^j n^j} - \left(\frac{\frac{5}{2}r^2\zeta\sum_j \mu^j n^j}{\sum_j \alpha^j n^j}\right)\left(\frac{T(0,t)\sum_j n^j(0,t)}{\int_0^R rdr \sum_j \mu^j n^j(r,t)}\right) - u\frac{\partial T}{\partial r} - \frac{u\frac{\partial}{\partial r}\left(T\sum_j n^j\right)}{\sum_j \alpha^j n^j} - \frac{q}{k_B \sum_j \alpha^j n^j}$$

$$\frac{\partial T}{\partial t} = -\zeta\left[3T\frac{\sum_j n^j}{\sum_j \alpha^j n^j} + \left(\frac{\frac{5}{2}r^2\sum_j \mu^j n^j}{\sum_j \alpha^j n^j}\right)\left(\frac{T(0,t)\sum_j n^j(0,t)}{\int_0^R rdr \sum_j \mu^j n^j(r,t)}\right) + r\frac{\partial T}{\partial r} + \frac{r\frac{\partial}{\partial r}\left(T\sum_j n^j\right)}{\sum_j \alpha^j n^j}\right] - \frac{q}{k_B \sum_j \alpha^j n^j}$$

(C-21)

APPENDIX D
CALCULATION OF ATOM, ION AND ELECTRON NUMBER DENSITIES IN MC-LIBS

The Saha equation is given by:

$$\frac{n_i^j}{n_a^j} n_e = 2\frac{U_i^j}{U_a^j}\left(\frac{2\pi m_e k_B T}{h^2}\right)^{3/2} \exp-\left(\frac{\chi^j - \Delta\chi}{k_B T}\right) = s^j(T) \tag{D-1}$$

where $j = 1,\ldots,N$, n_a^j, n_i^j, n_e are the number densities of atoms, ions and electrons, U_a^j and U_i^j are the atomic and ionic partition functions of the jth constituent, respectively, χ^j is the first ionization potential of j, $\Delta\chi$ is the defect or lowering of the ionization potential of atoms due to the electric field of surrounding electrons and the rest of the parameters are defined in pp. 19-23.

The mass conservation equation for each charge state and for each plasma constituent is given by:

$$n_i^j + n_a^j = n^j \tag{D-2}$$

The equation of charge equilibrium for N plasma constituents given by:

$$\sum_j n_i^j = n_e \tag{D-3}$$

The above algebraic system of equations determines the charge distribution for a fixed temperature and densities of elemental plasma constituents. From Eq. D-1, the ion number density is given by:

$$n_i^j = \frac{n_a^j s^j(T)}{n_e} \tag{D-4}$$

Substituting Eq. D-4 into Eq. D-3 yields:

$$\sum_j \frac{n_a^j s^j(T)}{n_e} = n_e \tag{D-5}$$

Multiplying Eq. D-5 by n_e yields:

$$\sum_j \frac{n_a^j s^j(T)}{n_e} n_e = n_e^2$$

$$\sum_j n_a^j s^j(T) = n_e^2 \tag{D-6}$$

Multiplying Eq. D-2 by n_e yields:

$$n_i^j n_e + n_a^j n_e = n^j n_e \tag{D-7}$$

Substituting Eq. D-4 into Eq. D-7 yields the atom number density:

$$n_i^j n_e + n_a^j n_e = n^j n_e$$

$$\frac{n_a^j s^j(T)}{n_e} n_e + n_a^j n_e = n^j n_e$$

$$n_a^j s^j(T) + n_a^j n_e = n^j n_e$$

$$n_a^j \left(s^j(T) + n_e\right) = n^j n_e$$

$$n_a^j = \frac{n^j n_e}{s^j(T) + n_e} \tag{D-8}$$

Substituting Eq. D-8 into Eq. D-6 yields the algebraic equation for n_e which has a unique positive solution:

$$\sum_j n_a^j s^j(T) = n_e^2$$

$$\sum_j \frac{n^j n_e}{s^j(T) + n_e} s^j(T) = n_e^2$$

$$\sum_j \frac{n^j s^j(T) n_e}{s^j(T) + n_e} = n_e^2$$

$$\sum_j \frac{n^j s^j(T)}{s^j(T) + n_e} = n_e \tag{D-9}$$

Substituting Eq. D-8 into Eq. D-4 yields the ion number density:

$$n_i^j = \frac{n_a^j s^j(T)}{n_e}$$

$$n_i^j = \frac{n^j n_e}{s^j(T) + n_e} \frac{s^j(T)}{n_e}$$

$$n_i^j = \frac{n^j s^j(T)}{s^j(T) + n_e} \tag{D-10}$$

APPENDIX E
CERTIFIED CONCENTRATION VALUES OF REFERENCE STANDARDS

Table E-1. Elemental percentage composition of South African aluminum alloy standards.

	B8	D33	S4	S11	SM10	V14	Z8
Al	87.980	84.920	83.791	89.197	84.670	86.742	78.797
Bi	0.099	0.680					
Cr	0.170	0.047	0.130	0.115	0.200	0.180	0.150
Cu	6.950	2.890	2.640	0.980	2.800	4.050	16.050
Fe	0.800	1.150	0.119	0.570	1.960	0.900	1.090
Mg	0.076	0.038	0.350	1.110	1.080	0.025	1.270
Mn	0.400	0.400	0.380	0.500	0.295	0.580	0.260
Ni	0.200	0.500	0.180	0.100	0.065	0.330	0.530
Pb	0.165	0.140	0.130		0.245		
Si	2.330	8.540	1.030	0.450	2.920	6.200	0.840
Sn	0.155	0.048	0.150		0.260	0.280	
Ti	0.160	0.055	0.120	0.065	0.055	0.170	0.170
Zn	0.520	0.590	10.900	6.850	5.450	0.420	0.790
Zr							

Table E-2. Elemental percentage composition of NIST brass standards.

	1107	1108	1110	1111	1112	1113	1114	1115	1116	1117
Cu	61.210	64.950	84.590	87.140	93.380	95.030	96.450	87.960	90.370	93.010
Fe	0.037	0.050	0.033	0.010	0.070	0.043	0.017	0.130	0.046	0.014
Mn		0.025								
Ni	0.098	0.033	0.053	0.022	0.100	0.057	0.021	0.074	0.048	0.020
P					0.009	0.008	0.009	0.005	0.008	0.002
Pb	0.180	0.063	0.033	0.013	0.057	0.026	0.012	0.013	0.042	0.069
Sn	1.040	0.390	0.051	0.019	0.120	0.064	0.027	0.100	0.044	0.021
Zn	37.340	34.420	15.200	12.810	6.300	4.800	3.470	11.730	9.440	6.870

Note: Certified values are obtained from the NIST standard reference materials database [208].

Table E-3. Elemental percentage composition of NIST and Canadian soil standards.

	NIST 1646	NIST 2704	NIST 2710	NIST 2711	CAN SO-2	CAN SO-3
Al	6.250	6.110	6.440	6.530	8.070	3.050
Ba					0.097	0.030
C		3.348				
Ca	0.830	2.600	1.250	2.880	1.960	14.630
Cu			0.295			
Fe	3.350	4.110	3.380	2.890	5.560	1.510
K	1.400	2.000	2.110	2.450	2.450	1.610
La						
Mg	1.090	1.200	0.853	1.050	0.540	4.980
Mn			1.010		0.072	0.052
Na	2.000	0.547	1.140	1.140	1.900	0.740
P		0.100	0.106	0.086	0.300	0.048
Pb			0.553	0.116		
S	0.960	0.400	0.240			
Si	31.000	29.080	28.970	30.440	24.990	15.860
Ti	0.510	0.457	0.283	0.306	0.860	0.200
Zn			0.695			

Note: Certified values are obtained from the NIST standard reference materials database [208] and Natural Resources Canada's Canadian certified reference materials project (CCRMP) database [209].

Table E-4. Elemental percentage composition of different alloy standards.

	NIST 1276a Cu-Ni	NIST 882 Ni Alloy	AA 88395* Ti-Al-V	NIST 654b Ti Alloy	NIST 627 Zn Alloy	NIST 629 Zn Alloy
Al		2.850	6.000	6.340	3.880	5.150
Co						
Cu	67.500	31.020			0.132	1.500
Fe	0.560			0.230	0.023	0.017
Mg	0.120					0.094
Mn	1.010					
Ni	30.800	65.250				
Si						0.078
Ti		0.570	90.000	89.120		
V			4.000	4.310		
Zn					95.965	93.161

Note: Certified values are obtained from the NIST standard reference materials database [208].
*Alfa Aesar standard.

LIST OF REFERENCES

[1] V. Lazic, F. Colao, R. Fantoni and V. Spizzicchino, *Spectrochim. Acta Part B*, 2005, **60**, 1014.

[2] L. G. Blevins, C. R. Shaddix, S. M. Sickafoose and P. M. Walsh, *Appl. Opt.*, 2003, **42**, 6107.

[3] J. A. Bolger, *Appl. Spectrosc.*, 2000, **54**, 181.

[4] R. Barbini, F. Colao, R. Fantoni, A. Palucci, S. Ribezzo, H. J. L. vanderSteen and M. Angelone, *Appl. Phys. B: Lasers Opt.*, 1997, **65**, 101.

[5] S. J. J. Tsai, S. Y. Chen, Y. S. Chung and P. C. Tseng, *Anal. Chem.*, 2006, **78**, 7432.

[6] L. Caneve, F. Colao, R. Fantoni and V. Spizzichino, *Appl. Phys. A: Mater. Sci. Process.*, 2006, **85**, 151.

[7] I. V. Cravetchi, M. Taschuk, Y. Y. Tsui and R. Fedosejevs, *Spectrochim. Acta Part B*, 2004, **59**, 1439.

[8] N. Carmona, M. Oujja, E. Rebollar, H. Romich and M. Castillejo, *Spectrochim. Acta Part B*, 2005, **60**, 1155.

[9] N. Carmona, M. Oujja, S. Gaspard, M. Garcia-Heras, M. A. Villegas and M. Castillejo, *Spectrochim. Acta Part B*, 2007, **62**, 94.

[10] C. M. Bridge, J. Powell, K. L. Steele, M. Williams, J. M. MacInnis and M. E. Sigman, *Appl. Spectrosc.*, 2006, **60**, 1181.

[11] P. Yaroshchyk, R. J. S. Morrison, D. Body and B. L. Chadwick, *Spectrochim. Acta Part B*, 2005, **60**, 986.

[12] P. Fichet, A. Toussaint and J. F. Wagner, *Appl. Phys. A: Mater. Sci. Process.*, 1999, **69**, S591.

[13] M. Lawrence-Snyder, J. Scaffidi, S. M. Angel, A. P. M. Michel and A. D. Chave, *Appl. Spectrosc.*, 2006, **60**, 786.

[14] Y. H. Chen, V. Bulatov, L. Singer, J. Stricker and I. Schechter, *Anal. Bioanal. Chem.*, 2005, **383**, 1090.

[15] P. B. Dixon and D. W. Hahn, *Anal. Chem.*, 2005, **77**, 631.

[16] B. C. Windom, P. K. Diwakar and D. W. Hahn, *Spectrochim. Acta Part B*, 2006, **61**, 788.

[17] D. Anglos, S. Couris and C. Fotakis, *Appl. Spectrosc.*, 1997, **51**, 1025.

[18] L. Burgio, R. J. H. Clark, T. Stratoudaki, M. Doulgeridis and D. Anglos, *Appl. Spectrosc.*, 2000, **54**, 463.

[19] J. H. Scholten, J. M. Teule, V. Zafiropulos and R. M. A. Heeren, *J. Cult. Heritage*, 2000, **1**, S215.

[20] A. J. Lopez, G. Nicolas, M. P. Mateo, V. Pinon, M. J. Tobar and A. Ramil, *Spectrochim. Acta Part B*, 2005, **60**, 1149.

[21] K. Melessanaki, M. Mateo, S. C. Ferrence, P. P. Betancourt and D. Anglos, *Appl. Surf. Sci.*, 2002, **197**, 156.

[22] P. Pouli, K. Melessanaki, A. Giakoumaki, V. Argyropoulos and D. Anglos, *Spectrochim. Acta Part B*, 2005, **60**, 1163.

[23] E. H. Piepmeier, in *Analytical Applications of Lasers*, ed. E. H. Piepmeier, Wiley-Interscience, New York. 1986.

[24] M. Sabsabi and P. Cielo, *Appl. Spectrosc.*, 1995, **49**, 499.

[25] A. Thorne, *Spectrophysics*, Wiley, New York. 1974.

[26] V. Lazic, R. Barbini, F. Colao, R. Fantoni and A. Palucci, *Spectrochim. Acta Part B*, 2001, **56**, 807.

[27] Y.-I. Lee, K. Song and J. Sneddon, *Laser-induced breakdown spectrometry*, Nova Science Publishers, Huntington, N.Y. 2000.

[28] A. K. Knight, N. L. Scherbarth, D. A. Cremers and M. J. Ferris, *Appl. Spectrosc.*, 2000, **54**, 331.

[29] B. Salle, J. L. Lacour, P. Mauchien, P. Fichet, S. Maurice and G. Manhes, *Spectrochim. Acta Part B*, 2006, **61**, 301.

[30] B. Salle, D. A. Cremers, S. Maurice and R. C. Wiens, *Spectrochim. Acta Part B*, 2005, **60**, 479.

[31] L. Niu, H. H. Cho, K. S. Song, H. K. Cha, Y. Kim and Y. I. Lee, *Appl. Spectrosc.*, 2002, **56**, 1511.

[32] M. A. Gondal and T. Hussain, *Talanta*, 2007, **71**, 73.

[33] C. Lopez-Moreno, S. Palanco and J. J. Laserna, *J. Anal. At. Spectrom.*, 2004, **19**, 1479.

[34] C. R. Dockery and S. R. Goode, *Appl. Opt.*, 2003, **42**, 6153.

[35] M. T. Taschuk, Y. Y. Tsui and R. Fedosejevs, *Appl. Spectrosc.*, 2006, **60**, 1322.

[36] T. Trejos and J. R. Almirall, *Talanta*, 2005, **67**, 388.

[37] F. C. DeLucia, A. C. Samuels, R. S. Harmon, R. A. Walters, K. L. McNesby, A. LaPointe, R. J. Winkel and A. W. Miziolek, *IEEE Sens. J.*, 2005, **5**, 681.

[38] R. S. Harmon, F. C. DeLucia, A. LaPointe, R. J. Winkel and A. W. Miziolek, *Anal. Bioanal. Chem.*, 2006, **385**, 1140.

[39] W. Schade, C. Bohling, K. Hohmann and D. Scheel, *Laser Part. Beams*, 2006, **24**, 241.

[40] R. Noll, H. Bette, A. Brysch, M. Kraushaar, I. Monch, L. Peter and V. Sturm, *Spectrochim. Acta Part B*, 2001, **56**, 637.

[41] J. Gruber, J. Heitz, H. Strasser, D. Bauerle and N. Ramaseder, *Spectrochim. Acta Part B*, 2001, **56**, 685.

[42] H. Balzer, M. Hoehne, R. Noll and V. Sturm, *Anal. Bioanal. Chem.*, 2006, **385**, 225.

[43] B. C. Castle, K. Talabardon, B. W. Smith and J. D. Winefordner, *Appl. Spectrosc.*, 1998, **52**, 649.

[44] M. A. Ismail, H. Imam, A. Elhassan, W. T. Youniss and M. A. Harith, *J. Anal. At. Spectrom.*, 2004, **19**, 489.

[45] R. Wisbrun, I. Schechter, R. Niessner, H. Schroder and K. L. Kompa, *Anal. Chem.*, 1994, **66**, 2964.

[46] A. S. Eppler, D. A. Cremers, D. D. Hickmott, M. J. Ferris and A. C. Koskelo, *Appl. Spectrosc.*, 1996, **50**, 1175.

[47] V. Bulatov, R. Krasniker and I. Schechter, *Anal. Chem.*, 1998, **70**, 5302.

[48] R. Krasniker, V. Bulatov and I. Schechter, *Spectrochim. Acta Part B*, 2001, **56**, 609.

[49] M. A. Gondal, T. Hussain, Z. H. Yamani and M. A. Baig, *Talanta*, 2007, **72**, 642.

[50] C. Chaleard, P. Mauchien, N. Andre, J. Uebbing, J. L. Lacour and C. Geertsen, *J. Anal. At. Spectrom.*, 1997, **12**, 183.

[51] L. Xu, V. Bulatov, V. V. Gridin and I. Schechter, *Anal. Chem.*, 1997, **69**, 2103.

[52] I. B. Gornushkin, B. W. Smith, G. E. Potts, N. Omenetto and J. D. Winefordner, *Anal. Chem.*, 1999, **71**, 5447.

[53] S. I. Gornushkin, I. B. Gornushkin, J. M. Anzano, B. W. Smith and J. D. Winefordner, *Appl. Spectrosc.*, 2002, **56**, 433.

[54] D. Bulajic, M. Corsi, G. Cristoforetti, S. Legnaioli, V. Palleschi, A. Salvetti and E. Tognoni, *Spectrochim. Acta Part B*, 2002, **57**, 339.

[55] A. Ciucci, V. Palleschi, S. Rastelli, A. Salvetti, D. P. Singh and E. Tognoni, *Laser Part. Beams*, 1999, **17**, 793.

[56] A. Ciucci, M. Corsi, V. Palleschi, S. Rastelli, A. Salvetti and E. Tognoni, *Appl. Spectrosc.*, 1999, **53**, 960.

[57] *USA*, Patent No. 6657721, 2003.

[58] V. I. Mazhukin, V. V. Nossov, G. Flamant and I. Smurov, *J. Quant. Spectrosc. Radiat. Transfer*, 2002, **73**, 451.

[59] A. De Giacomo, V. A. Shakhatov, G. S. Senesi and S. Orlando, *Spectrochim. Acta Part B*, 2001, **56**, 1459.

[60] A. Casavola, G. Colonna and M. Capitelli, *Appl. Surf. Sci.*, 2003, **208**, 85.

[61] I. B. Gornushkin, A. Y. Kazakov, N. Omenetto, B. W. Smith and J. D. Winefordner, *Spectrochim. Acta Part B*, 2004, **59**, 401.

[62] I. B. Gornushkin, A. Y. Kazakov, N. Omenetto, B. W. Smith and J. D. Winefordner, *Spectrochim. Acta Part B*, 2005, **60**, 215.

[63] I. B. Gornushkin, C. L. Stevenson, B. W. Smith, N. Omenetto and J. D. Winefordner, *Spectrochim. Acta Part B*, 2001, **56**, 1769.

[64] I. B. Gornushkin, S. V. Shabanov, N. Omenetto and J. D. Winefordner, *J. Appl. Phys.*, 2006, **100**.

[65] C. E. Harvey, *Spectrochemical Procedures*, Applied Research Laborratories, Glendale. 1950.

[66] D. A. Cremers and L. J. Radziemski, *Handbook of laser-induced breakdown spectroscopy*, John Wiley, Chichester, England ; Hoboken, NJ. 2006.

[67] K. Song, Y. I. Lee and J. Sneddon, *Appl. Spectrosc. Rev.*, 1997, **32**, 183.

[68] J. Sneddon and Y. I. Lee, *Anal. Lett.*, 1999, **32**, 2143.

[69] L. J. Radziemski, *Spectrochim. Acta Part B*, 2002, **57**, 1109.

[70] K. Song, Y. I. Lee and J. Sneddon, *Appl. Spectrosc. Rev.*, 2002, **37**, 89.

[71] E. Tognoni, V. Palleschi, M. Corsi and G. Cristoforetti, *Spectrochim. Acta Part B*, 2002, **57**, 1115.

[72] J. D. Winefordner, I. B. Gornushkin, T. Correll, E. Gibb, B. W. Smith and N. Omenetto, *J. Anal. At. Spectrom.*, 2004, **19**, 1061.

[73] D. A. Rusak, B. C. Castle, B. W. Smith and J. D. Winefordner, *Crit. Rev. Anal. Chem.*, 1997, **27**, 257.

[74] D. A. Rusak, B. C. Castle, B. W. Smith and J. D. Winefordner, *Trac-Trend Anal. Chem.*, 1998, **17**, 453.

[75] J. M. Vadillo and J. J. Laserna, *Spectrochim. Acta Part B*, 2004, **59**, 147.

[76] M. Z. Martin, M. D. Cheng and R. C. Martin, *Aerosol Sci. Technol.*, 1999, **31**, 409.

[77] T. H. Maiman, *J. Opt. Soc. Am.*, 1960, **50**, 1134.

[78] F. Brech and L. Cross, *Appl. Spectrosc.*, 1962, **16**, 59.

[79] J. Debras-Guedon and N. Liodec, *Comptes Rendus Hebdomadaires Des Seances De L Academie Des Sciences*, 1963, **257**, 3336.

[80] E. F. Runge, R. W. Minck and F. R. Bryan, *Spectrochim. Acta*, 1964, **20**, 733.

[81] H. I. Ferguson, J. E. Mentall and R. W. Nicholls, *Nature*, 1964, **204**, 1295.

[82] Y. P. Raizer, *Sov. Phys. Uspekhi*, 1966, **8**, 650.

[83] L. M. Biberman and G. E. Norman, *Sov. Phys. Uspekhi*, 1967, **10**, 52.

[84] Y. V. Afanasev and O. N. Krokhin, *Soviet Physics Jetp-Ussr*, 1967, **25**, 639.

[85] I. U. P. Raizer, *Laser-induced discharge phenomena*, Consultants Bureau, New York. 1977.

[86] E. Cerrai and R. Trucco, *Energia Nucleare*, 1968, **15**, 581.

[87] K. W. Marich, P. W. Carr, W. J. Treytl and D. Glick, *Anal. Chem.*, 1970, **42**, 1775.

[88] W. J. Treytl, A. J. Saffir, D. Glick, K. W. Marich and J. B. Orenberg, *Anal. Chem.*, 1972, **44**, 1903.

[89] J. D. Blacic, D. R. Pettit and D. A. Cremers, Proceedings of the International Symposium on Spectral Sensing Research, Maui, HI, 1992.

[90] K. Y. Kane, D. A. Cremers, R. C. Elphic and D. S. Mckay, Joint Workshop on New Technologies for Lunar Resource Assessment, Santa Fe, NM, 1992.

[91] D. A. Cremers and L. Radziemski, in *Laser-Induced Breakdown Spectroscopy*, ed. A. Miziolek, V. Palleschi and I. Schechter, Cambridge, New York. 2006.

[92] R. E. Russo, *Appl. Spectrosc.*, 1995, **49**, A14.

[93] C. Boulmer-Leborgne, J. Hermann and B. Dubreuil, *Plasma Sources Sci. Technol.*, 1993, **2**, 219.

[94] M. Von Allmen, *Laser-beam interactions with materials: physical principles and applications*, Springer-Verlag, Berlin ; New York. 1987.

[95] S. B. Wen, X. L. Mao, R. Greif and R. E. Russo, *J. Appl. Phys.*, 2007, **101**.

[96] G. C. Y. Chan, W. T. Chan, X. L. Mao and R. E. Russo, *Spectrochim. Acta Part B*, 2001, **56**, 77.

[97] D. C. Smith and R. G. Meyerand, in *Principles of Laser Plasmas*, ed. G. Bekefi, Wiley-Interscience, New York. 1976, pp. 457.

[98] G. M. Weyl, in *Laser-Induced Plasmas and Applications*, ed. L. Radziemski and D. A. Cremers, Marcel Dekker, New York. 1989, pp. 1.

[99] R. G. Root, in *Laser-Induced Plasmas and Applications*, ed. L. Radziemski and D. A. Cremers, Marcel Dekker, New York. 1989.

[100] S. B. Wen, X. L. Mao, R. Greif and R. E. Russo, *J. Appl. Phys.*, 2007, **101**.

[101] H. Schittenhelm, G. Callies, P. Berger and H. Hugel, *Appl. Surf. Sci.*, 1997, **110**, 493.

[102] J. D. Winefordner, I. B. Gornushkin, D. Pappas, O. I. Matveev and B. W. Smith, *J. Anal. At. Spectrom.*, 2000, **15**, 1161.

[103] S. Yalcin, D. R. Crosley, G. P. Smith and G. W. Faris, *Appl. Phys. B: Lasers Opt.*, 1999, **68**, 121.

[104] G. Callies, H. Schittenhelm, P. Berger and H. Hugel, *Appl. Surf. Sci.*, 1998, **129**, 134.

[105] O. Barthelemy, J. Margot, M. Chaker, M. Sabsabi, F. Vidal, T. W. Johnston, S. Laville and B. Le Drogoff, *Spectrochim. Acta Part B*, 2005, **60**, 905.

[106] J. D. Ingle Jr and S. R. Crouch, *Spectrochemical Analysis*, Prentice-Hall, New Jersey. 1988.

[107] W. Demtroder, *Laser Spectroscopy: Basic Concepts and Instrumentation*, Springer-Verlag, New York. 1982.

[108] A. P. Thorne, U. Litzén and S. Johansson, *Spectrophysics: principles and applications*, Springer, New York. 1999.

[109] I. B. Gornushkin, L. A. King, B. W. Smith, N. Omenetto and J. D. Winefordner, *Spectrochim. Acta Part B*, 1999, **54**, 1207.

[110] N. Konjevic, *Phys. Rep.*, 1999, **316**, 339.

[111] C. T. J. Alkemade, *Metal vapours in flames*, Pergamon Press, Oxford [Oxfordshire] ; New York. 1982.

[112] *Melles Griot Catalog: The Practical Application of Light*, Barloworld Scientific. 2007.

[113] C. Palmer and E. Loewen, *Diffraction Grating Handbook*, Newport Corporation. 2005.

[114] The Optics of Spectroscopy - A TUTORIAL, http://www.jobinyvon.com/, Last Accessed April 14, 2008.

[115] *Andor Technology: Scientific Digital Camera Solutions*. 2006.

[116] G. Cristoforetti, S. Legnaioli, V. Palleschi, A. Salvetti, E. Tognoni, P. A. Benedetti, F. Brioschi and F. Ferrario, *J. Anal. At. Spectrom.*, 2006, **21**, 697.

[117] W. T. Y. Mohamed, *Optics & Laser Technology*, 2008, **40**, 30.

[118] C. Latkoczy and T. Ghislain, *J. Anal. At. Spectrom.*, 2006, **21**, 1152.

[119] L. Radziemski, D. A. Cremers, K. Benelli, C. Khoo and R. D. Harris, *Spectrochim. Acta Part B*, 2005, **60**, 237.

[120] V. Hohreiter and D. W. Hahn, *Anal. Chem.*, 2005, **77**, 1118.

[121] C. Lopez-Moreno, K. Amponsah-Manager, B. W. Smith, I. B. Gornushkin, N. Omenetto, S. Palanco, J. J. Laserna and J. D. Winefordner, *J. Anal. At. Spectrom.*, 2005, **20**, 552.

[122] *USA*, Patent No. 6657721, 2003.

[123] A. M. El Sherbini, T. M. El Sherbini, H. Hegazy, G. Cristoforetti, S. Legnaioli, V. Palleschi, L. Pardini, A. Salvetti and E. Tognoni, *Spectrochim. Acta Part B*, 2005, **60**, 1573.

[124] E. Tognoni, V. Palleschi, M. Corsi, G. Cristoforetti, N. Omenetto, I. Gornushkin, B. W. Smith and J. D. Winefordner, in *Laser Induced Breakdown Spectroscopy*, ed. A. Miziolek, V. Palleschi and H. Schechter, Cambridge University Press, New York. 2006.

[125] M. Corsi, G. Cristoforetti, V. Palleschi, A. Salvetti and E. Tognoni, Proceedings of the International Conference on LASERS, Albuquerque, NM (USA), 2000.

[126] W. T. Chan and R. E. Russo, *Spectrochim. Acta Part B*, 1991, **46**, 1471.

[127] R. E. Russo, X. L. Mao and S. S. Mao, *Anal. Chem.*, 2002, **74**, 70a.

[128] D. Bleiner, Z. Y. Chen, D. Autrique and A. Bogaerts, *J. Anal. At. Spectrom.*, 2006, **21**, 910.

[129] X. L. Mao, A. C. Ciocan, O. V. Borisov and R. E. Russo, *Appl. Surf. Sci.*, 1998, **129**, 262.

[130] H. W. Drawin and P. Felenbok, *Data for Plasmas in Local Thermodynamic Equilibrium*, Gauthier-Villars, Paris. 1965.

[131] H. R. Griem, *Plasma Spectroscopy*, McGraw-Hill, New York. 1964.

[132] O. Barthelemy, J. Margot, S. Laville, F. Vidal, M. Chaker, B. Le Drogoff, T. W. Johnston and M. Sabsabi, *Appl. Spectrosc.*, 2005, **59**, 529.

[133] M. Capitelli, F. Capitelli and A. Eletskii, *Spectrochim. Acta Part B*, 2000, **55**, 559.

[134] H. Moon, K. Herrera, B. W. Smith, J. D. Winefordner and N. Omenetto, in *Pittcon*, New Orleans. 2008.

[135] A. Sola, M. D. Calzada and A. Gamero, *J. Phys. D: Appl. Phys.*, 1995, **28**, 1099.

[136] F. Bredice, F. O. Borges, H. Sobral, M. Villagran-Muniz, H. O. Di Rocco, G. Cristoforetti, S. Legnaioli, V. Palleschi, L. Pardini, A. Salvetti and E. Tognoni, *Spectrochim. Acta Part B*, 2006, **61**, 1294.

[137] NIST Atomic Spectra Database, http://physics.nist.gov/PhysRefData/ASD/Html/ref.html, Last Accessed April 14, 2008.

[138] E. Tognoni, G. Cristoforetti, S. Legnaioli, V. Palleschi, A. Salvetti, M. Mueller, U. Panne and I. Gornushkin, *Spectrochim. Acta Part B*, 2007, **62**, 1302.

[139] H. R. Griem, *Spectral line broadening by plasmas*, Academic Press, New York. 1974.

[140] N. Konjevic, A. Lesage, J. R. Fuhr and W. L. Wiese, *J. Phys. Chem. Ref. Data*, 2002, **31**, 819.

[141] N. Konjevic and W. L. Wiese, *J. Phys. Chem. Ref. Data*, 1990, **19**, 1307.

[142] N. Konjevic, M. S. Dimitrijevic and W. L. Wiese, *J. Phys. Chem. Ref. Data*, 1984, **13**, 619.

[143] N. Konjevic, M. S. Dimitrijevic and W. L. Wiese, *J. Phys. Chem. Ref. Data*, 1984, **13**, 649.

[144] A. Escarguel, B. Ferhat, A. Lesage and J. Richou, *J. Quant. Spectrosc. Radiat. Transfer*, 2000, **64**, 353.

[145] J. Ashkenazy, R. Kipper and M. Caner, *Phys. Rev. A*, 1991, **43**, 5568.

[146] Y. Hanaoka, T. Sakurai, M. Noguchi and K. Ichimoto, *New X-Ray Results, the Next Generation of X-Ray Observatories and Gamma Ray Burst Afterglow Physics*, 2004, **34**, 2753.

[147] A. M. El Sherbini, H. Hegazy and T. M. El Sherbini, *Spectrochim. Acta Part B*, 2006, **61**, 532.

[148] V. Fischer, V. Bernshtam, H. Golten and Y. Maron, *Phys. Rev. A: At. Mol. Opt. Phys.*, 1996, **53**, 2425.

[149] J. P. Nicholson, *Plasma Phys. Controlled Fusion*, 1989, **31**, 1433.

[150] F. Schreier, *J. Quant. Spectrosc. Radiat. Transfer*, 1992, **48**, 743.

[151] N. Metropolis, A. W. Rosenbluth, M. N. Rosenbluth, A. H. Teller and E. Teller, *J. Chem. Phys.*, 1953, **21**, 1087.

[152] S. Kirkpatrick, C. D. Gelatt and M. P. Vecchi, *Science*, 1983, **220**, 671.

[153] W. H. Press, *Numerical recipes in C: the art of scientific computing*, Cambridge University Press, Cambridge Cambridgeshire ; New York. 1992.

[154] I. B. Gornushkin, A. Ruiz-Medina, J. M. Anzano, B. W. Smith and J. D. Winefordner, *J. Anal. At. Spectrom.*, 2000, **15**, 581.

[155] S. Palanco and J. J. Laserna, *J. Anal. At. Spectrom.*, 2000, **15**, 1321.

[156] F. R. Doucet, T. F. Belliveau, J. L. Fortier and J. Hubert, *Appl. Spectrosc.*, 2007, **61**, 327.

[157] L. Barrette and S. Turmel, *Spectrochim. Acta Part B*, 2001, **56**, 715.

[158] M. Z. Martin, N. Labbe, T. G. Rials and S. D. Wullschleger, *Spectrochim. Acta Part B*, 2005, **60**, 1179.

[159] H. Fink, U. Panne and R. Niessner, *Anal. Chem.*, 2002, **74**, 4334.

[160] B. Bousquet, J. B. Sirven and L. Canioni, *Spectrochim. Acta Part B*, 2007, **62**, 1582.

[161] J. B. Sirven, B. Bousquet, L. Canioni, L. Sarger, S. Tellier, M. Potin-Gautier and I. Le Hecho, *Anal. Bioanal. Chem.*, 2006, **385**, 256.

[162] L. E. Garcia-Ayuso, J. Amador-Hernandez, J. M. Fernandez-Romero and M. D. L. de Castro, *Anal. Chim. Acta*, 2002, **457**, 247.

[163] J. B. Sirven, B. Bousquet, L. Canioni and L. Sarger, *Anal. Chem.*, 2006, **78**, 1462.

[164] A. Jurado-Lopez and M. D. L. de Castro, *Appl. Spectrosc.*, 2003, **57**, 349.

[165] C. Bohling, D. Scheel, K. Hohmann, W. Schade, M. Reuter and G. Holl, *Appl. Opt.*, 2006, **45**, 3817.

[166] P. Yaroshchyk, D. Body, R. J. S. Morrison and B. L. Chadwick, *Spectrochim. Acta Part B*, 2006, **61**, 200.

[167] A. De Giacomo, M. Dell'Aglio, O. De Pascale, R. Gaudiuso, R. Teghil, A. Santagata and G. P. Parisi, *Appl. Surf. Sci.*, 2007, **253**, 7677.

[168] Kurucz Atomic Spectral Line Database, http://www.pmp.uni-hannover.de/cgi-bin/ssi/test/kurucz/sekur.html, Last Accessed April 14, 2008.

[169] J. Halenka, *Astron. Astrophys. Sup.*, 1989, **81**, 303.

[170] J. Halenka and J. Madej, *Acta Astronomica*, 2002, **52**, 195.

[171] G. Cristoforetti, S. Legnaioli, V. Palleschi, A. Salvetti and E. Tognoni, *Spectrochim. Acta Part B*, 2004, **59**, 1907.

[172] J. A. Aguilera and C. Aragon, *Appl. Surf. Sci.*, 2002, **197-198**, 273.

[173] *Personal communication with Dr. Igor Gornushkin*, 2008.

[174] J. A. Aguilera and C. Aragon, *Spectrochim. Acta Part B*, 2004, **59**, 1861.

[175] J. A. Aguilera, J. Bengoechea and C. Aragon, *Spectrochim. Acta Part B*, 2003, **58**, 221.

[176] C. A. D'Angelo, D. M. D. Pace, G. Bertuccelli and D. Bertuccelli, *Spectrochim. Acta Part B*, 2008, **63**, 367.

[177] C. Aragon and J. A. Aguilera, *Appl. Spectrosc.*, 1997, **51**, 1632.

[178] E. M. Monge, C. Aragon and J. A. Aguilera, *Appl. Phys. A: Mater. Sci. Process.*, 1999, **69**, S691.

[179] J. A. Aguilera, C. Aragon and J. Bengoechea, *Appl. Opt.*, 2003, **42**, 5938.

[180] C. Aragon, F. Penalba and J. A. Aguilera, *Appl. Phys. A: Mater. Sci. Process.*, 2004, **79**, 1145.

[181] C. Aragon, F. Penalba and J. A. Aguilera, *Anal. Bioanal. Chem.*, 2006, **385**, 295.

[182] S. H. Tavassoli, I. V. Cravetchi and R. Fedosejevs, *IEEE Transactions on Plasma Science*, 2006, **34**, 2594.

[183] J. Scaffidi, W. Pearman, M. Lawrence, J. C. Carter, B. W. Colston and S. M. Angel, *Appl. Opt.*, 2004, **43**, 5243.

[184] M. Corsi, G. Cristoforetti, M. Giuffrida, M. Hidalgo, S. Legnaioli, V. Palleschi, A. Salvetti, E. Tognoni and C. Vallebona, *Spectrochim. Acta Part B*, 2004, **59**, 723.

[185] R. Noll, R. Sattmann, V. Sturm and S. Winkelmarm, *J. Anal. At. Spectrom.*, 2004, **19**, 419.

[186] B. C. Castle, K. Visser, B. W. Smith and J. D. Winefordner, *Appl. Spectrosc.*, 1997, **51**, 1017.

[187] M. Corsi, G. Cristoforetti, M. Hidalgo, D. Iriarte, S. Legnaioli, V. Palleschi, A. Salvetti and E. Tognoni, *Appl. Spectrosc.*, 2003, **57**, 715.

[188] T. M. Di Palma, S. Orlando, A. Giardiniguidoni, A. J. Paul, J. W. Hastie and A. Mele, *Appl. Surf. Sci.*, 1995, **86**, 68.

[189] I. Borgia, L. Burgio, M. Corsi, R. Fantoni, V. Palleschi, A. Salvetti, M. Squarcialupi and E. Tognoni, *J. Cult. Heritage*, 2000, **1**, S281.

[190] M. Corsi, G. Cristoforetti, V. Palleschi, A. Salvetti and E. Tognoni, *Eur. Phys, J. D*, 2001, **13**, 373.

[191] M. Corsi, V. Palleschi, A. Salvetti and E. Tognoni, *Clean Air*, 2002, **3**, 69.

[192] M. Corsi, G. Cristoforetti, M. Hidalgo, S. Legnaioli, V. Palleschi, A. Salvetti, E. Tognoni and C. Vallebona, *Appl. Opt.*, 2003, **42**, 6133.

[193] F. Colao, R. Fantoni, V. Lazic, L. Caneve, A. Giardini and V. Spizzichino, *J. Anal. At. Spectrom.*, 2004, **19**, 502.

[194] V. S. Burakov and S. N. Raikov, *Spectrochim. Acta Part B*, 2007, **62**, 217.

[195] J. M. Baldwin, *Appl. Spectrosc.*, 1970, **24**, 429.

[196] X. L. Mao, A. C. Ciocan and R. E. Russo, *Appl. Spectrosc.*, 1998, **52**, 913.

[197] O. V. Borisov, X. L. Mao, A. Fernandez, M. Caetano and R. E. Russo, *Spectrochim. Acta Part B*, 1999, **54**, 1351.

[198] E. F. Cromwell and P. Arrowsmith, *Appl. Spectrosc.*, 1995, **49**, 1652.

[199] M. Gagean and J. M. Mermet, *Spectrochim. Acta Part B*, 1998, **53**, 581.

[200] Y. Iida, *Appl. Spectrosc.*, 1989, **43**, 229.

[201] S. L. Lui and N. H. Cheung, *Spectrochim. Acta Part B*, 2003, **58**, 1613.

[202] J. M. Vadillo, J. M. F. Romero, C. Rodriguez and J. J. Laserna, *Surf. Interface Anal.*, 1999, **27**, 1009.

[203] J. R. Thompson, R. C. Wiens, J. E. Barefield, D. T. Vaniman, H. E. Newsom and S. M. Clegg, *J. Geophys. Res.-Planet*, 2006, **111**.

[204] B. Salle, J. L. Lacour, E. Vors, P. Fichet, S. Maurice, D. A. Cremers and R. C. Wiens, *Spectrochim. Acta Part B*, 2004, **59**, 1413.

[205] Z. A. Arp, D. A. Cremers, R. C. Wiens, D. M. Wayne, B. A. Salle and S. Maurice, *Appl. Spectrosc.*, 2004, **58**, 897.

[206] F. Colao, R. Fantoni, V. Lazic, A. Paolini, F. Fabbri, G. G. Ori, L. Marinangeli and A. Baliva, *Planet. Space Sci.*, 2004, **52**, 117.

[207] R. Brennetot, J. L. Lacour, E. Vors, A. Rivoallan, D. Vailhen and S. Maurice, *Appl. Spectrosc.*, 2003, **57**, 744.

[208] NIST Standard Reference Materials, http://ts.nist.gov/measurementservices/referencematerials/index.cfm, Last Accessed April 14, 2008.

[209] Natural Resources Canada's Canadian Certified Reference Materials Project, http://www.nrcan-rncan.gc.ca/mms/canmet-mtb/mmsl-lmsm/ccrmp/ccrmp-e.htm., Last Accessed April 14, 2008.

[210] J. Bublitz, C. Dolle, W. Schade, A. Hartmann and R. Horn, *Eur. J. Soil Sci.*, 2001, **52**, 305.

[211] R. Barbini, F. Colao, R. Fantoni, A. Palucci and F. Capitelli, *Appl. Phys. A: Mater. Sci. Process.*, 1999, **69**, S175.

[212] M. Z. Martin, N. Labbe, N. Andre, R. Harris, M. Ebinger, S. D. Wullschleger and A. A. Vass, *Spectrochim. Acta Part B*, 2007, **62**, 1426.

[213] M. Corsi, G. Cristoforetti, M. Hidalgo, S. Legnaioli, V. Palleschi, A. Salvetti, E. Tognoni and C. Vallebona, *Appl. Geochem.*, 2006, **21**, 748.

[214] A. Y. Kazakov, I. B. Gornushkin, N. Omenetto, B. W. Smith and J. D. Winefordner, *Appl. Opt.*, 2006, **45**, 2810.

BIOGRAPHICAL SKETCH

Kathleen Kate Herrera was born on December 3, 1979 in Manila, Philippines. She attended Our Lady of Grace Academy and graduated salutatorian of the high school class of 1996. She pursued her Bachelor's degree in Chemistry at the University of the Philippines in Diliman, Quezon City and graduated in April 2000. In October 2000, she passed the Chemistry board licensure examination. Afterwards, Kate joined the junior faculty of the Institute of Chemistry at the University of the Philippines where she worked as a chemistry laboratory instructor for three years. In August 2003, Kate moved to Gainesville, Florida and began her graduate studies in analytical chemistry at the University of Florida. She completed her doctoral research under the supervision on Dr. James D. Winefordner in August 2008.